

UC Berkeley

UC Berkeley Electronic Theses and Dissertations

Title

Experimental Studies of Physiological Flow Through a Cerebral Saccular Aneurysm

Permalink

<https://escholarship.org/uc/item/2w9037fh>

Author

Tsai, William W.

Publication Date

2009

Peer reviewed|Thesis/dissertation

**Experimental Studies of Physiological Flow Through a Cerebral Saccular
Aneurysm**

by

William W. Tsai

Bachelor of Science (University of California, Berkeley) 2003
Masters of Science (University of California, Berkeley) 2006

A dissertation submitted in partial satisfaction of the
requirements for the degree of
Doctor of Philosophy

in

Engineering - Mechanical Engineering

in the

GRADUATE DIVISION
of the
UNIVERSITY of CALIFORNIA, BERKELEY

Committee in charge:

Professor Ömer Savas, Chair
Professor Andrew Szeri
Professor David Saloner

Fall 2009

The dissertation of William W. Tsai is approved:

Chair

Date

Date

Date

University of California, Berkeley

Fall 2009

**Experimental Studies of Physiological Flow Through a Cerebral Saccular
Aneurysm**

Copyright Fall 2009

by

William W. Tsai

Abstract

Experimental Studies of Physiological Flow Through a Cerebral Saccular Aneurysm

by

William W. Tsai

Doctor of Philosophy in Engineering - Mechanical Engineering

University of California, Berkeley

Professor Ömer Savaş, Chair

Experiments are conducted to model the flow within a cerebral saccular aneurysm located at the basilar artery bifurcation. The flow phantom modeling the aneurysm consists of a nearly spherical dome located at the flow divider of a 90° bifurcation. To ensure that the experiments are physiologically relevant, a pulsatile pumping system replicates a measured basilar artery waveform at the inlet. In addition, the Reynolds and Sexl-Womersley numbers are matched with physiological conditions. The flow rate through the outlets of the bifurcation are controlled by a pair of needle valves. This control allows study of the effect of branching ratio. Three techniques are applied to characterize the flow. Flow visualization provides pathline images that are used to qualitatively define flow structures and patterns. Particle image velocimetry is used to measure the flow velocity across multiple cross sections of the flow. Post-processing of the data allows in-plane wall shear stresses to be calculated. Lastly, stereoscopic particle image velocimetry allows the

3D velocity field and in-plane wall shear stresses to be determined on an orthogonal cross section of the flow. Combining the information obtained through the experiments, the flow behavior over a single physiological waveform is characterized.

The flow characterization centers around two major features: an inlet wall jet that originates from the neck of the aneurysm and wraps around the dome and a circulation region that dominates the center volume of the dome. The motion of these structures during the waveform are captured and detailed. Wall shear stresses are found for points along the dome over the course of a waveform. In-plane maximum wall shear stress magnitudes over the entire dome vary from $6.8-18.6 \frac{\text{dynes}}{\text{cm}^2}$ in the PIV planes and $13.9-31.0 \frac{\text{dynes}}{\text{cm}^2}$ in the SPIV planes. Total wall shear stress magnitudes can be calculated for three points intersection points. Mean wall shear stress magnitudes at these points range from $3.28-7.94 \frac{\text{dynes}}{\text{cm}^2}$. In particular, the flow conditions that had nearly symmetric outlet flow rates had the lower WSS magnitudes of the test cases.

The primary effect of the branching ratio on the flow behavior is to alter the location and displacement of the circulation region and inlet jet. For flows with a large outlet differentials, the inlet flow shows strong direction preference entering as a wall jet. For flows with small outlet differentials, the inlet flow forms a expanding inlet jet that does not show strong direction preferences. The WSS measurements matches well with computational fluid dynamics simulations of cerebral saccular aneurysms, reinforcing the theory that lower than normal WSS values plays a role in aneurysm growth. Future experimental research will need to focus on implementing techniques that provide the complete 3D flow field and that uses a non-Newtonian working fluid to better simulate the behavior of blood.

Professor Ömer Savaş
Dissertation Committee Chair

Contents

List of Figures	iii
List of Tables	xiii
Symbols and Abbreviations	xv
1 Introduction	1
1.1 Aneurysm Formation, Growth, and Rupture	2
1.2 Examining Cerebral Aneurysm Growth Through <i>In Vitro</i> Experimental Techniques	7
2 Experimental Setup	11
2.1 Flow Phantom	11
2.2 Flow Parameters	13
2.2.1 Working Fluid	13
2.2.2 Similarity	15
2.2.3 Newtonian versus Non-Newtonian Fluid Behavior	16
2.3 Flow Waveform	18
2.4 Pulsatile Pumping System	18
2.4.1 Pumping System	20
2.4.2 Evaluating System Performance	22
2.5 Flow Loop	25
2.6 Experimental Variables	28
3 Flow Visualization	31
3.1 FV: Theory	31
3.2 FV: Experimental Setup	32
3.2.1 Seed Particles	33
3.2.2 Illumination	34
3.2.3 Imaging	36
3.3 FV: Results	36
3.4 FV: Discussion	64

3.4.1	Relaxation Phase	64
3.4.2	Ramp Up Phase	68
3.4.3	Ramp Down Phase	70
3.5	FV: Conclusion	72
4	Particle Image Velocimetry	74
4.1	PIV: Theory	74
4.2	PIV: Setup	75
4.2.1	Illumination	75
4.2.2	Seed Particles	77
4.2.3	Imaging	77
4.2.4	Algorithms	77
4.3	PIV: Post Processing	79
4.3.1	Phase Averaging	79
4.3.2	Wall Shear Stress	80
4.3.3	Second Invariant of the Velocity Gradient, Q	82
4.4	PIV: Results	83
4.5	PIV: Discussion	169
4.5.1	Velocity	169
4.5.2	Q	170
4.5.3	WSS	171
4.6	Conclusion	176
5	Stereoscopic Particle Image Velocimetry	178
5.1	SPIV: Theory	178
5.1.1	SPIV Imaging Configurations	179
5.2	SPIV: Setup	185
5.2.1	Seed Particles	185
5.2.2	Illumination	185
5.2.3	Imaging	186
5.2.4	Algorithms	189
5.3	SPIV:Post-Processing	192
5.4	SPIV: Results	194
5.5	SPIV: Discussion	233
5.5.1	Velocity and Q	233
5.5.2	WSS	240
6	Closing Remarks	243
	Bibliography	247

List of Figures

1.1	The bifurcation of the basilar artery into the posterior cerebral artery relative to the brain (left) and a magnified inset (right) [24].	8
1.2	The geometric differences between (a) saccular and (b) fusiform aneurysms. The top images represent healthy arterial geometries while the lower images show diseased arterial geometries. The saccular aneurysm is labeled to define parts that will be commonly referenced.	9
2.1	Dimensions of the simplified model of a cerebral saccular basilar aneurysm.	13
2.2	Upper: Photograph of the side (left) and front (right) of the flow phantom. Lower: Diagram of the side (left) and front (right) of the flow phantom. The BK-7 glass windows are shaded in gray.	14
2.3	Comparison of the viscous properties of blood, glycerol, and Separan solution at shear rates from 0.25 to $400s^{-1}$ carried out by Steiger et al. [59].	17
2.4	Input waveform for pulsatile flow pattern based on measurements by Kato et al. [33].	19
2.5	Diagram (a) and photograph (b) of the gear-piston pumping system.	23
2.6	Comparison of the sinusoidal input waveform (solid line), mean output flow (dashed line), and spread of the extrema (dotted lines).	25
2.7	Frequency response of the system.	26
2.8	Comparison of the coronary waveform [39] (solid line), mean output flow (dashed line), and spread of the extrema (dotted lines).	26
2.9	Comparison of the carotid input waveform [32] (solid line), mean output flow (dashed line), and spread of the extrema (dotted lines).	27
2.10	Phase-adjusted flow output measurements for a basilar artery bifurcation experiment. The input waveform (solid line) drives the pump. The output flow is divided into two outlets (broken lines).	27
2.11	Diagram of the complete experimental setup.	28
2.12	Planes along which data are collected for FV and PIV.	30
3.1	Laser sheet lens configuration using a spherical and cylindrical lens as seen from (a) above (e.g. the point of view of the camera), and (b) the side.	35

3.2	Flow visualization images at the midplane for branching ratio of 20:80 over one cycle indicated by the points in the plot of the waveform cycle.	37
3.3	Flow visualization images at the midplane for branching ratio of 25:75 over one cycle indicated by the points in the plot of the waveform cycle.	38
3.4	Flow visualization images at the midplane for branching ratio of 33:67 over one cycle indicated by the points in the plot of the waveform cycle.	39
3.5	Flow visualization images at the midplane for branching ratio of 46:54 over one cycle indicated by the points in the plot of the waveform cycle.	40
3.6	Flow visualization images at the midplane for branching ratio of 48:52 over one cycle indicated by the points in the plot of the waveform cycle.	41
3.7	Flow visualization images at the midplane for branching ratio of 50:50 over one cycle indicated by the points in the plot of the waveform cycle.	42
3.8	Flow visualization images at the midplane for branching ratio of 67:33 over one cycle indicated by the points in the plot of the waveform cycle.	43
3.9	Flow visualization images at the midplane for branching ratio of 75:25 over one cycle indicated by the points in the plot of the waveform cycle.	44
3.10	Flow visualization images at the midplane for branching ratio of 80:20 over one cycle indicated by the points in the plot of the waveform cycle.	45
3.11	Flow visualization images at the upper-quarter plane for branching ratio of 20:80 over one cycle indicated by the points in the plot of the waveform cycle.	46
3.12	Flow visualization images at the upper-quarter plane for branching ratio of 25:75 over one cycle indicated by the points in the plot of the waveform cycle.	47
3.13	Flow visualization images at the upper-quarter plane for branching ratio of 33:67 over one cycle indicated by the points in the plot of the waveform cycle.	48
3.14	Flow visualization images at the upper-quarter for branching ratio of 46:54 over one cycle indicated by the points in the plot of the waveform cycle. .	49
3.15	Flow visualization images at the upper-quarter for branching ratio of 48:52 over one cycle indicated by the points in the plot of the waveform cycle. .	50
3.16	Flow visualization images at the upper-quarter plane for branching ratio of 50:50 over one cycle indicated by the points in the plot of the waveform cycle.	51
3.17	Flow visualization images at the upper-quarter plane for branching ratio of 67:33 over one cycle indicated by the points in the plot of the waveform cycle.	52
3.18	Flow visualization images at the upper-quarter plane for branching ratio of 75:25 over one cycle indicated by the points in the plot of the waveform cycle.	53
3.19	Flow visualization images at the upper-quarter plane for branching ratio of 80:20 over one cycle indicated by the points in the plot of the waveform cycle.	54
3.20	Flow visualization images at the lower-quarter for branching ratio of 20:80 over one cycle indicated by the points in the plot of the waveform cycle. .	55
3.21	Flow visualization images at the lower-quarter for branching ratio of 25:75 over one cycle indicated by the points in the plot of the waveform cycle. .	56
3.22	Flow visualization images at the lower-quarter for branching ratio of 33:67 over one cycle indicated by the points in the plot of the waveform cycle. .	57
3.23	Flow visualization images at the lower-quarter for branching ratio of 46:54 over one cycle indicated by the points in the plot of the waveform cycle. .	58

3.24	Flow visualization images at the lower-quarter for branching ratio of 48:52 over one cycle indicated by the points in the plot of the waveform cycle.	59
3.25	Flow visualization images at the lower-quarter for branching ratio of 50:50 over one cycle indicated by the points in the plot of the waveform cycle.	60
3.26	Flow visualization images at the lower-quarter for branching ratio of 67:33 over one cycle indicated by the points in the plot of the waveform cycle.	61
3.27	Flow visualization images at the lower-quarter for branching ratio of 75:25 over one cycle indicated by the points in the plot of the waveform cycle.	62
3.28	Flow visualization images at the lower-quarter for branching ratio of 80:20 over one cycle indicated by the points in the plot of the waveform cycle.	63
3.29	The division of the waveform that are used to in the discussion of the flow visualization images.	65
3.30	A pair of sample flow visualization images during relaxation (above) and rapid rise (below) labeled with terms that are used in the describing the flow visualization results from the midplane (<i>top row</i>), the upper quarter-plane (<i>middle row</i>), and the lower quarter-plane (<i>bottom row</i>).	66
4.1	An illustration of the key components of a PIV setup [50].	76
4.2	Definition of <i>angle from tip</i> that is used to describe dome coordinates in the PIV WSS plots)	82
4.3	Velocity vector with velocity vector field and instantaneous streamlines overlaid for the midplane for a branching ratio of 20:80 over one cycle indicated by the points on the waveform cycle.	85
4.4	Velocity vector with velocity vector field and instantaneous streamlines overlaid for the midplane for a branching ratio of 25:75 over one cycle indicated by the points on the waveform cycle.	86
4.5	Velocity vector with velocity vector field and instantaneous streamlines overlaid for the midplane for a branching ratio of 33:67 over one cycle indicated by the points on the waveform cycle.	87
4.6	Velocity vector with velocity vector field and instantaneous streamlines overlaid for the midplane for a branching ratio of 46:54 over one cycle indicated by the points on the waveform cycle.	88
4.7	Velocity vector with velocity vector field and instantaneous streamlines overlaid for the midplane for a branching ratio of 48:52 over one cycle indicated by the points on the waveform cycle.	89
4.8	Velocity vector with velocity vector field and instantaneous streamlines overlaid for the midplane for a branching ratio of 50:50 over one cycle indicated by the points on the waveform cycle.	90
4.9	Velocity vector with velocity vector field and instantaneous streamlines overlaid for the midplane for a branching ratio of 67:33 over one cycle indicated by the points on the waveform cycle.	91
4.10	Velocity vector with velocity vector field and instantaneous streamlines overlaid for the midplane for a branching ratio of 75:25 over one cycle indicated by the points on the waveform cycle.	92

4.11	Velocity vector with velocity vector field and instantaneous streamlines overlaid for the midplane for a branching ratio of 80:20 over one cycle indicated by the points on the waveform cycle.	93
4.12	Velocity vector with velocity vector field and instantaneous streamlines overlaid for the upper quarter-plane for a branching ratio of 20:80 over one cycle indicated by the points on the waveform cycle.	94
4.13	Velocity vector with velocity vector field and instantaneous streamlines overlaid for the upper quarter-plane for a branching ratio of 25:75 over one cycle indicated by the points on the waveform cycle.	95
4.14	Velocity vector with velocity vector field and instantaneous streamlines overlaid for the upper quarter-plane for a branching ratio of 33:67 over one cycle indicated by the points on the waveform cycle.	96
4.15	Velocity vector with velocity vector field and instantaneous streamlines overlaid for the upper quarter-plane for a branching ratio of 46:54 over one cycle indicated by the points on the waveform cycle.	97
4.16	Velocity vector with velocity vector field and instantaneous streamlines overlaid for the upper quarter-plane for a branching ratio of 48:52 over one cycle indicated by the points on the waveform cycle.	98
4.17	Velocity vector with velocity vector field and instantaneous streamlines overlaid for the upper quarter-plane for a branching ratio of 50:50 over one cycle indicated by the points on the waveform cycle.	99
4.18	Velocity vector with velocity vector field and instantaneous streamlines overlaid for the upper quarter-plane for a branching ratio of 67:33 over one cycle indicated by the points on the waveform cycle.	100
4.19	Velocity vector with velocity vector field and instantaneous streamlines overlaid for the upper quarter-plane for a branching ratio of 75:25 over one cycle indicated by the points on the waveform cycle.	101
4.20	Velocity vector with velocity vector field and instantaneous streamlines overlaid for the upper quarter-plane for a branching ratio of 80:20 over one cycle indicated by the points on the waveform cycle.	102
4.21	Velocity vector with velocity vector field and instantaneous streamlines overlaid for the lower quarter-plane for a branching ratio of 20:80 over one cycle indicated by the points on the waveform cycle.	103
4.22	Velocity vector with velocity vector field and instantaneous streamlines overlaid for the lower quarter-plane for a branching ratio of 25:75 over one cycle indicated by the points on the waveform cycle.	104
4.23	Velocity vector with velocity vector field and instantaneous streamlines overlaid for the lower quarter-plane for a branching ratio of 33:67 over one cycle indicated by the points on the waveform cycle.	105
4.24	Velocity vector with velocity vector field and instantaneous streamlines overlaid for the lower quarter-plane for a branching ratio of 46:54 over one cycle indicated by the points on the waveform cycle.	106

4.25	Velocity vector with velocity vector field and instantaneous streamlines overlaid for the lower quarter-plane for a branching ratio of 48:52 over one cycle indicated by the points on the waveform cycle.	107
4.26	Velocity vector with velocity vector field and instantaneous streamlines overlaid for the lower quarter-plane for a branching ratio of 50:50 over one cycle indicated by the points on the waveform cycle.	108
4.27	Velocity vector with velocity vector field and instantaneous streamlines overlaid for the lower quarter-plane for a branching ratio of 67:33 over one cycle indicated by the points on the waveform cycle.	109
4.28	Velocity vector with velocity vector field and instantaneous streamlines overlaid for the lower quarter-plane for a branching ratio of 75:25 over one cycle indicated by the points on the waveform cycle.	110
4.29	Velocity vector with velocity vector field and instantaneous streamlines overlaid for the lower quarter-plane for a branching ratio of 80:20 over one cycle indicated by the points on the waveform cycle.	111
4.30	Plots of the second invariant of the velocity gradient tensor for the midplane for a branching ratio of 20:80 over one cycle indicated by the points on the waveform cycle.	112
4.31	Plots of the second invariant of the velocity gradient tensor for the midplane for a branching ratio of 25:75 over one cycle indicated by the points on the waveform cycle.	113
4.32	Plots of the second invariant of the velocity gradient tensor for the midplane for a branching ratio of 33:67 over one cycle indicated by the points on the waveform cycle.	114
4.33	Plots of the second invariant of the velocity gradient tensor for the midplane for a branching ratio of 46:54 over one cycle indicated by the points on the waveform cycle.	115
4.34	Plots of the second invariant of the velocity gradient tensor for the midplane for a branching ratio of 48:52 over one cycle indicated by the points on the waveform cycle.	116
4.35	Plots of the second invariant of the velocity gradient tensor for the midplane for a branching ratio of 50:50 over one cycle indicated by the points on the waveform cycle.	117
4.36	Plots of the second invariant of the velocity gradient tensor for the midplane for a branching ratio of 67:33 over one cycle indicated by the points on the waveform cycle.	118
4.37	Plots of the second invariant of the velocity gradient tensor for the midplane for a branching ratio of 75:25 over one cycle indicated by the points on the waveform cycle.	119
4.38	Plots of the second invariant of the velocity gradient tensor for the midplane for a branching ratio of 80:20 over one cycle indicated by the points on the waveform cycle.	120

4.39	Plots of the second invariant of the velocity gradient tensor for the upper quarter-plane for a branching ratio of 20:80 over one cycle indicated by the points on the waveform cycle.	121
4.40	Plots of the second invariant of the velocity gradient tensor for the upper quarter-plane for a branching ratio of 25:75 over one cycle indicated by the points on the waveform cycle.	122
4.41	Plots of the second invariant of the velocity gradient tensor for the upper quarter-plane for a branching ratio of 33:67 over one cycle indicated by the points on the waveform cycle.	123
4.42	Plots of the second invariant of the velocity gradient tensor for the upper quarter-plane for a branching ratio of 46:54 over one cycle indicated by the points on the waveform cycle.	124
4.43	Plots of the second invariant of the velocity gradient tensor for the upper quarter-plane for a branching ratio of 48:52 over one cycle indicated by the points on the waveform cycle.	125
4.44	Plots of the second invariant of the velocity gradient tensor for the upper quarter-plane for a branching ratio of 50:50 over one cycle indicated by the points on the waveform cycle.	126
4.45	Plots of the second invariant of the velocity gradient tensor for the upper quarter-plane for a branching ratio of 67:33 over one cycle indicated by the points on the waveform cycle.	127
4.46	Plots of the second invariant of the velocity gradient tensor for the upper quarter-plane for a branching ratio of 75:25 over one cycle indicated by the points on the waveform cycle.	128
4.47	Plots of the second invariant of the velocity gradient tensor for the upper quarter-plane for a branching ratio of 80:20 over one cycle indicated by the points on the waveform cycle.	129
4.48	Plots of the second invariant of the velocity gradient tensor for the lower quarter-plane for a branching ratio of 20:80 over one cycle indicated by the points on the waveform cycle.	130
4.49	Plots of the second invariant of the velocity gradient tensor for the lower quarter-plane for a branching ratio of 25:75 over one cycle indicated by the points on the waveform cycle.	131
4.50	Plots of the second invariant of the velocity gradient tensor for the lower quarter-plane for a branching ratio of 33:67 over one cycle indicated by the points on the waveform cycle.	132
4.51	Plots of the second invariant of the velocity gradient tensor for the lower quarter-plane for a branching ratio of 46:54 over one cycle indicated by the points on the waveform cycle.	133
4.52	Plots of the second invariant of the velocity gradient tensor for the lower quarter-plane for a branching ratio of 48:52 over one cycle indicated by the points on the waveform cycle.	134

4.53	Plots of the second invariant of the velocity gradient tensor for the lower quarter-plane for a branching ratio of 50:50 over one cycle indicated by the points on the waveform cycle.	135
4.54	Plots of the second invariant of the velocity gradient tensor for the lower quarter-plane for a branching ratio of 67:33 over one cycle indicated by the points on the waveform cycle.	136
4.55	Plots of the second invariant of the velocity gradient tensor for the lower quarter-plane for a branching ratio of 75:25 over one cycle indicated by the points on the waveform cycle.	137
4.56	Plots of the second invariant of the velocity gradient tensor for the lower quarter-plane for a branching ratio of 80:20 over one cycle indicated by the points on the waveform cycle.	138
4.57	In-plane WSS history along the aneurysm dome in the midplane for a branching ratio of 20:80)	139
4.58	In-plane WSS history along the aneurysm dome in the midplane for a branching ratio of 25:75)	140
4.59	In-plane WSS history along the aneurysm dome in the midplane for a branching ratio of 33:67)	141
4.60	In-plane WSS history along the aneurysm dome in the midplane for a branching ratio of 46:54)	142
4.61	In-plane WSS history along the aneurysm dome in the midplane for a branching ratio of 48:52)	143
4.62	In-plane WSS history along the aneurysm dome in the midplane for a branching ratio of 50:50)	144
4.63	In-plane WSS history along the aneurysm dome in the midplane for a branching ratio of 67:33)	145
4.64	In-plane WSS history along the aneurysm dome in the midplane for a branching ratio of 75:25)	146
4.65	In-plane WSS history along the aneurysm dome in the midplane for a branching ratio of 80:20)	147
4.66	In-plane WSS history along the aneurysm dome in the upper quarter-plane for a branching ratio of 20:80)	148
4.67	In-plane WSS history along the aneurysm dome in the upper quarter-plane for a branching ratio of 25:75)	149
4.68	In-plane WSS history along the aneurysm dome in the upper quarter-plane for a branching ratio of 33:67)	150
4.69	In-plane WSS history along the aneurysm dome in the upper quarter-plane for a branching ratio of 46:54)	151
4.70	In-plane WSS history along the aneurysm dome in the upper quarter-plane for a branching ratio of 48:52)	152
4.71	In-plane WSS history along the aneurysm dome in the upper quarter-plane for a branching ratio of 50:50)	153
4.72	In-plane WSS history along the aneurysm dome in the upper quarter-plane for a branching ratio of 67:33)	154

4.73	In-plane WSS history along the aneurysm dome in the upper quarter-plane for a branching ratio of 75:25)	155
4.74	In-plane WSS history along the aneurysm dome in the upper quarter-plane for a branching ratio of 80:20)	156
4.75	In-plane WSS history along the aneurysm dome in the lower quarter-plane for a branching ratio of 20:80)	157
4.76	In-plane WSS history along the aneurysm dome in the lower quarter-plane for a branching ratio of 25:75)	158
4.77	In-plane WSS history along the aneurysm dome in the lower quarter-plane for a branching ratio of 33:67)	159
4.78	In-plane WSS history along the aneurysm dome in the lower quarter-plane for a branching ratio of 46:54)	160
4.79	In-plane WSS history along the aneurysm dome in the lower quarter-plane for a branching ratio of 48:52)	161
4.80	In-plane WSS history along the aneurysm dome in the lower quarter-plane for a branching ratio of 50:50)	162
4.81	In-plane WSS history along the aneurysm dome in the lower quarter-plane for a branching ratio of 67:33)	163
4.82	In-plane WSS history along the aneurysm dome in the lower quarter-plane for a branching ratio of 75:25)	164
4.83	In-plane WSS history along the aneurysm dome in the lower quarter-plane for a branching ratio of 80:20)	165
4.84	Plot of the mean over time of the in-plane WSS for each point along the midplane of the aneurysm dome.	166
4.85	Plot of the mean over time of the in-plane WSS for each point along the upper quarter-plane of the aneurysm dome.	167
4.86	Plot of the mean over time of the in-plane WSS for each point along the lower quarter-plane of the aneurysm dome.	168
5.1	Diagrams of the standard translational SPIV configuration (a) and the modified translational SPIV configuration (b) used by Arroyo and Greated [5].	180
5.2	Diagram of the standard angular displacement SPIV configuration.	182
5.3	An illustration of the camera positions and angles used in velocity reconstruction based on works by Willert [69] and Brücker [7].	184
5.4	Camera configuration for SPIV experiments.	187
5.5	Distorted images (<i>left</i>) and dewarped images (<i>right</i>) of the calibration target (<i>top</i>) and the flow plane (<i>bottom</i>).	188
5.6	Validation of SPIV measurements by comparing out-of-plane SPIV velocity measurements (<i>solid line</i>) to the corresponding PIV velocity (<i>dashed line</i>).	193
5.7	Diagram of the PIV and SPIV planes along the dome from an overhead view, as well as the intersection points. The middle intersection point is the tip of the dome.	194
5.8	Definition of <i>angle from tip</i> that is used to describe dome coordinates in the SPIV WSS plots)	195

5.9	Plot of the in-plane velocity vector field (left) and and out-of-plane velocity (right) for a branching ratio of 20:80 over one cycle indicated by the points in the plot of the waveform cycle.	196
5.10	Plot of the in-plane velocity vector field (left) and and out-of-plane velocity (right) for a branching ratio of 25:75 over one cycle indicated by the points in the plot of the waveform cycle.	197
5.11	Plot of the in-plane velocity vector field (left) and and out-of-plane velocity (right) for a branching ratio of 33:67 over one cycle indicated by the points in the plot of the waveform cycle.	198
5.12	Plot of the in-plane velocity vector field (left) and and out-of-plane velocity (right) for a branching ratio of 46:54 over one cycle indicated by the points in the plot of the waveform cycle.	199
5.13	Plot of the in-plane velocity vector field (left) and and out-of-plane velocity (right) for a branching ratio of 48:52 over one cycle indicated by the points in the plot of the waveform cycle.	200
5.14	Plot of the in-plane velocity vector field (left) and and out-of-plane velocity (right) for a branching ratio of 50:50 over one cycle indicated by the points in the plot of the waveform cycle.	201
5.15	Plot of the in-plane velocity vector field (left) and and out-of-plane velocity (right) for a branching ratio of 67:33 over one cycle indicated by the points in the plot of the waveform cycle.	202
5.16	Plot of the in-plane velocity vector field (left) and and out-of-plane velocity (right) for a branching ratio of 75:25 over one cycle indicated by the points in the plot of the waveform cycle.	203
5.17	Plot of the in-plane velocity vector field (left) and and out-of-plane velocity (right) for a branching ratio of 80:20 over one cycle indicated by the points in the plot of the waveform cycle.	204
5.18	Plot of the second invariant of the velocity gradient, Q , for a branching ratio of 20:80 over one cycle indicated by the points in the plot of the waveform cycle.	205
5.19	Plot of the second invariant of the velocity gradient, Q , for a branching ratio of 25:75 over one cycle indicated by the points in the plot of the waveform cycle.	206
5.20	Plot of the second invariant of the velocity gradient, Q , for a branching ratio of 33:67 over one cycle indicated by the points in the plot of the waveform cycle.	207
5.21	Plot of the second invariant of the velocity gradient, Q , for a branching ratio of 46:54 over one cycle indicated by the points in the plot of the waveform cycle.	208
5.22	Plot of the second invariant of the velocity gradient, Q , for a branching ratio of 48:52 over one cycle indicated by the points in the plot of the waveform cycle.	209

5.23	Plot of the second invariant of the velocity gradient, Q , for a branching ratio of 50:50 over one cycle indicated by the points in the plot of the waveform cycle.	210
5.24	Plot of the second invariant of the velocity gradient, Q , for a branching ratio of 67:33 over one cycle indicated by the points in the plot of the waveform cycle.	211
5.25	Plot of the second invariant of the velocity gradient, Q , for a branching ratio of 75:25 over one cycle indicated by the points in the plot of the waveform cycle.	212
5.26	Plot of the second invariant of the velocity gradient, Q , for a branching ratio of 80:20 over one cycle indicated by the points in the plot of the waveform cycle.	213
5.27	In plane WSS history a for a branching ratio of 20:80.	214
5.28	In plane WSS history a for a branching ratio of 25:75.	215
5.29	In plane WSS history a for a branching ratio of 33:67.	216
5.30	In plane WSS history a for a branching ratio of 46:54.	217
5.31	In plane WSS history a for a branching ratio of 48:52.	218
5.32	In plane WSS history a for a branching ratio of 50:50.	219
5.33	In plane WSS history a for a branching ratio of 67:33.	220
5.34	In plane WSS history a for a branching ratio of 75:25.	221
5.35	In plane WSS history a for a branching ratio of 80:20.	222
5.36	WSS magnitudes at the intersection points of the PIV and SPIV imaging planes for a branching ratio of 20:80.	223
5.37	WSS magnitudes at the intersection points of the PIV and SPIV imaging planes for a branching ratio of 25:75.	224
5.38	WSS magnitudes at the intersection points of the PIV and SPIV imaging planes for a branching ratio of 33:67.	225
5.39	WSS magnitudes at the intersection points of the PIV and SPIV imaging planes for a branching ratio of 46:54.	226
5.40	WSS magnitudes at the intersection points of the PIV and SPIV imaging planes for a branching ratio of 48:52.	227
5.41	WSS magnitudes at the intersection points of the PIV and SPIV imaging planes for a branching ratio of 50:50.	228
5.42	WSS magnitudes at the intersection points of the PIV and SPIV imaging planes for a branching ratio of 67:33.	229
5.43	WSS magnitudes at the intersection points of the PIV and SPIV imaging planes for a branching ratio of 75:25.	230
5.44	WSS magnitudes at the intersection points of the PIV and SPIV imaging planes for a branching ratio of 80:20.	231
5.45	Simplified streamlines from the front view (<i>left</i>) and right view (<i>middle</i>) and a diagram of the rotational filament (<i>right</i>) for the general experimental cases.	236
5.46	Simplified streamlines from the front view (<i>left</i>) and right view (<i>middle</i>) and a diagram of the rotational filament (<i>right</i>) for an idealized symmetric case.	239

List of Tables

2.1	Reynolds numbers, Re , and volumetric flow rates, Q , for the experimental fluid [33].	16
5.1	Maximum WSS values at the intersection points of the PIV and SPIV imaging planes.	232
5.2	Mean WSS values at the intersection points of the PIV and SPIV imaging planes.	232

Acknowledgements

I will take this opportunity to thank the countless number of people who have helped my decade at the University of California, Berkeley. While I cannot list them all, I would like to thank a handful who have been particularly influential. This work would never have been possible without the experience, guidance, and patience of my advisor, Professor Ömer Savaş. I owe a great deal my fellow researchers who not only provided their technical expertise but their friendship as well: Gregory McCauley, Victoria Sturgeon, Jason Ortega, and Phillippe Bardet. Lastly, I would like to thank my family, who have been patient and supportive throughout the entire education experience: my parents, Pei-San and Jing-Hong Tsai, my uncle, Eugene Yuh, and my younger brother, Wilson Tsai.

Symbols

Variables

d	diameter
\mathbf{e}_t	tangential unit vector
\mathbf{e}_n	normal unit vector
\mathbf{e}_b	binormal unit vector
f	focal length
h	general function
q	flow rate
q_{max}	maximum flow rate
q_{mean}	mean flow rate
q_{min}	minimum flow rate
q_0	initial flow rate
r	radius
t	time
t_s	settling time
\mathbf{u}	velocity vector
u	x-component of velocity
v	y-component of velocity
v_s	sedimentation velocity
w	z-component of velocity

x	projection of u on the x-y plane
x_1	projection of u on the x-y plane as seen from camera 1
x_2	projection of u on the x-y plane as seen from camera 2
y	projection of v on the x-y plane
y_1	projection of v on the x-y plane as seen from camera 1
y_2	projection of v on the x-y plane as seen from camera 2
L	length scale
L'	entrance length
L_1	distance between camera 1 and the target point on the object plane
L_2	distance between camera 2 and the target point on the object plane
Q	section invariant of the velocity gradient
S_{ij}	strain rate tensor
α_1	angle between camera 1 and a point p in the x-z plane
α_2	angle between camera 2 and a point p in the y-z plane
β_1	angle between camera 1 and a point p in the x-z plane
β_2	angle between camera 2 and a point p in the y-z plane
δx	distance between two discrete points
μ	dynamic viscosity
ν	$\frac{\mu}{\rho}$, kinematic viscosity
ω	angular frequency
ρ	density
τ	shear stress

τ_w wall shear stress

Ω_{ij} rate of rotation tensor

Dimensionless Parameters

c_τ Coefficient of Shear Stress, $c_\tau \equiv \tau / \frac{1}{2} \rho U^2$

Re Reynolds number, $Re \equiv \rho U L / \mu$

α Wormersley number, $\alpha^2 \equiv r^2 \frac{\omega}{\nu}$

Chapter 1

Introduction

An aneurysm is an uncontrolled dilation of a blood vessel associated with the weakening of an arterial wall; it may continue to grow until it overwhelms the arterial wall and ruptures. The rupture can be dangerous if it impairs blood flow to a vital organ or the resulting hemorrhage creates a life-threatening complication. Cerebral aneurysms, also referred to as intracranial aneurysms, are particularly dangerous being located among the brain's complex vasculature. Current research is still unable to explain the formation, growth, and rupture mechanisms of cerebral aneurysms. Improving the understanding of intracranial aneurysms may advance diagnosis and treatment techniques.

The importance of early diagnosis and treatment is underscored by the prevalence of cerebral aneurysms in the population and the potential harm they can cause. Adults of any age can develop aneurysms with the majority being in their 50's to 70's [14, 44]. It is estimated that 5% of Americans are affected, but the majority of them are unaware due to symptom absence [55, 65]. Raps et al. [51] found just over half of those diagnosed

are asymptomatic and another 15% showed only acute symptoms. Approximately 25-38% of symptomatic patients have severe headaches, ocular findings, focal neurological defects, seizures, or altered level of consciousness. These symptoms are associated with other common ailments, leading to misdiagnoses. Obtaining the proper diagnoses through patient re-evaluations take anywhere from 24 hours to 6 months, with an average of 6 days [41, 17].

If undiagnosed or allowed to grow untreated, the aneurysm risks rupturing. The rupture may either be small, causing a contained “warning” bleed, or catastrophic, causing a subarachnoid hemorrhage (SAH), a type of stroke characterized by bleeding between the membranes that surround the central nervous system [15]. Without immediate medical attention, the increased intracranial pressure, decreased usable blood flow, and reduced oxygen supply causes severe brain damage and possibly death [65]. Studies found that 11-14% of patients with SAH expire within a week after rupture, while the 6 month mortality rates were 40-67% [18, 29, 40, 54]. Even with treatment, Longstrech et al. [40] found that one third of the sample group did not survive past the first month, while another third never regained full mental capacity and function after rupture. Overall, almost all SAH survivors experience a quality of life decrease [26].

1.1 Aneurysm Formation, Growth, and Rupture

Given the risks and dangers of cerebral aneurysms, researchers have focused their efforts on understanding them from beginning to end. The life cycle of an aneurysm consists of three phases: 1) pathogenesis or the formation, 2) growth, and 3) rupture. The following sections will present research and theories for each of these stages.

The pathogenesis of cerebral aneurysms has been examined but capturing the precise moments of natural formation is nearly impossible. As a result, hypotheses have been developed using observations, correlations, and artificially induced aneurysms. Reduced external elastic lamina, supporting perivascular tissue, and medial elastin in the cerebral arteries make them more susceptible to aneurysm formation compared to the rest of the circulatory system [28]. However, predispositions alone cannot explain pathogenesis. Most aneurysm formation theories focus on causes that trigger a localized weakening of the endothelial cells that line the artery wall. One possible candidate is high wall shear stress (WSS). Fry [20] extracted samples of arterial wall and determined that wall shear stress values exceeding $379 \pm 85 \frac{\text{dynes}}{\text{cm}^2}$ led to rapid deterioration of the endothelial layer. Kondo et al. [35] artificially induced cerebral aneurysm formation in rats and found the aneurysms formed at locations with locally elevated WSS. They found the response to the increased WSS was artery dilation and thinning the endothelial layer, leaving the artery prone to aneurysm formation. Inci and Spetzler [30] hypothesized that the primary mechanism of aneurysm formation is hypertension; blood pressure increase leads to endothelial injury, occlusion of the vasa vasorum, and disturbance of elastin-collagen synthesis. Krex et al. [36] proposed that the root causes of aneurysm formation are genetic defects favoring remodeling of arterial walls that make it susceptible to aneurysm formation. Hypertension, atherosclerosis, and exogenous factors play a secondary role in aneurysm formation. Meng et al. [42] suggested the spatial gradients and distribution of shear stress along the arterial wall are as much a factor as the magnitude of WSS. It is likely that a combination of these factors is required to fully explain aneurysm pathogenesis, but given the complex nature of

the problem, improved research techniques will be required.

Aneurysm growth is equally as challenging to explain. Researchers have been able to follow the growth of aneurysm in diagnosed patients. While large amounts of data have been published, even the rate of aneurysm expansion has been difficult to isolate. Allcock et al. [3] tracked the growth of 82 aneurysms for up to 10 years but found no consistent rate of growth. Wiebers et al. [66] drew some conclusions by dividing subjects into two groups: the first group was made up of cerebral aneurysm patients with no history of rupture, while the second group was made up of cerebral aneurysm patients that had a history of rupture. The first group had a higher percentage of rupture in large aneurysms ($>10\text{mm}$) and a lower percentage of rupture in small aneurysms ($<10\text{mm}$) compared to the second group. This indicated that in the first group the aneurysms grew to a large steady size and took a long time to rupture, while in the second group aneurysms tended to rupture while they were smaller and growing. Mitchell and Jakubowski [44] hypothesized that the aneurysm experienced a period of rapid growth after genesis, estimated to be 41 weeks. During this period, the aneurysm wall is susceptible to rupture; after this period, growth rate decelerates dramatically, reducing to nearly zero.

It is difficult to develop a theory that explains these unusual growth patterns; there are several hypotheses about an explanation. The difficulty lies in the complexity of the processes involved. Cerebral aneurysm growth cannot be reduced to a simple “balloon” analysis. Such a model could not predict the erratic growth pattern and irreversibility of aneurysm growth [9]. Shojima et al. [57] showed that the variations of normal pressures on aneurysm walls are only 1-2% of peak intravascular pressure suggesting pressure loading

alone is an unlikely candidate. In addition, it is important to consider, as Peters [48] states: “Aneurysmal dilation results in a highly dynamic cellular environment which extensive wound healing and tissue/extracellular matrix remodeling are taking place.” A ballooning aneurysm growth model would neglect the biological aspects of the aneurysm wall and the dynamic blood flow within it.

Several theories examine the characteristics of blood flow within an aneurysm, particularly low WSS and its effects on the wall. Low WSS was initially examined because of its involvement in the development of atherosclerosis and plaque deposition. Caro et al. [10] correlated WSS to nutrient and chemical concentration gradients near the wall. Lower than normal WSS correlated with reduced mass transfer to the endothelial cells. Walpolo et al. [64] found WSS values of approximately $3 \frac{\text{dynes}}{\text{cm}^2}$ in a modified rabbit aorta generated a feedback response leading to arterial contraction and endothelial cell count reduction. In addition, fewer endothelial cells were aligned with the flow direction; they were also less elongated in the flow direction and contained fewer and shorter microfilaments, signaling reduced directional strength. Steiger et al. [60] measured WSS in the aneurysm and found them to be on the order of $50 \frac{\text{dynes}}{\text{cm}^2}$, which is considerably lower than the neighboring non-diseased arterial wall. Shojima et al. [56], using patient-specific CFD simulations, found the peak WSS magnitude within the aneurysm to be less than half the value in the parent arteries (16.4 and $36.4 \frac{\text{dynes}}{\text{cm}^2}$, respectively). While the simulated values are not as low as the values discussed in [64], the researchers hypothesized that a severe drop in WSS caused changes in endothelial cell behavior. Boussel et al. found correlations between low WSS and regions of aneurysm growth; using MRI and CFD simulations, aneurysm wall expansion

rates were highest where simulations found a $2.5 \frac{\text{dynes}}{\text{cm}^2}$ mean WSS. Others have proposed examining the temporal aspects of WSS. The oscillatory shear index (OSI) measures the WSS magnitude and direction changes at a point over a period of time. Cebal et al. [11] hypothesized that a combination of OSI and WSS magnitude plays a role in aneurysm growth.

An alternative cause of aneurysm growth suggested by Humphrey et al. [28] derives from the combination of the non-linear material properties of the artery wall and the flow dynamics including transient pressure effects. WSS alone is inconclusive because the transient behavior of the artery wall must be modeled at the same time. Humphrey et al. argue the practice of assuming a prescribed outlet pressure field in CFD simulations skews the results. The focus on WSS in aneurysm growth theories results from the inability to develop a precise solution for pressure fields. It was proposed that simulations which couple both fluid and solid changes, a fluid-solid-growth (FSG) model, could accurately predict aneurysm growth and rupture.

Research into modeling aneurysm rupture has focused on finding correlations that offer precise indicators. The aforementioned study by Wiebers' et al. [65] provided mixed correlations between aneurysm size and rupture. Several geometric characteristics of the aneurysm (Figure 1.2) are considered. Other studies have shown that a cerebral saccular aneurysm with an aspect ratio of the maximum diameter, d_{max} , to the inlet diameter, d_{inlet} , of >1.6 had a rupture rate near 80% [63, 67]. Crawford [13] and Crompton [14] noted that the majority of aneurysms (60-70%) failed at the aneurysm tip as opposed to the lateral walls or at the neck. Humphrey et al. [28] argued that it is not diameter, but Cauchy

principal stresses that determine rupture location. Shojima et al. [56] suggested that if low WSS phenomena are responsible for growth, rupture is the byproduct of weakening the wall until it can not remain intact under the stresses applied. Cebal et al. [11] found correlations between rupture and the size and strength of the impingement jet that enters the aneurysm. They found that 74% of the patient-specific simulations had jets that impinged at the dome walls. However, Burleson et al. [8] found that the highest WSS occurred at the walls around the inlet of the aneurysm and argued that rupture must start from these locations and propagate rapidly across the dome. Although the WSS magnitudes were considerably less than Fry [20], Burleson suggested that the aneurysm's endothelial cells were less adaptive to changes in shear stress. Ahn et al. [2] found that the aneurysm tip was subjected to higher WSS relative to other parts within the dome but still less than the neck. The researchers suggest a local high WSS and a possible weakness in the material may play a role in rupture. As with aneurysm growth, there is no accurate theory explaining the complex nature of aneurysm rupture.

1.2 Examining Cerebral Aneurysm Growth Through *In Vitro*

Experimental Techniques

Extensive research into cerebral aneurysms has produced no conclusive explanation of formation, growth, and rupture. The long term goals are understanding aneurysm mechanics, improving detection techniques, and developing treatments. A short term goal is gathering enough information to construct accurate modeling tools to aid physicians in evaluating treatment options.

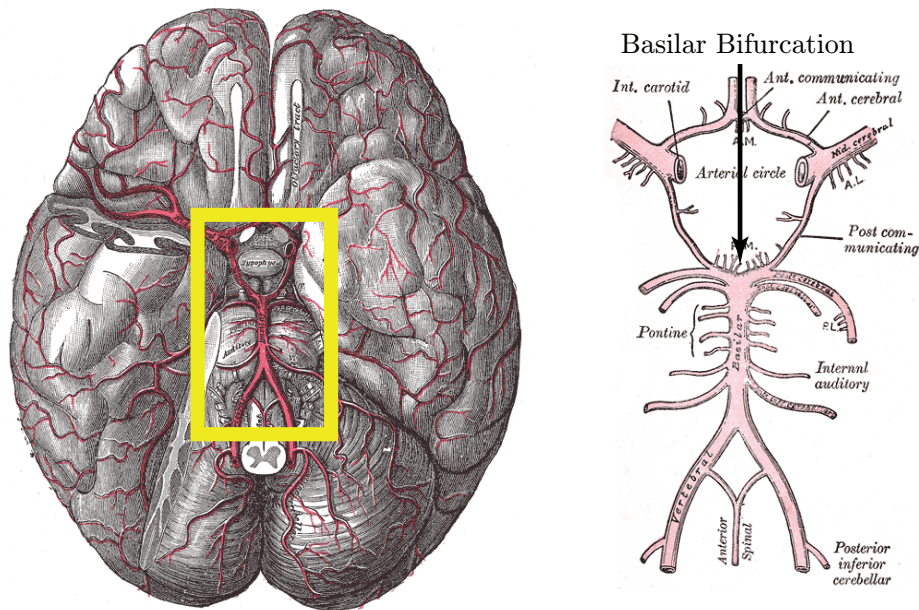


Figure 1.1: The bifurcation of the basilar artery into the posterior cerebral artery relative to the brain (left) and a magnified inset (right) [24].

The goal of this dissertation is to further the understanding of cerebral aneurysm growth. The experiments presented in what follows model a cerebral saccular aneurysm that has formed at the bifurcation of the basilar artery. The basilar artery runs along the spinal column into the base of the skull, where it bifurcates into the posterior communicating arteries which supply the Circle of Willis and the network of arteries that distribute blood to the brain (Figure 1.1). The experiments are conducted on a simplified model of the saccular aneurysm to determine the basic flow behaviors and physics. Discussion in this dissertation will be confined to saccular cerebral aneurysms and will not consider fusiform aneurysms, which entail radial arterial growth (Figure 1.2).

In this dissertation three experimental techniques are used to characterize the flow field within the aneurysm model. Before discussion of any techniques, the details of the

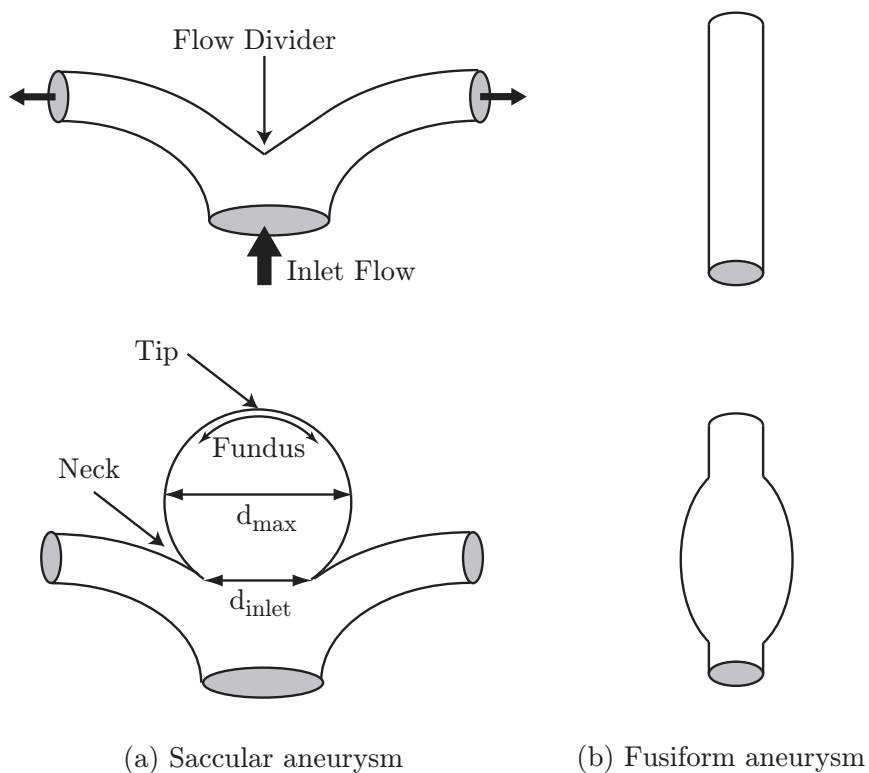


Figure 1.2: The geometric differences between (a) saccular and (b) fusiform aneurysms. The top images represent healthy arterial geometries while the lower images show diseased arterial geometries. The saccular aneurysm is labeled to define parts that will be commonly referenced.

flow model and setup used in all experiments are presented. The qualitative behavior of the flow is established through the use of flow visualization. With an understanding of the major structures and characteristics of the flow, particle image velocimetry is used to determine the 2D velocity fields and in-plane WSS over multiple planes within the dome. Lastly, stereoscopic particle image velocimetry is used to determine the 3D velocity field and in-plane WSS on along the center plane of the dome. Each experimental technique is described in a chapter devoted to the theory of operation, instrumentation setup, results, and conclusions. Finally, the conclusion of the dissertation involves consolidating the results and connecting them to the background research and theory that have been presented.

Chapter 2

Experimental Setup

This chapter describes the simplified physical model of a cerebral saccular aneurysm. This flow phantom captures basic aspects of the aneurysm and is transparent allowing the use of visual flow measurement techniques. The test fluid simulates blood flow by ensuring dynamic conditions similar to physiological conditions. To mimic the oscillatory nature of physiological blood flow, a pulsatile pumping system controls flow waveform generation. The experimental variables, the flow rate ratio through the outlets and imaging planes, are defined at the close of the chapter.

2.1 Flow Phantom

Data are acquired from the flow phantom, a simplified bifurcation with an aneurysm (Figure 2.1), rather than using a complex physiological model from patient specific magnetic resonance imaging (MRI) data. The model dimensions are based on patient measurements by Parlea et al. [47] of a cerebral saccular aneurysm located at the basilar bifurcation.

The basilar artery is modeled by the inlet pipe, measuring 3.2mm in diameter. The outlet posterior cerebral arteries (PCA) are modeled by the outlet pipes, measuring 2mm in diameter. These bifurcate at right angles to the basilar artery, forming a “T” shape. The aneurysm dome is nearly spherical, with a major diameter of 11.7mm and a minor diameter of 11.3mm. It replaces the bifurcation flow divider.

The model geometry is the same used in parallel computational fluid dynamics (CFD) simulations by Oretga et al. [46]. The simulations include a fully developed inlet boundary conditions which is applied to the experiment. For a laminar flow, the entrance length required for fully developed flow is

$$L' = 0.058dRe, \quad (2.1)$$

where L' is the entrance length and Re is the Reynolds number (Section 2.2). For this flow, the minimum entrance length required is 18 diameters; for safety the inlet length is chosen to be 25 diameters prior to entering the bifurcation. The outlets are similarly 25 diameters in length before taking a 90° bend so that connections to both the inlet and the outlet can be mounted in the rear.

The geometry described is cast within a silicone (Polydimethylsiloxane) block encased in acrylic panels (Figure 2.2). While the model is transparent, distortions are introduced by small density variations in the silicone during manufacturing, and by the finish of the acrylic surfaces. In addition, parts of the experiment requires optical access at 45° angle to the walls, which is accompanied by severe distortion. To address these effects, five optically clear and polished BK-7 glass viewing windows (Figure 2.2) provide views of the dome and bifurcation through the x-axis, z-axis, and $\pm 45^\circ$ off of the z-axis on the x-z plane.

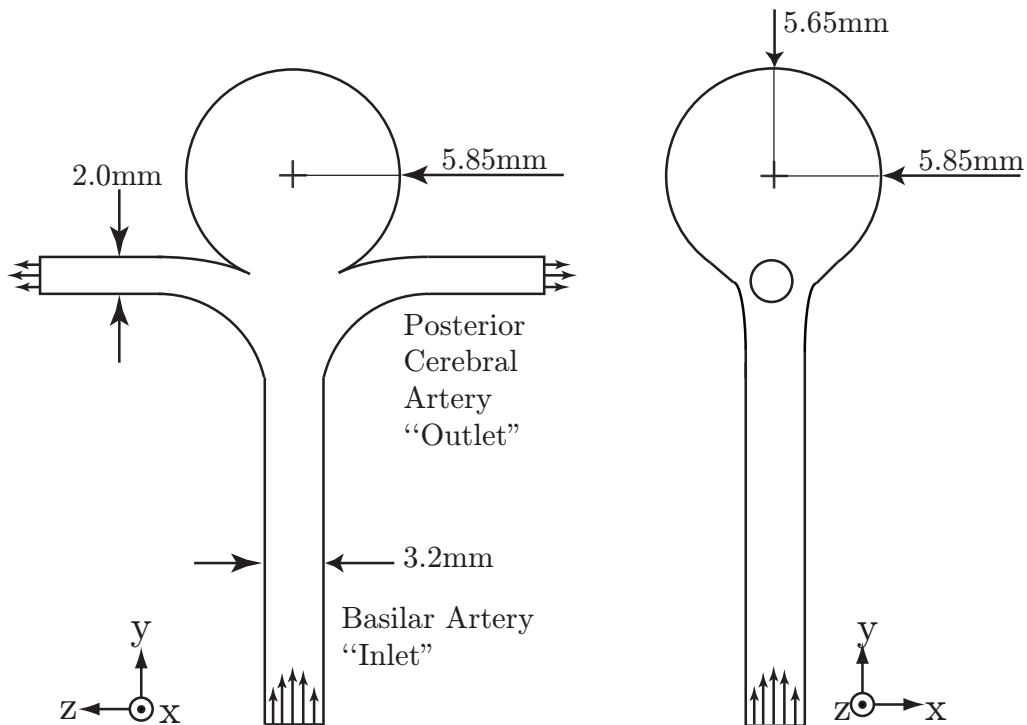


Figure 2.1: Dimensions of the simplified model of a cerebral saccular basilar aneurysm.

The glass blocks are placed as close as possible to the dome, minimizing the distortions introduced by the silicone.

2.2 Flow Parameters

2.2.1 Working Fluid

The working fluid must have a viscosity that allows dimensionless parameters to match physiological conditions within the capabilities of the experimental setup. In addition, the working fluid's index of refraction must match silicone's ($n=1.41$) to minimize optical distortion. The appropriate mixture is chosen through empirically determined op-

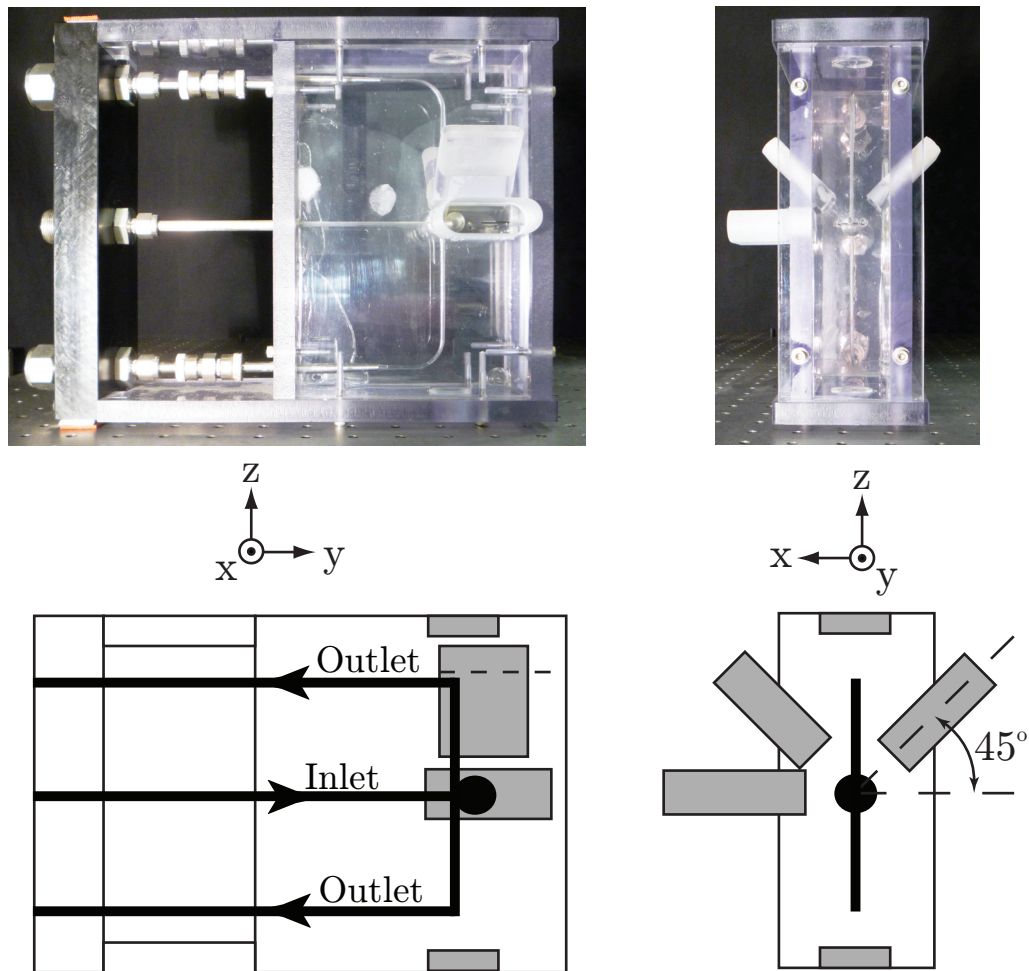


Figure 2.2: Upper: Photograph of the side (left) and front (right) of the flow phantom. Lower: Diagram of the side (left) and front (right) of the flow phantom. The BK-7 glass windows are shaded in gray.

timization equations by Nguyen et al. [45] for modeling blood flows. The fluid used is a mixture of 55% glycerin and 45% water by weight maintained at $30^{\circ}C$. The density of the solution is $1.135g/cm^3$ [12]. No direct viscosity measurements for this mixture are available. Using the Grunberg-Nissan model of Type 1 and available information for glycerine-water solutions, the average mixture activation energy is calculated to be $21.25J/mol$, yielding a dynamic viscosity of $\mu = 5.73cP$ [12].

2.2.2 Similarity

Reynolds and Sexl-Womersley numbers are matched with physiological conditions to achieve dynamic similarity. The Reynolds number, Re , is the ratio of inertial forces to viscous forces and is defined as

$$Re = \frac{\rho UL}{\mu}, \quad (2.2)$$

where ρ is the density of the fluid, U is the mean velocity magnitude, L is the characteristic length scale, and μ is the dynamic viscosity of the fluid. For this experiment, the characteristic length scale is the diameter of the basilar artery, d . In this calculation, blood is assumed to be Newtonian with a dynamic viscosity of $3.5cP$ [68]; this approximation for a non-Newtonian fluid is discussed in the next section. Based on measurements made by Kato [33], Reynolds numbers are determined for the minimum, mean, and maximum flow rates over one waveform and converted to corresponding experimental flow rates (Table 2.1).

The Sexl-Womersley number, α , is the ratio of oscillatory forcing on the fluid to the viscous forces within the fluid, or equivalently a ratio of the timescale for diffusion of

Table 2.1: Reynolds numbers, Re , and volumetric flow rates, Q , for the experimental fluid [33].

	Re	$Q[\frac{mL}{min}]$
Peak	376	290
Mean	221	170
Minimum	110	85

vorticity to the timescale for oscillatory forcing. It is defined as

$$\alpha^2 = \frac{r^2\omega}{\nu}, \quad (2.3)$$

where $r = d/2$ is the radius of the basilar artery, ω is the angular frequency, and $\nu = (\mu/\rho)$ is the kinematic viscosity. The Sexl-Womersley number for the physiological condition is calculated using a frequency of 1Hz, the equivalent to a pulse of 60 beat per minute. The Sexl-Womersley number is calculated to be 2.23. The Sexl-Womersley number is matched in the experiments by using a frequency of 1.53Hz for the piston pump.

2.2.3 Newtonian versus Non-Newtonian Fluid Behavior

In the experiment, blood is modeled as a Newtonian fluid. In actuality, blood is a shear-thinning, non-Newtonian fluid due to its complex mixture of plasma, red blood cells, platelets, white blood cells, etc. This results in some differences between the behavior of the working fluid and blood. Fung [21] modeled laminar flow in a tube using a non-Newtonian model for blood. He found that blood behaves like a Newtonian fluid near the walls. The velocity profile deviates from the Newtonian flow profile as shear rates approach zero. Steiger et al. [59] compared the behavior of blood versus a 54% glycerin - 46% water by weight mixture (Figure 2.3). The viscosity of blood and the mixture do not vary greatly in the shear rate range of 50-400s⁻¹ [68, 21]. It is in this high shear rate limit beyond

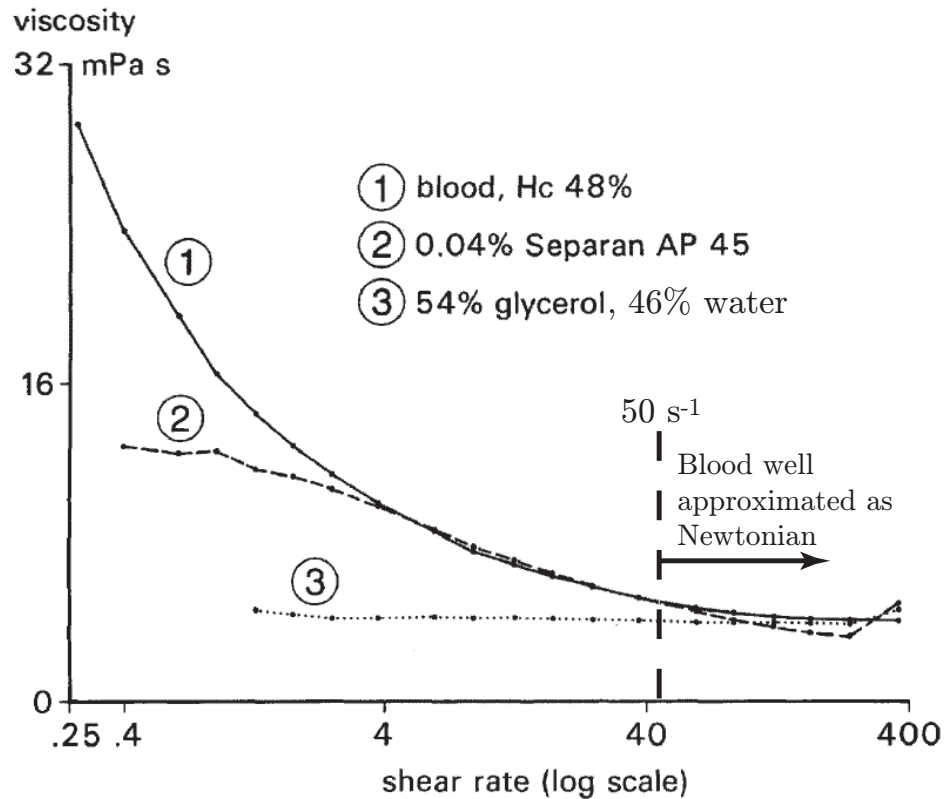


Figure 2.3: Comparison of the viscous properties of blood, glycerol, and Separan solution at shear rates from 0.25 to 400s^{-1} carried out by Steiger et al. [59].

50s^{-1} where blood is approximated to be Newtonian with a high shear limit viscosity, μ_{∞} , of 3.5cP

Through simulations using both Newtonian and non-Newtonian models, the errors from using the high shear rate limit have been researched and documented. Gijsen et al. [22, 23] compared experiments and computational models of Newtonian and non-Newtonian flow steady flows in the carotid bifurcation and unsteady flows in the aortic arch. They found that using the viscosity corresponding to the average shear rate yielded more accurate results than the high shear rate limit. However, if the flow is in the high shear rate regime, this is less applicable. An example of this is the variation in the average shear rate with

age; the expected characteristic shear rate is higher in older individuals [53]. Ku et al. [37] found that flow simulations using Newtonian fluids matched well with *in vivo* MRI flow rate measurements, with a maximum variation of 10.6%. Khanafer et al. [34] found that Newtonian fluids underestimated the wall shear stress (WSS) compared to non-Newtonian fluids, varying $1-3 \frac{\text{dynes}}{\text{cm}^2}$ or a relative error of up to 25%. Rayz et al. [52] compared Newtonian and non-Newtonian simulations of fusiform basilar aneurysms and found that the Newtonian simulations underestimated average WSS values by up to 23%. The highest local variations (29%) were observed in stagnation regions. In addition, Rayz et al. found that the velocity fields in the two cases were similar. Based on the literature, the expectation is that the experiments will capture the overall flow field behavior correctly but will underestimate WSS values by up to 30%.

2.3 Flow Waveform

The inlet flow must replicate the physiological flow through the basilar artery. The waveform (Figure 2.4) used here comes from measurements in the basilar artery during a study of posterior circulation ischemia by Kato et al. [33]. The measurements include the average flow rates for the healthy control group which are used for scaling the flow waveform. There is no reverse flow in the basilar bifurcation ($q > 0$).

2.4 Pulsatile Pumping System

Simulating the pulsatile nature of blood flow is essential in fluid mechanics experiments of the human circulatory system. Flow waveforms at numerous locations in the

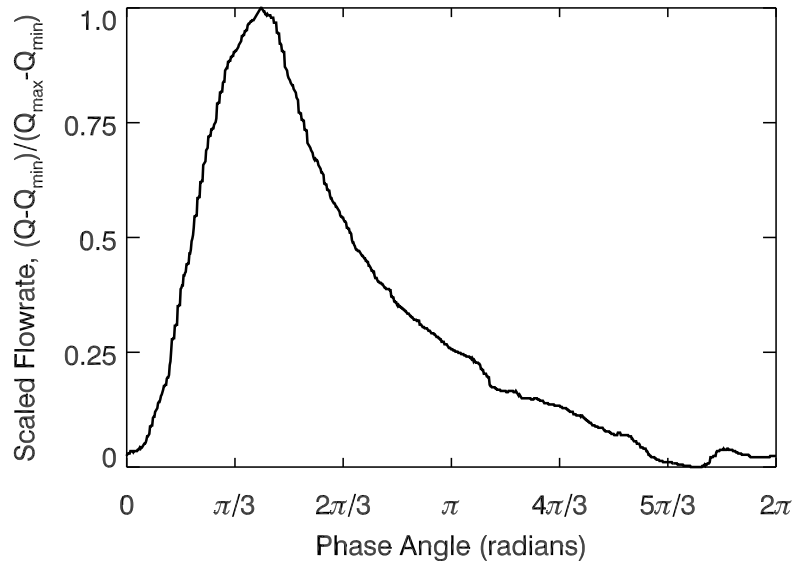


Figure 2.4: Input waveform for pulsatile flow pattern based on measurements by Kato et al. [33].

body have been measured *in vivo* using a variety of methods, such as magnetic resonance imaging (MRI) and Doppler ultrasound (DUS). This allows for the design of pumps capable of replicating physiological flow conditions *in vitro*.

A commercially available, dual-chamber pump (Shelly Imaging Systems, London, Ontario, Canada) uses a reversing cylinder-piston to generate pulsatile flow [19, 25]. The piston divides the cylinder into two chambers, each with fluid ports at the end. As the piston is driven under computer control in one direction, the pulsatile waveform is output from a chamber while its complement is refilled from the return line. Once the piston has been driven to one end of the cylinder, the piston reverses and the sequence repeats. All fluid ports connect to a computer-controlled 4-way valve which sequences the flow directions.

Alternative systems have been developed. Hoskins et al. [27] explored using a

signal-controlled gear pump to generate simple pulsatile waveforms. Plewes et al. [49] advanced the system by improving computer waveform generation through the addition of a closed feedback calibration circuit. While Plewes' pump is simpler than the dual-chamber pump, it requires electronics to carry out initial iterative calibration adjustments for each new waveform. P. Wong et al. [70] modified the design by introducing a software feedback loop using real-time velocity feedback from MRI scans.

The pumping system presented in this paper is developed for generating pulsatile flows in flow phantoms using a variety of fluids (e.g. water, glycerin, isopropyl alcohol, and their mixtures). This design allows users to optimize the flow parameters and tune the system to the needs of the experiment.

2.4.1 Pumping System

The pulsatile pumping system consists of a gear and a piston pump in series (Fig. 2.5). All components are mounted on a plate for easy access. The Teflon coated stainless steel gear pump provides the steady mean component of the desired flow waveform. Unlike the aforementioned designs, the output gear pump does not oscillate, and instead is operated under a constant load. The gear pump is preloaded with a back-pressure valve at its discharge, keeping the gears in constant contact and preventing reverse flow. The back-pressure valve also insures that the gear pump operates as a positive displacement device. For this experimental setup, an Oberdorfer Chemsteel S207 Pump (Oberdorfer Pumps, Syracuse, NY) is used with a maximum throughput of 300 ml/s. A Nikkiso Hydrogard back-pressure valve (Nikkiso Pumps, Houston, TX) is placed at the discharge of the gear

pump.

The piston pump provides the oscillatory component of the flow waveform. It consists of a stainless steel, honed cylinder housing of 5.45cm bore and 10cm stroke containing a Delrin piston. The capped end of the cylinder has the flow ports. To achieve reverse output flow, the piston pump draws fluid at a faster rate than the gear pump outputs. The piston is driven by a servo motor attached to a Thomson Precision Plus Lead Screw with zero backlash (Thomson BSA, San Jose, CA).

The gear pump is driven by an Applied Motion Products Alpha Series II 600W Servo Motor, with a rated maximum speed of 3000rpm (Applied Motion Products, Watsonville, CA). A 400W version of the servo motor drives the piston pump. Both motors connect to Applied Motion Products BluAC5 controllers, which include velocity control using an external signal. A single PC generates signals for both controllers through a Measurement Computing PCI-DAS6086 Data Acquisition Card (Measurement Computing, Norton, MA). The controlling C++ program drives the gear pump with a constant voltage output to generate the mean flow and drives the piston pump with a variable voltage output based on a waveform input file. Once connected with an experimental setup, the system must be tuned. The Quick Tuner Software, included with the controller, allows the user to adjust the motor parameters and test the settings until an acceptable response is achieved.

A simple closed flow loop filled with distilled water is used for characterizing the system. The pump is supplied by a reservoir elevated one meter to avoid cavitation at the inlet of the gear pump. Copper tubing, 57cm long with two 90° bends, connects from the pump outlet to the flow probe. Rigid tubing is selected over compliant tubing to

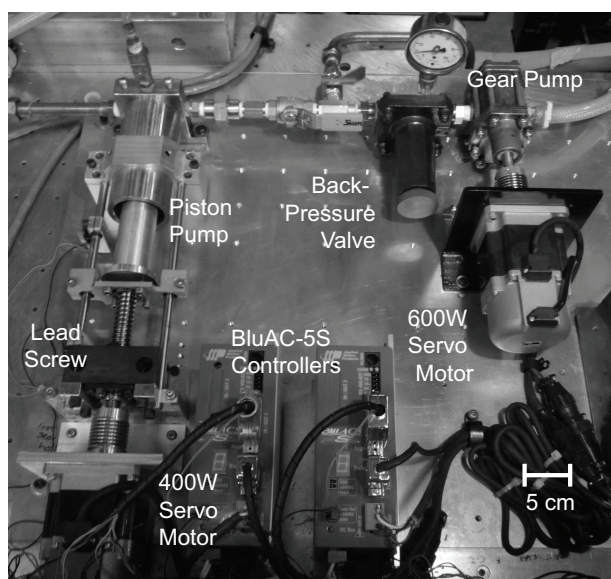
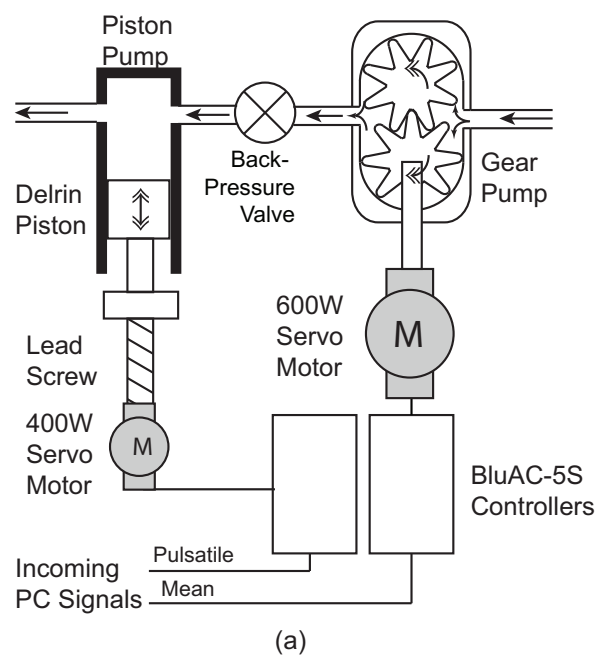
avoid corruption of the waveform downstream. Flow rates are measured by a Transonic 4N ultrasonic flow probe in conjunction with a T206 flow meter (Transonic Systems Inc., Ithica, NY). Polyester reinforced PVC tubing is used to connect the reservoir to the pump inlet and the flow probe outlet to the reservoir.

2.4.2 Evaluating System Performance

A series of tests was conducted to evaluate the performance of the pumping system. The system frequency response is determined by comparing output amplitude (i.e. flow rate) to a fixed amplitude sinusoidal waveform with varying frequency from 1-8Hz. The accuracy and repeatability of the system are tested by measuring the output flow rate for a sinusoidal waveform as well as measured coronary [39] and carotid waveforms [32]. A frequency of 0.5Hz is used for the sinusoidal waveform tests, while a frequency of 1.0Hz is used for the coronary and carotid waveform tests. Output data are recorded over fifteen waveforms and compared to the input signal. To characterize the fidelity of the mean output flow rate to the input signal, the root mean square deviation, σ , between the input signal and the mean output measurement is calculated.

Sinusoidal test results are displayed in Figure 2.6. The input signal (solid line) is plotted against the mean output signal (dashed line) and the upper and lower limits (dotted lines) of the set of 15 output waveforms. At this frequency, the mean output nearly matches the input waveform.

The frequency response to sinusoidal input is shown in Figure 2.7. It displays small variations in amplitude response in the 1-2Hz range covering the frequency of most



(b)

Figure 2.5: Diagram (a) and photograph (b) of the gear-piston pumping system.

experiments modeling physiological blood flows. The frequency response shows a damped resonant frequency near 5Hz. At higher frequencies, the amplitude decays rapidly, with the response falling to 28% of original amplitude at 7Hz and less than 10% of original amplitude at 8Hz. The frequency response depends on the impedance of the downstream flow loop and the system components. As an example, changing the copper tubing to a shorter segment with no bends changes the peak response frequency to approximately 3.5Hz. Because of this sensitivity to impedance, it is important to tune and characterize the system while connected to the experimental flow loop.

The accuracy and repeatability tests display the performance of the system for physiological inputs: coronary (Figure 2.8) and carotid (Figure 2.9) waveforms. Root mean square deviations of the mean output flow curve to the sinusoidal, coronary, and carotid input waveforms are 0.03, 0.10, and 0.05 respectively. For a system without any feedback correction, the pumps are capable of replicating physiological waveforms. The greatest deviations occur when steep changes are present in the waveforms; this effect is evident in the coronary waveform. The mean, minimum, and maximum curves show a steep slope response, but the system is clearly unable to generate the instantaneous response requested. The data from the carotid waveform illustrates that this system has the least error at constant acceleration. The largest error can be seen in diastole during the small oscillations.

For the purposes of waveform validation for this dissertation, basilar input and output waveforms from this experiment are compared (Figure 2.10). The basilar artery flow waveform is set to a frequency of 1.53 Hz. The working fluid is changed from water to the prescribed glycerine-water mixture. The measurements from the system are obtained

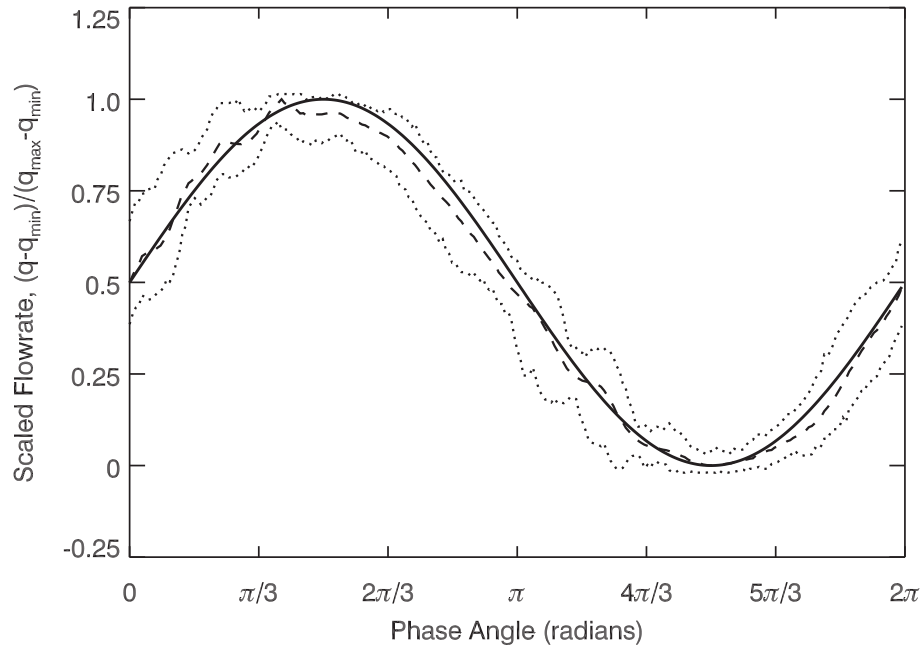


Figure 2.6: Comparison of the sinusoidal input waveform (solid line), mean output flow (dashed line), and spread of the extrema (dotted lines).

from flow meters placed at each of the outlet arteries and are phase shifted to adjust for lag introduced by the flow probes and motor controllers. Validation tests show good agreement between the input and outlet waveforms (Figure 2.10). While the width of the outlet peak is wider than the input peak, the major features of the waveform are captured.

2.5 Flow Loop

The flow loop consists of the model, pumping system, flow meter, and other components necessary to complete the system. The pumping system draws fluid from an elevated reservoir and pushes it through rigid 1/2" diameter copper tubing to the flow model. A heat tape with built-in temperature controller is wrapped around the tubing, maintaining the fluid at 30°C. The fluid flows into the model through the inlet fittings. The model's

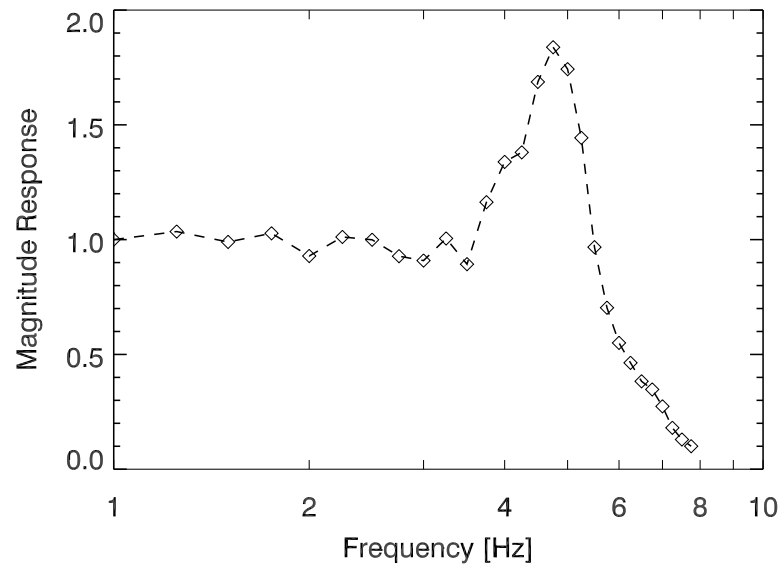


Figure 2.7: Frequency response of the system.

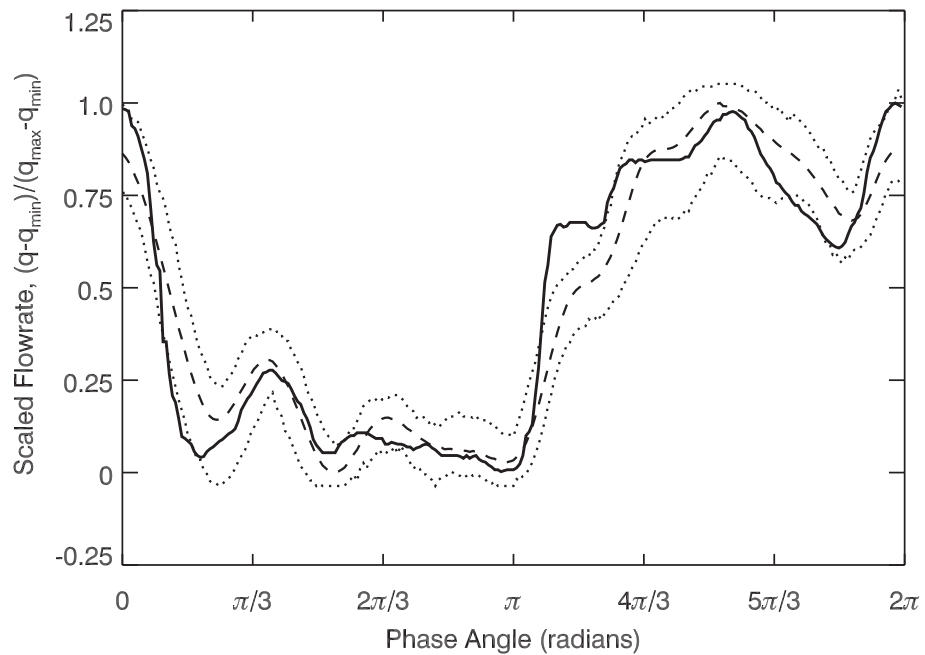


Figure 2.8: Comparison of the coronary waveform [39] (solid line), mean output flow (dashed line), and spread of the extrema (dotted lines).

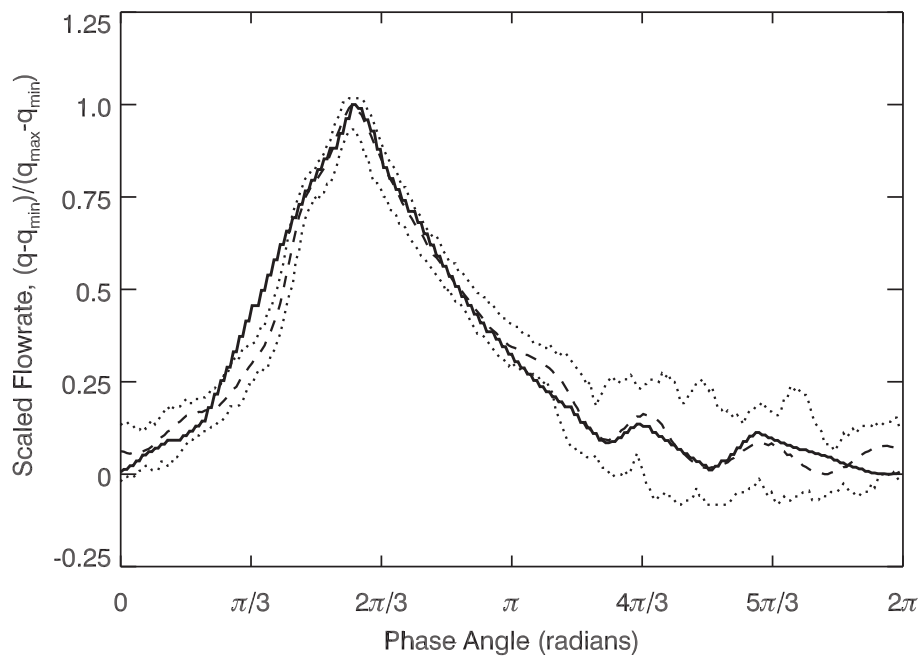


Figure 2.9: Comparison of the carotid input waveform [32] (solid line), mean output flow (dashed line), and spread of the extrema (dotted lines).

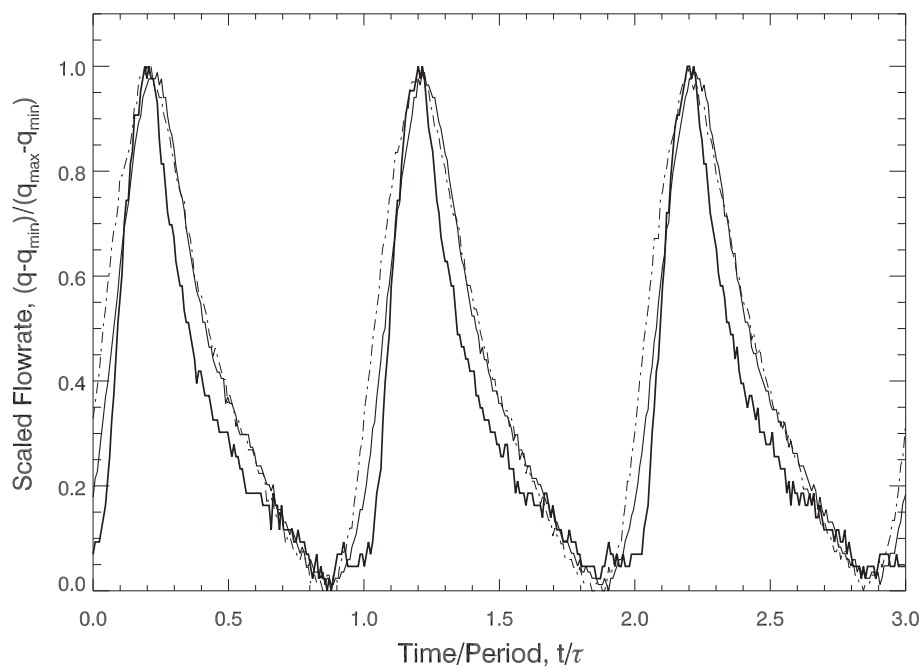


Figure 2.10: Phase-adjusted flow output measurements for a basilar artery bifurcation experiment. The input waveform (solid line) drives the pump. The output flow is divided into two outlets (broken lines).

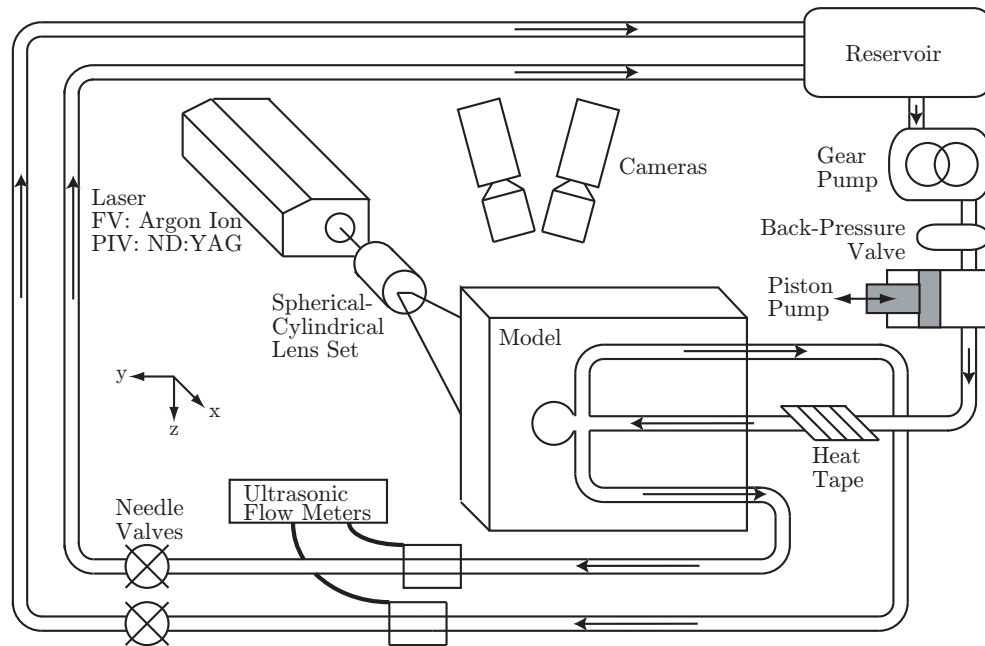


Figure 2.11: Diagram of the complete experimental setup.

outlet fittings are connected via rigid copper tubing to a pair of Transonic Inline flow probes mentioned in the previous section. The flow meter is calibrated for the working fluid. Downstream of the flow probes, a pair of needle valves allow the operator to control the flow rate between the two outlets. From the valves, the flows return to the reservoir. To reduce heat loss, most exposed sections of tubing are insulated.

2.6 Experimental Variables

In the experiments reported in this dissertation, three different techniques are employed to study the flow: flow visualization (FV), particle image velocimetry (PIV), and stereo particle image velocimetry (SPIV). The following chapters are a presentation of each technique in depth including the experimental setup, and results. First, however, it is

important to establish the parameters that will vary in each of the experiments.

Branching Ratio

The branching ratio is defined as the volumetric flow ratio through the left and right outputs, where left is in the $+z$ direction and right is in the $-z$ direction (Figure 2.1). This ratio is controlled by adjusting the needle valves and verified using the flow meter. A symmetric flow ratio is defined as 50:50. During planning, branching ratios of 20:80, 25:75, 33:67, 50:50, 67:33, 75:25, and 80:20 are used. Two more ratios were used after the preliminary observations. Between the 50:50 and 33:67 cases, a jet within the dome abruptly change from occupying the left half to the right half of the dome. During experimentation, this transition was found to occur near a 47:53 branching ratio. The precise ratio could not be captured because the behavior is highly unstable. As a result, flow ratios of 48:52 and 46:54 are employed to examine this transition regime.

Flow Planes

The views used in image acquisition are limited and vary depending on the type of experimental technique. For SPIV, images of the x - y plane are captured through the two 45° windows; because two views are required, the plane that contains the intersection point of the windows' axes is the only one that can be captured. FV and PIV images of the y - z plane are captured through the windows above and below the dome in the x -direction; the system is free to move and capture images at any value along the x -axis. Three planes were selected (Figure 2.12): the midline of the model ("midplane"), half the distance between the midplane and the upper limit of the dome ("upper quarter-plane"), and half the distance

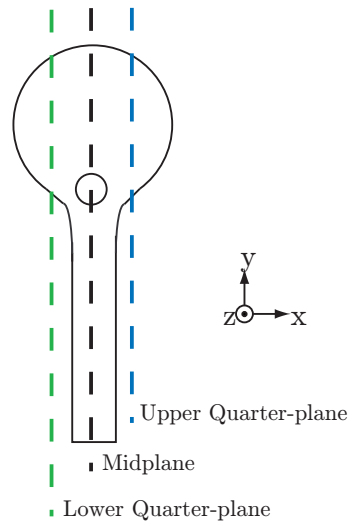


Figure 2.12: Planes along which data are collected for FV and PIV.

between the midplane and the lower end of the dome (“lower quarter-plane”).

Chapter 3

Flow Visualization

Flow visualization (FV) is an extremely useful tool that yields the qualitative features of flow fields. This tool is particularly useful in observing flow behaviors, structures, and patterns. FV is an essential compliment to later quantitative experiments. This chapter will review the principles behind FV, describe the experimental setup, present the results from the experiments, and discuss the implications of the results.

3.1 FV: Theory

The goal of FV is to visualize a flow that often has no intrinsic visual markers that can be followed. This problem is exacerbated by the fact that the working fluid in this experiment is transparent. Thus, FV requires the introduction of visible identifying markers, usually an attribute of the flow such as density variations or foreign materials. The latter is used in this experiment in the form of particles added to the working fluid to seed the flow. The particles are made visible by laser illumination. To be effective, the

particles must meet two requirements: 1) the particles must reflect, scatter, transmit, or emit enough light to be visible compared to the working fluid, and 2) the particles must be of the proper density and size so they do not significantly influence nor significantly deviate from the flow.

The next consideration is converting a field of visible particles into usable information. Because each particle is visible, it appears as a point of light to the camera imaging the flow. When recording the flow for an exposure time, Δt , the particle will travel a distance approximately equal to $u\Delta t$, where u is the magnitude of the local fluid velocity. During the motion of the particle, the camera will capture the accumulation of scattered light over the path incident on the lens. Applying this to the entire field of particles that seed the flow yields an image with streaks that can provide good approximations to local velocities throughout the flow if Δt is sufficiently small. If Δt is large, then particle paths are recorded. For the case of unsteady flow considered here, the path lines will likely overlap, hence yielding undecipherable images. FV images can be recorded in a sequence to form a movie which helps visualize flow patterns within the imaging plane. Out-of-plane motions are captured as particle motion into and out of the laser sheet, causing particles appear or disappear on images. As a result, streak pictures cannot distinguish between a slow moving particle and one moving out-of-plane.

3.2 FV: Experimental Setup

This section details the components of the experiment specific to the FV setup. As introduced in the previous section, FV requires seeding the working fluid with particles,

illuminating the particles, and imaging the particle field.

3.2.1 Seed Particles

FV requires a flow seeded with particles that reflect or emit enough light to be visible during imaging. The particles must be small enough to follow the flow without causing any changes in the flow behavior, while being large enough to be imaged. Duke Scientific $15\mu\text{m}$ Fluorescent Polymer Microspheres are the particles used for the experiments. The particles fluoresce at a wavelength 75nm longer than absorbed. In the FV experiments, the particles absorb 514nm light and fluoresce 589nm light. Fluorescing particles were chosen over reflective or scattering particles because the fluoresced light can be separated from the illumination, increasing the contrast and visibility of the particles.

The other consideration is the ability of the particles to follow the flow. Ideally, the particles should be neutrally buoyant, but this requirement is dependent on the working fluid and particles available. To evaluate the deviation that gravity may cause, the sedimentation velocity is considered.

Using Stokes analysis, the sedimentation speed for a spherical particle is given by [43]:

$$v_s = \left[\frac{\rho_{particle}}{\rho_{fluid}} - 1 \right] \frac{gd_{particle}^2}{18\nu_{fluid}}, \quad (3.1)$$

where $\rho_{particle}$ is the particle density and $d_{particle}$ is the particle diameter. In the ideal case where the particle is neutrally buoyant, $v_s = 0$. For this experiment, the sedimentation speed is $10.7\mu\text{m/s}$. For an exposure time of 1s, a $10.7\mu\text{m}$ (0.71 times the diameter of the particle) drift is negligible given the size of the flow area. Therefore, the effects of gravity

on the particle are considered a negligible source of error in these experiments.

To ensure that the particles are acceptable for FV usage, another source of error is considered: the effect of drag on the particles in the direction of travel [50]. The Stokes response time, t_s , also called the relaxation time, is a measure of the time for a particle to achieve velocity equilibrium with the surrounding fluid. It is defined as

$$t_s = \frac{1}{18} \frac{\rho_{particle}}{\mu} d_{particle}^2, \quad (3.2)$$

Using values for the fluorescent particle and working fluid, the relaxation time is $1.02\mu s$, which is several orders smaller than the timescales of this experiment. This alleviates any concern that the particles may deviate during accelerations in the flow.

3.2.2 Illumination

The illumination for the experiment is provided by a Lexel Model 85 Argon-Ion laser, which outputs a continuous 514nm light beam at 1W. A thin, focused laser sheet is required for planar flow visualization. This is achieved by directing the laser through a spherical-cylindrical lens pair (Figure 3.1). A 200mm focal length spherical lens focuses the beam on the center of the model and a -75mm focal length cylindrical lens expands the beam into a planar sheet. A negative focal length cylindrical lens is used to avoid focusing the laser light at the focal line in front of the optics prior to the model. Combined, the lenses turn the laser beam into a 0.5mm thick laser sheet at the region of interest, which illuminates the y-z plane (Figure 2.1). The x-coordinate of the laser and optics can be adjusted providing a single degree of freedom.

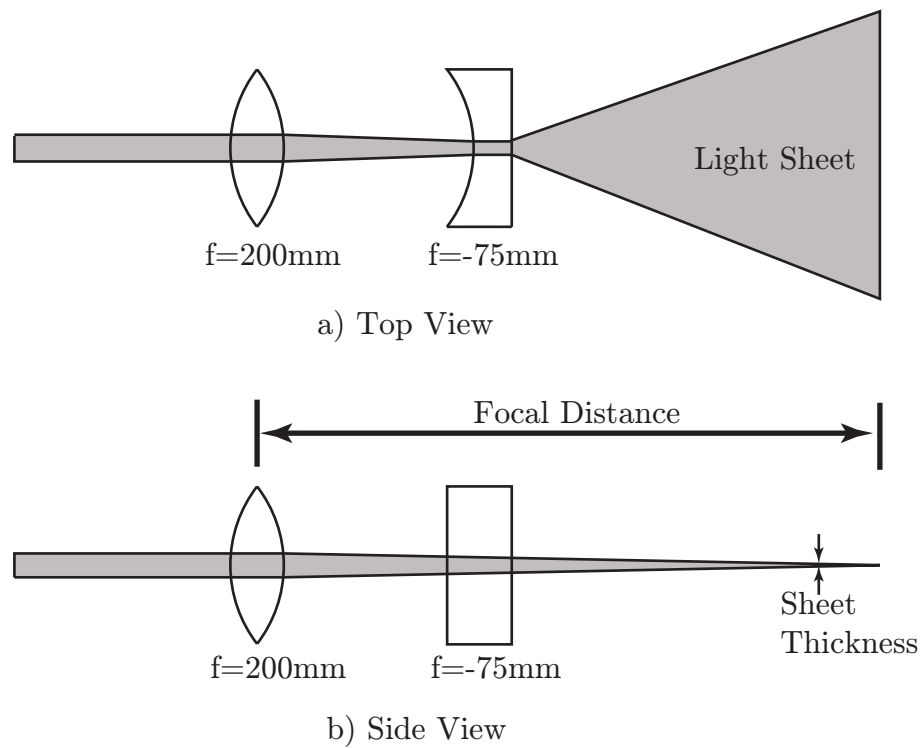


Figure 3.1: Laser sheet lens configuration using a spherical and cylindrical lens as seen from (a) above (e.g. the point of view of the camera), and (b) the side.

3.2.3 Imaging

An Integrated Design Tools MotionPro X-3 Camera is used for image acquisition. The camera has a 1280 x 1024 CCD, capable of capturing full resolution images at rates of up to 1000Hz. Full resolution images are captured at 100 images per waveform. The camera aligned with the x-axis (Figure 2.1) above the center of the dome and perpendicular to the laser sheet. The camera's position along the x-axis can be adjusted to maintain the laser sheet in focus. A C-mount to Canon lens adapter is used for commercially available lenses which control aperture and focus. The primary lens is a Canon f=28mm lens. A set of +1, +2, and +4 Hoya diopter closeup lenses are mounted in front of the lens to magnify the image of the dome. Mounted within the C-mount adapter is an Edmund Optics 550nm longpass glass color filter to allow light of wavelength $>550\text{nm}$ to pass. This filter allows the 589nm light fluoresced from the particles to pass, but blocks the 514nm laser light that is scattered by the working fluid.

3.3 FV: Results

Figures 3.2-3.28 display images captured for nine branching ratios at three imaging planes (Figure 2.12). Each figure displays seven FV images and the corresponding points on the input waveform. The figures are divided into groups based on the image plane. Figures 3.2-3.10 are from the midplane. Figures 3.11-3.19 are from the upper quarter-plane. Figures 3.20-3.28 are from the lower quarter-plane. The streaking provides an estimate of relative speed but not directionality. The following paragraphs describes the observations that are apparent in watching the images as a movie in sequence.

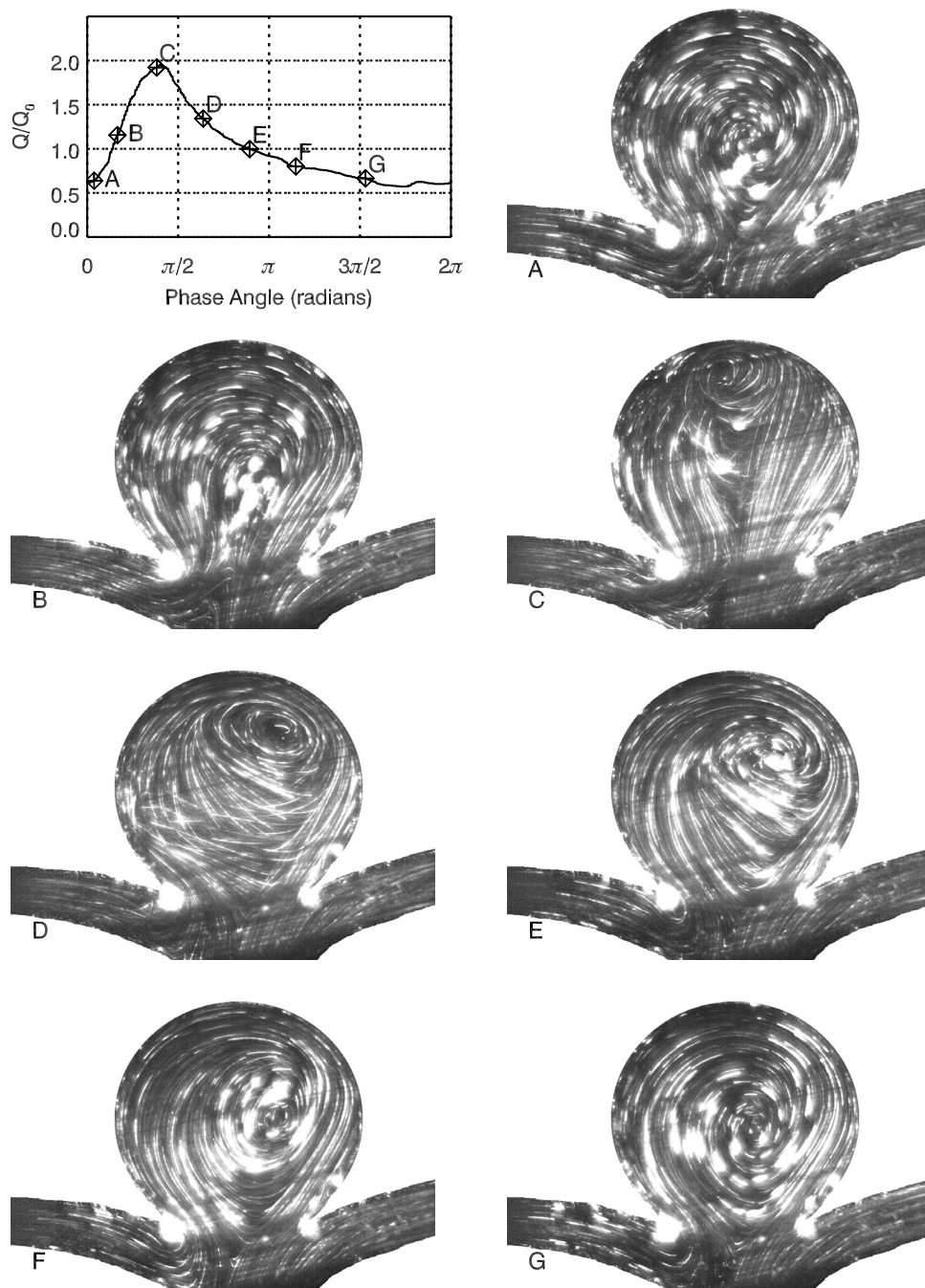


Figure 3.2: Flow visualization images at the midplane for branching ratio of 20:80 over one cycle indicated by the points in the plot of the waveform cycle.

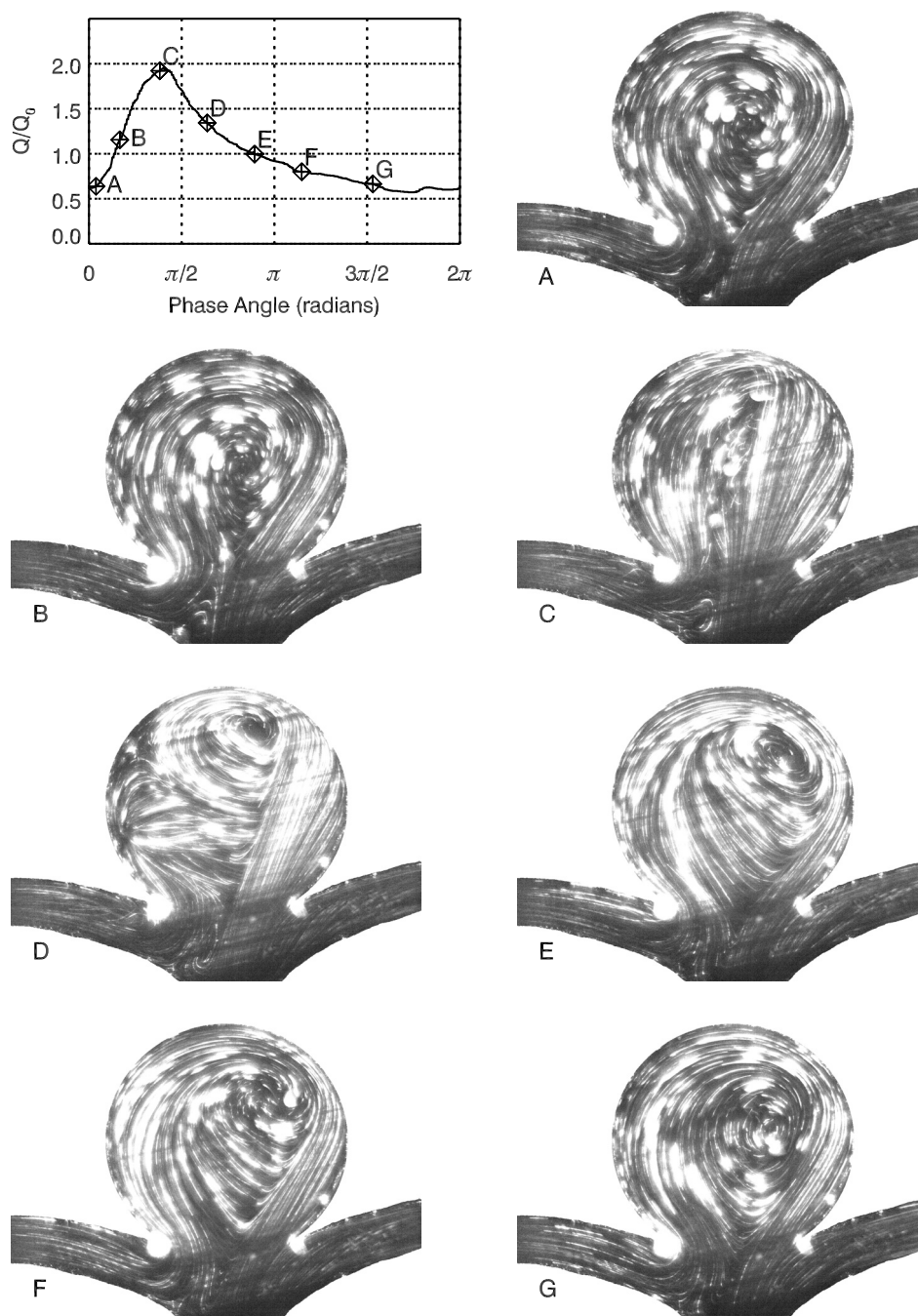


Figure 3.3: Flow visualization images at the midplane for branching ratio of 25:75 over one cycle indicated by the points in the plot of the waveform cycle.

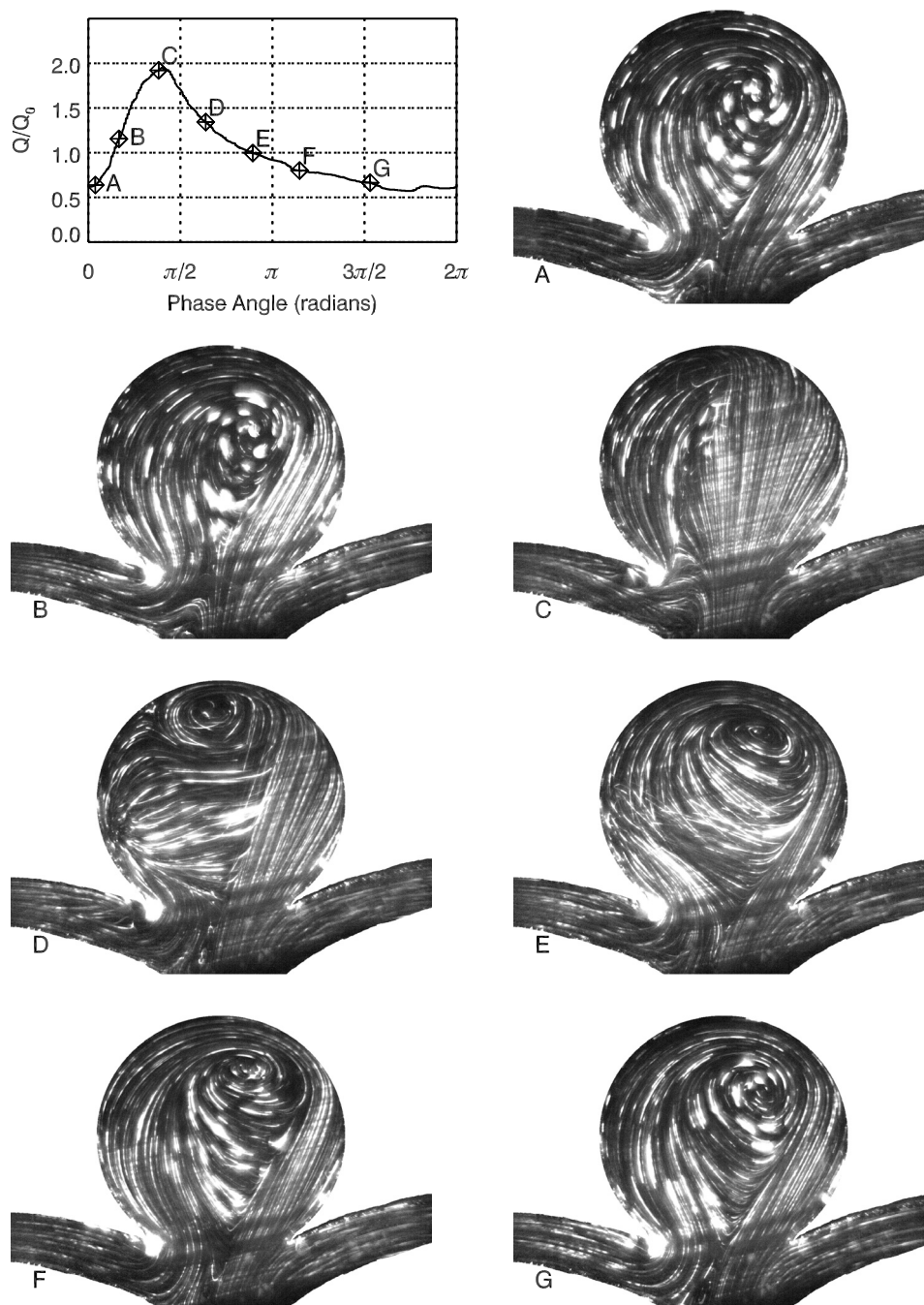


Figure 3.4: Flow visualization images at the midplane for branching ratio of 33:67 over one cycle indicated by the points in the plot of the waveform cycle.

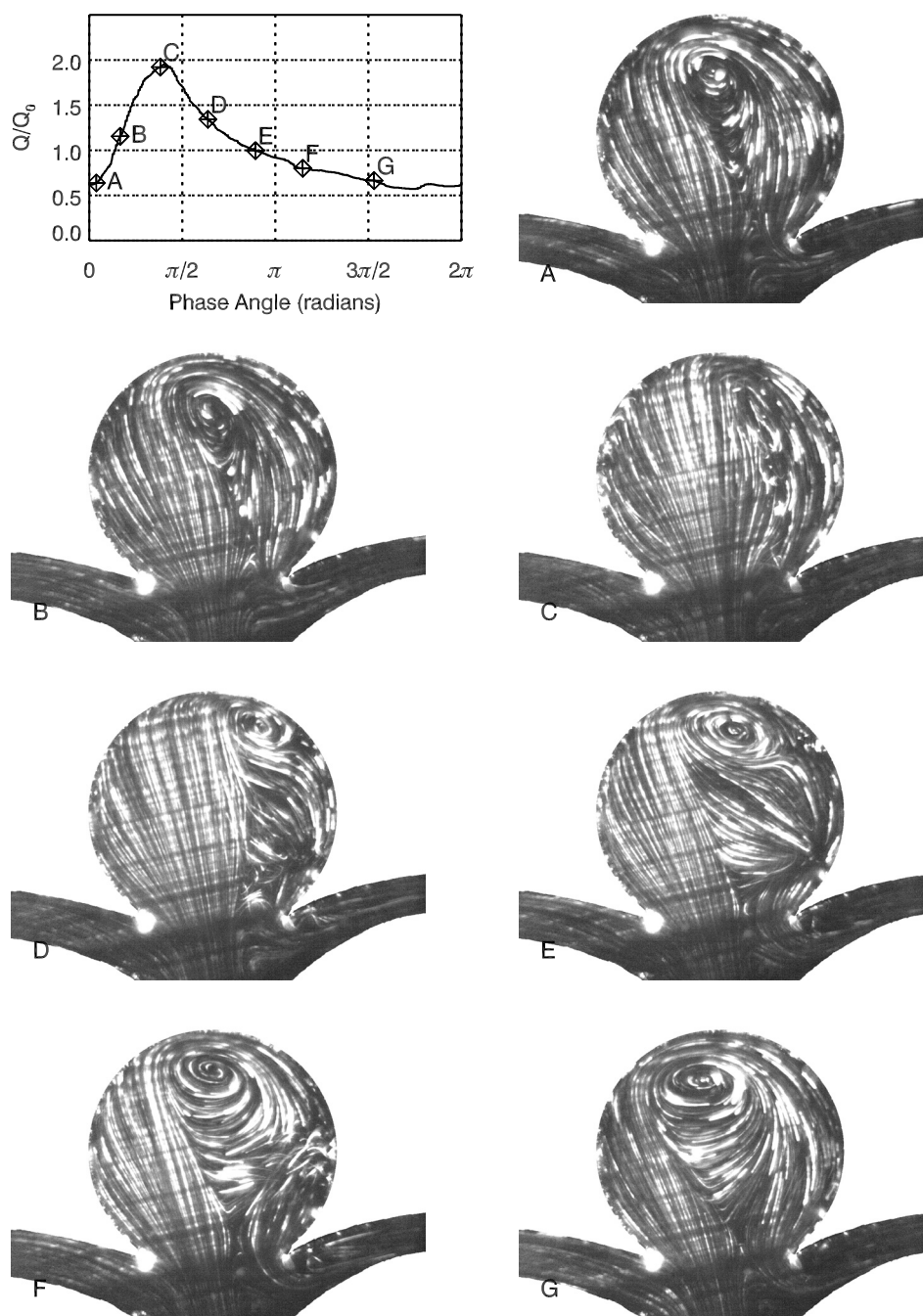


Figure 3.5: Flow visualization images at the midplane for branching ratio of 46:54 over one cycle indicated by the points in the plot of the waveform cycle.

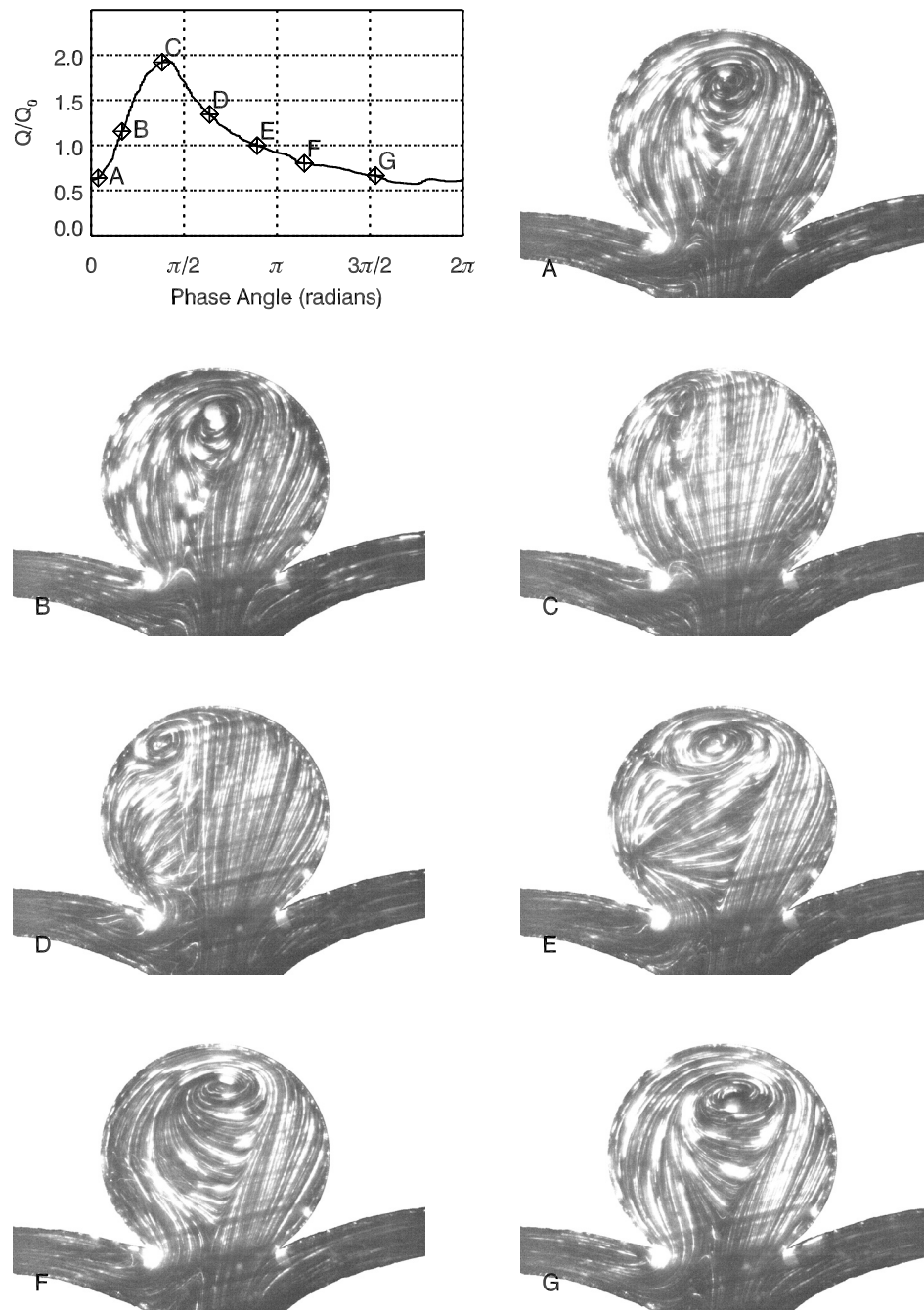


Figure 3.6: Flow visualization images at the midplane for branching ratio of 48:52 over one cycle indicated by the points in the plot of the waveform cycle.

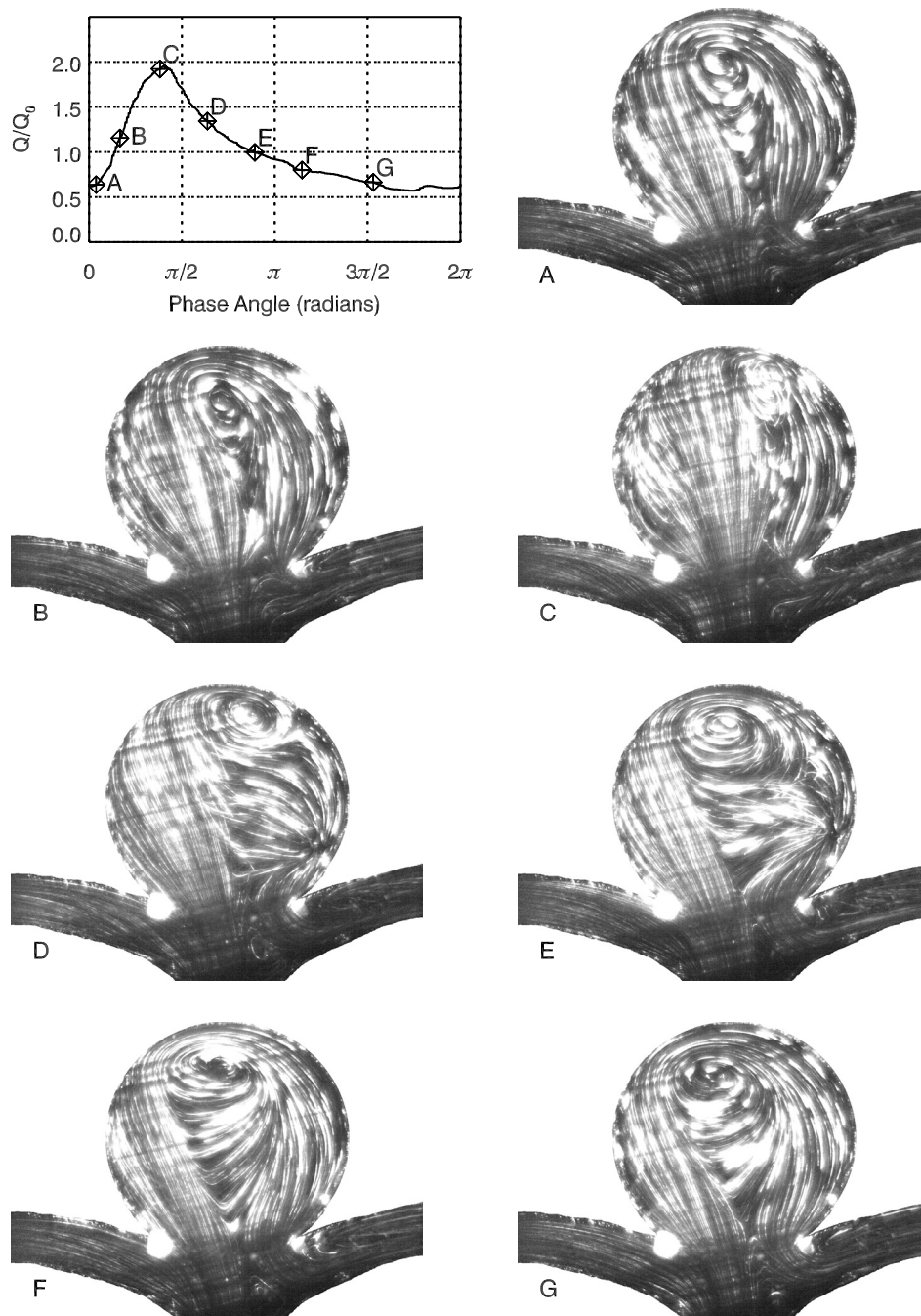


Figure 3.7: Flow visualization images at the midplane for branching ratio of 50:50 over one cycle indicated by the points in the plot of the waveform cycle.

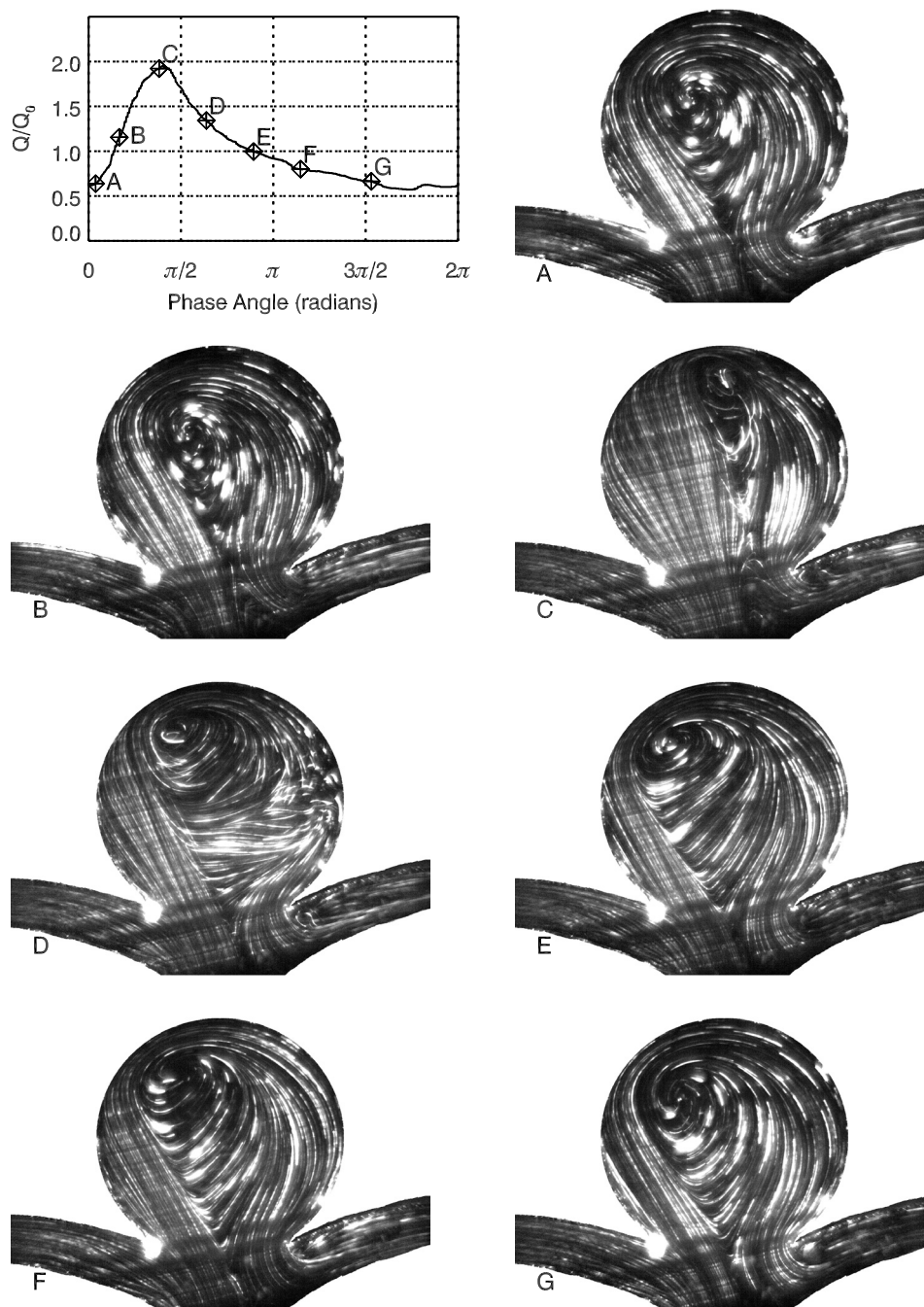


Figure 3.8: Flow visualization images at the midplane for branching ratio of 67:33 over one cycle indicated by the points in the plot of the waveform cycle.

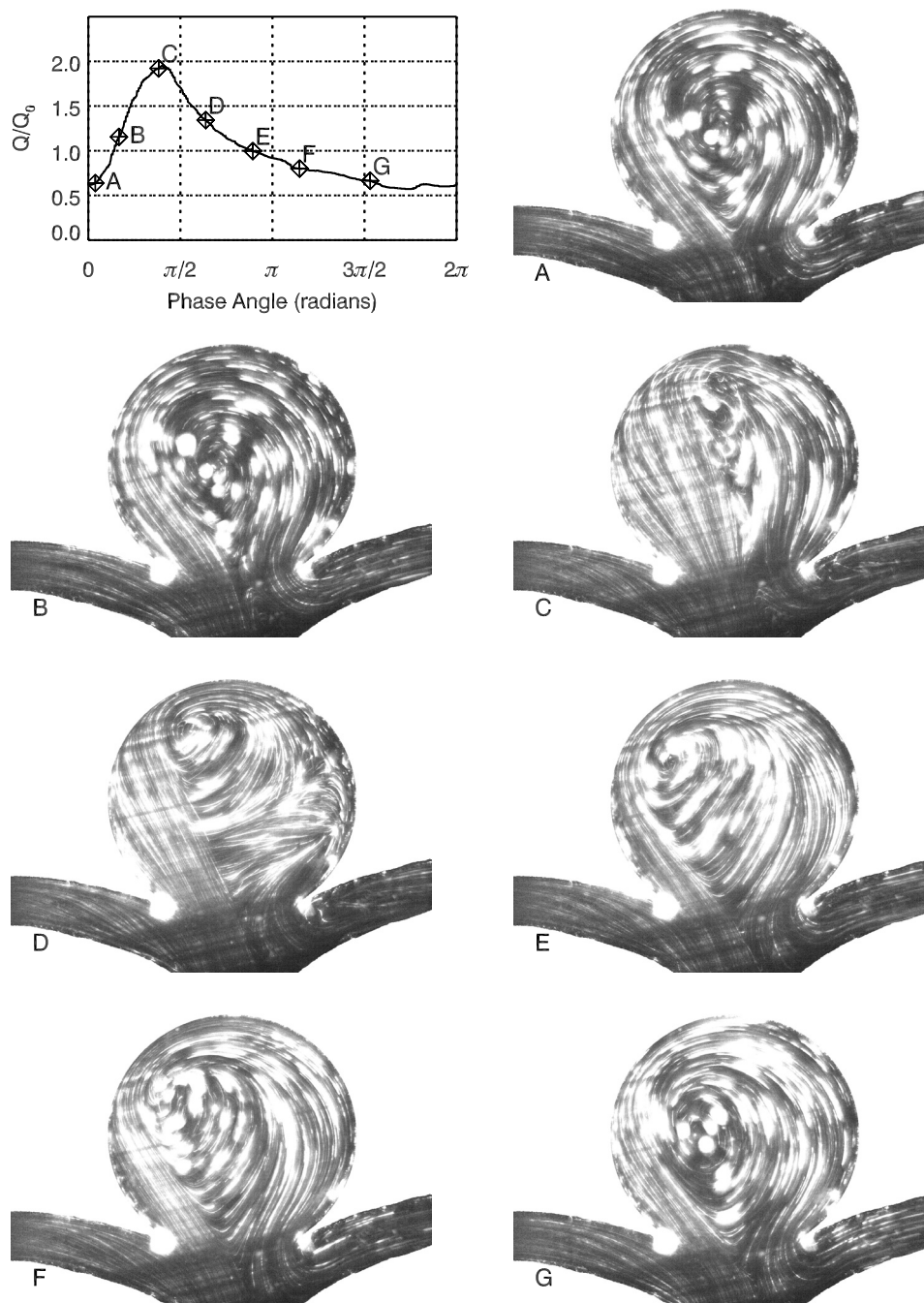


Figure 3.9: Flow visualization images at the midplane for branching ratio of 75:25 over one cycle indicated by the points in the plot of the waveform cycle.

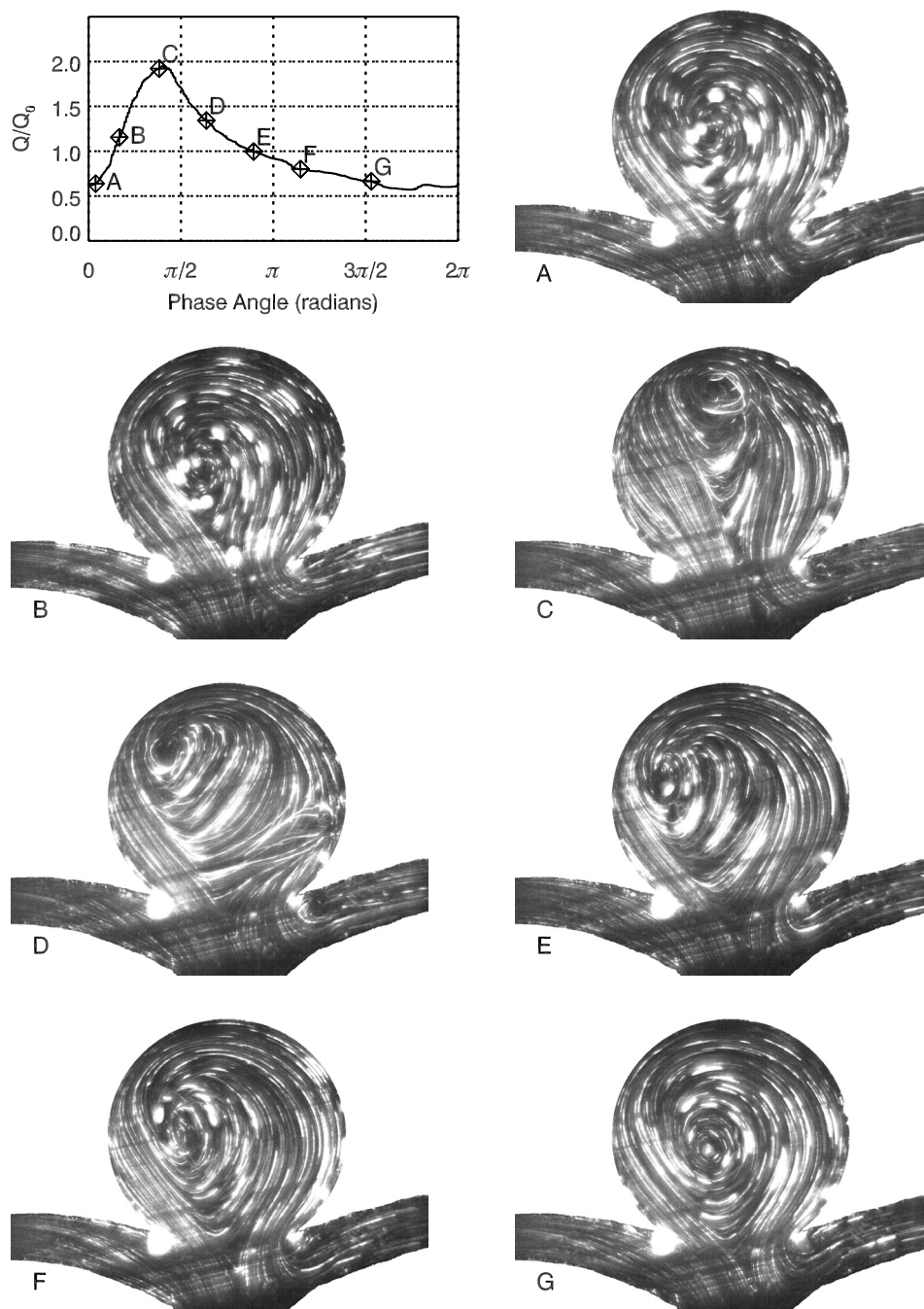


Figure 3.10: Flow visualization images at the midplane for branching ratio of 80:20 over one cycle indicated by the points in the plot of the waveform cycle.

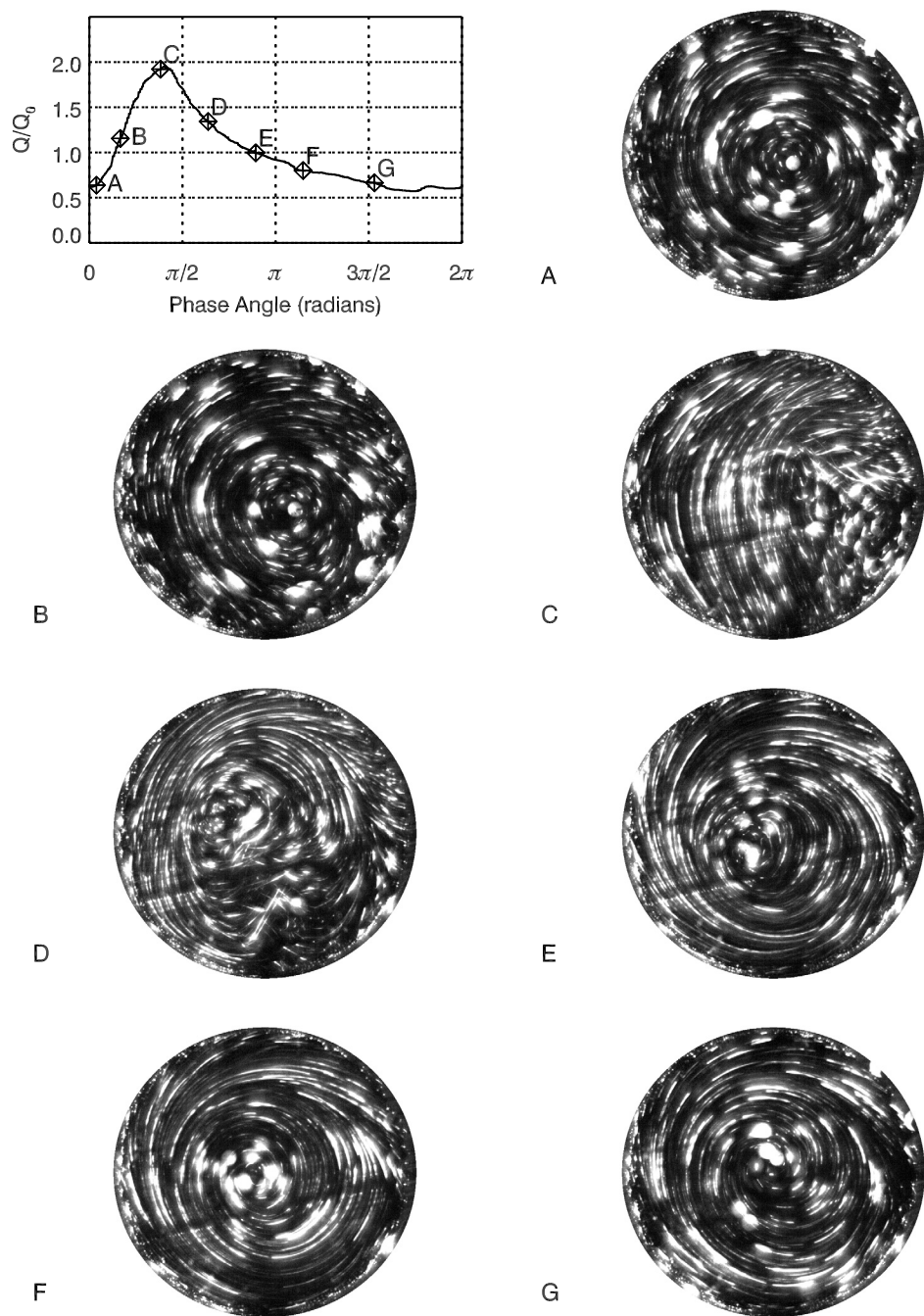


Figure 3.11: Flow visualization images at the upper-quarter plane for branching ratio of 20:80 over one cycle indicated by the points in the plot of the waveform cycle.

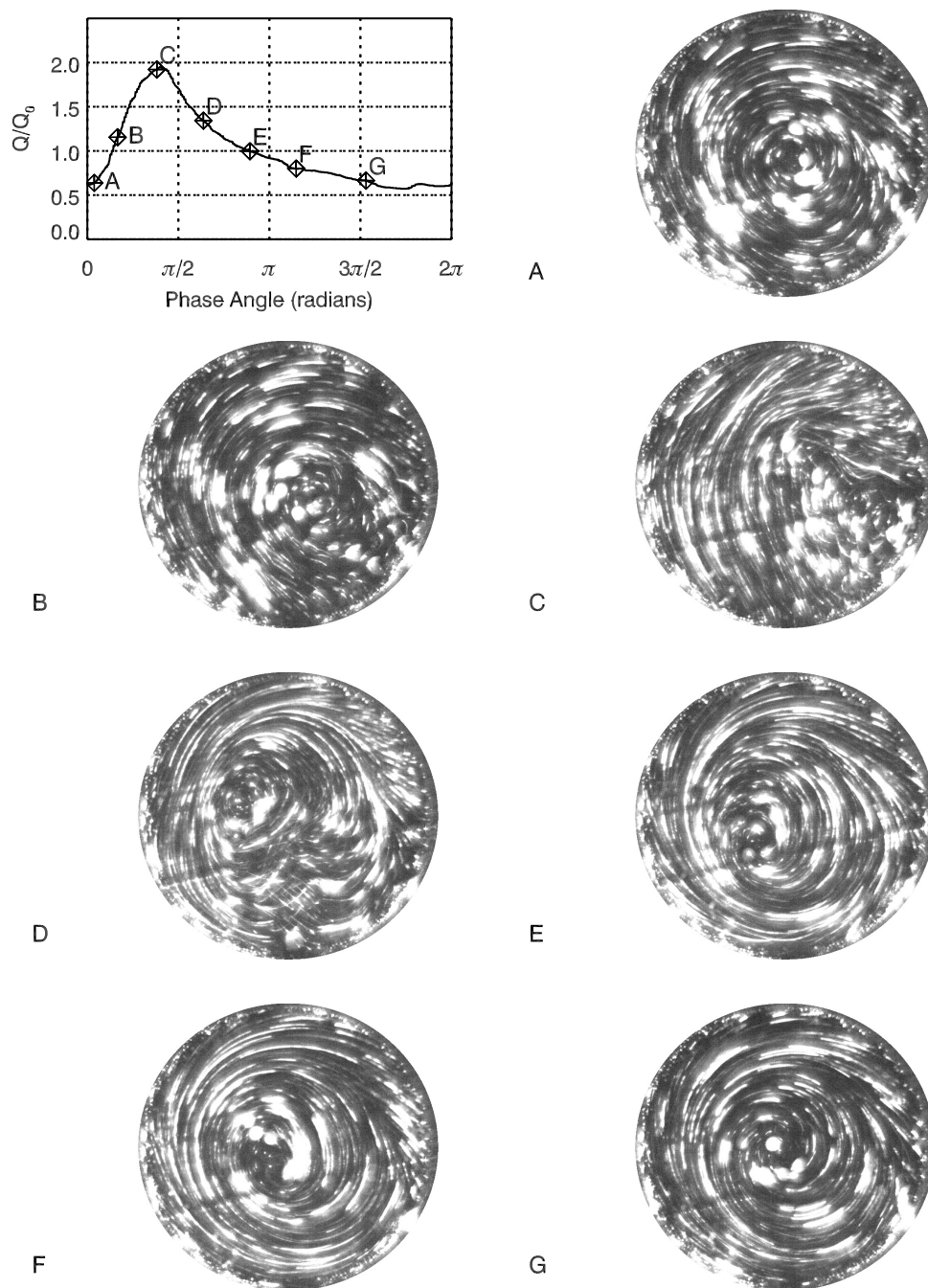


Figure 3.12: Flow visualization images at the upper-quarter plane for branching ratio of 25:75 over one cycle indicated by the points in the plot of the waveform cycle.

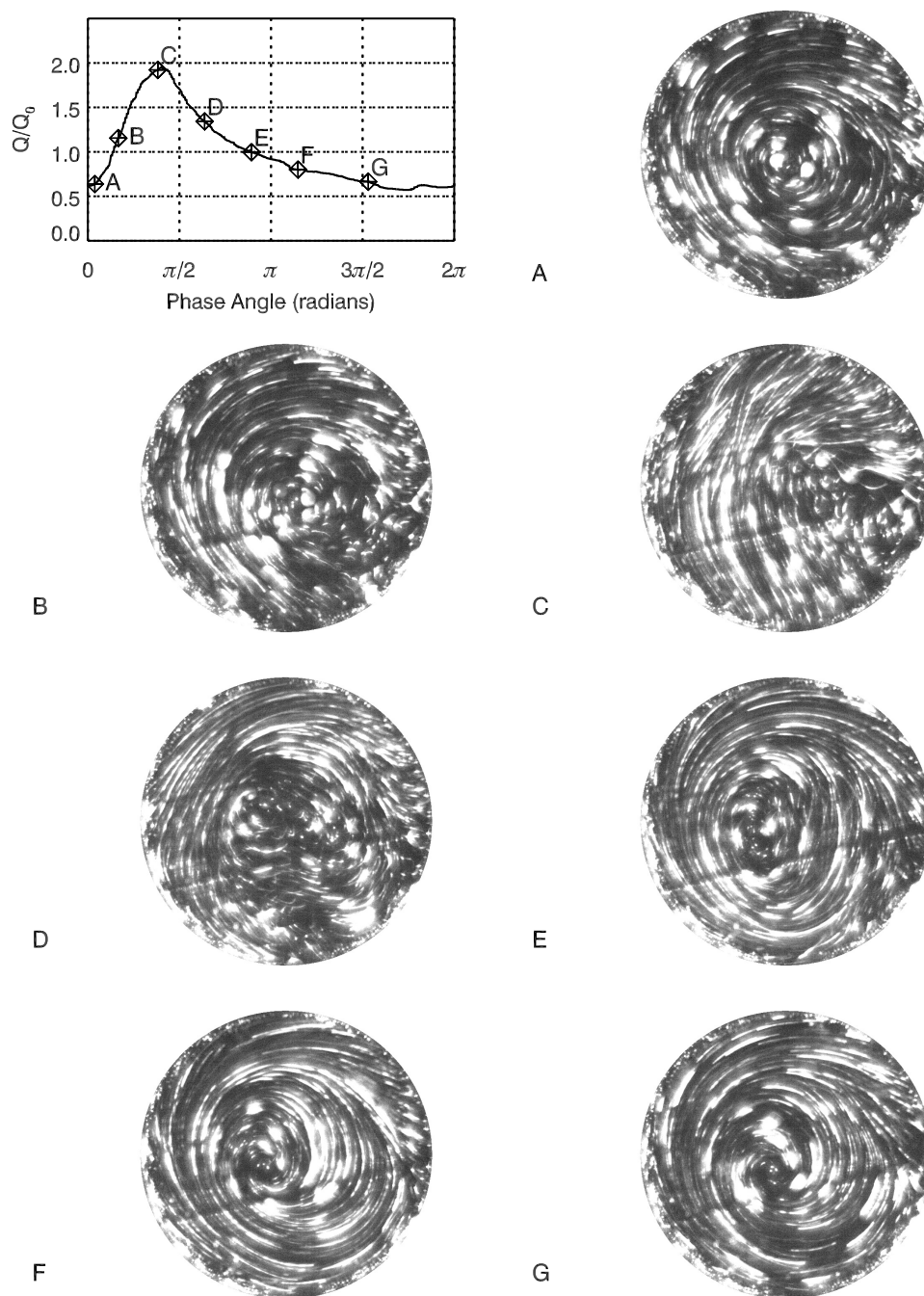


Figure 3.13: Flow visualization images at the upper-quarter plane for branching ratio of 33:67 over one cycle indicated by the points in the plot of the waveform cycle.

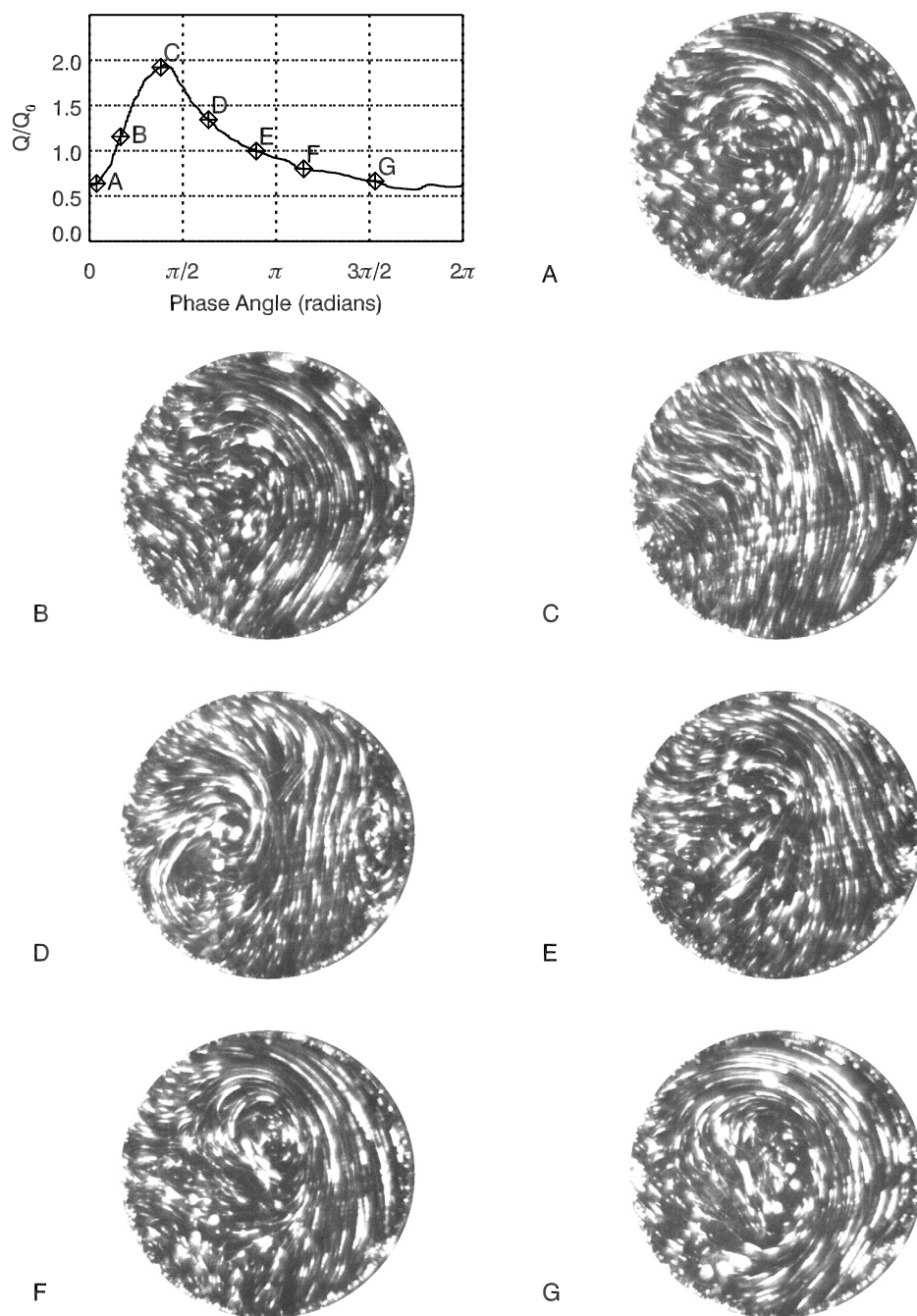


Figure 3.14: Flow visualization images at the upper-quarter for branching ratio of 46:54 over one cycle indicated by the points in the plot of the waveform cycle.

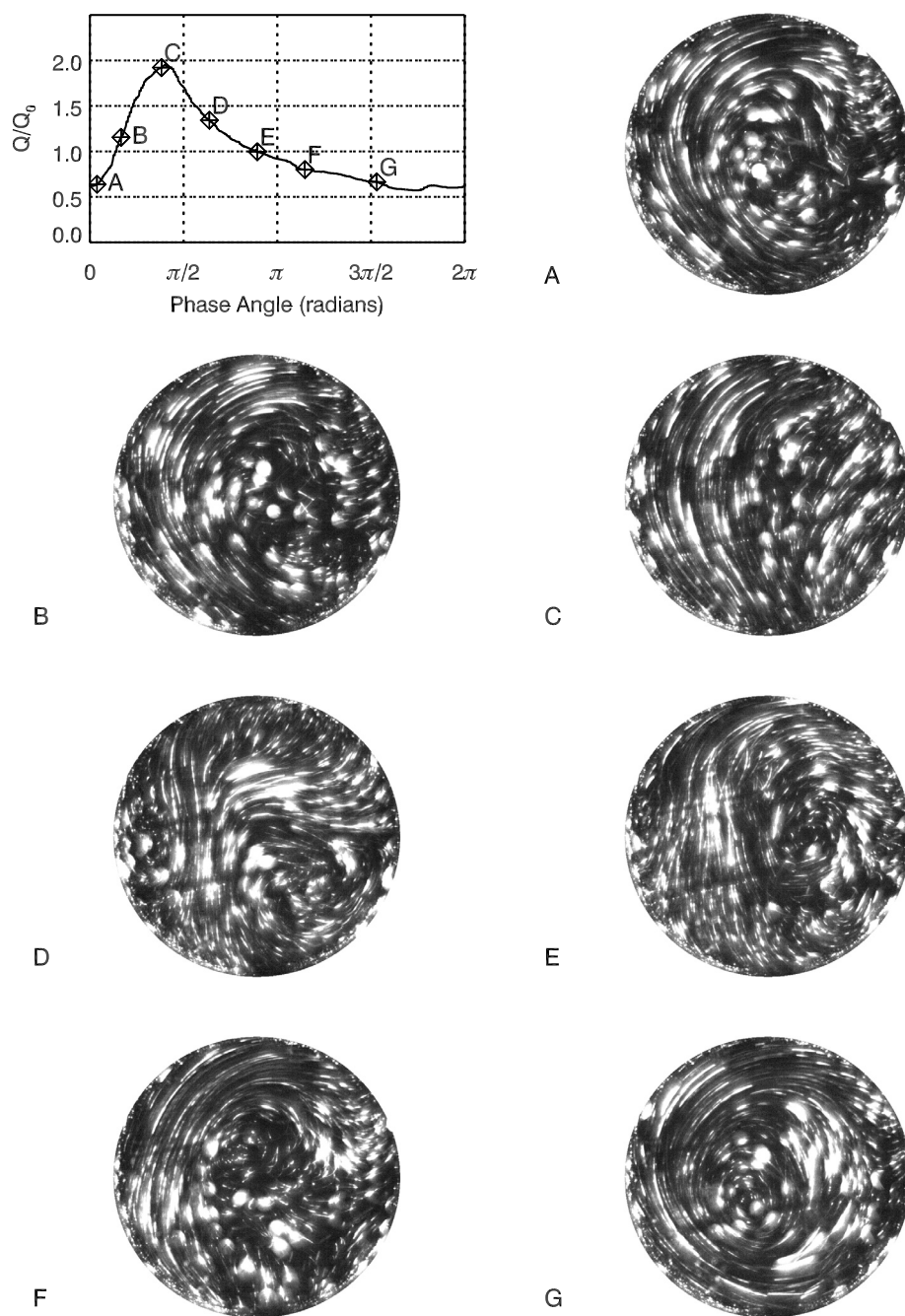


Figure 3.15: Flow visualization images at the upper-quarter for branching ratio of 48:52 over one cycle indicated by the points in the plot of the waveform cycle.

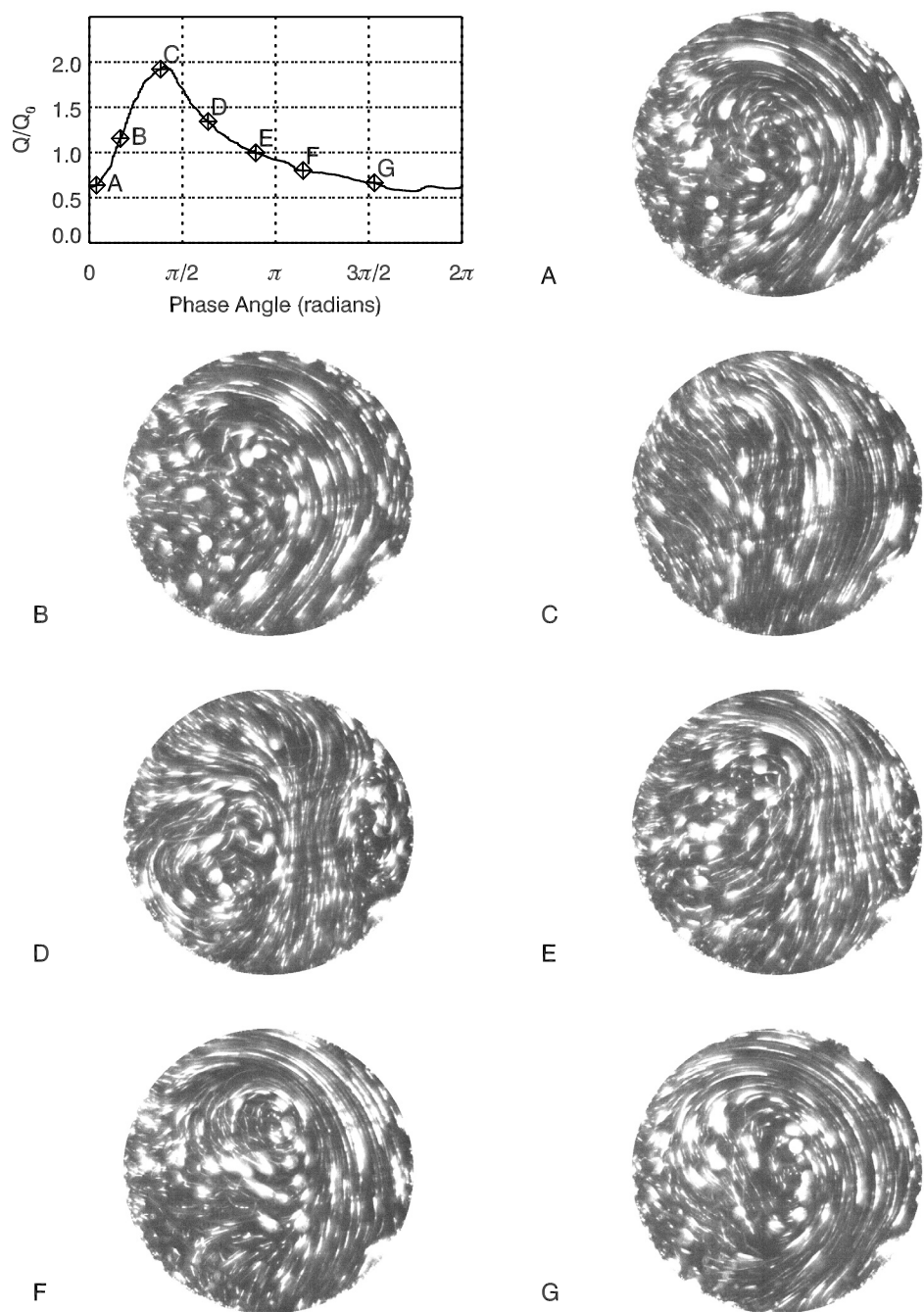


Figure 3.16: Flow visualization images at the upper-quarter plane for branching ratio of 50:50 over one cycle indicated by the points in the plot of the waveform cycle.

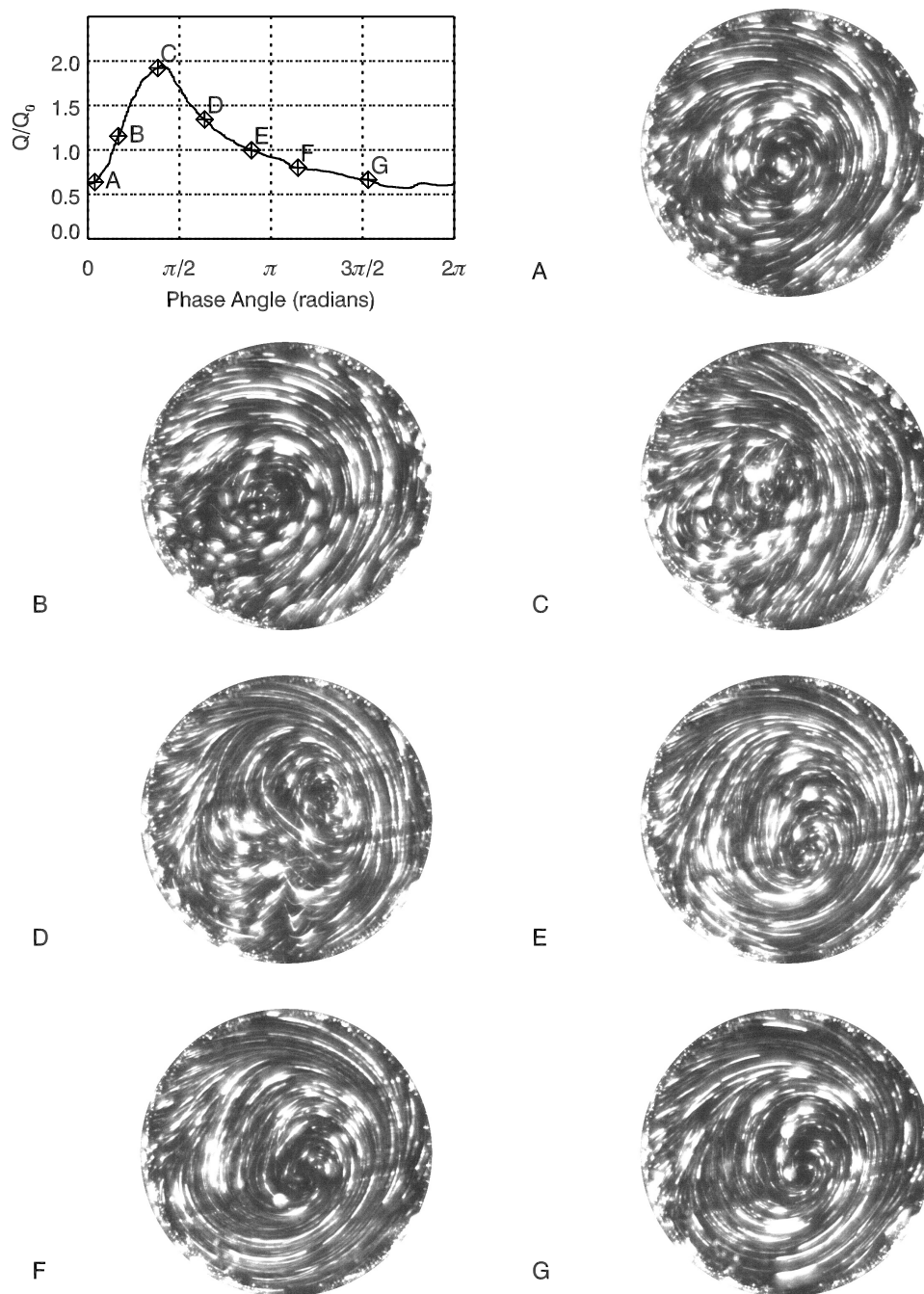


Figure 3.17: Flow visualization images at the upper-quarter plane for branching ratio of 67:33 over one cycle indicated by the points in the plot of the waveform cycle.

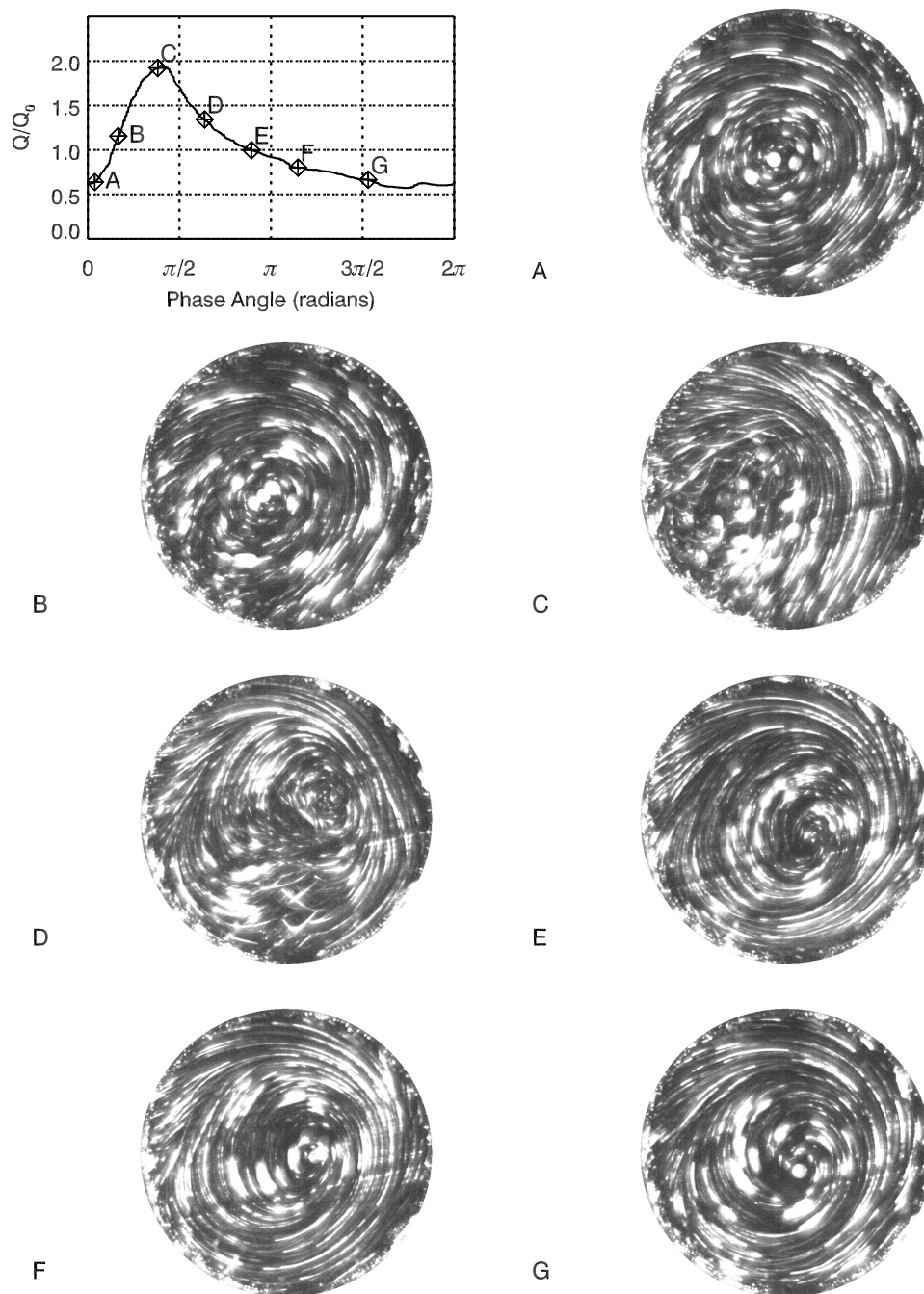


Figure 3.18: Flow visualization images at the upper-quarter plane for branching ratio of 75:25 over one cycle indicated by the points in the plot of the waveform cycle.

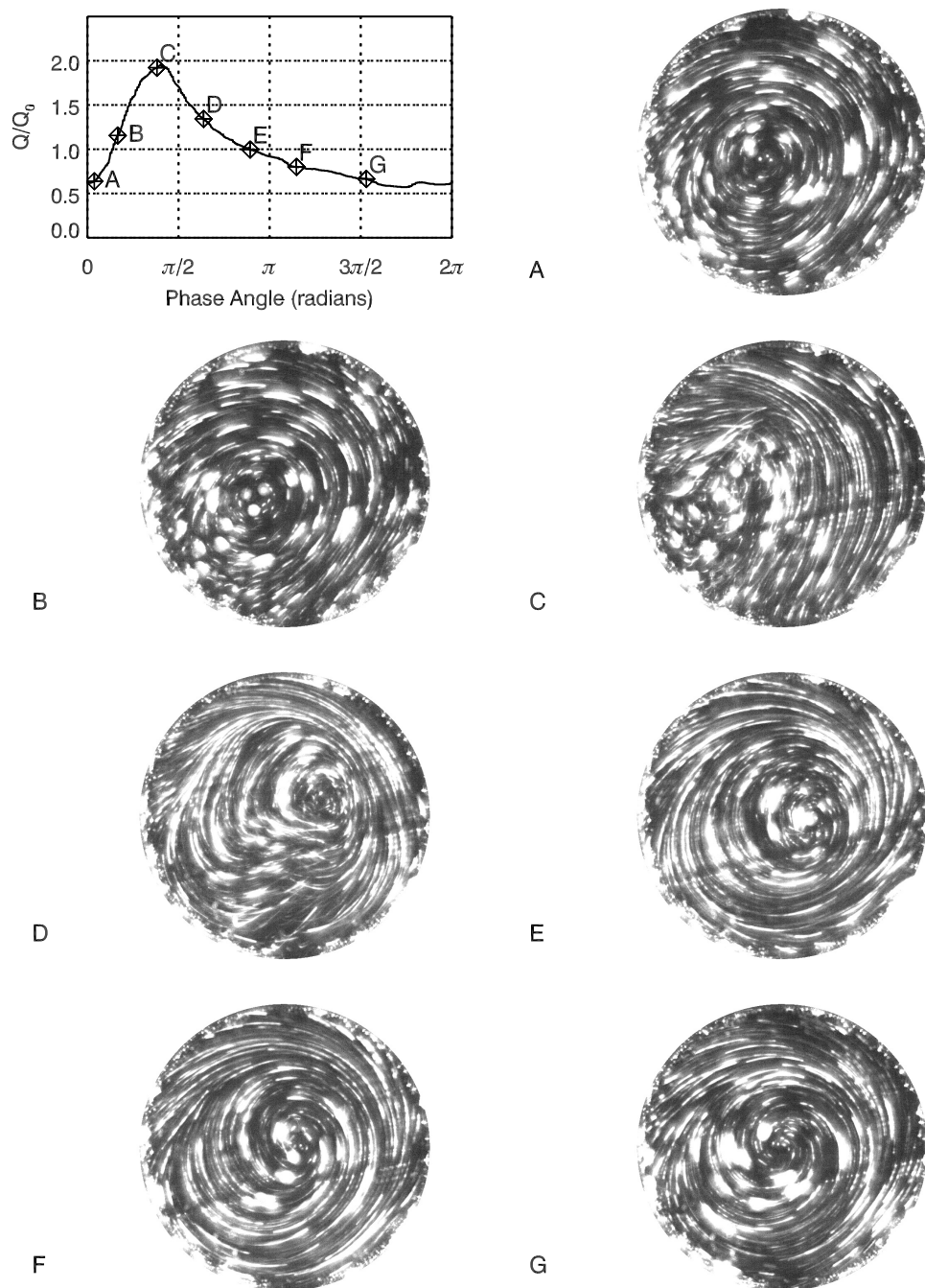


Figure 3.19: Flow visualization images at the upper-quarter plane for branching ratio of 80:20 over one cycle indicated by the points in the plot of the waveform cycle.

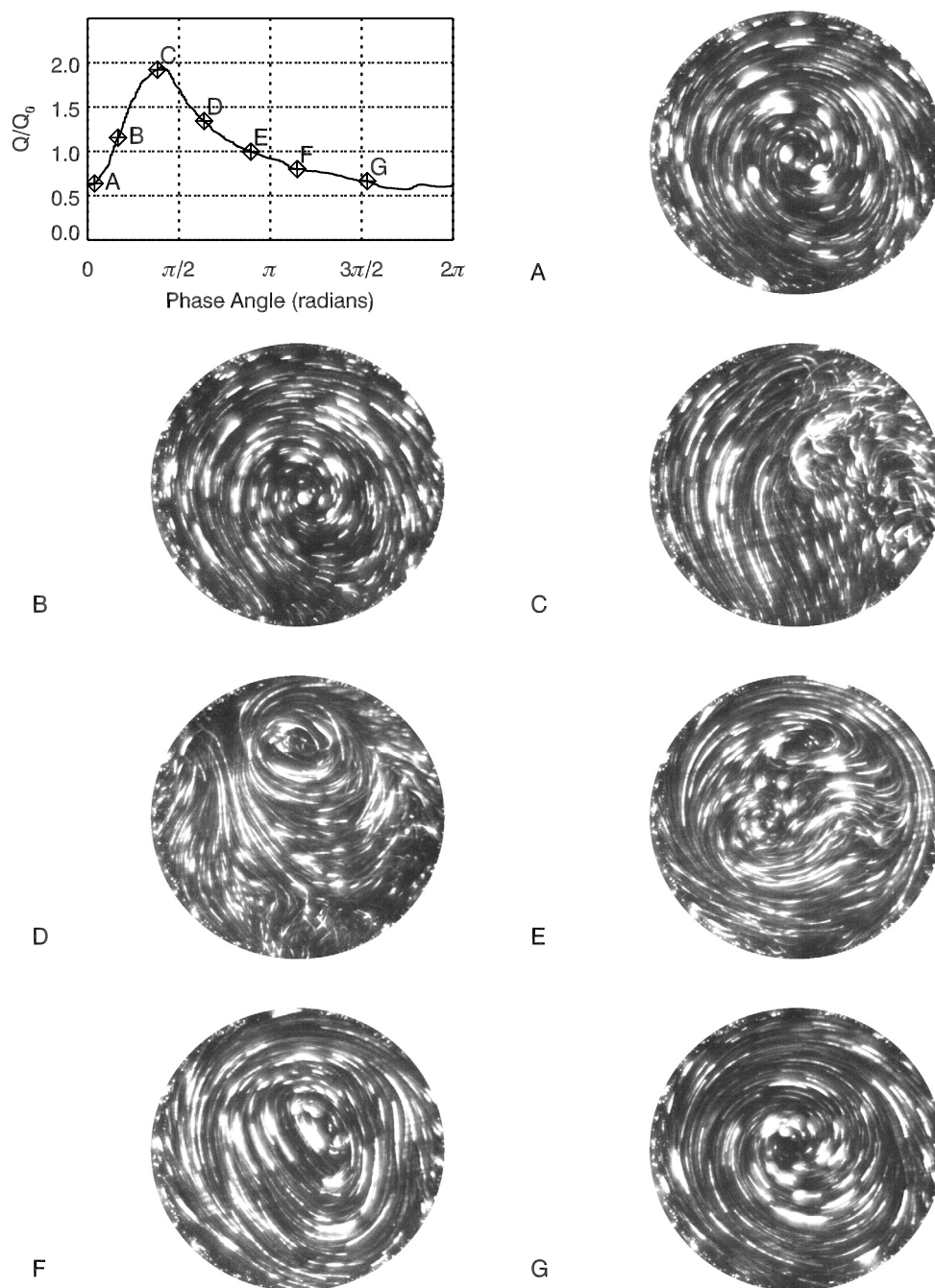


Figure 3.20: Flow visualization images at the lower-quarter for branching ratio of 20:80 over one cycle indicated by the points in the plot of the waveform cycle.

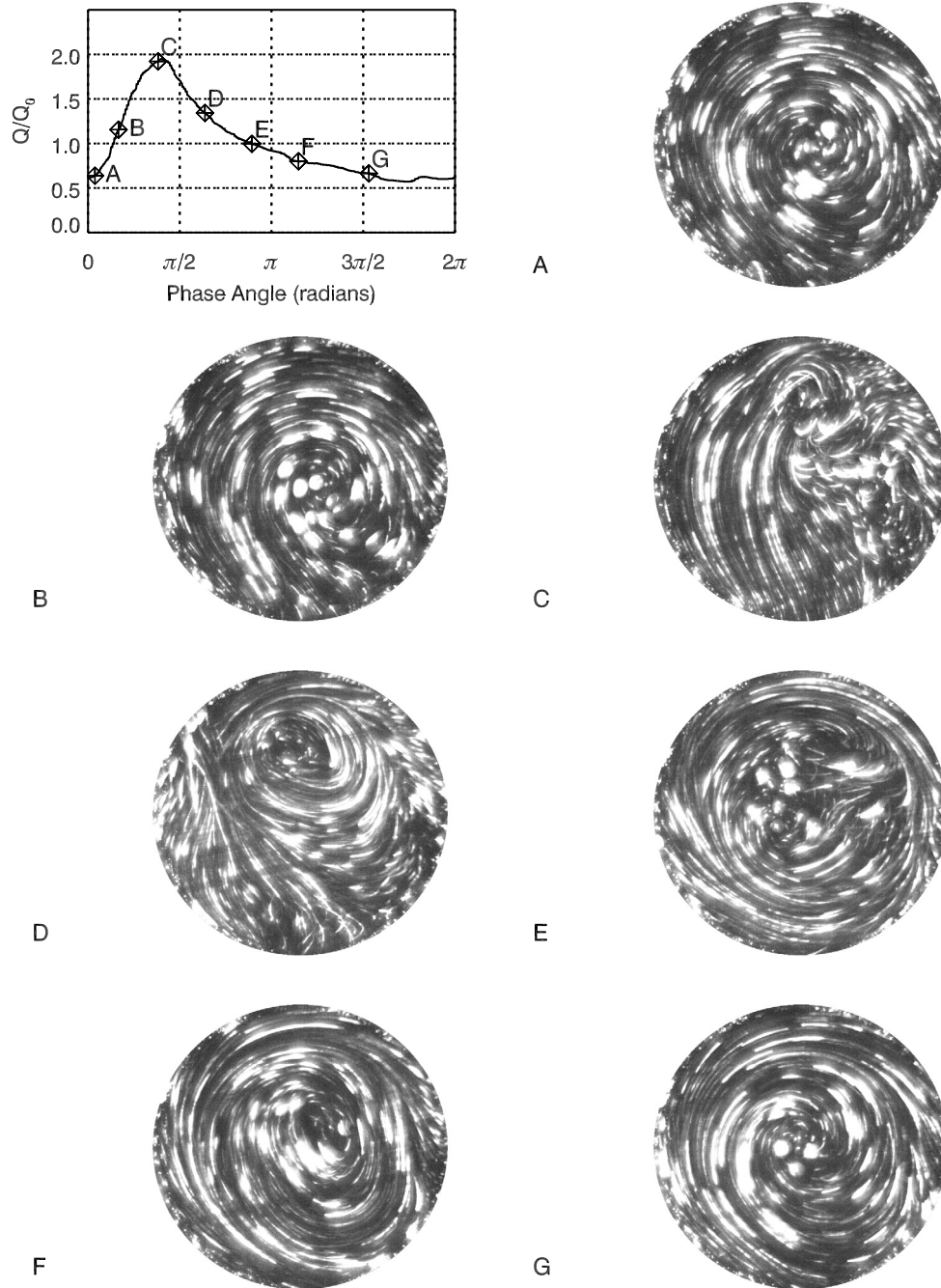


Figure 3.21: Flow visualization images at the lower-quarter for branching ratio of 25:75 over one cycle indicated by the points in the plot of the waveform cycle.

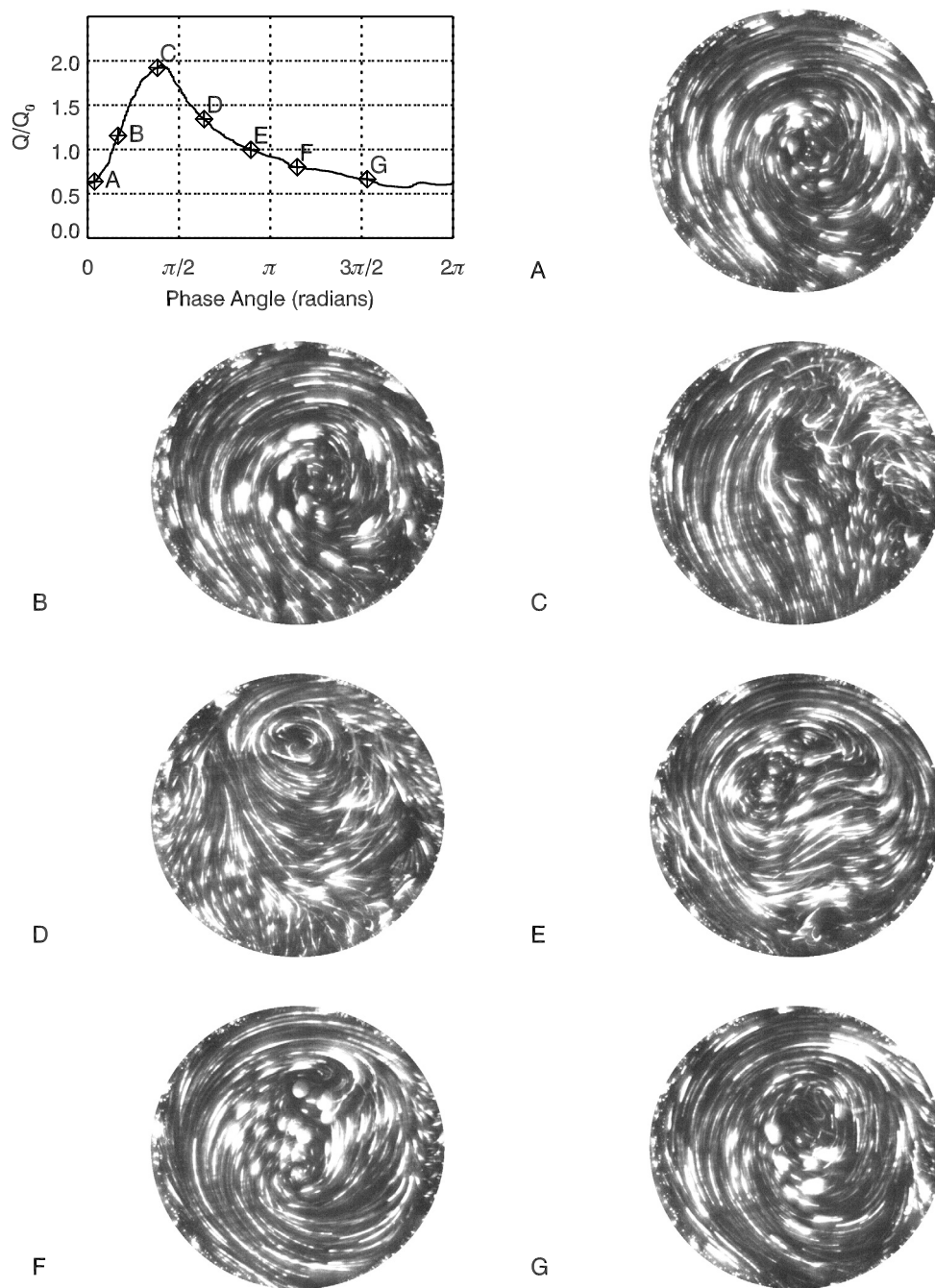


Figure 3.22: Flow visualization images at the lower-quarter for branching ratio of 33:67 over one cycle indicated by the points in the plot of the waveform cycle.

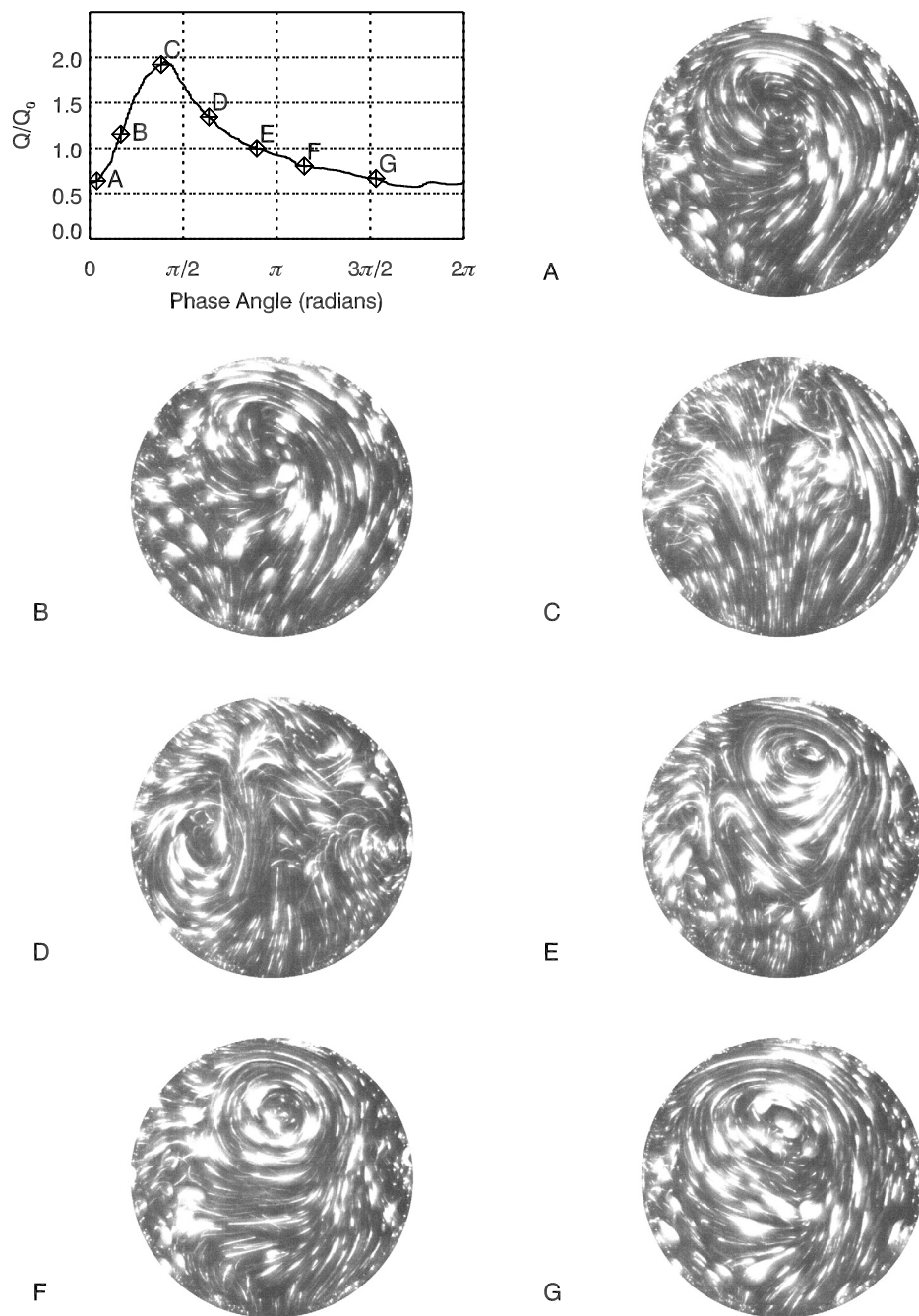


Figure 3.23: Flow visualization images at the lower-quarter for branching ratio of 46:54 over one cycle indicated by the points in the plot of the waveform cycle.

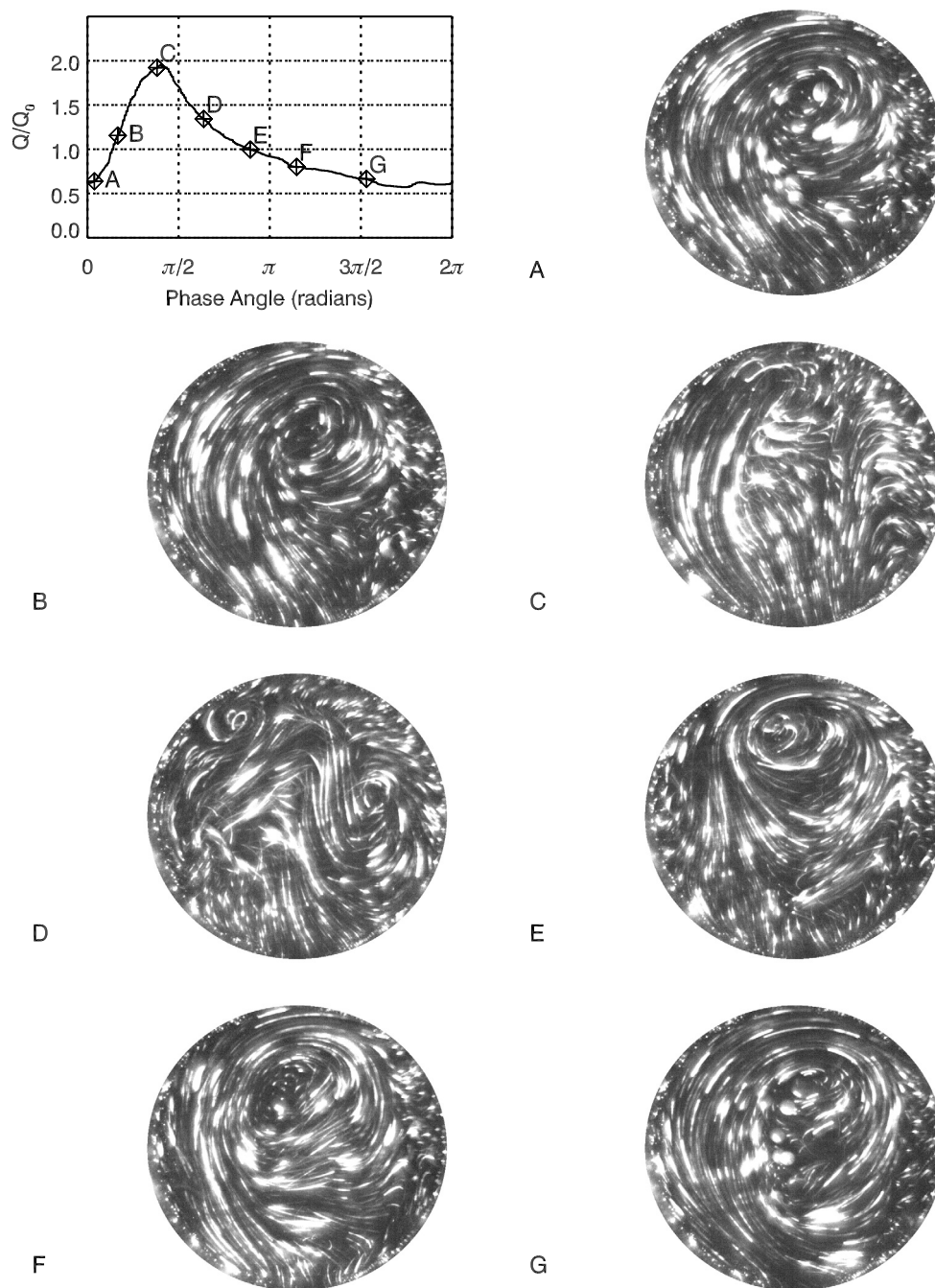


Figure 3.24: Flow visualization images at the lower-quarter for branching ratio of 48:52 over one cycle indicated by the points in the plot of the waveform cycle.

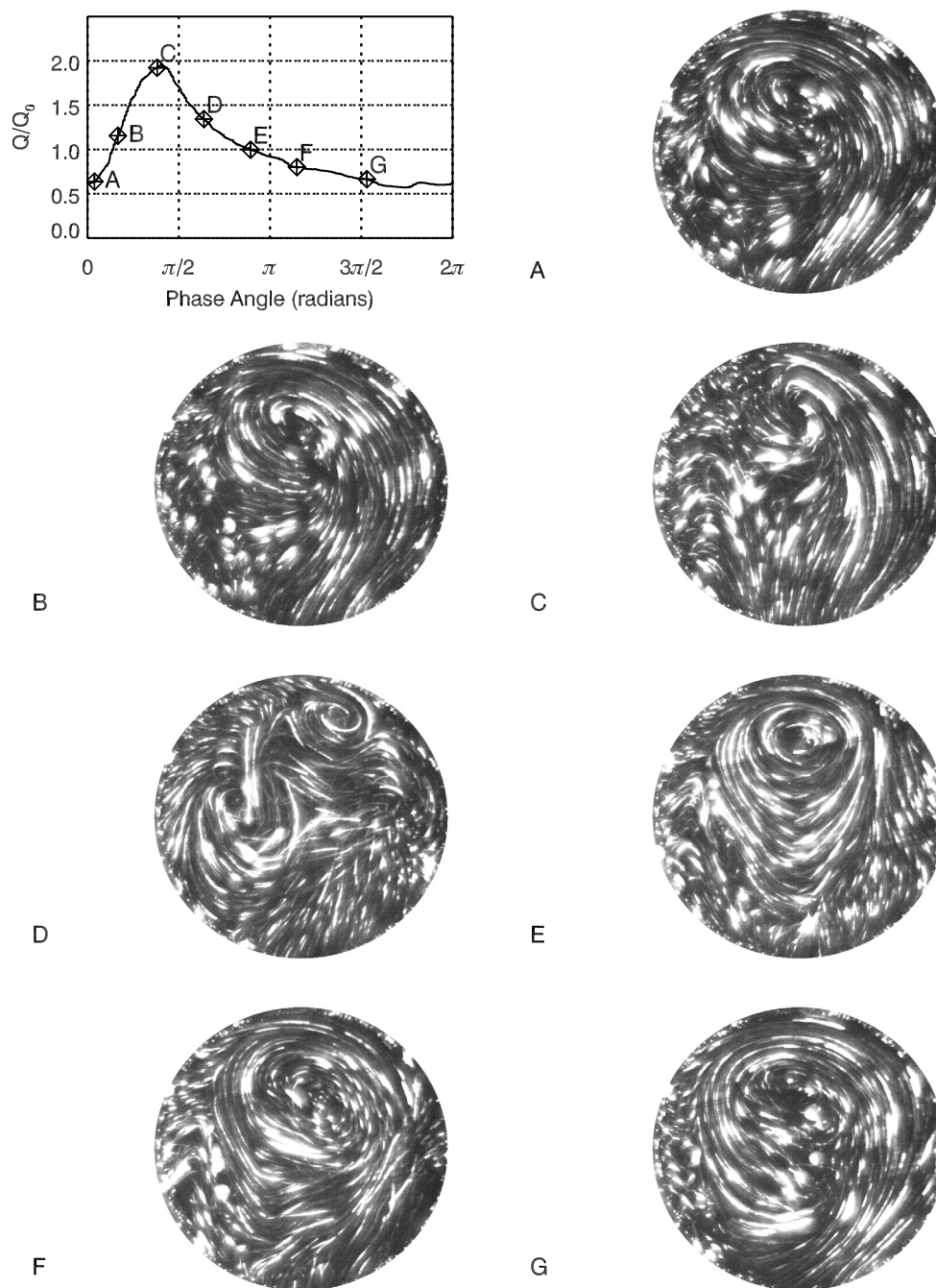


Figure 3.25: Flow visualization images at the lower-quarter for branching ratio of 50:50 over one cycle indicated by the points in the plot of the waveform cycle.

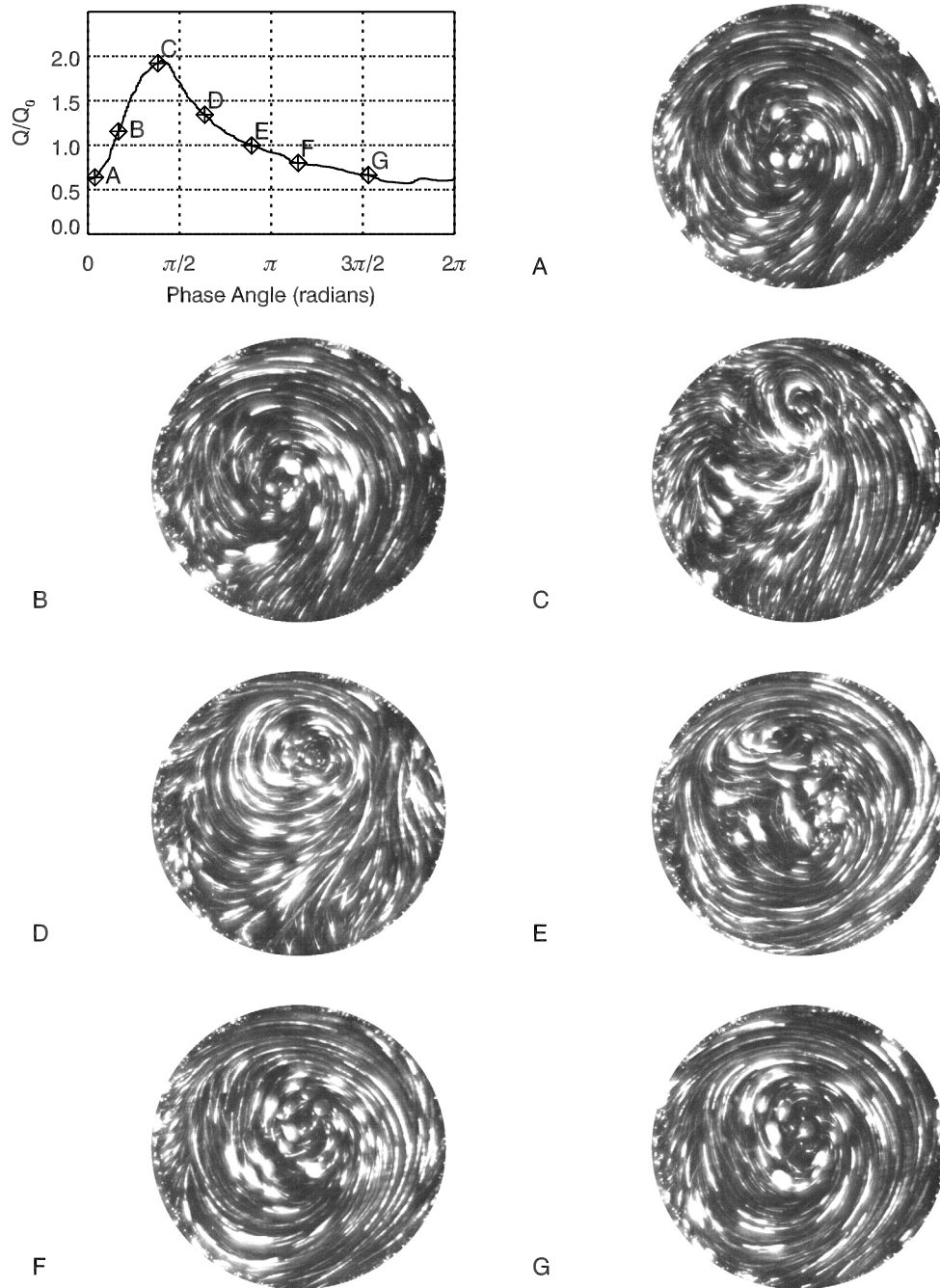


Figure 3.26: Flow visualization images at the lower-quarter for branching ratio of 67:33 over one cycle indicated by the points in the plot of the waveform cycle.

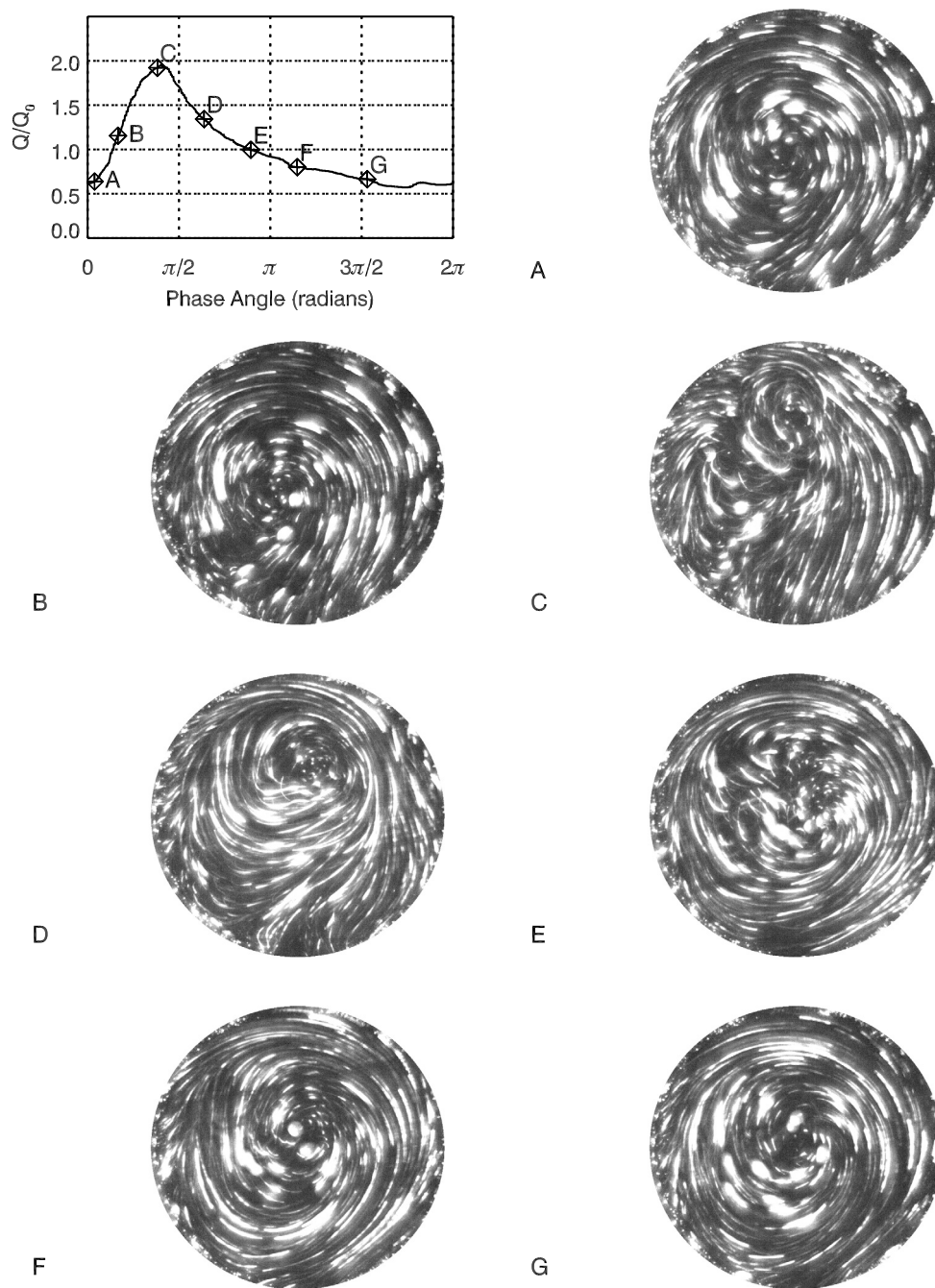


Figure 3.27: Flow visualization images at the lower-quarter for branching ratio of 75:25 over one cycle indicated by the points in the plot of the waveform cycle.

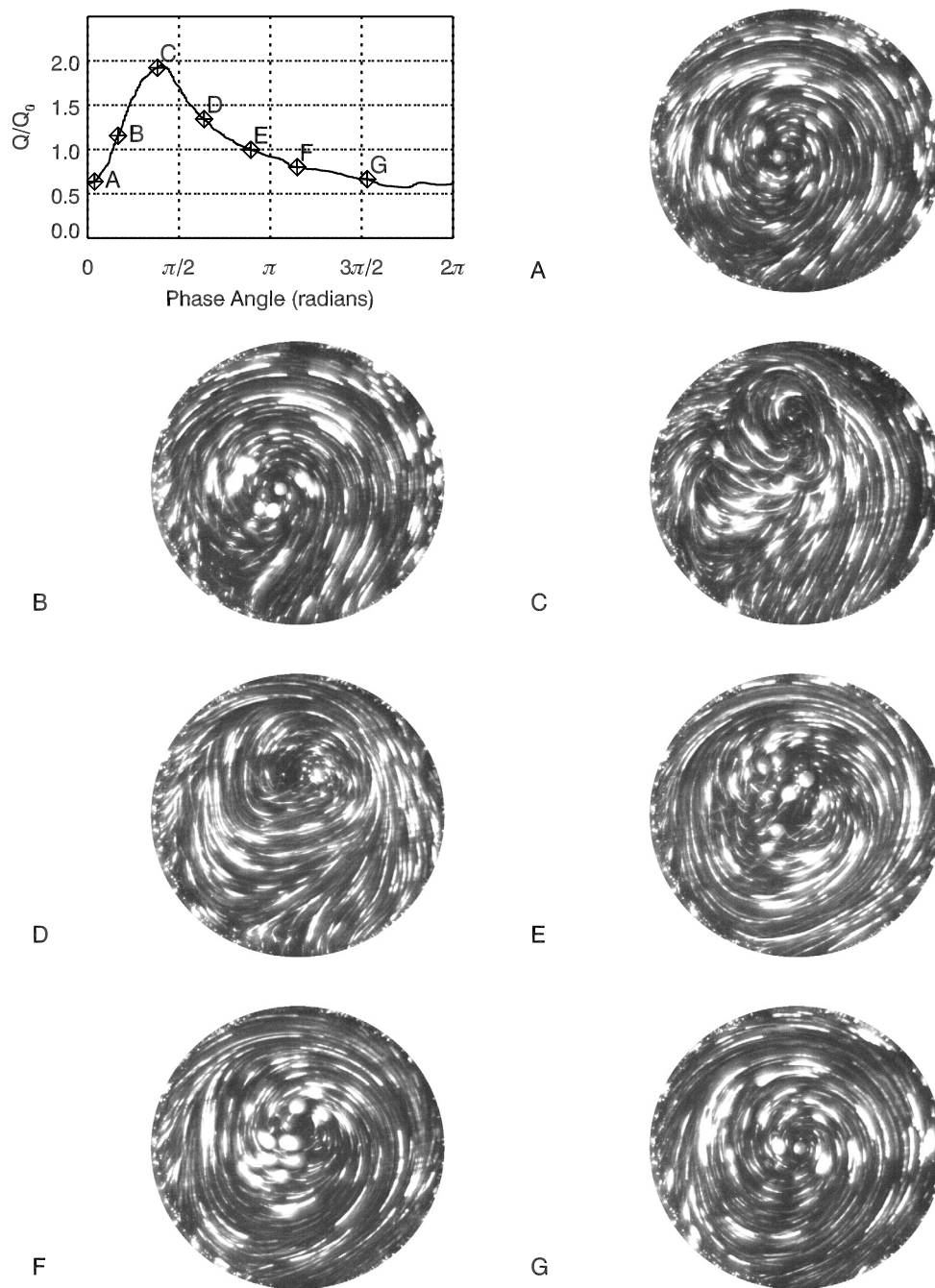


Figure 3.28: Flow visualization images at the lower-quarter for branching ratio of 80:20 over one cycle indicated by the points in the plot of the waveform cycle.

3.4 FV: Discussion

The following section details the results presented in Figures 3.2-3.28. To organize the presentation, the sections are divided by phases of the waveform (Figure 3.29). The interval between the minimum and maximum flow rates on the waveform is referred to as the *ramp up* phase. The remaining interval which consists of the drop from the peak flow rate is referred to as the *ramp down* phase. Within each of these sections, the basic flow patterns are discussed for each plane before describing the variations that result from changing the flow ratio. The latter half of the waveform which ends at the minimum flow rate, is referred to as the *relaxation* phase. The discussion of FV results begins with the relaxation phase to establish the main flow structures present. The discussion continues by examining the changes that occur through the ramp up and ramp down phases.

3.4.1 Relaxation Phase

The relaxation phase corresponds to points F, G, and A in Figures 3.2-3.28. It is characterized by relatively little change in the flow structure other than continued deceleration of the flow. This phase is examined first to establish the underlying flow pattern. For clarity, Figure 3.30 identifies some of the salient features frequently referred to in the discussion below and the following chapters.

The description of the flow begins with the midplane because it shows flow patterns common to all test cases. The flow enters the bifurcation from the inlet pipe but does not continue symmetrically. Instead, the flow deflects towards one of the outlets, generally the side with the higher fraction of the flow. The half of the model that the flow favors will

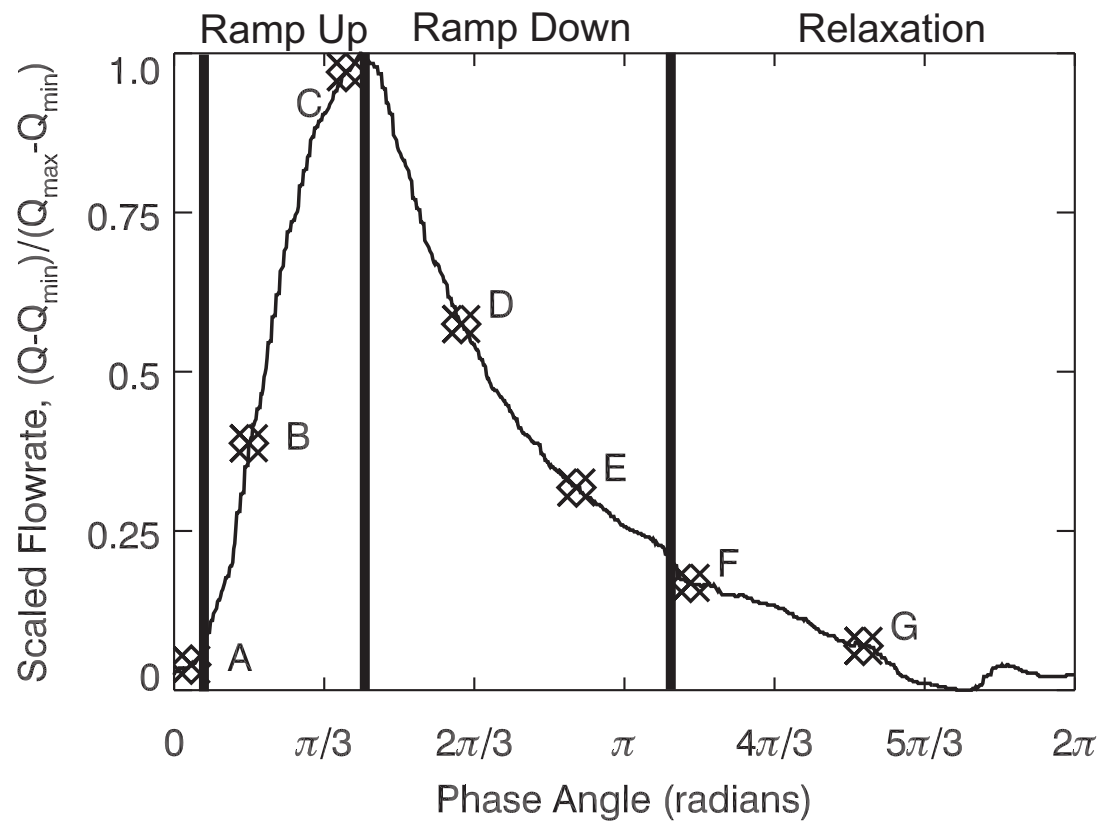


Figure 3.29: The division of the waveform that are used to in the discussion of the flow visualization images.

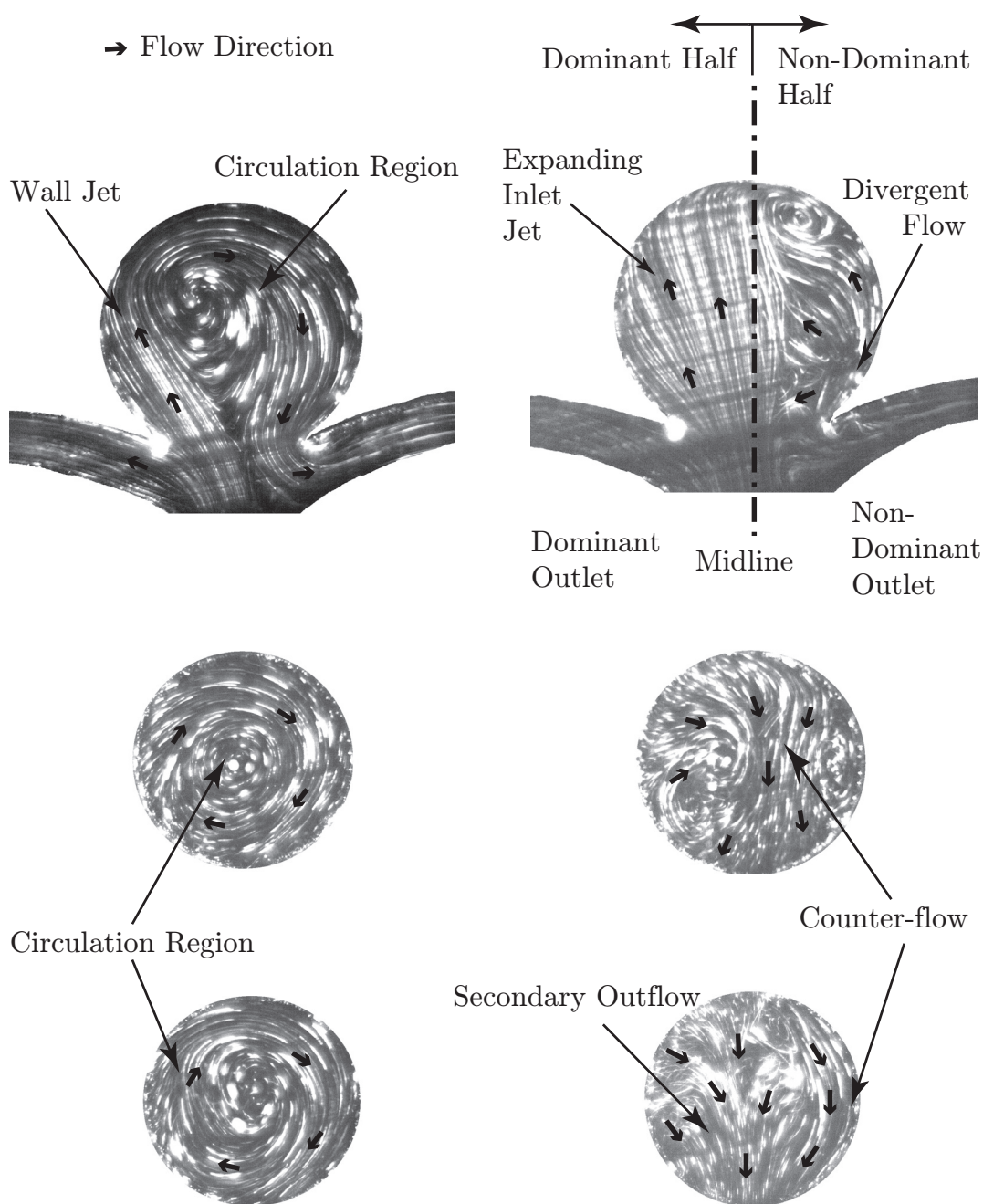


Figure 3.30: A pair of sample flow visualization images during relaxation (above) and rapid rise (below) labeled with terms that are used in the describing the flow visualization results from the midplane (*top row*), the upper quarter-plane (*middle row*), and the lower quarter-plane (*bottom row*).

be considered *dominant*. All of flow through the dominant outlet comes directly from the inlet. The remainder of the inlet enters the dome along the neck above the dominant outlet and forms a wall jet that travels along the dome wall, wraps around the neck, and exits through the non-dominant outlet. Based on the streak lines at the bifurcation, almost all of the flow through the non-dominant outlet originates from within the dome. A circulation region dominates the flow within the dome. The stagnant center of the circulation region can be easily seen in the figures because it is surrounded by nearly circular or elliptical streak patterns.

The flow ratios can be divided into two sets based on which half is dominant. For flow ratios of 20:80, 25:75, 33:67, and 48:52, the right outlet is dominant and the circulation region rotates counterclockwise. For flow ratios of 46:54, 50:50, 67:33, 75:25, and 80:20, the left outlet is dominant and the circulation region rotates clockwise. The critical case of 46:54 appears to deviate from the general pattern described above. When changing the flow ratio from 33:67 to 50:50, the switch in the dominant direction occurs at 48:52. However, when changing the flow ratio from 50:50 to 33:67, the switch in the dominant direction occurs at 46:54. This appears to be a hysteresis effect; the switch in incoming flow direction does not occur until after the flow has crossed the 47:53 flow ratio. This slight variation is likely the result of minor asymmetries within the model. This tendency for experiments to have a direction preference has been studied by Steinmann et al. [61].

The results also provide another means by which the flow rate can be divided. There are behavior differences based on the ratio of the flow rate through the dominant outlet to the flow rate through the non-dominant outlet. The behavior of the 46:54, 48:52,

and 50:50 share common flow behavior, as do the collection of the remaining test cases. For ease of description, the former can be categorized as having *small outlet differentials* and the latter as having *large outlet differentials*.

In the upper quarter-plane, the flow is dominated by a region of circulation which is an extension of the midplane circulation region. On the dominant side of the dome, streak lines originating from the wall indicate out-of-plane flow. A possible source may be the inlet flow fanning out and expanding in the out-of-plane direction as it travels around the dome. The stagnant circulation center is clearly visible when there is a large outlet differential. However, for the 50:50 and critical cases, the circulation region does not appear to be circular or elliptical.

Similar patterns during this phase of the waveform can be seen in the lower quarter-plane images. The circulation region occupies much of the dome. For large outlet differentials, the circulation region is relatively well behaved with nearly circular streak lines. For small outlet differentials, there is a layer of outflow on the non-dominant side. In points G and A, it is visible as a region of short disorganized streak lines near the wall.

3.4.2 Ramp Up Phase

Unlike the relaxation phase, the ramp up phase is marked by rapid changes in the behavior of the flow. On the waveform, this phase is defined by a sudden rise of flow rate through the inlet. Point B captures the beginning of the increase in flow rate. Point C captures the peak flow rate.

In the midplane, the most noticeable change is the transition of the flow that

enters the dome. Previously, the inlet flow was a wall jet with little thickness variation. The sudden increase in the flow rate both accelerates and expands the wall jet into an *expanding inlet jet*. The expanding inlet jet is characterized by an inlet flow that fans out from the inlet with a linear centerline that does not follow the dome wall. The increase of the inlet flow also leads to a proportionate increase in the outflow through the non-dominant side. The outflow continues to follow the walls of the dome, but its width increases with flow rate. As a result, the circulation region decreases in size and the circulation center moves away from the neck and the dominant side. When peak flow rate is reached, the circulation region has nearly disappeared in all of the cases.

In the upper quarter-plane, the growing expanding inlet jet disturbs the circulation pattern, particularly for small outlet differentials. The wall jet widens on the non-dominant side, presumably due to the expanding inlet jet wrapping around the dome wall in the out-of-plane direction. This widening forces the circulation region downward and toward the dominant side. By point C, a *counter-flow* forms that consists of flow traveling from the fundus to the outlet down the center of the dome. This structure grows to encompass half to nearly all of the dome depending on the flow ratio. There is no upwelling motion, meaning the inlet expanding inlet jet has no direct effect on the flow in this plane.

In the lower quarter-plane, similarities can be seen to the upper quarter-plane in point B. The wall jet widens causing a slight shift of the circulation center. At the peak flow rate (Point C), the counter-flow dominates the plane. For large outlet differentials, the flow is similar to the upper quarter-plane with much of the area being occupied by the counter-flow. For small outlet differentials, the counter-flow region remains along the

non-dominant wall. A *secondary outflow* appears on the dominant side that originates near the wall. It consists of a converging flow parallel to the midline directed toward the neck. The secondary outflow is supplied by fluid from outside the plane. The difference in the two cases will directly affect the flow behavior during the ramp down phase.

3.4.3 Ramp Down Phase

The ramp down phase is the transition from the flow pattern set up by the ramp up phase back to the behavior seen during the relaxation phase. The ramp down phase includes points D and E.

Flow in the midplane during this phase shares features with the relaxation phase as the flow decelerates. Point D is marked by a return of a distinct and visible circulation region in the upper part of the dome in the dominant half. A *divergent flow* occurs on the non-dominant side, where the fluid appears to originate from a point along the dome wall and fans out in the y-direction. The upper portion of this flow, in combination with the expansion jet, reform the circulation zone. The lower portion of this flow wraps past the neck into the outlet. The center portion of this flow is directed toward the inlet jet, where it is entrained. Point E marks the transition of the expanding inlet jet back to resemble the wall jet. The jet begins to follow the dome walls, but the thickness still varies with the entry width being greater than the exit width. The circulation region increases in area and shifts back toward the center of the dome. The divergent flow decreases in size until it is replaced by the wall jet in the relaxation phase.

In the upper quarter-plane, the ramp down phase marks the transition from the

flow being dominated by the counter-flow during the rapid rise phase to the circulation region during the relaxation phase. For large outlet differentials, the counter-flow reduces in width and the inlet flow that follows the dominant side wall returns. These combine to recreate the circulation region by point E or F. For small outlet differentials, the counter-flow persists in the center of the flow, reducing in width slowly. Two small circulation regions form on either side of the counter-flow. By point E, the counter-flow returns to following the dome wall along the non-dominant side, eliminating one of the circulation zones. The remaining circulation region grows returning to the size and shape seen in the relaxation phase.

The lower quarter-plane shows evidence of similar changes during the ramp down phase. For large outlet differentials, the flow more closely resembles the relaxation phase. At point D, the circulation region begins to return to its original size and position. The divergent flow seen in the midplane prevents the counter-flow from realigning with the wall in this view. The circulation region that will come to dominate the flow in the relaxation phase begins to grow and shift back towards the center of the dome. By point E, the wall jet returns to following the dome wall. Within the center of the dome the flow is not as well organized. Rather than the near circular streaklines seen on the exterior, the center is divided and disrupted by a flow in the z-direction that bisects the dome. It is not until point F that this flow disappears and the circulation region establishes itself throughout the entire dome. For small outlet differentials, the counter-flow on the non-dominant side is disrupted, leaving only the secondary outflow down the center. The flow combines with the out-of-plane flow along the wall to create two circulation regions. The smaller of the

two is aligned with the circulation region seen in the midplane and is closer to the fundus of the dome. The larger circulation region occurs just above the neck on the dominant side. While the wall jet does not appear by point E, there is a distinct oblong elliptical flow pattern that resembles it. There remains some out-of-plane flow on the side walls. The smaller circulation grows and moves towards the center while the larger circulation region has disappeared.

3.5 FV: Conclusion

The experiments in this chapter describe the overall behavior of the flow in the cerebral saccular aneurysm model on three planes. The major structures are the inlet wall jet and the circulation region. The circulation region dominates the flow in all three planes during the relaxation period. However, during the ramp up period, the jet becomes the dominant flow feature in the midplane and the counter-flow dominates the quarter-planes. This suggests that an orthogonal view shows the presence of the inlet jet dividing at the wall into two flows that travel around the dome. During the ramp down period there is an upwelling of material across the mid and lower quarter-planes as indicated by the presence of a divergent flow present near the non-dominant neck. This feature delays the return of the flow to the patterns seen in the relaxation phase until the upwelling has disappeared. These experiments were useful in determining the critical conditions where the dominant side of the flow changes.

While velocity variations are clearly evident in the wall jet, no firm conclusions can be drawn about spatial gradients and therefore wall shear stress (WSS). WSS magnitude

and direction will change over the fundus of the dome in the midplane due to the transition of the flow from a wall jet to an expanding inlet jet. The data does indicate that WSS in the out-of-plane direction are present and need to be considered. WSS calculations are understood from quantitative techniques such as PIV and SPIV to provide measurements. This is the main objective of the work in the following chapters.

Chapter 4

Particle Image Velocimetry

Particle image velocimetry (PIV) is a tool of choice for field measurements of fluid flows. Whereas flow visualization (FV) provided a basic understanding of a flow, PIV measures the planar velocity field in cross sections in a flow field, which are used to determine quantitative results, such as speed and shear stress. This chapter reviews the principles behind PIV, describes the setup, presents and discusses post-processing results.

4.1 PIV: Theory

PIV systems share some basic operating principles with FV. In both, the flow must contain visual markers that travel with the local fluid parcel. The markers, in this instance particles, require illumination to be visible and an imaging device to record the flow. Unlike FV, which captures a single image with a long exposure time, PIV records two nearly simultaneous images in rapid succession. This experiment uses a dual image/single exposure setup (Figure 4.1). In each PIV image, the particles appear as a collection of illuminated

points rather than streaks. Between the images in a pair, moving particles are displaced a small distance. A balance must be achieved when determining the appropriate time between images in a pair. Insufficient time between images makes it difficult to distinguish between zero velocity and slow velocities, such as near a wall. Too much time between images allows time for particles to travel out of plane creating a similar problem to long exposure times in FV. [50] In addition, long displacements between images causes very large displacements which can become computationally expensive during the PIV processing.

PIV processing involves converting the image pairs into numerical flow measurements by calculating the displacement of fluid parcels marked by particles between image pairs. The images are processed by matching the motion of fluid parcels between the two images. Images are processed through the cross-correlation of subdivisions, or windows, of the two images. Processing begins by dividing the images into overlapping rectangular interrogation windows. Intensities of subregions of the image are cross-correlated, searching for the closest signal match to determine the displacement. With a displacement length and direction, dividing by the known time between the two images, the projected local velocity vector is determined. This process is repeated for all of the windows on the first image generating a velocity field for the entire space.

4.2 PIV: Setup

4.2.1 Illumination

For optical illumination, dual image/single exposure PIV applies more constraints than FV. The very small exposure times are required to capture the particles and avoid

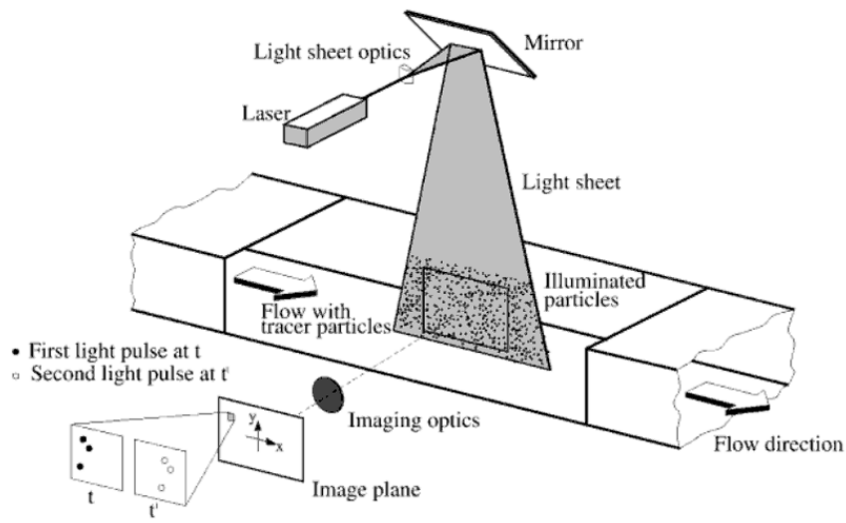


Figure 4.1: An illustration of the key components of a PIV setup [50].

streaking. The short exposure time requires shutter speeds beyond the capabilities of the lenses and cameras available. The particles must fluoresce at a higher intensity than in FV to compensate for the shorter exposure time. A NewWave Gemini90 Nd:Yag Laser addresses these concerns. The laser consists of two synchronized lasers, each emitting light at 532nm in 5-7ns pulses rated at a maximum of 90mJ at a maximum of 30Hz. The dual laser allows the firing of two pulses in rapid succession, shifting the exposure time control from the imaging systems to the laser. The timing of the pulses is controlled by a series of external square waves. The time between image pairs is $800\mu\text{s}$ for all of the experiments discussed in this chapter. The spherical-cylindrical lenses used to make the laser sheet in FV are also used in the PIV setup. As in FV, the laser and optics have a single degree of freedom in the x-direction (Figure 4.2).

4.2.2 Seed Particles

The particles for PIV experiments are the same Duke Scientific $15\mu\text{m}$ Fluorescent Polymer Microspheres used in FV. Illumination of wavelength 532nm is used for the experiments causing the particles fluoresce at 607nm . The considerations in particle selection are discussed in Section 3.2.1

4.2.3 Imaging

As with FV, an Integrated Design Tools MotionPro X-3 Camera is used for imaging. For PIV experiments, the camera is set to double exposure mode to capture image pairs with each trigger. Full resolution frame rates in this mode are well in excess of the 30Hz available from the laser. The camera has one degree of freedom in the x-axis to maintain a focus on the laser sheet. The lens configuration is identical to FV. The 550nm band-pass filter is used, passing the 607nm light from the particles while blocking the 532nm light from the laser.

4.2.4 Algorithms

In Section 4.1, a basic single pass PIV processing technique was discussed. It lacks robustness because it assumes the particles move homogeneously and fails to consider any deformation or rotation of the fluid. A FORTRAN-90 code for processing PIV images in this experiment uses an adaptive Lagrangian parcel tracking (aLPT) routine based on Sholl and Savas [58]. The aLPT algorithm takes multiple passes, each refined by modification of the interrogation windows through calculation of advection and deformation based on

the local velocity field and gradients. The cross correlations, derivative calculations, and smoothing operations all computed using fast Fourier Transforms (FFT). The velocity array is centered in the smallest 2^n by 2^m array so that the FFT algorithm can be employed for fast calculation. The data are smoothly extended to zero values at the edges of the newly constructed FFT domain to insure continuity of the slopes and prevent ringing artifacts in the frequency domain. In the wave number domain, the transform is multiplied with the appropriate powers of the wave numbers to construct the transforms of the derivatives, which can be obtained by subsequent inverse transforms. Derivatives up to the 3rd order are obtained for aLPT where they are used to reconstruct deformed interrogation windows. In particular, second order deformations are used where the deformation of a rectangular fluid parcel is traced to the second order, resulting in a cushion parcel with curved edges rather than a parallelogram. During these calculations, the raw data are filtered in the frequency domain using a low pass filter kernel $1 - \exp(-1/k^2)$, where k is the modulus of the wave vector (normalized with the desired cut-off wave number). Before the aLPT processing begins, a routine PIV correlation technique is used to identify outliers which are subsequently recalculated at doubled, and if needed quadrupled, windows. If this process fails, the outliers are replaced with the mean of the neighboring vectors. However, the final output of aLPT is not scanned for individual outliers, but passed through the low pass filter kernel. An initial window size of 64 x 64 pixels with a step size of 16 pixels is used for overall velocity measurements. Because velocities adjacent to the wall are slower than at the center of the flow, a smaller initial window size of 32 x 32 pixels is used. This allows for a step size of 8 pixels, doubling the number of points along the wall.

A problem in PIV arises when interrogation windows include features that are not part of the flow, such as a wall. This discontinuity causes a bias in the cross-correlations resulting in errors in the calculated velocities along the wall and enforcing the no-slip boundary condition. To overcome this problem, the image parity exchange (IPX) algorithm developed by Tsuei and Savas [62] is employed. The algorithm takes a strip of the image on the flow side of the interface, one window size in width, from the first image. It then mirrors the strip across the interface and applies it to the second image and vice versa. Applying the mirrored strip to its complementary image completes the interrogation windows in that occur along the wall. This alleviates the error in cross correlation while preserving a smooth gradient across the interface.

4.3 PIV: Post Processing

The processed PIV output is an array of velocities and gradients for each of the image pairs. The data are post-processed to extract information pertinent to the goals of this experiment. This section discusses the methods used.

4.3.1 Phase Averaging

Phase shifting of the PIV data improves temporal resolution over a single waveform. The laser's maximum repetition rate of 30Hz combined with the basilar waveform frequency of 1.53Hz means that a maximum of 19 PIV pairs can be captured in one cycle. This limits the temporal resolution when trying to determine flow behavior over the entire waveform. Rather than continuously capturing images at the same points on every wave-

form, a small phase shift is added. This increases the number of points captured over the waveform cycle, but not in sequence. By calculating the corresponding location of each PIV pair to a point on the waveform, it is possible to reorganize the data as a sequence over a single cycle. Multiple sets are collected and averaged to reduce the effects of the variations that come from using different waveforms. For the PIV experiments, 6 samples are collected for each point with a total of 120 points per waveform. This procedure assumes that the flow is repeatable, meaning it is a behaved flow with few transient variations from one cycle to the next. However, the averaging will smooth any small scale flow structures, random behaviors, or characteristics lasting much longer than one cycle.

4.3.2 Wall Shear Stress

Shear stress at a solid surface, τ , is the tangential force that results from the no-slip boundary condition. Using a tangent, normal, binormal coordinate system relative to the surface, where $\mathbf{u} = (u_t, u_n, u_b)$, shear stress is

$$\tau = \mu \left[\left(\frac{\partial u_t}{\partial n} + \frac{\partial u_n}{\partial t} \right) \mathbf{e}_t + \left(\frac{\partial u_b}{\partial n} + \frac{\partial u_n}{\partial b} \right) \mathbf{e}_b \right]. \quad (4.1)$$

In the model, the force of interest is the wall shear stresses (WSS), τ_w , along the dome. Using the model's coordinate system, the binormal direction is \mathbf{e}_x . The tangent and normal directions depend on the local wall coordinates, but are converted to the Cartesian coordinate system by the IPX code. During PIV processing, only the in-plane component of WSS is calculated; there is insufficient information to determine the gradients in the \mathbf{e}_x direction which are needed for calculation of the out-of-plane component. As seen in FV, the flow is highly three dimensional and the resultant WSS from that aspect of the flow is

undetermined. This suggests that the WSS values calculated in this section provide only a lower limit to the total WSS magnitude.

WSS values in the experiment must be extrapolated with physiological conditions. It is not sufficient to replace the kinematic viscosity in Equation 4.1. Dynamic and geometric similarities allow the development of a dimensionless shear stress coefficient. To relate the two cases, the following scaling method presented by Bale-Glickman [6] is used. This shear stress coefficient, c_τ , is

$$c_\tau = \frac{\tau}{\frac{1}{2}\rho U^2}, \quad (4.2)$$

where the denominator is simply the dynamic head. An intermediary step relates the experimental and physiological velocities using dynamic similarity. Matching Reynolds numbers

$$Re_p = Re_e \frac{\rho_p U_p d_p}{\mu_p} = \frac{\rho_e U_e d_e}{\mu_e} \quad (4.3)$$

$$\frac{U_p}{U_e} = \left(\frac{\rho_e}{\rho_p}\right) \left(\frac{\mu_p}{\mu_e}\right) \left(\frac{d_e}{d_p}\right), \quad (4.4)$$

where the subscript p represents physiological conditions and the subscript e represents experimental conditions. The diameter of the model inlet is based on physiological measurements of the basilar artery; therefore, $\frac{d_e}{d_p} = 1$. This relationship combined with Equation 4.2 to convert the gradient results from the PIV data into a physiological WSS as follows

$$\tau_{w,p} = \left(\frac{\frac{1}{2}\rho_p U_p^2}{\frac{1}{2}\rho_e U_e^2}\right) \tau_{w,e} \quad (4.5)$$

$$= \left(\frac{\rho_e}{\rho_p}\right) \left(\frac{\mu_p}{\mu_e}\right)^2 \tau_{w,e}. \quad (4.6)$$

All WSS values presented undergo this rescaling.

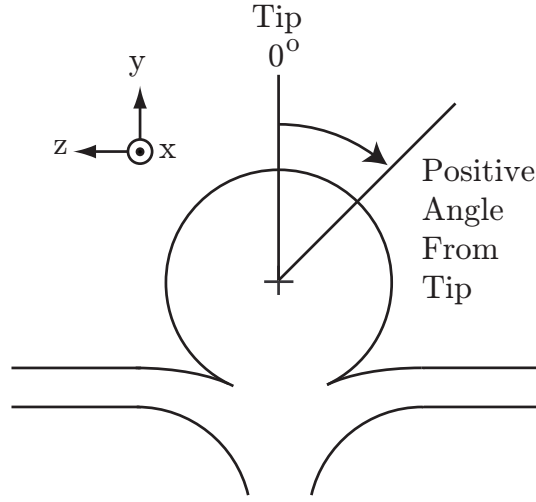


Figure 4.2: Definition of *angle from tip* that is used to describe dome coordinates in the PIV WSS plots)

An angular coordinate system is defined to describe WSS at different points along the dome. For an origin at the center of the dome, all points on the tip can be defined at an angle relative to the tip (Figure 4.2). The coordinate system is clockwise positive, such that all points to the right of the tip are defined by a positive angle and all points to the left of the tip are defined by negative angles.

4.3.3 Second Invariant of the Velocity Gradient, Q

The second invariant of the velocity gradient tensor, Q , is used to determine coherent vortex structures [31, 16]. Q is defined as

$$Q = \frac{1}{2}(\Omega_{ij}\Omega_{ij} - S_{ij}S_{ij}), \quad (4.7)$$

where the rotation tensor, Ω_{ij} , is defined as

$$\Omega_{ij} = \frac{1}{2} \begin{pmatrix} 0 & \frac{\partial u}{\partial y} - \frac{\partial v}{\partial x} \\ \frac{\partial v}{\partial x} - \frac{\partial u}{\partial y} & 0 \end{pmatrix},$$

and the strain rate tensor, S_{ij} , is defined as

$$S_{ij} = \frac{1}{2} \begin{pmatrix} 2\frac{du}{dx} & \frac{du}{dy} + \frac{dv}{dx} \\ \frac{du}{dy} + \frac{dv}{dx} & 2\frac{dv}{dy} \end{pmatrix}.$$

The expression for the Q-criterion for a two dimensional local x-y Cartesian coordinate system is represented as

$$Q = \frac{1}{4} \left[\frac{\partial u}{\partial y} - \frac{\partial v}{\partial x} \right]^2 - \left[\frac{\partial u^2}{\partial x} + \frac{1}{2} \left(\frac{\partial u}{\partial y} + \frac{\partial v}{\partial x} \right)^2 + \frac{\partial v^2}{\partial y} \right] \quad (4.8)$$

Q compares the rotation rate versus the strain rate. Positive Q values indicate that circulation dominates the flow. Conversely, negative Q values indicate strain dominated flow. Q has been used in the post processing of the PIV data to isolate concentrated vortex structures that pass through the plane [31]. It is more effective than evaluating vorticity, whose values can vary greatly and developing a uniform criterion can be difficult. In these experiments, Q is used to isolate areas of dominant circulation.

4.4 PIV: Results

Velocity, Q, and WSS are plotted in the following figures in sets that cover the nine test cases at three planes. Figures 4.3-4.29 plot speed, velocity vector fields, and

instantaneous streamlines. Each figure contains six plots whose corresponding points indicated on the plot of the flow waveform in the upper left hand corner. The speed range and color scale are indicated in the upper right hand corner. These plots are designed to identify the instantaneous and overall flow patterns in the flow; these also serve as a means of comparing and quantifying the results from FV. Figures 4.3-4.11 are from the midplane. Figures 4.12-4.20 are from the upper quarter-plane. Figures 4.21-4.29 are from the lower quarter-plane.

Figures 4.30-4.56 are plots of Q . Each figure contains seven plots whose corresponding points indicated on the flow waveform in the upper left hand corner. These plots are useful in identifying regions of the flow where rotation dominates such as vortex cores. Figures 4.30-4.38 are from the midplane. Figures 4.39-4.47 are from the upper quarter-plane. Figures 4.48-4.56 are from the lower quarter-plane.

Figures 4.57-4.83 are plots of WSS along the dome over a single waveform. Each figure includes a plot of the curvilinear wall coordinate system along the dome in the lower left hand corner and a range and color scale in the lower right hand corner. Figures 4.57-4.65 are from the midplane. Figures 4.66-4.74 are from the upper quarter-plane. Figures 4.75-4.83 are from the lower quarter-plane. The final plots of the WSS data set, Figures 4.84-4.86, contains the mean WSS over time for each of the points along the dome wall using the same wall coordinates.

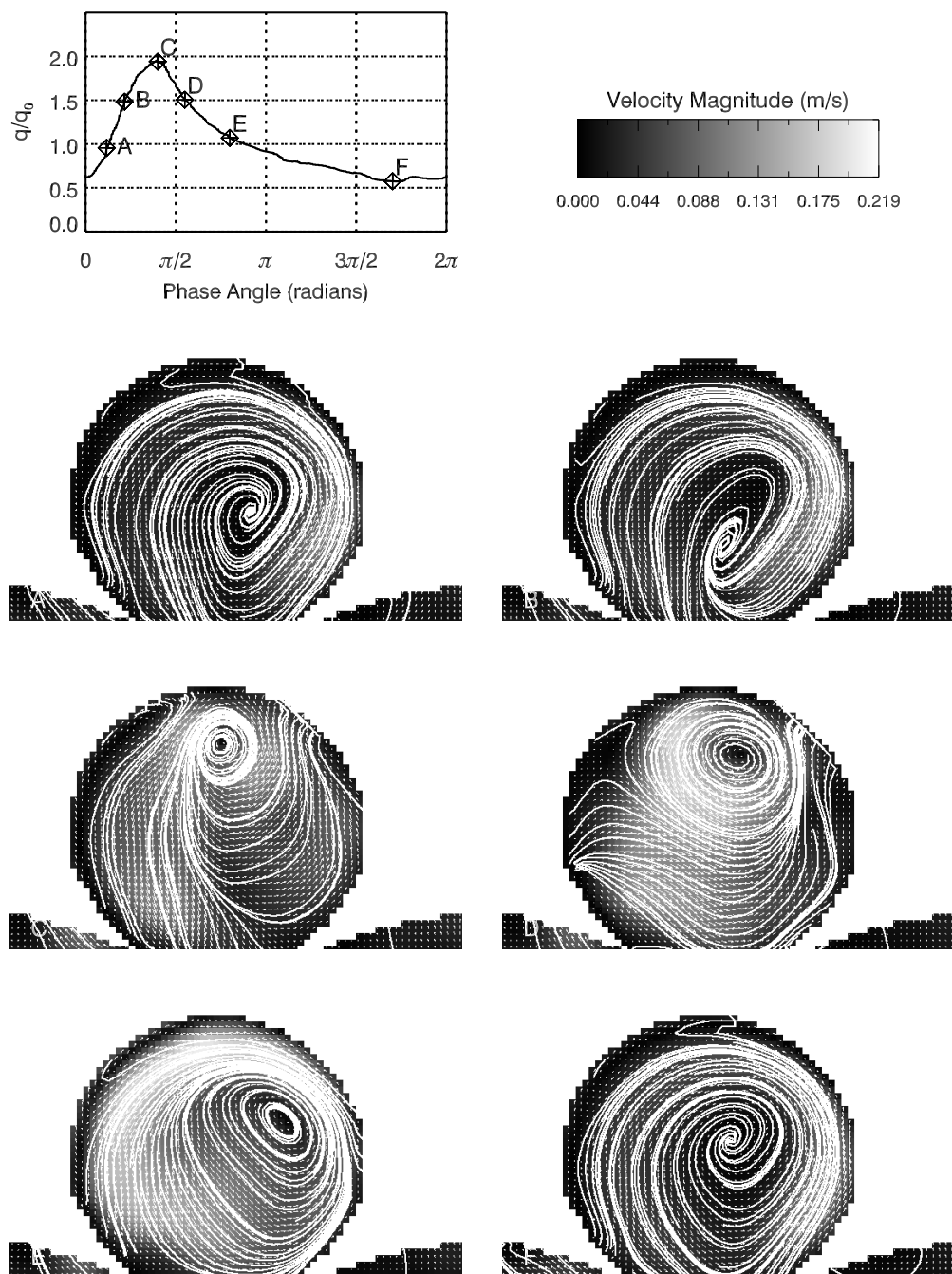


Figure 4.3: Velocity vector with velocity vector field and instantaneous streamlines overlaid for the midplane for a branching ratio of 20:80 over one cycle indicated by the points on the waveform cycle.

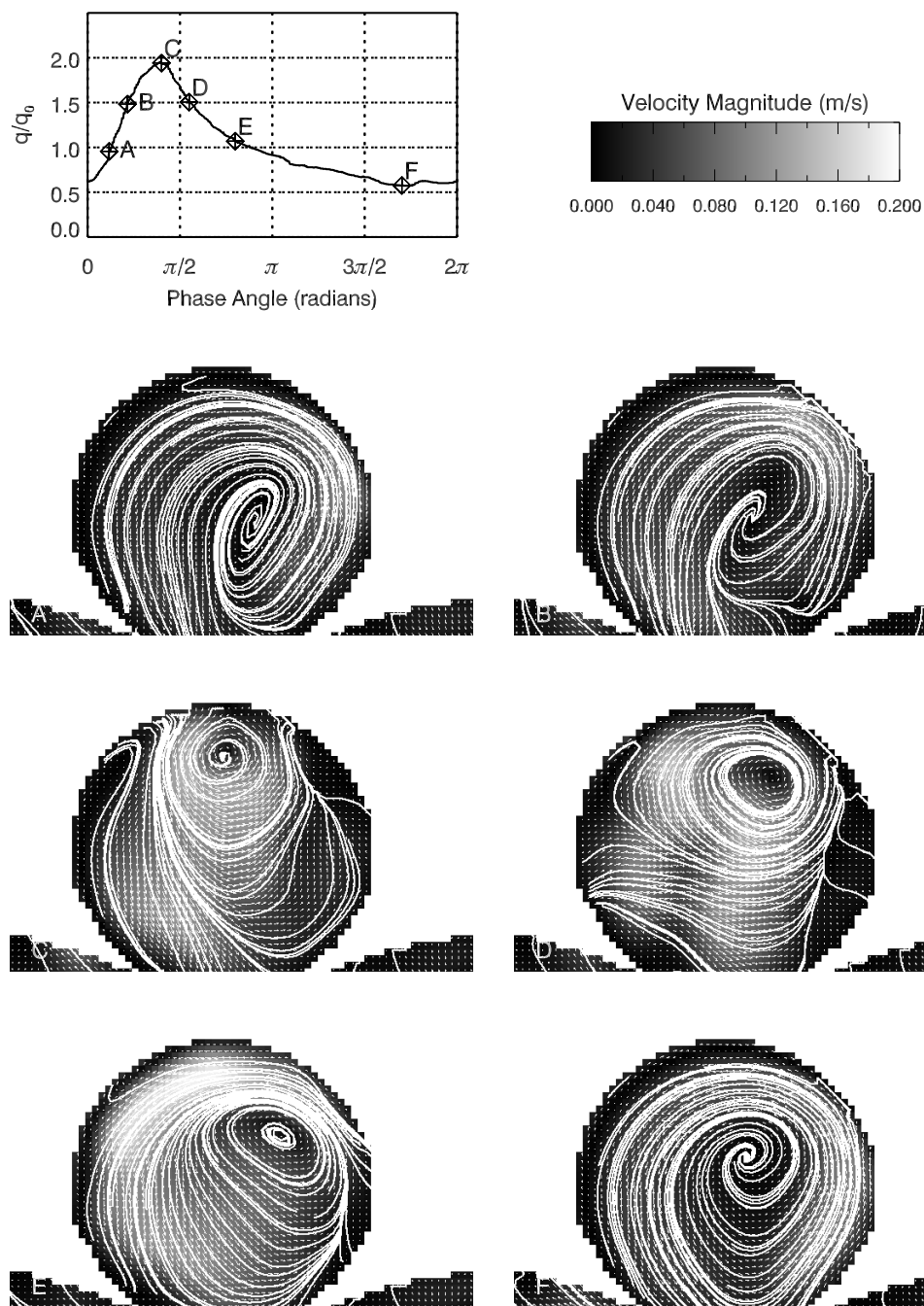


Figure 4.4: Velocity vector with velocity vector field and instantaneous streamlines overlaid for the midplane for a branching ratio of 25:75 over one cycle indicated by the points on the waveform cycle.

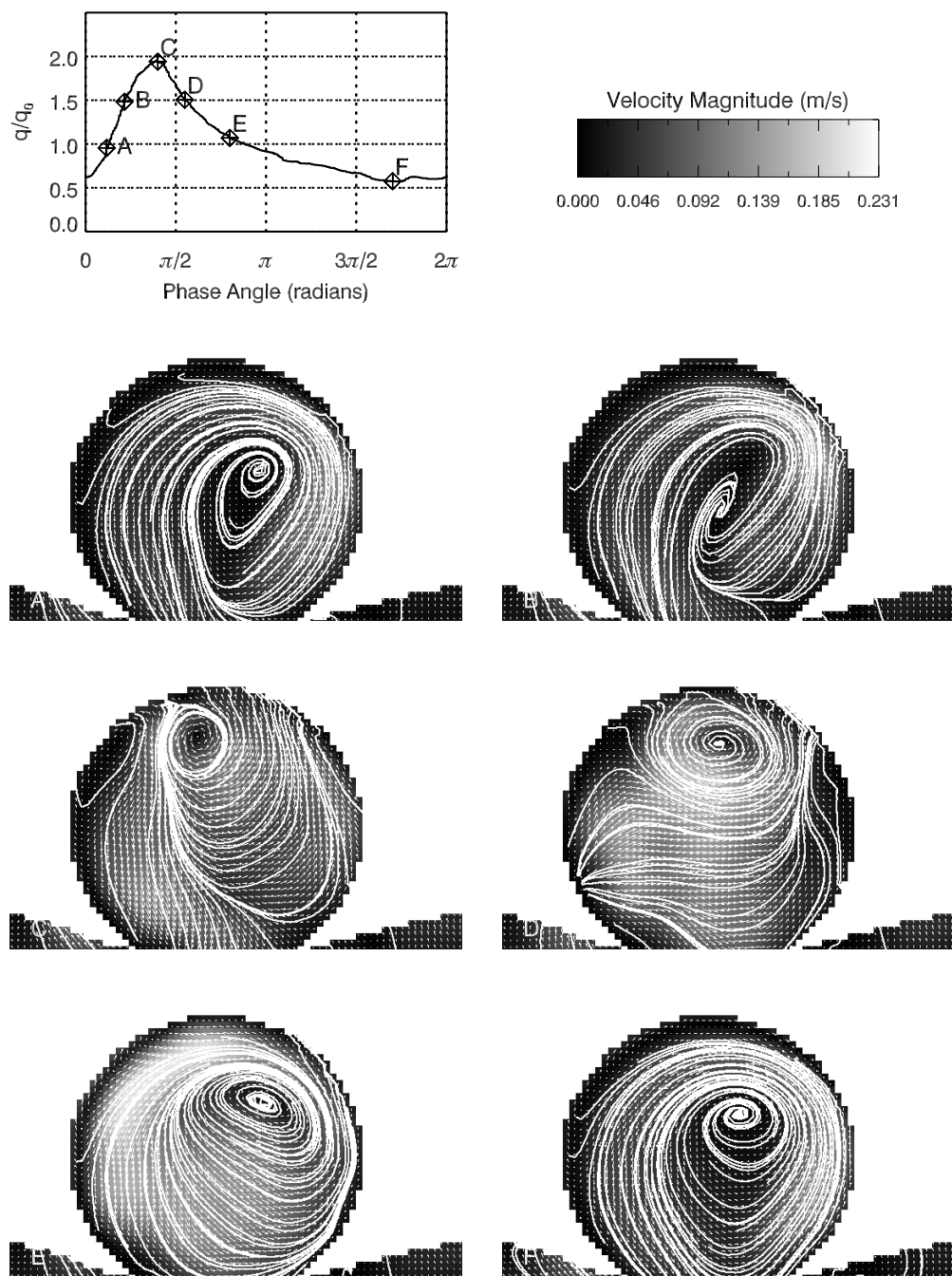


Figure 4.5: Velocity vector with velocity vector field and instantaneous streamlines overlaid for the midplane for a branching ratio of 33:67 over one cycle indicated by the points on the waveform cycle.

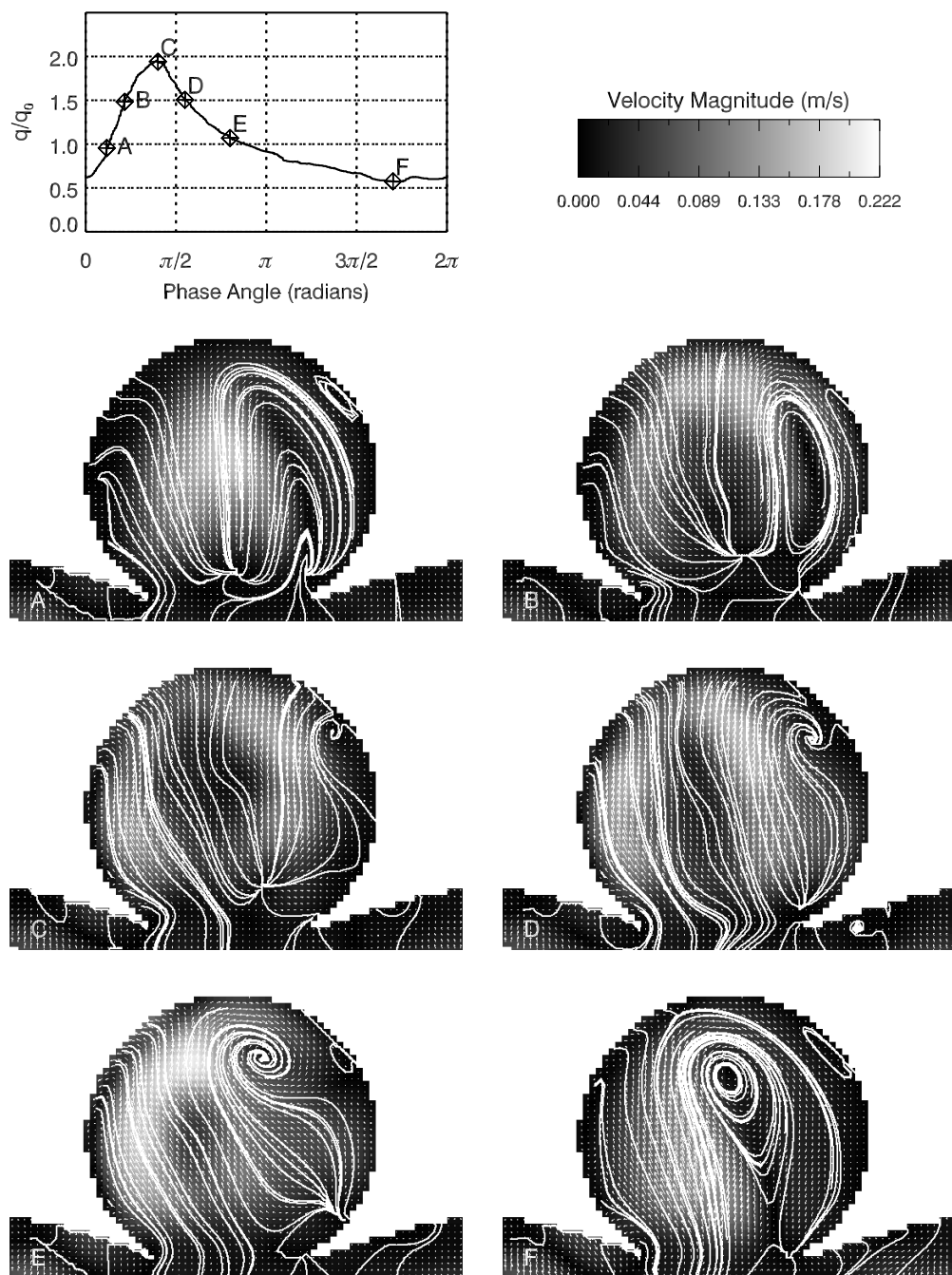


Figure 4.6: Velocity vector with velocity vector field and instantaneous streamlines overlaid for the midplane for a branching ratio of 46:54 over one cycle indicated by the points on the waveform cycle.

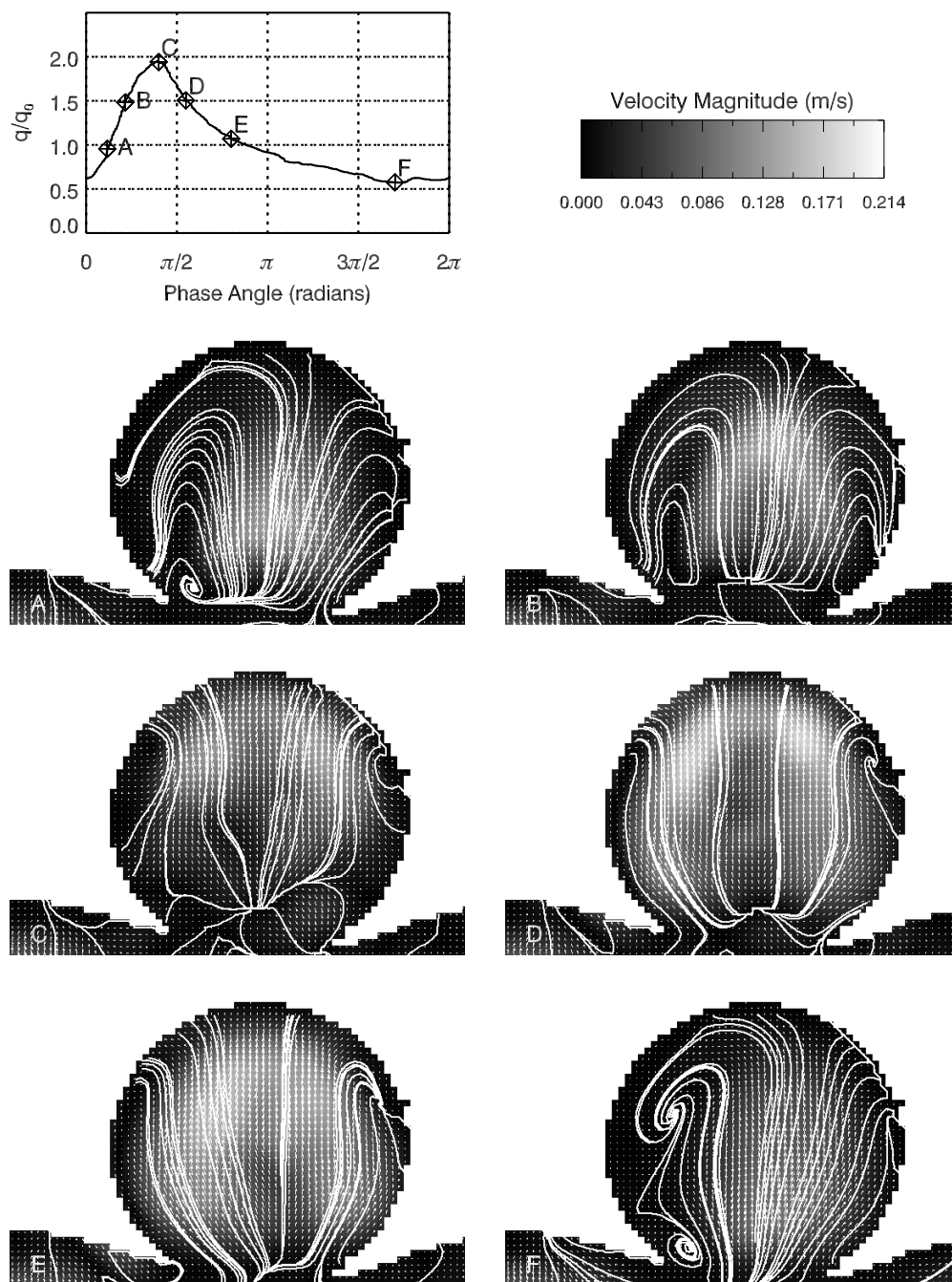


Figure 4.7: Velocity vector with velocity vector field and instantaneous streamlines overlaid for the midplane for a branching ratio of 48:52 over one cycle indicated by the points on the waveform cycle.

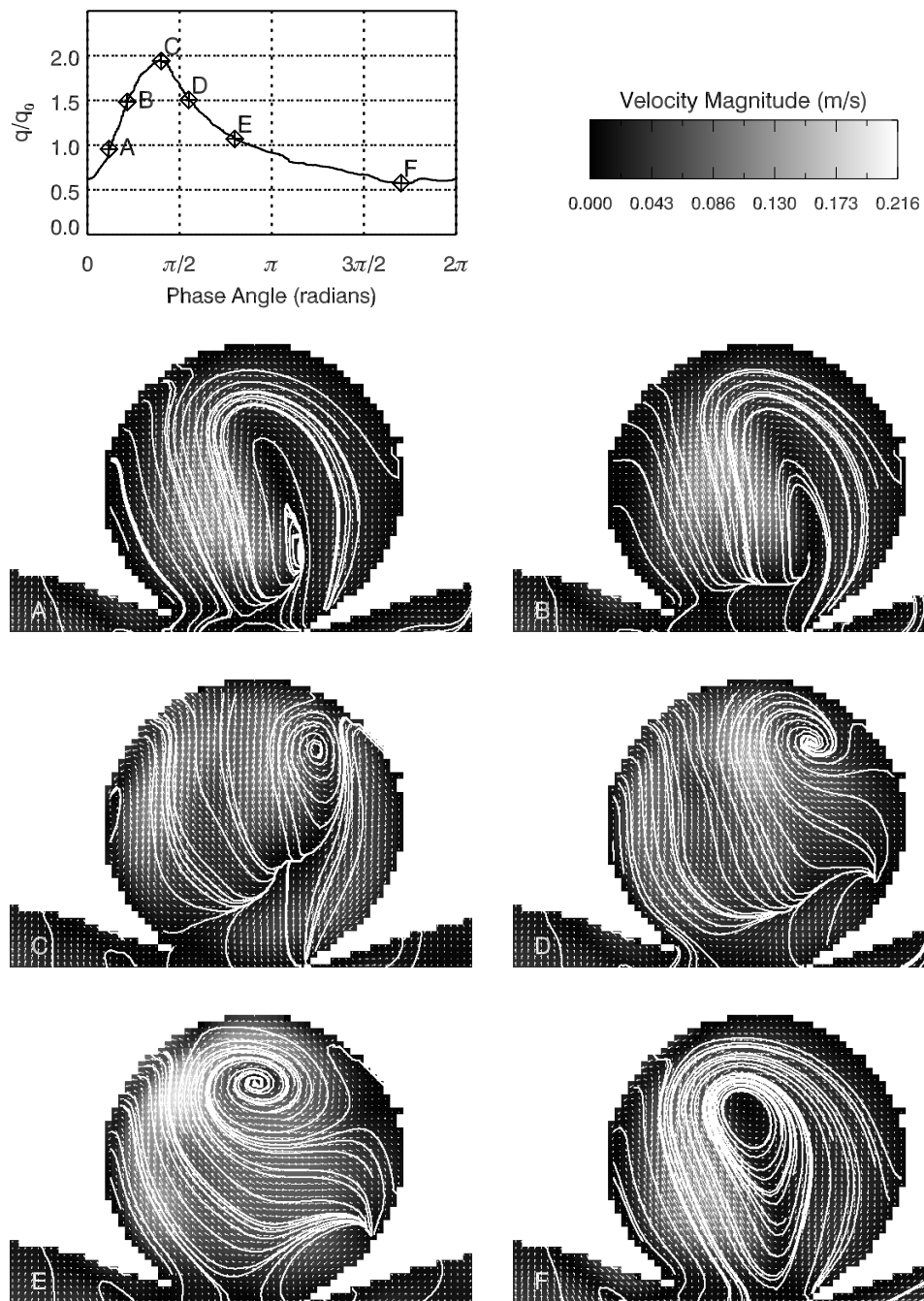


Figure 4.8: Velocity vector with velocity vector field and instantaneous streamlines overlaid for the midplane for a branching ratio of 50:50 over one cycle indicated by the points on the waveform cycle.

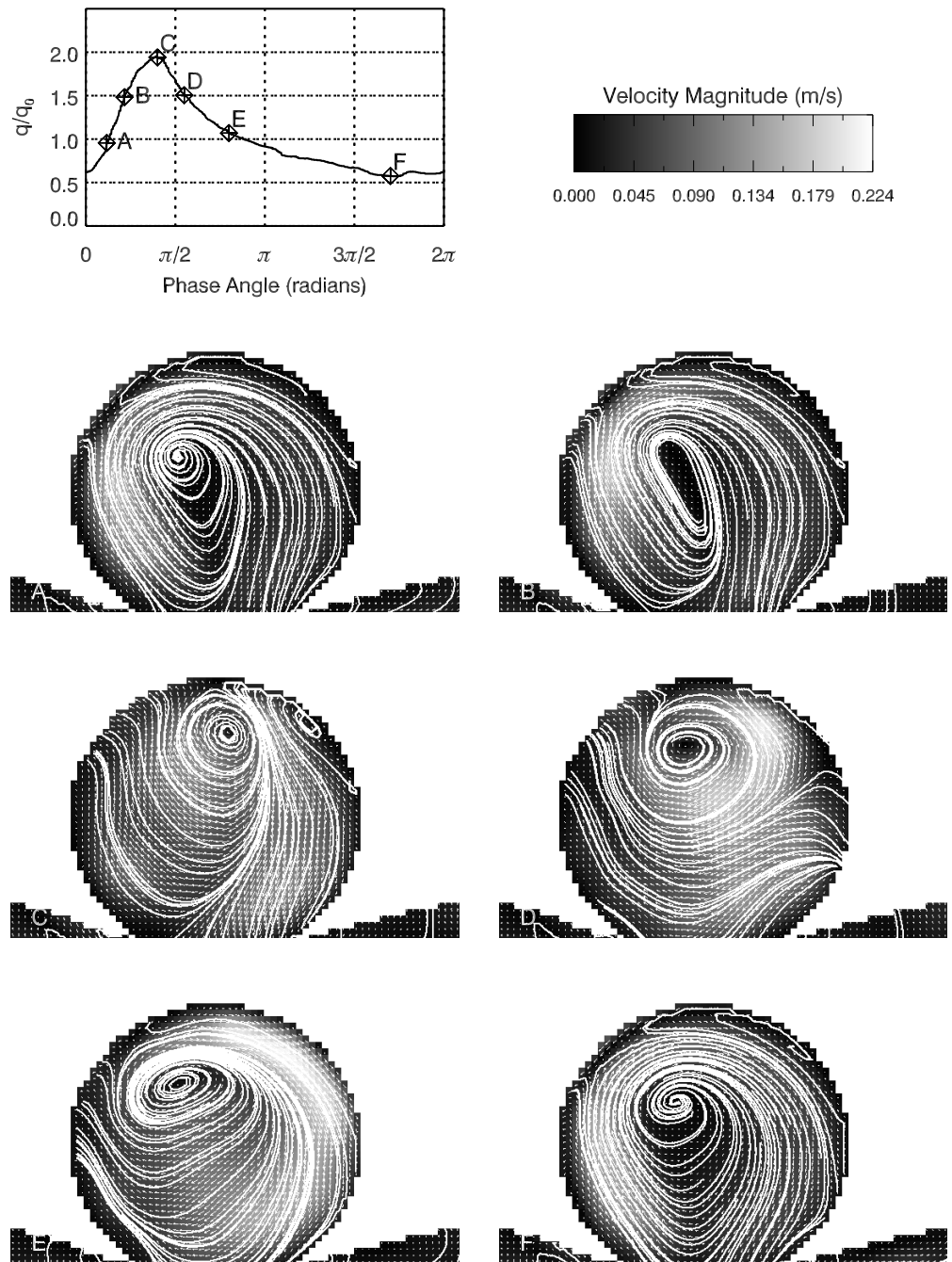


Figure 4.9: Velocity vector with velocity vector field and instantaneous streamlines overlaid for the midplane for a branching ratio of 67:33 over one cycle indicated by the points on the waveform cycle.

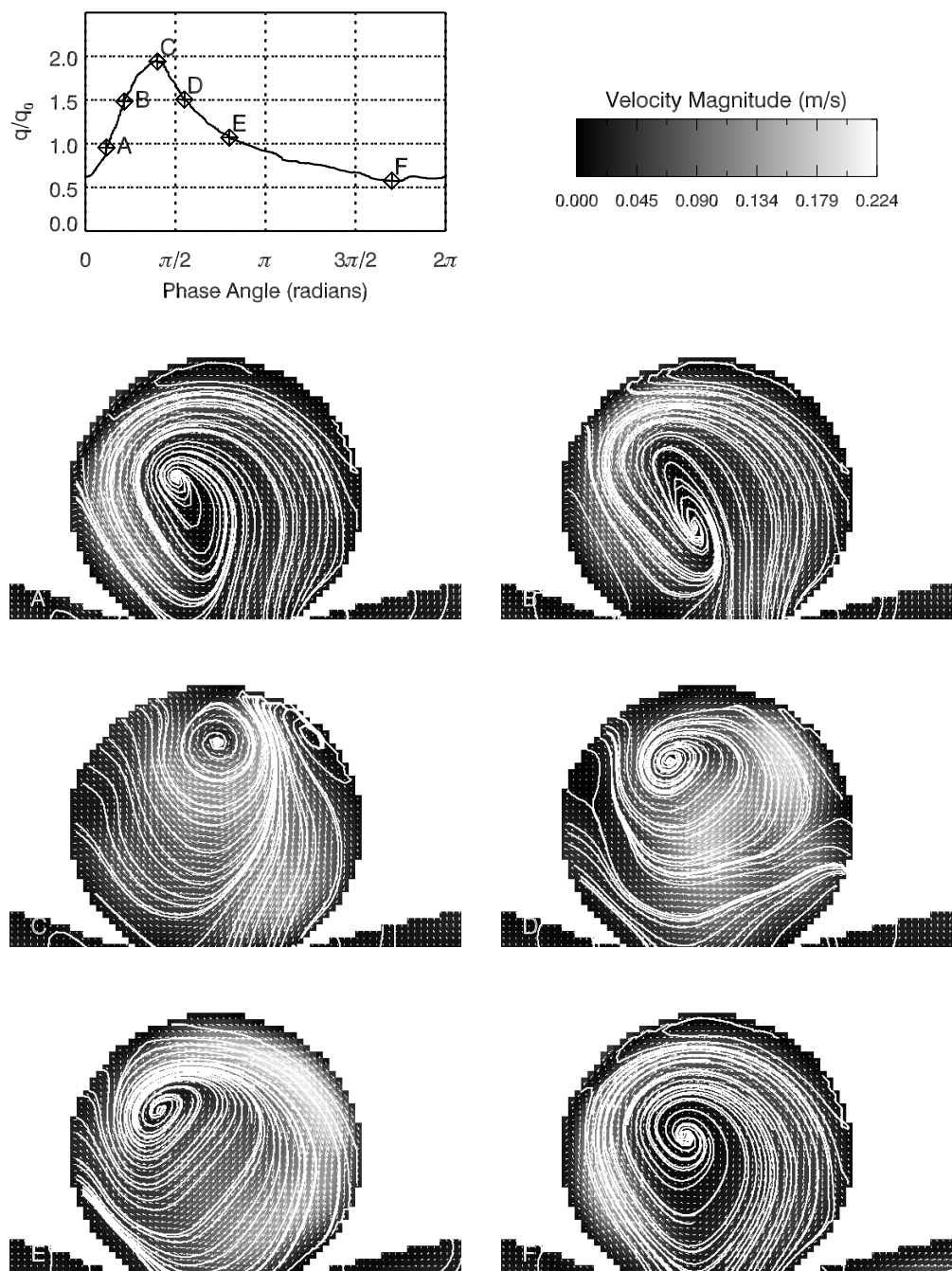


Figure 4.10: Velocity vector with velocity vector field and instantaneous streamlines overlaid for the midplane for a branching ratio of 75:25 over one cycle indicated by the points on the waveform cycle.

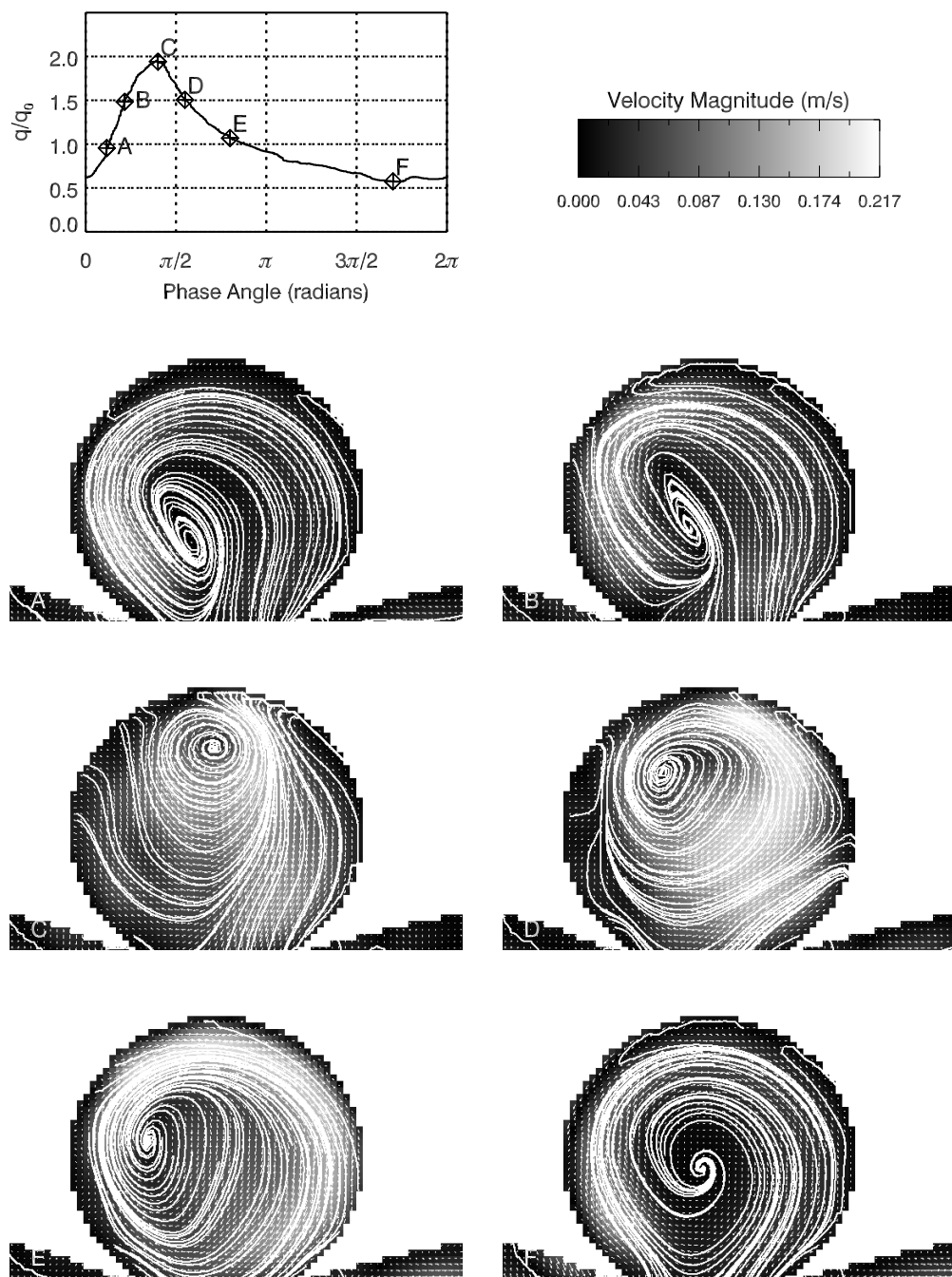


Figure 4.11: Velocity vector with velocity vector field and instantaneous streamlines overlaid for the midplane for a branching ratio of 80:20 over one cycle indicated by the points on the waveform cycle.

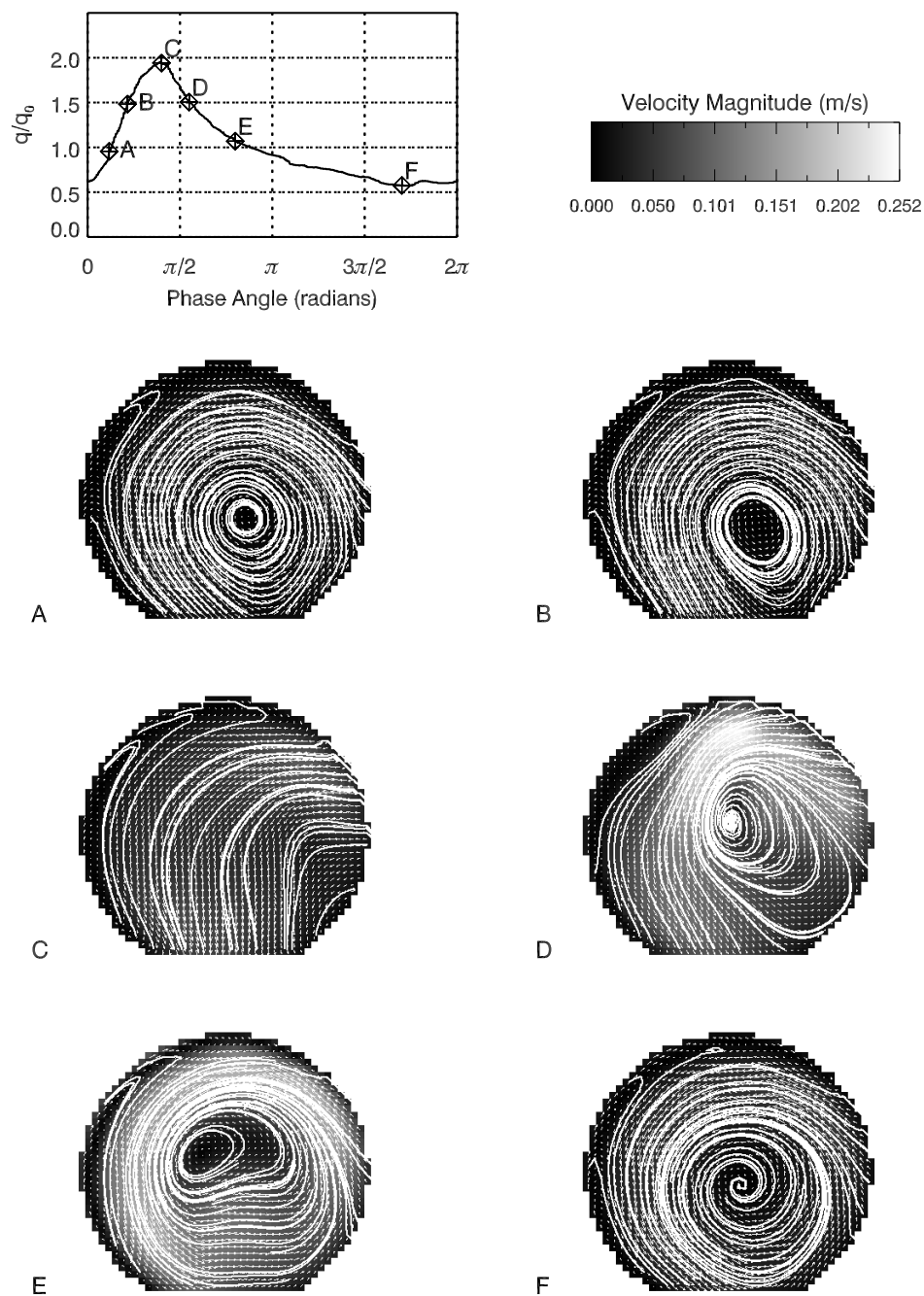


Figure 4.12: Velocity vector with velocity vector field and instantaneous streamlines overlaid for the upper quarter-plane for a branching ratio of 20:80 over one cycle indicated by the points on the waveform cycle.

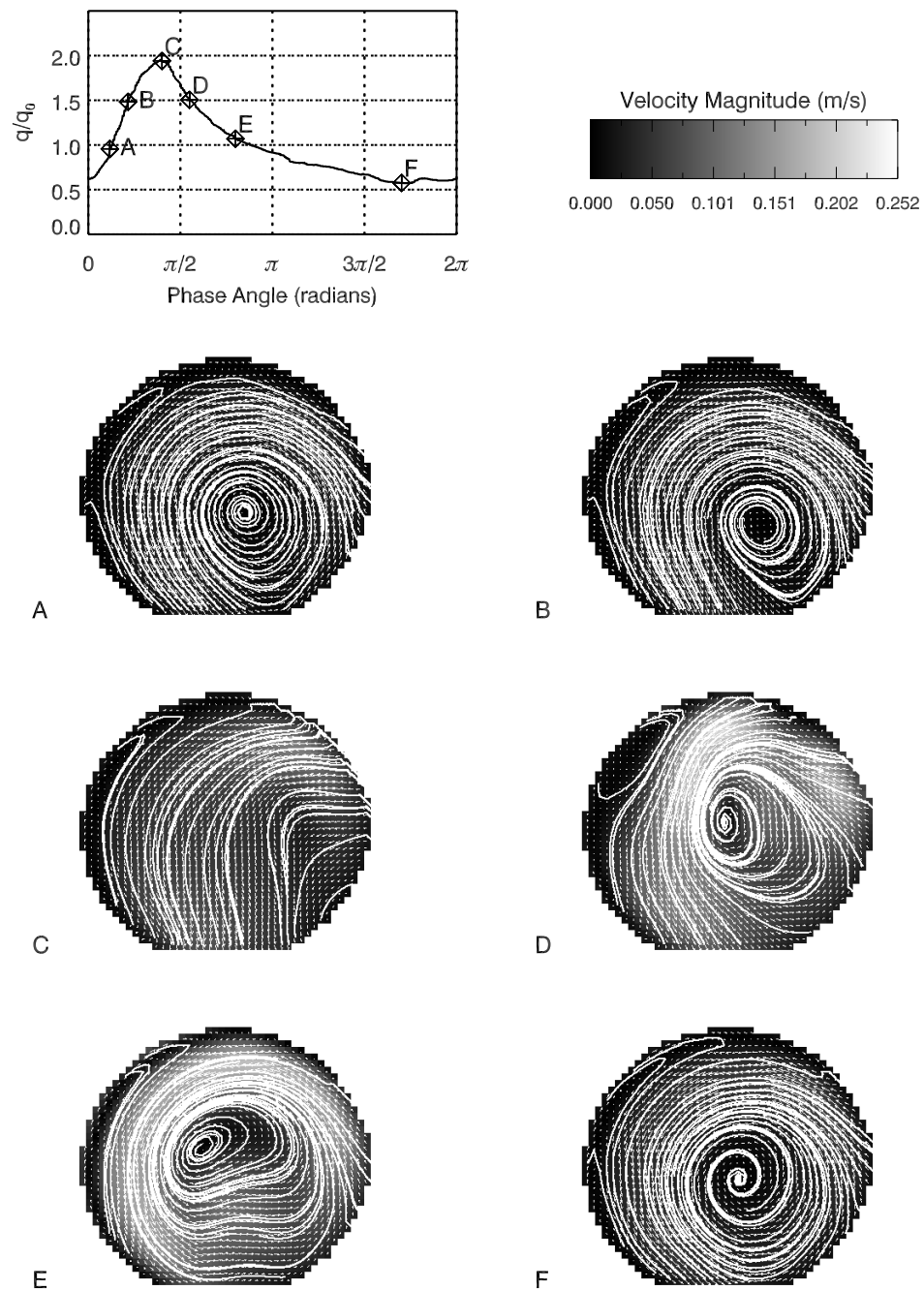


Figure 4.13: Velocity vector with velocity vector field and instantaneous streamlines overlaid for the upper quarter-plane for a branching ratio of 25:75 over one cycle indicated by the points on the waveform cycle.

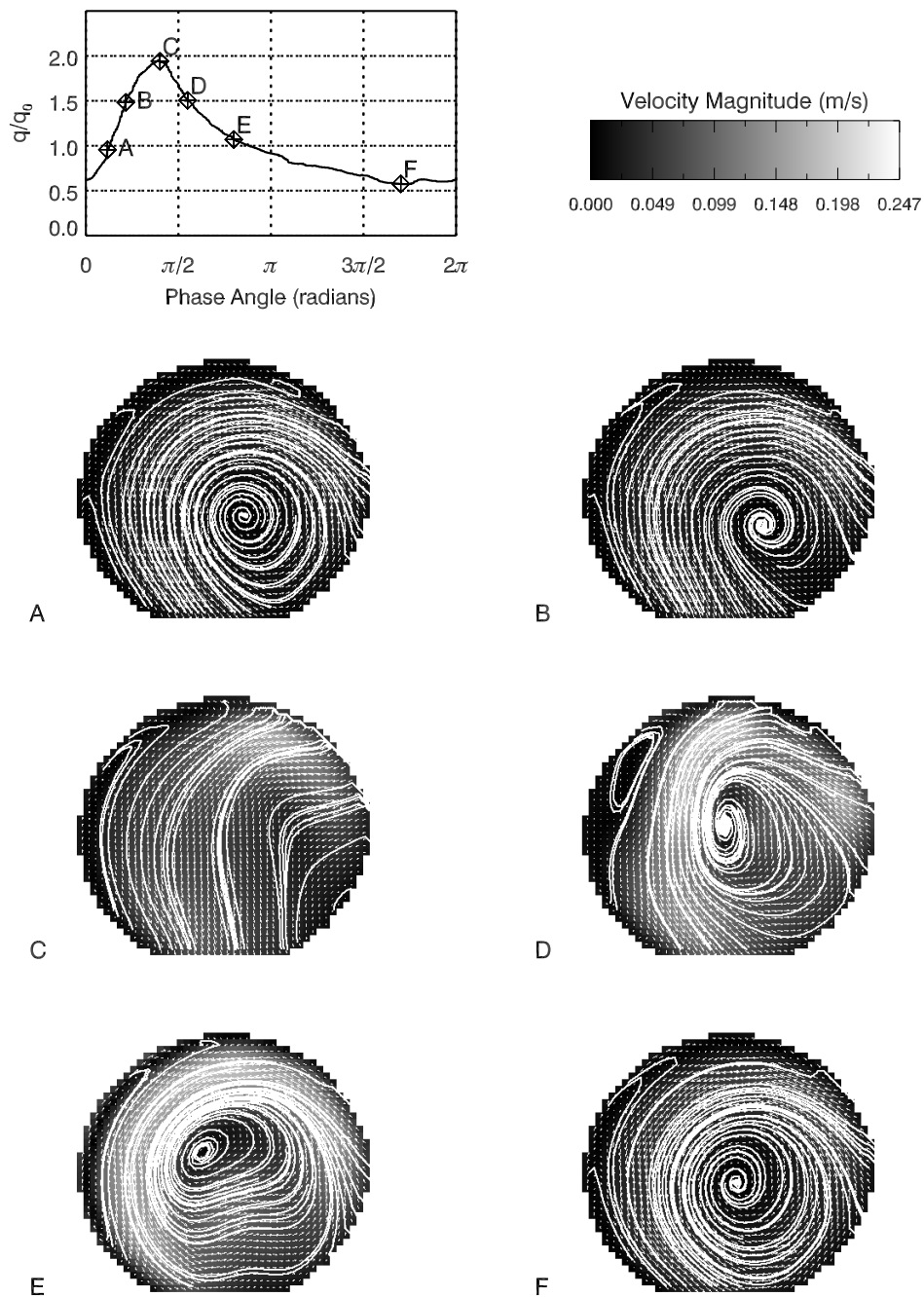


Figure 4.14: Velocity vector with velocity vector field and instantaneous streamlines overlaid for the upper quarter-plane for a branching ratio of 33:67 over one cycle indicated by the points on the waveform cycle.

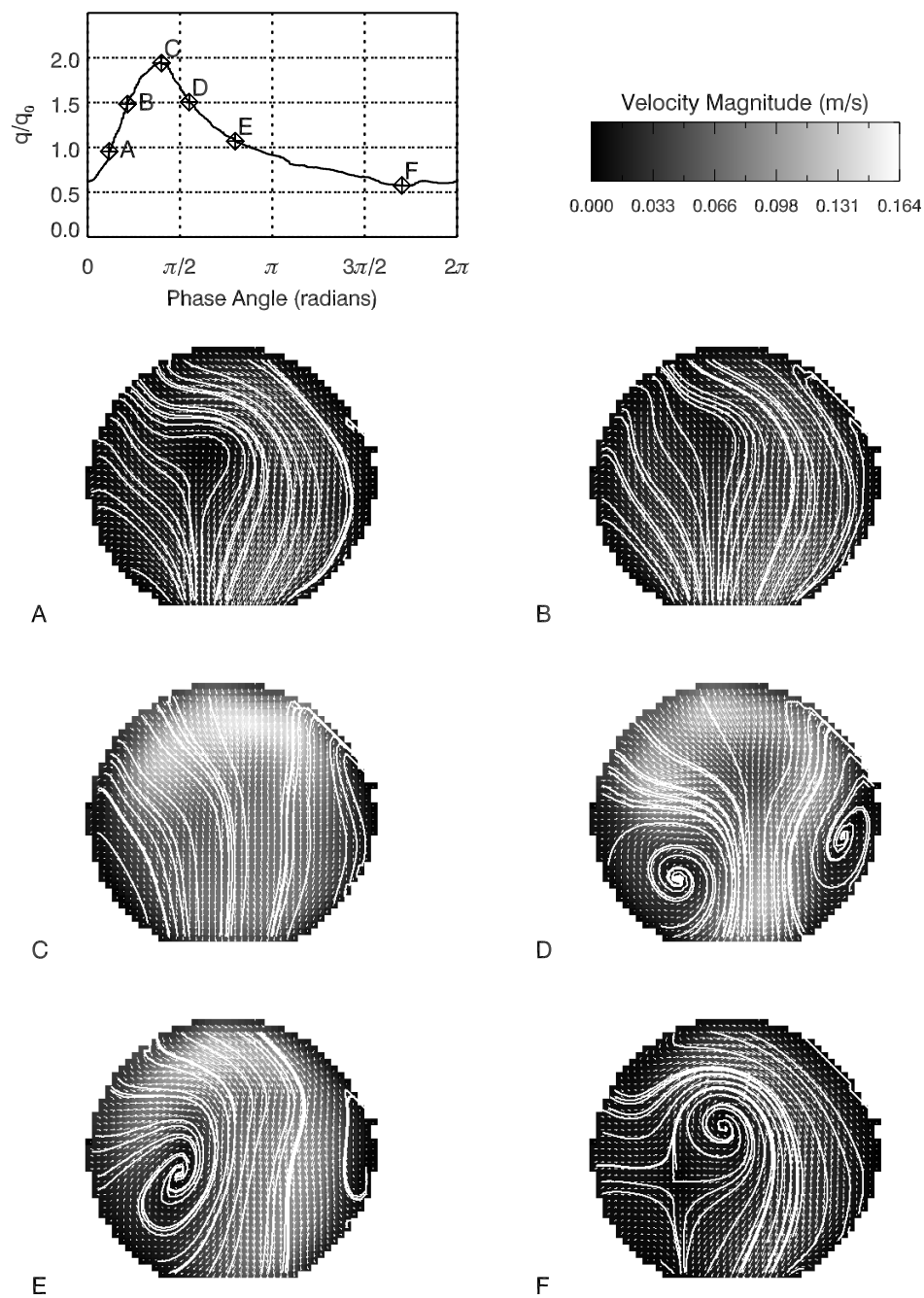


Figure 4.15: Velocity vector with velocity vector field and instantaneous streamlines overlaid for the upper quarter-plane for a branching ratio of 46:54 over one cycle indicated by the points on the waveform cycle.

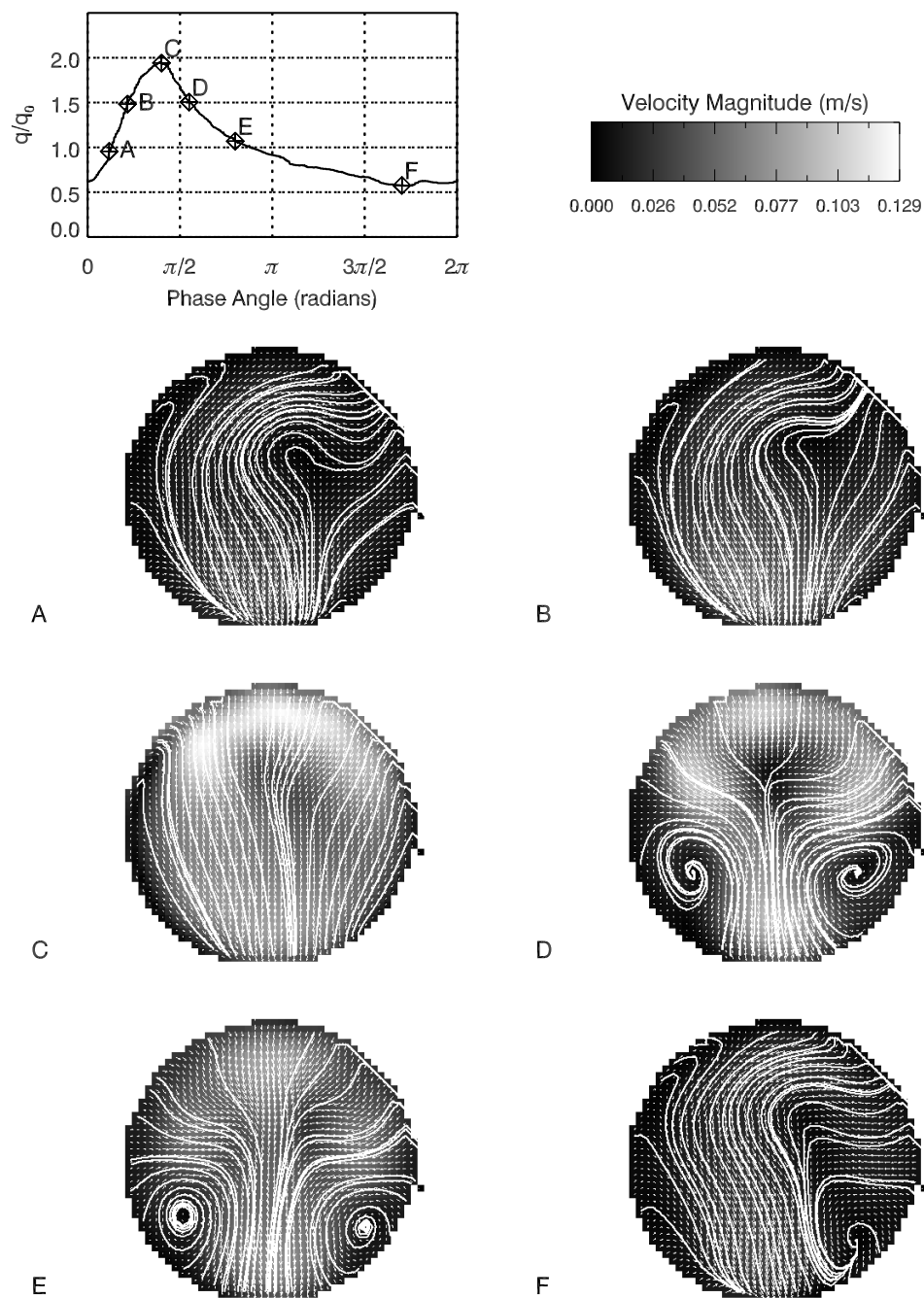


Figure 4.16: Velocity vector with velocity vector field and instantaneous streamlines overlaid for the upper quarter-plane for a branching ratio of 48:52 over one cycle indicated by the points on the waveform cycle.

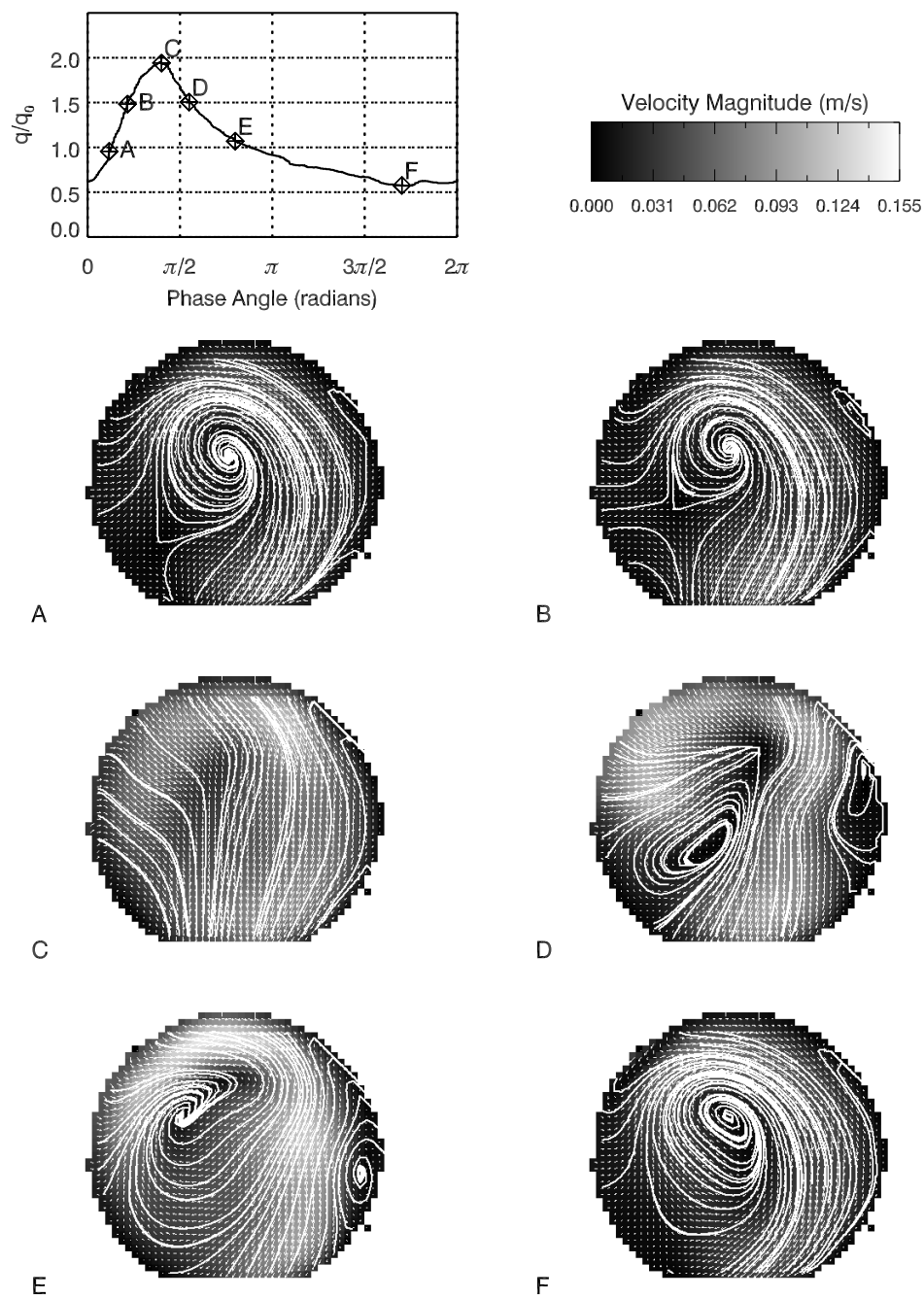


Figure 4.17: Velocity vector with velocity vector field and instantaneous streamlines overlaid for the upper quarter-plane for a branching ratio of 50:50 over one cycle indicated by the points on the waveform cycle.

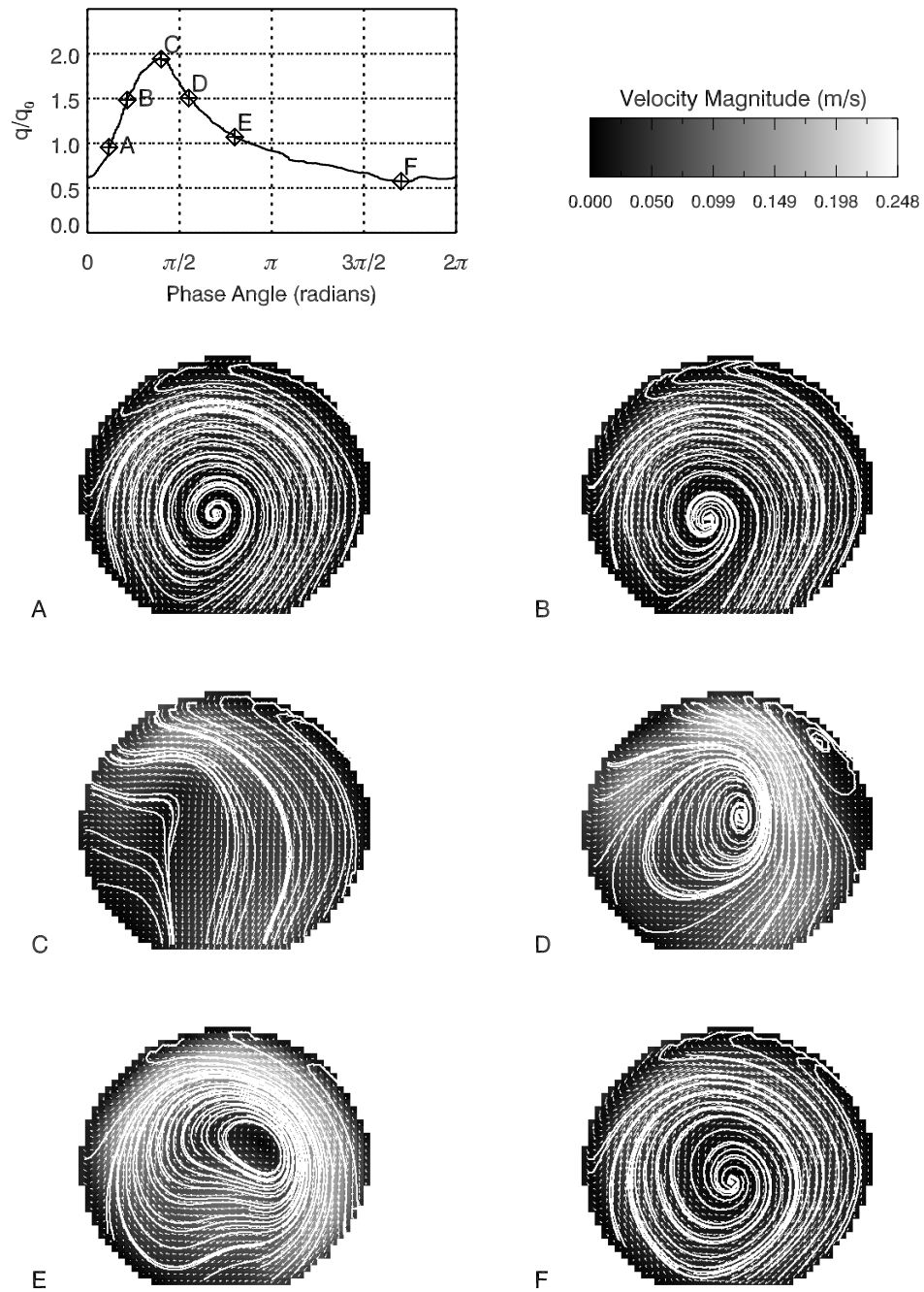


Figure 4.18: Velocity vector with velocity vector field and instantaneous streamlines overlaid for the upper quarter-plane for a branching ratio of 67:33 over one cycle indicated by the points on the waveform cycle.

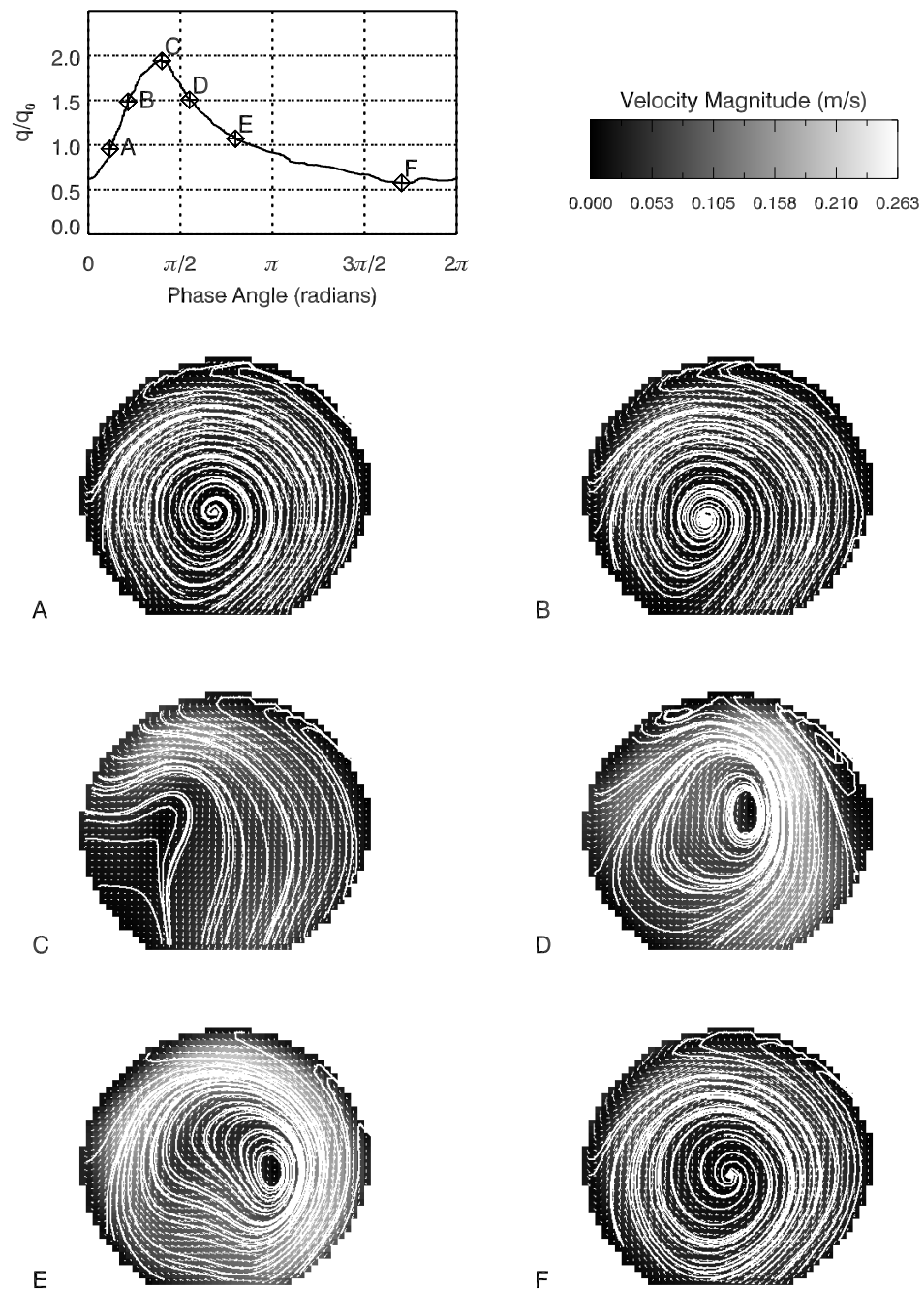


Figure 4.19: Velocity vector with velocity vector field and instantaneous streamlines overlaid for the upper quarter-plane for a branching ratio of 75:25 over one cycle indicated by the points on the waveform cycle.

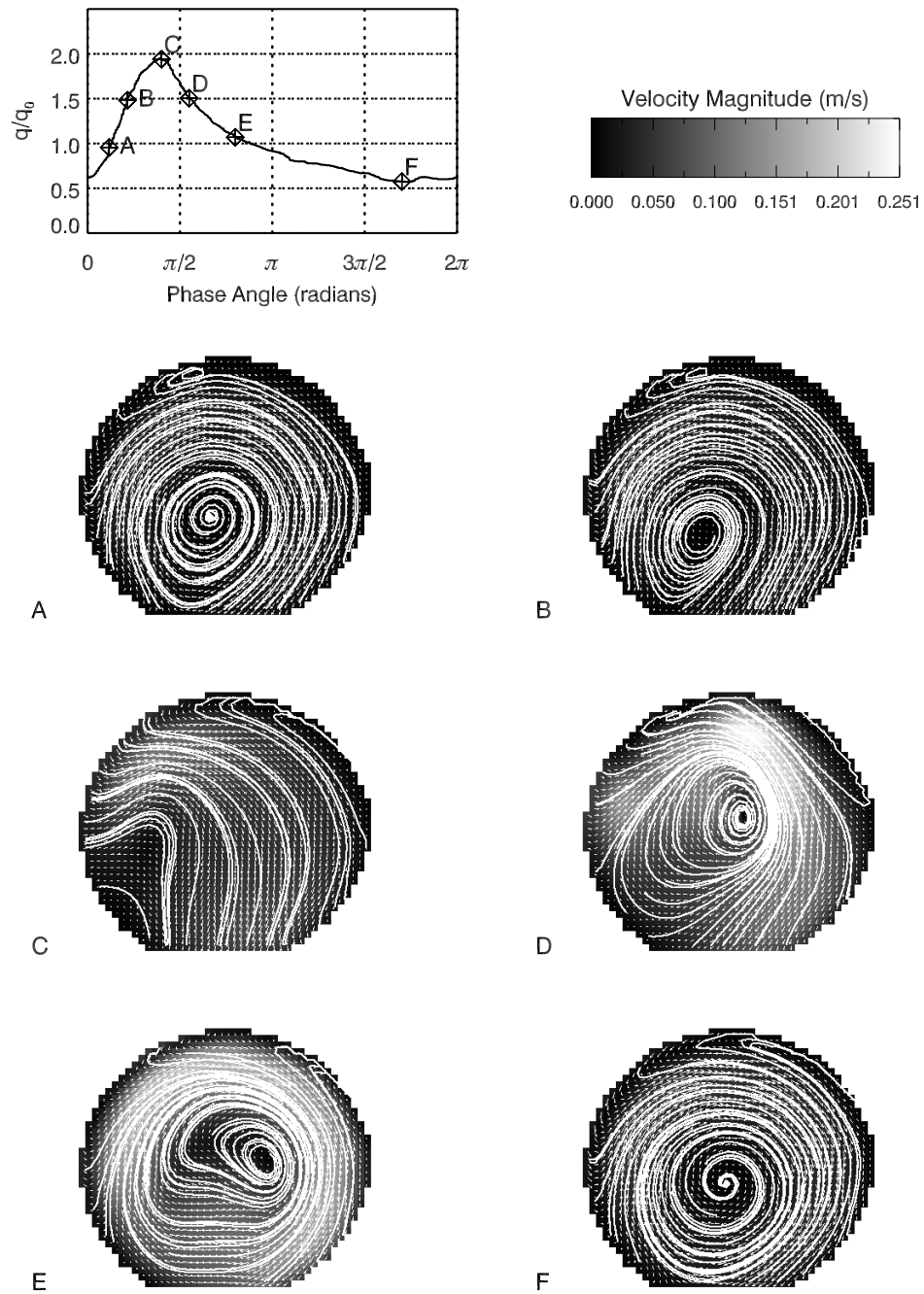


Figure 4.20: Velocity vector with velocity vector field and instantaneous streamlines overlaid for the upper quarter-plane for a branching ratio of 80:20 over one cycle indicated by the points on the waveform cycle.

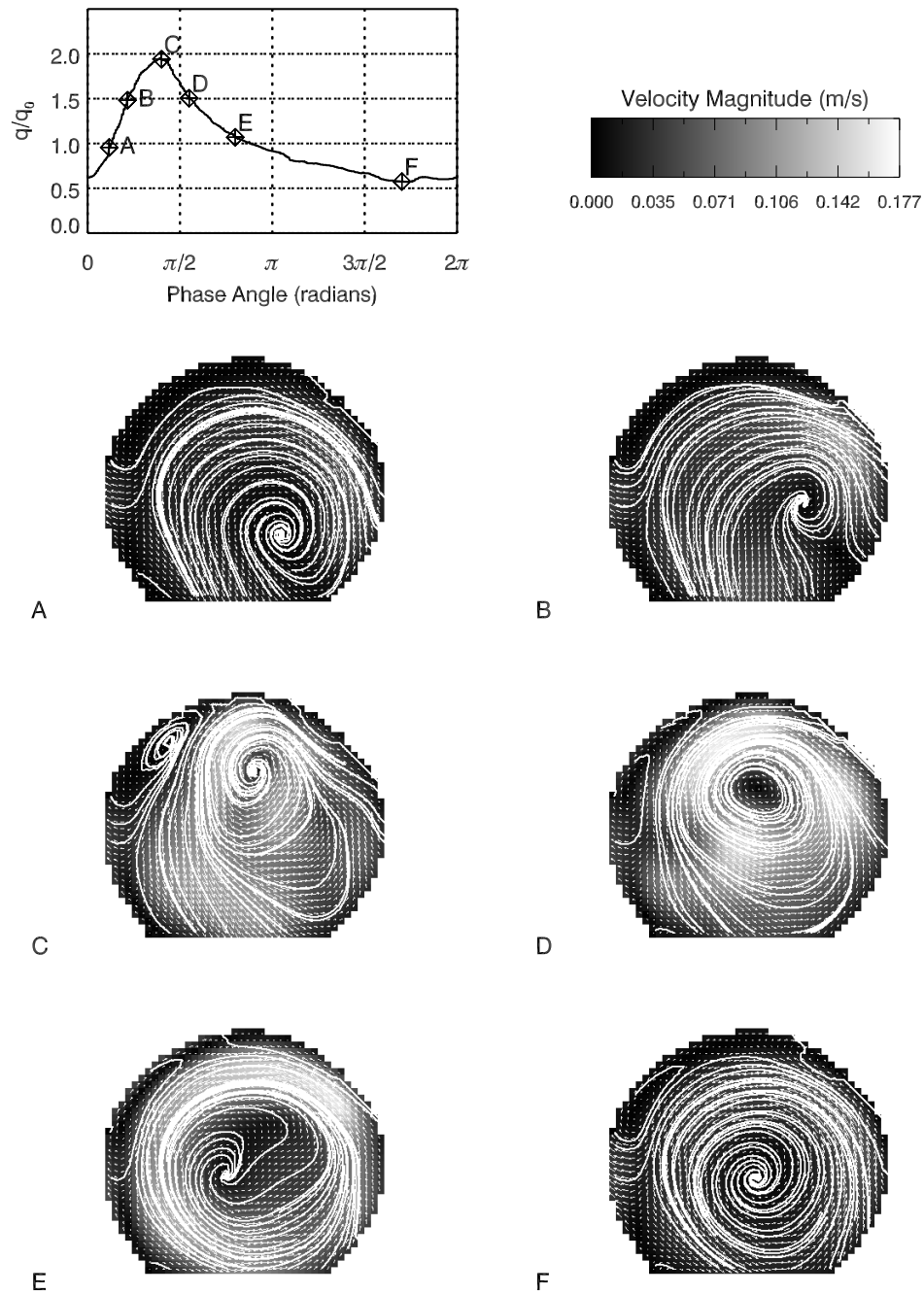


Figure 4.21: Velocity vector with velocity vector field and instantaneous streamlines overlaid for the lower quarter-plane for a branching ratio of 20:80 over one cycle indicated by the points on the waveform cycle.

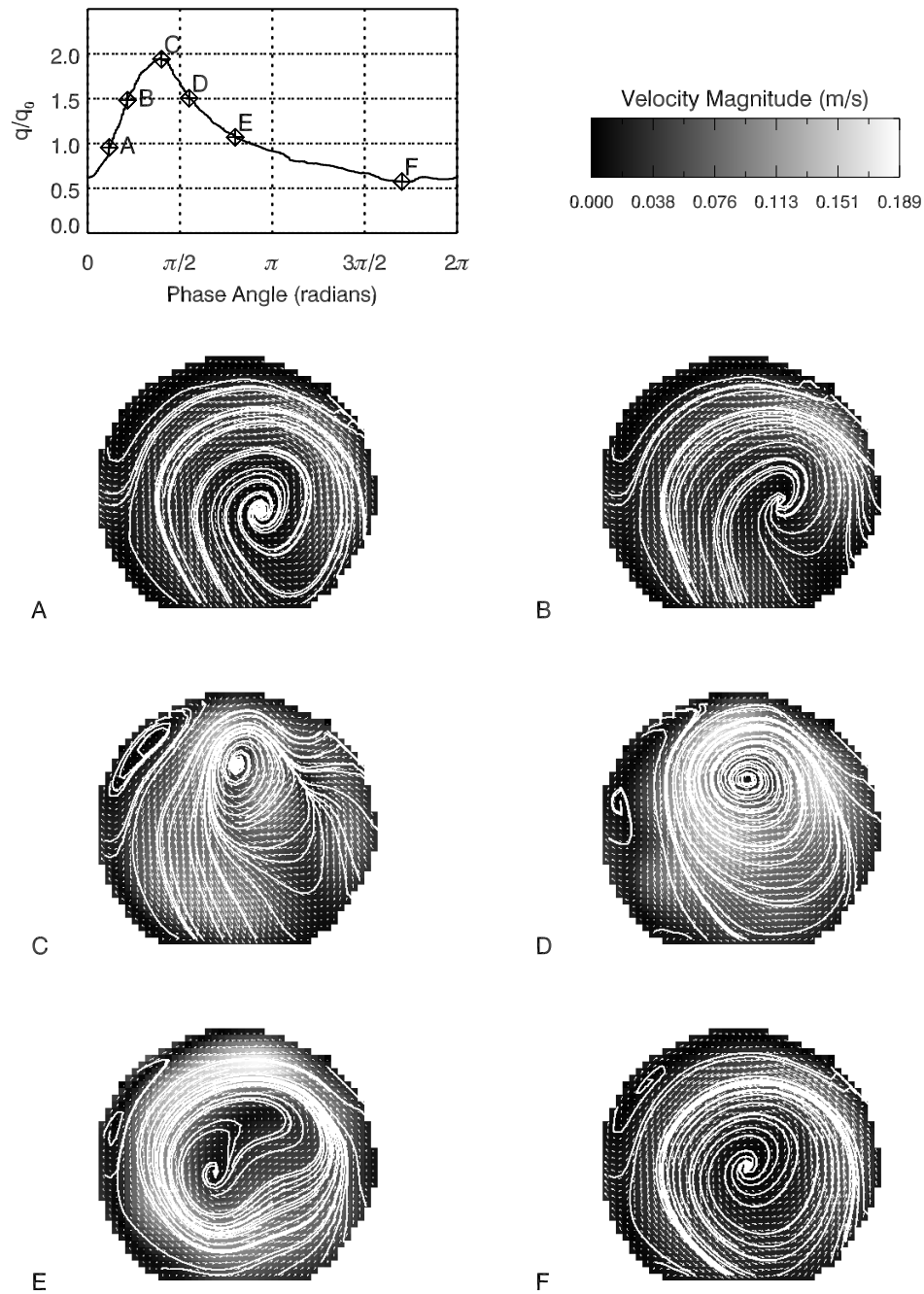


Figure 4.22: Velocity vector with velocity vector field and instantaneous streamlines overlaid for the lower quarter-plane for a branching ratio of 25:75 over one cycle indicated by the points on the waveform cycle.

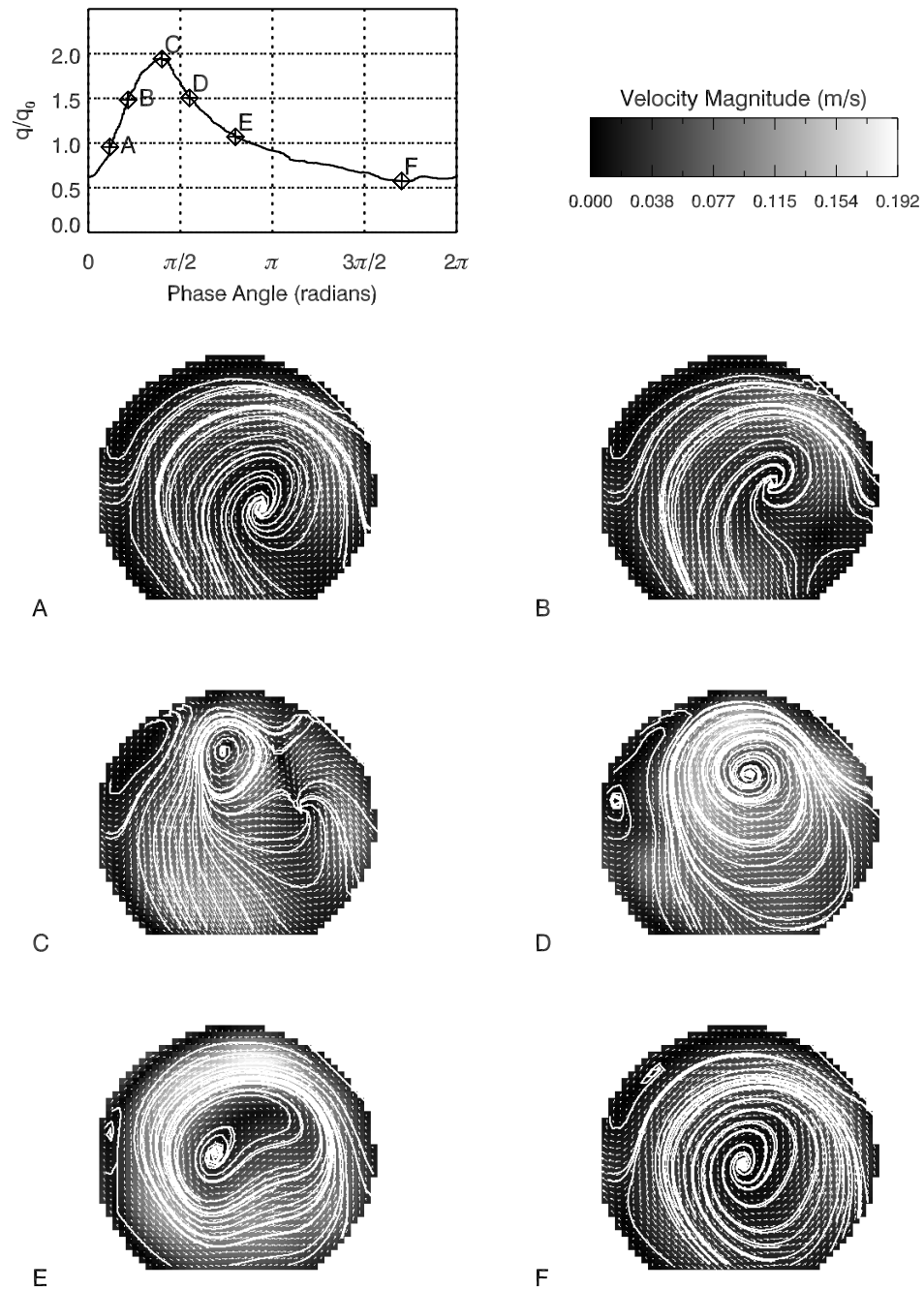


Figure 4.23: Velocity vector with velocity vector field and instantaneous streamlines overlaid for the lower quarter-plane for a branching ratio of 33:67 over one cycle indicated by the points on the waveform cycle.

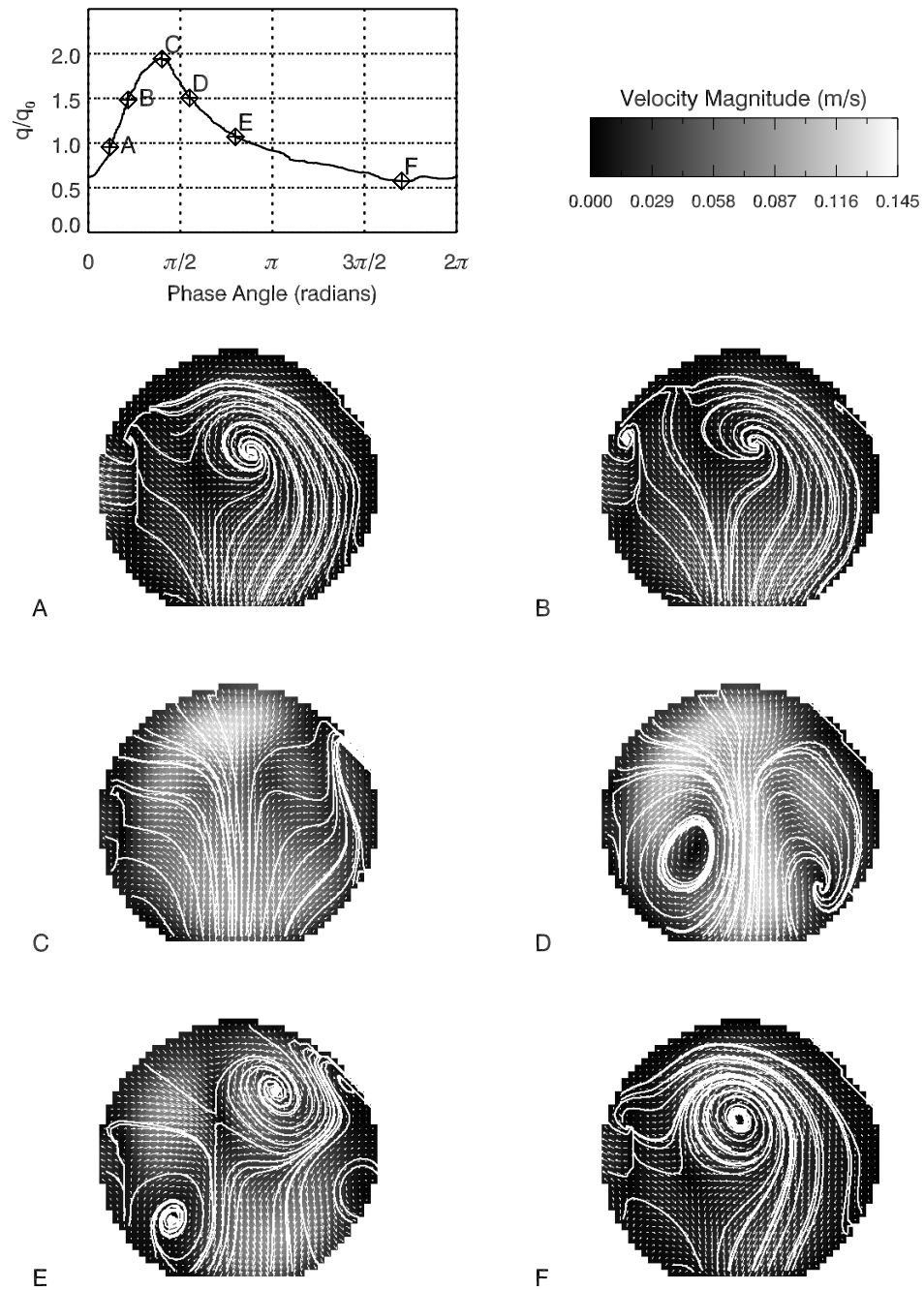


Figure 4.24: Velocity vector with velocity vector field and instantaneous streamlines overlaid for the lower quarter-plane for a branching ratio of 46:54 over one cycle indicated by the points on the waveform cycle.

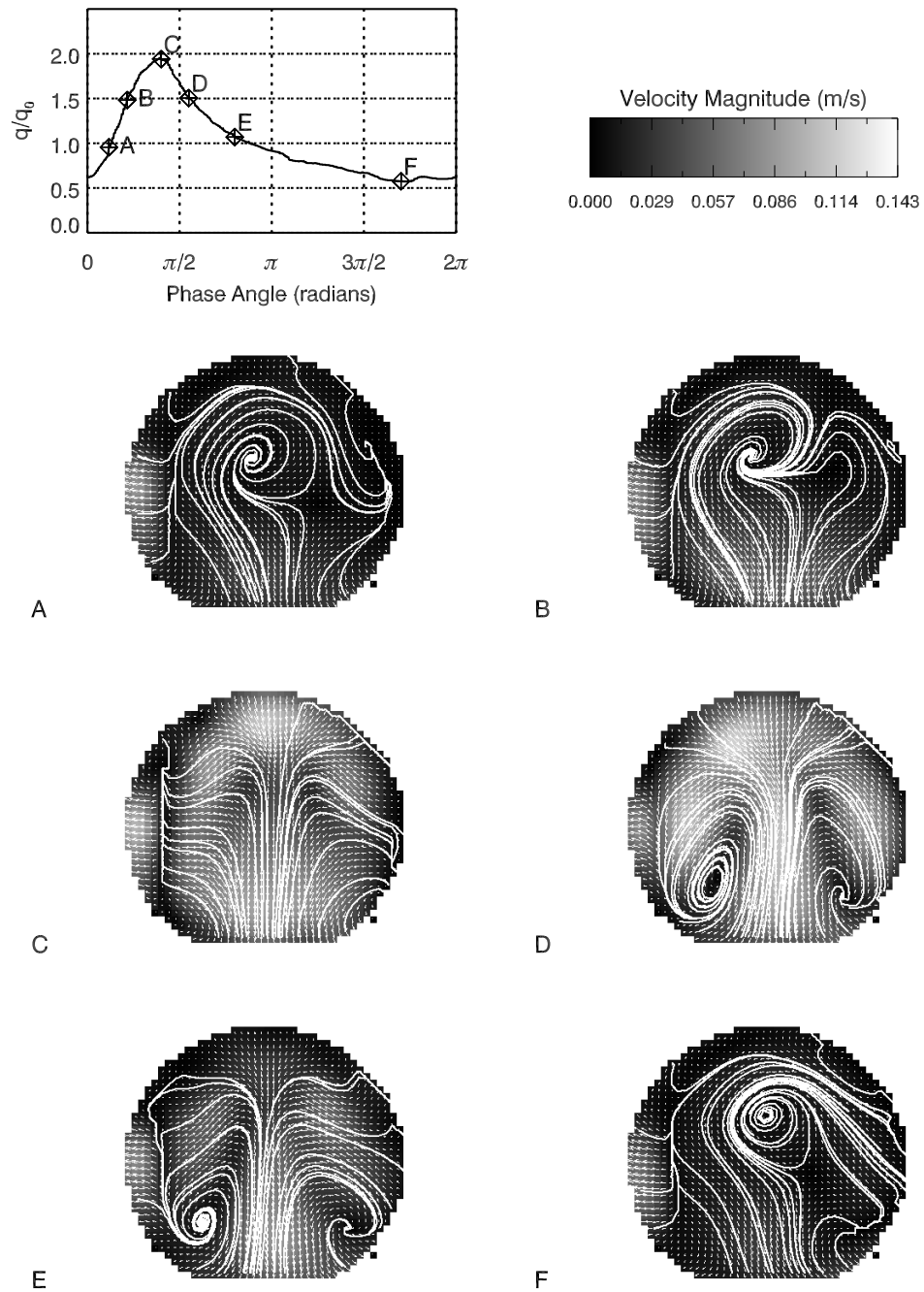


Figure 4.25: Velocity vector with velocity vector field and instantaneous streamlines overlaid for the lower quarter-plane for a branching ratio of 48:52 over one cycle indicated by the points on the waveform cycle.

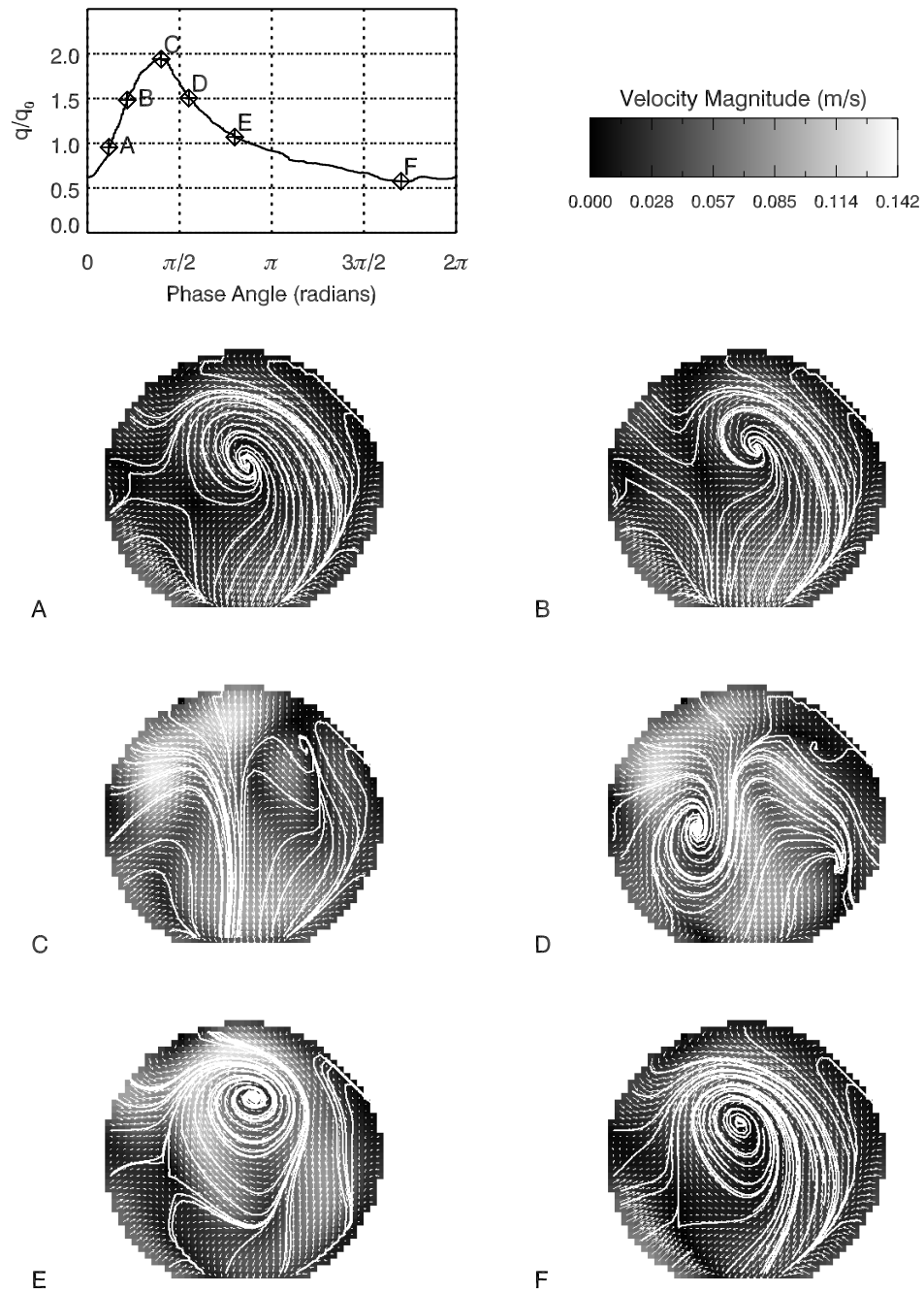


Figure 4.26: Velocity vector with velocity vector field and instantaneous streamlines overlaid for the lower quarter-plane for a branching ratio of 50:50 over one cycle indicated by the points on the waveform cycle.

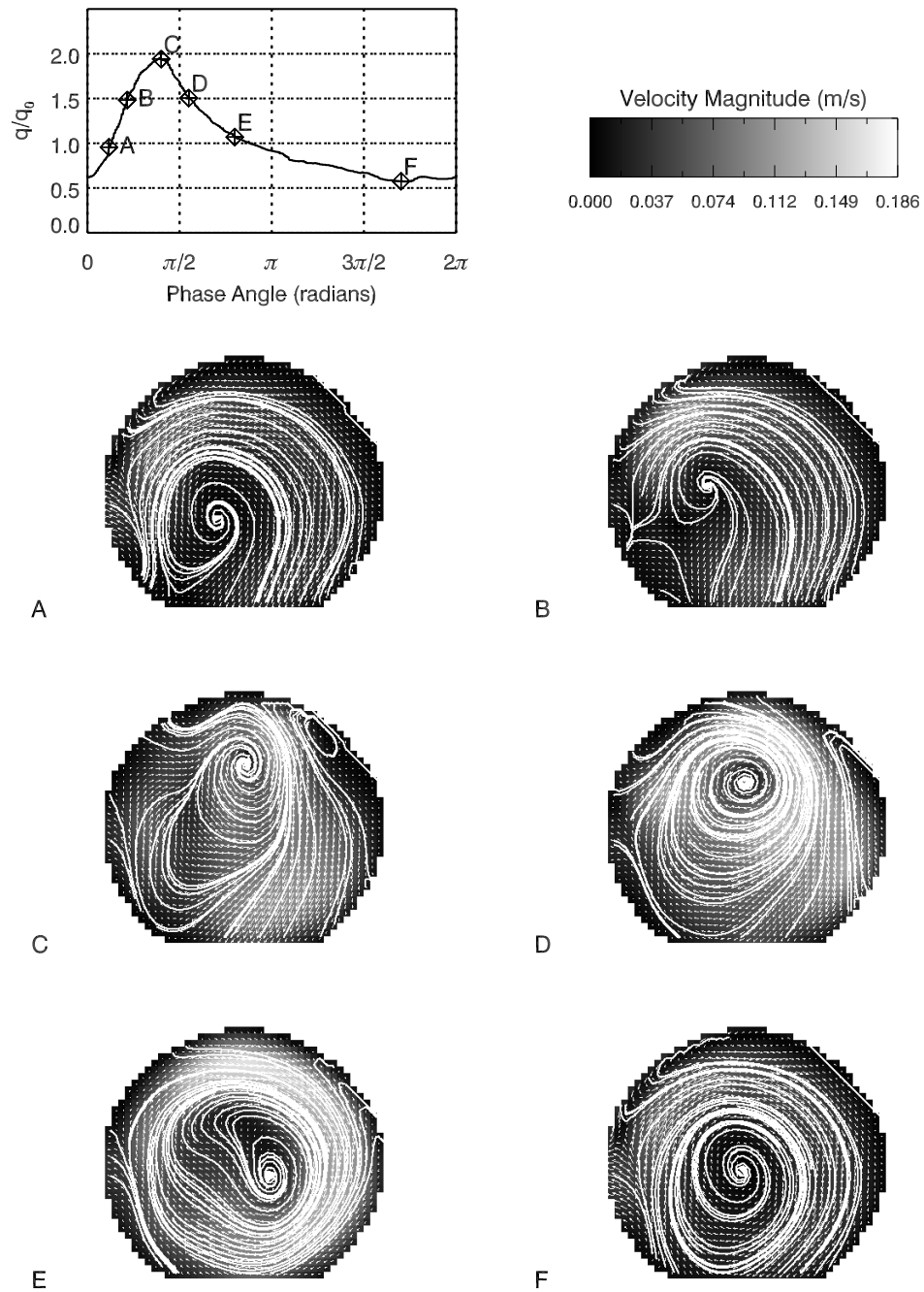


Figure 4.27: Velocity vector with velocity vector field and instantaneous streamlines overlaid for the lower quarter-plane for a branching ratio of 67:33 over one cycle indicated by the points on the waveform cycle.

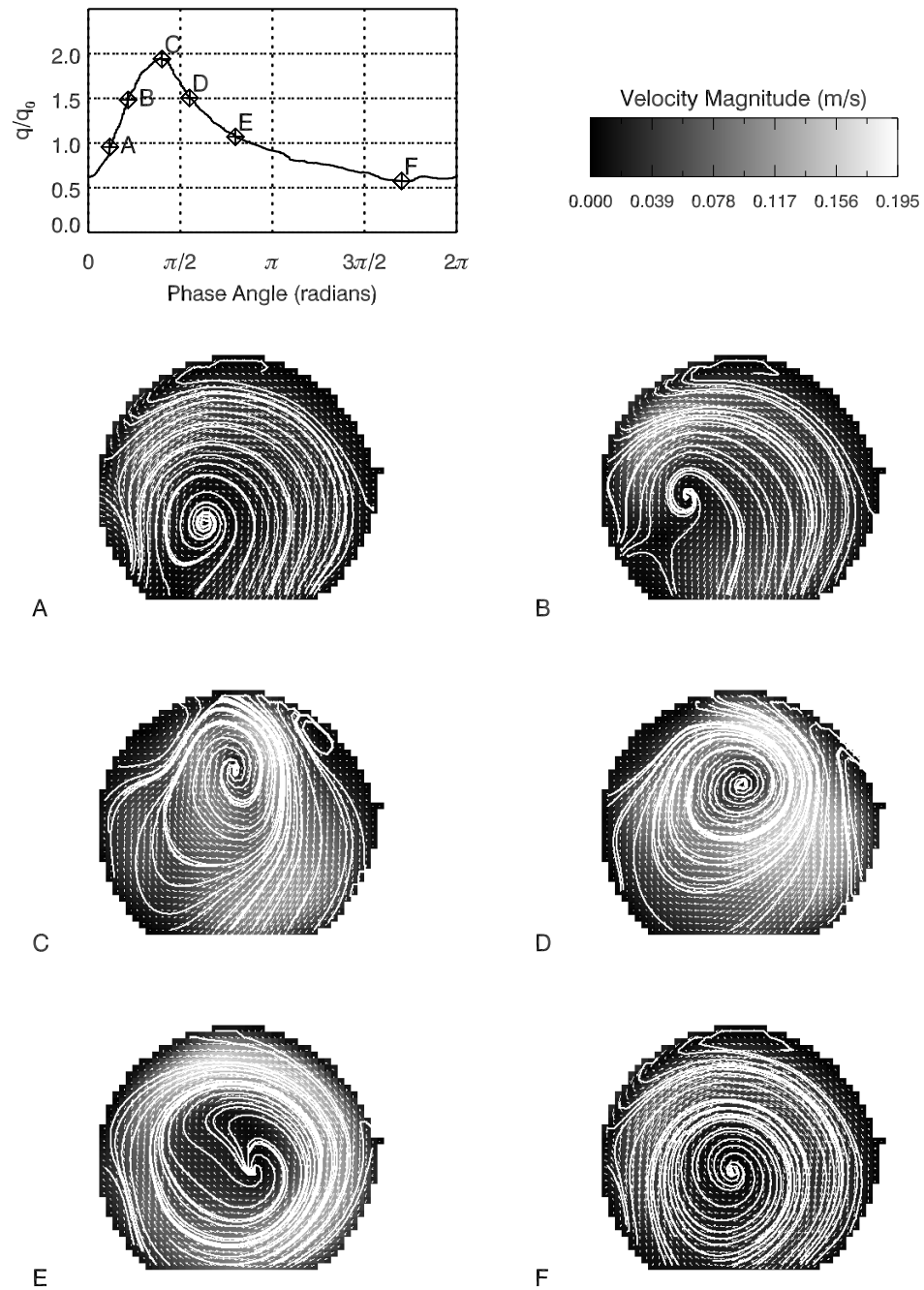


Figure 4.28: Velocity vector with velocity vector field and instantaneous streamlines overlaid for the lower quarter-plane for a branching ratio of 75:25 over one cycle indicated by the points on the waveform cycle.

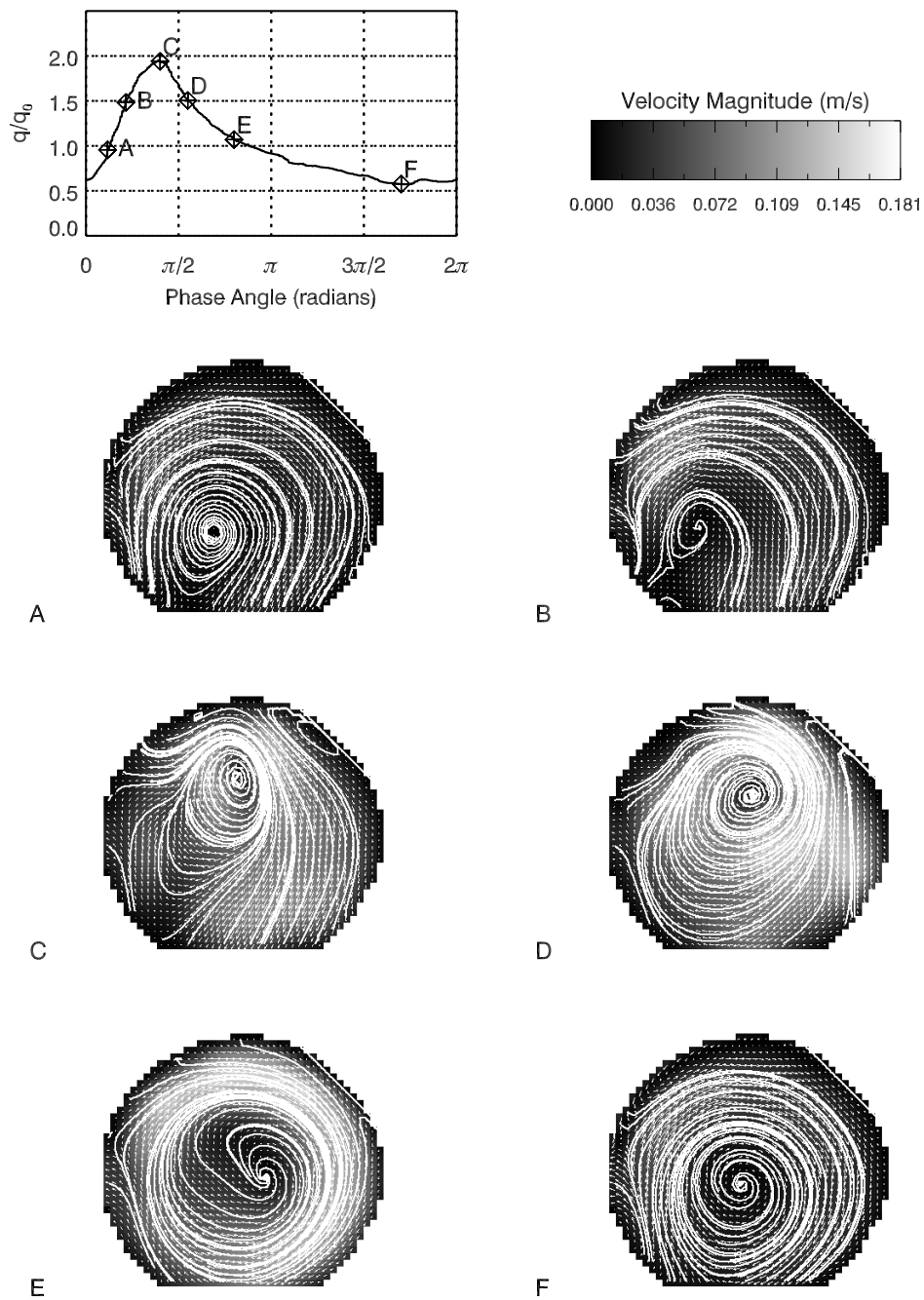


Figure 4.29: Velocity vector with velocity vector field and instantaneous streamlines overlaid for the lower quarter-plane for a branching ratio of 80:20 over one cycle indicated by the points on the waveform cycle.

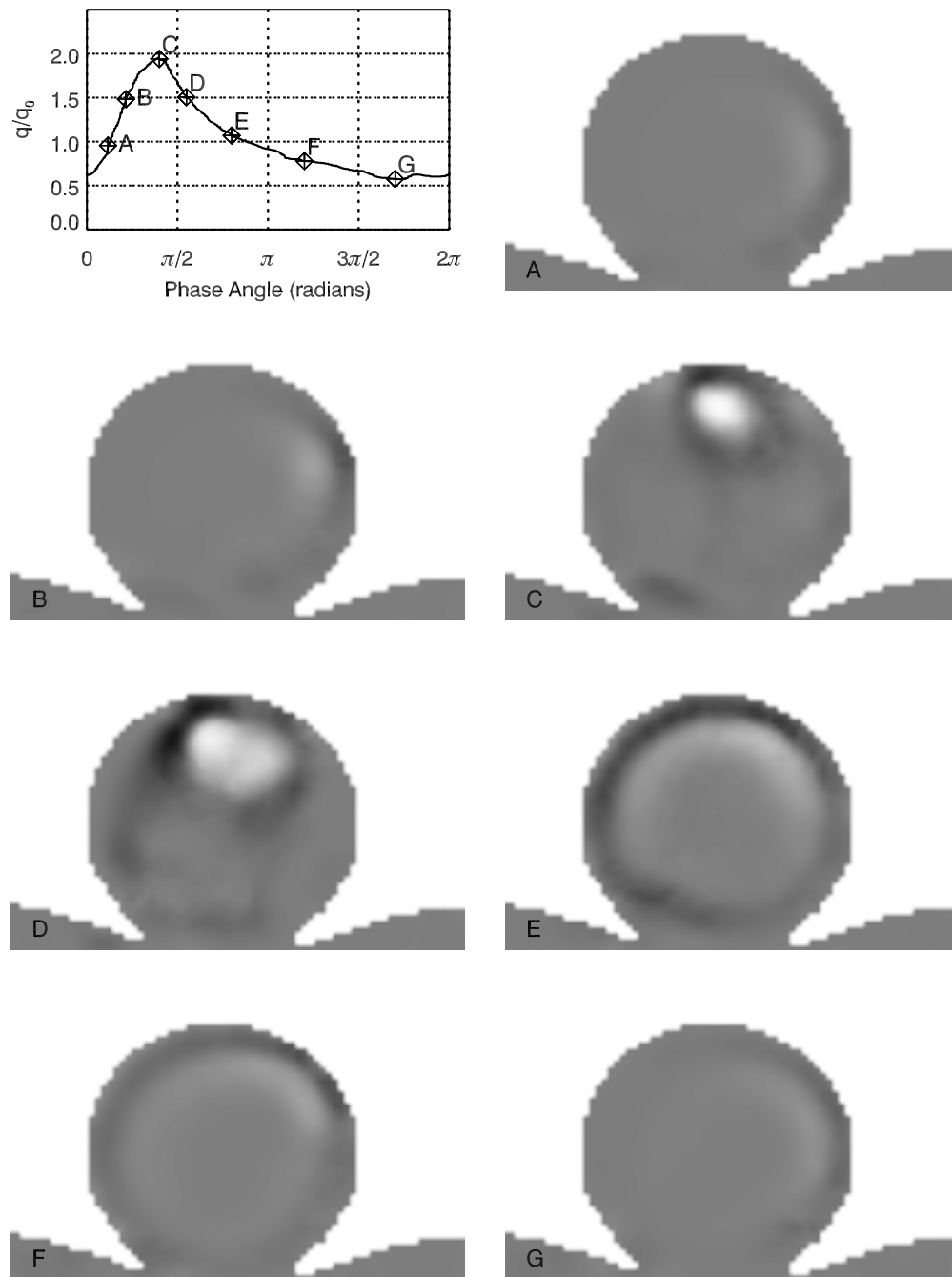


Figure 4.30: Plots of the second invariant of the velocity gradient tensor for the midplane for a branching ratio of 20:80 over one cycle indicated by the points on the waveform cycle.

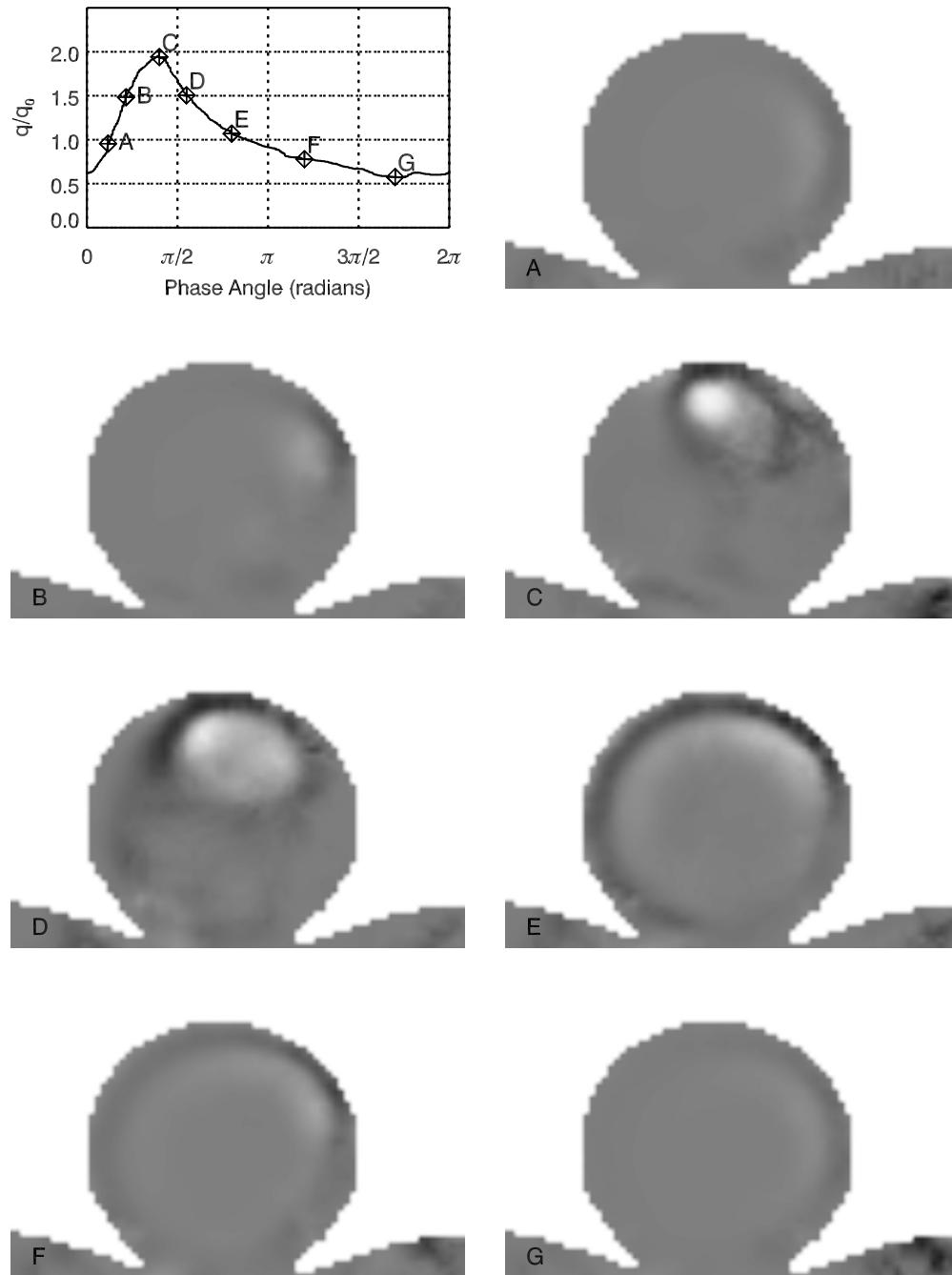


Figure 4.31: Plots of the second invariant of the velocity gradient tensor for the midplane for a branching ratio of 25:75 over one cycle indicated by the points on the waveform cycle.

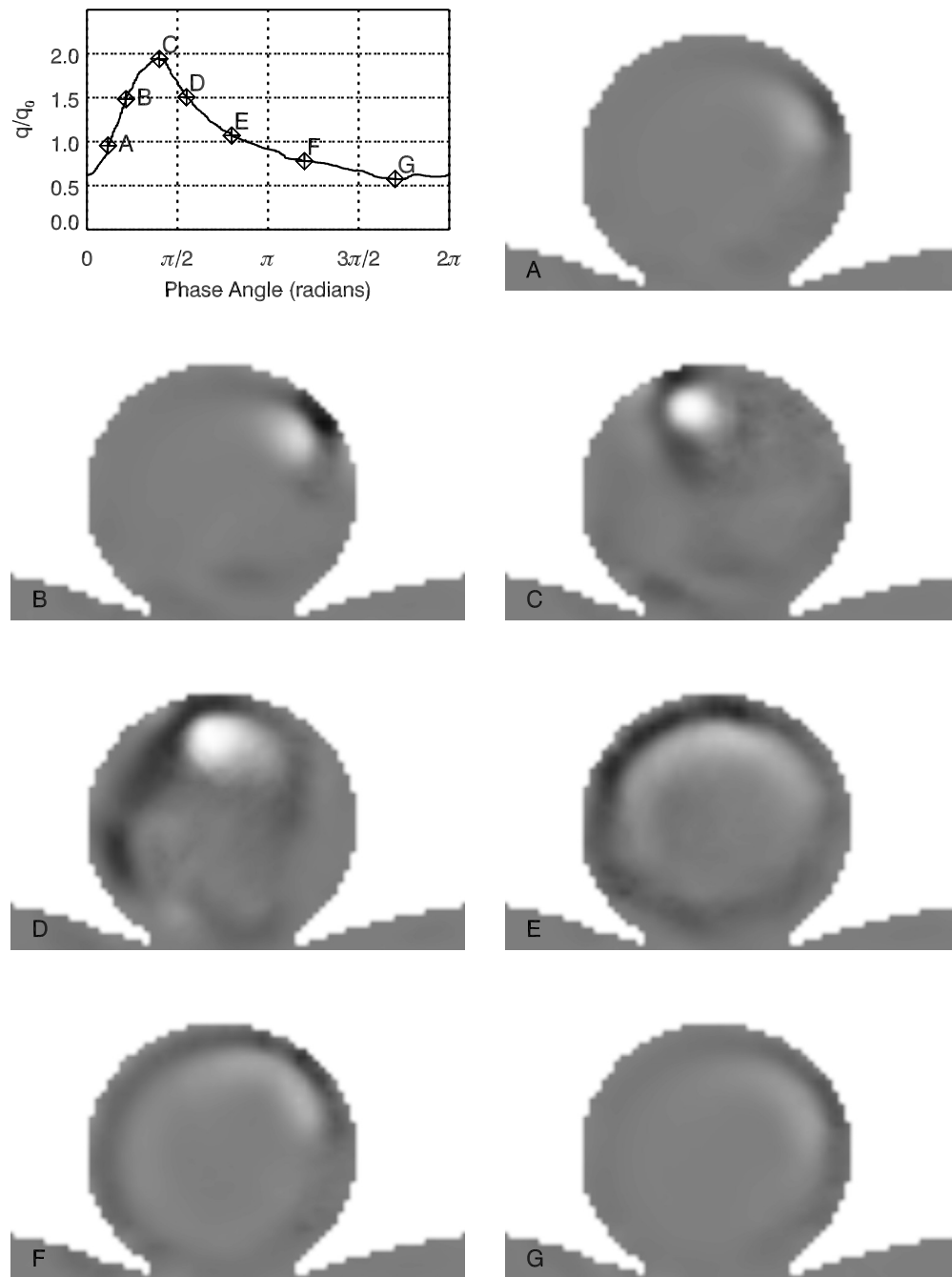


Figure 4.32: Plots of the second invariant of the velocity gradient tensor for the midplane for a branching ratio of 33:67 over one cycle indicated by the points on the waveform cycle.

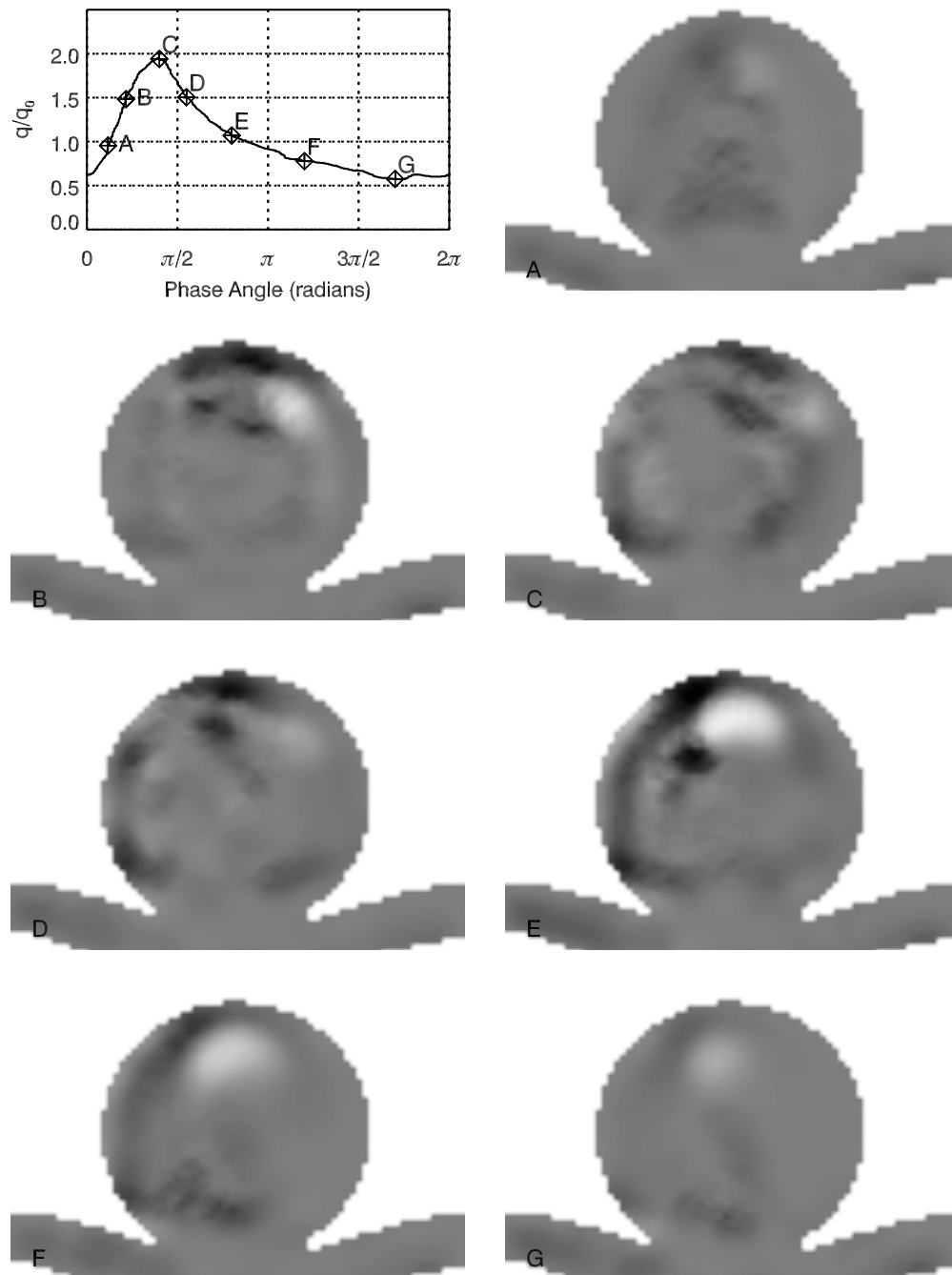


Figure 4.33: Plots of the second invariant of the velocity gradient tensor for the midplane for a branching ratio of 46:54 over one cycle indicated by the points on the waveform cycle.

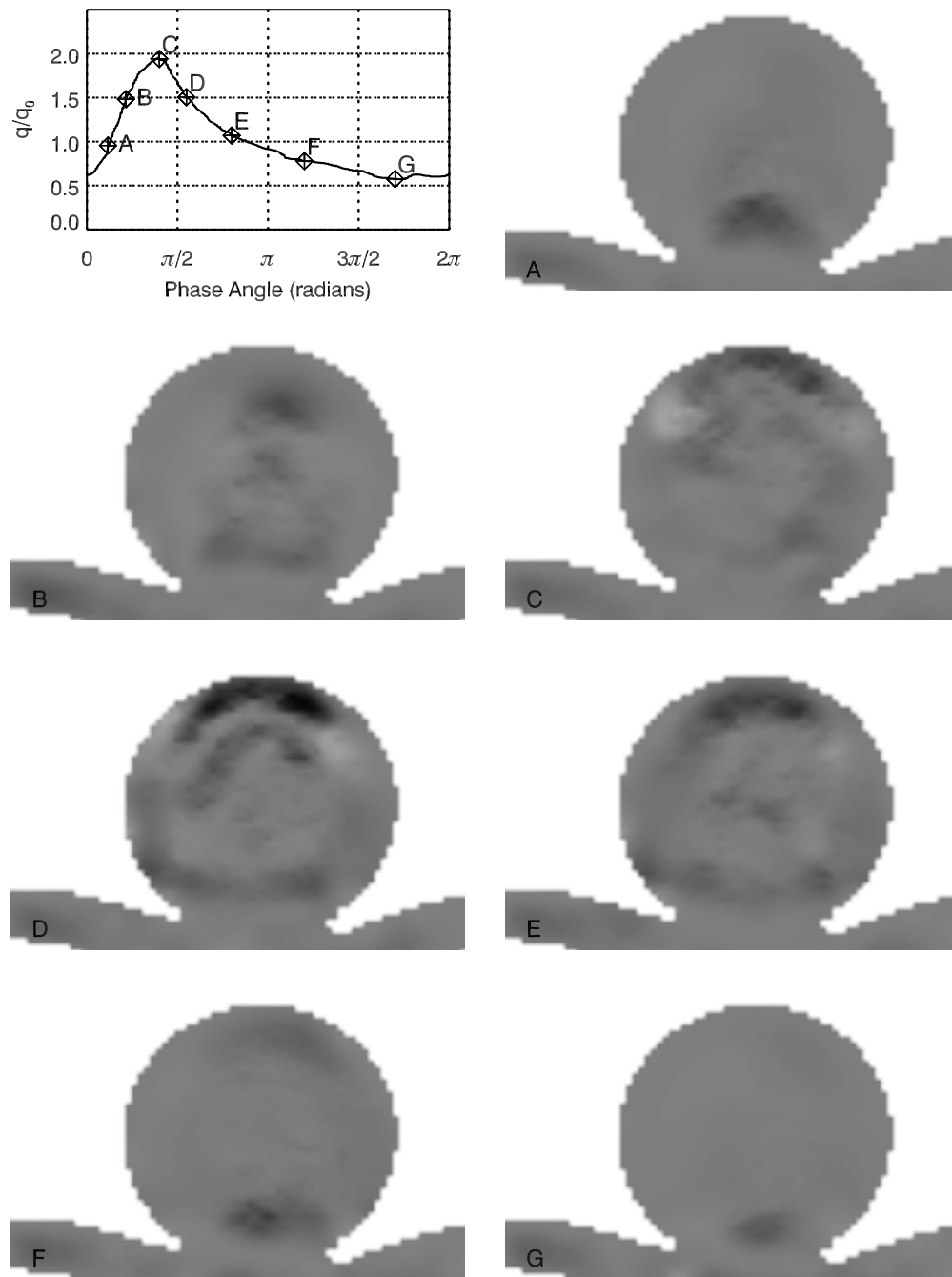


Figure 4.34: Plots of the second invariant of the velocity gradient tensor for the midplane for a branching ratio of 48:52 over one cycle indicated by the points on the waveform cycle.

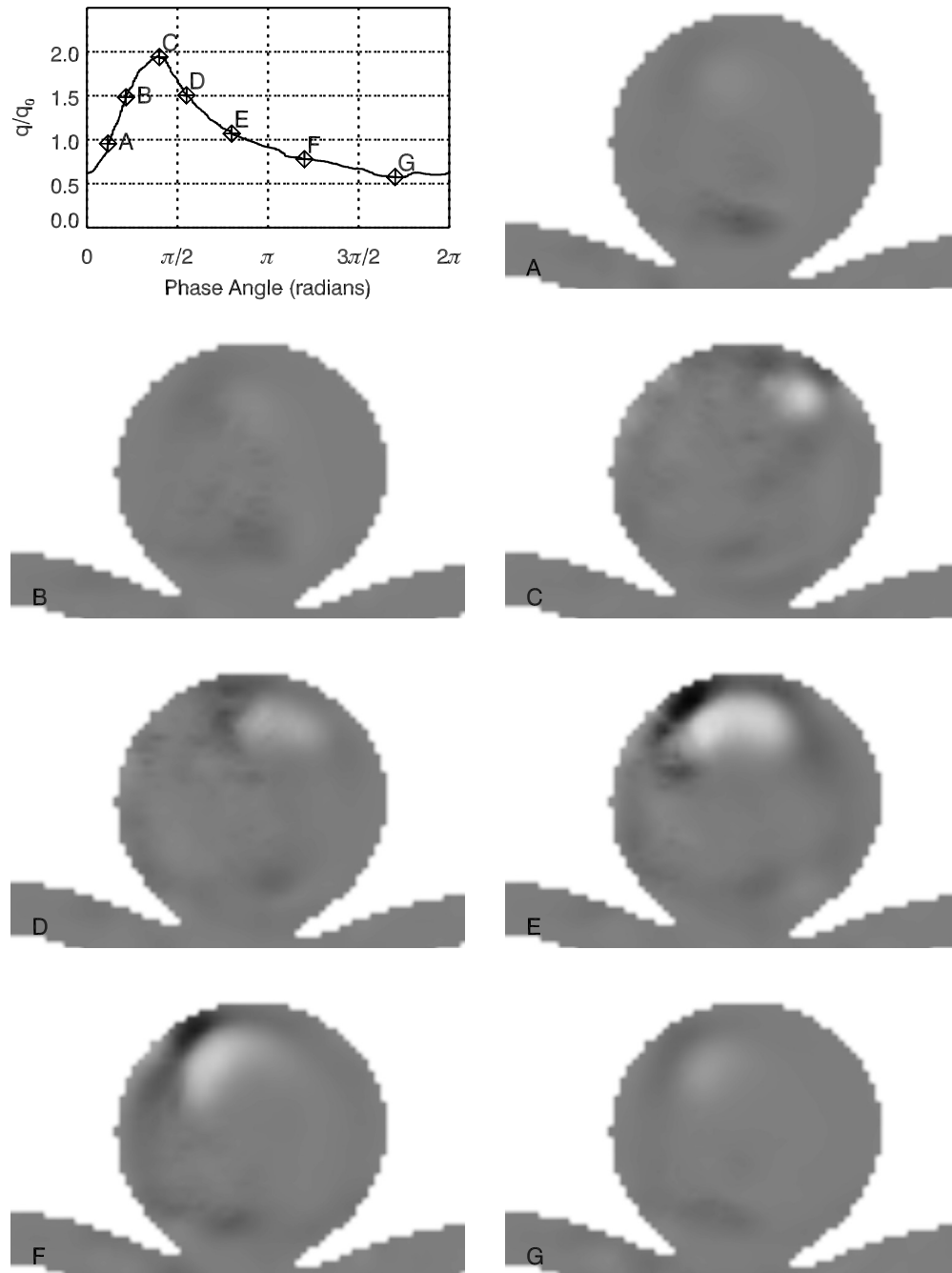


Figure 4.35: Plots of the second invariant of the velocity gradient tensor for the midplane for a branching ratio of 50:50 over one cycle indicated by the points on the waveform cycle.

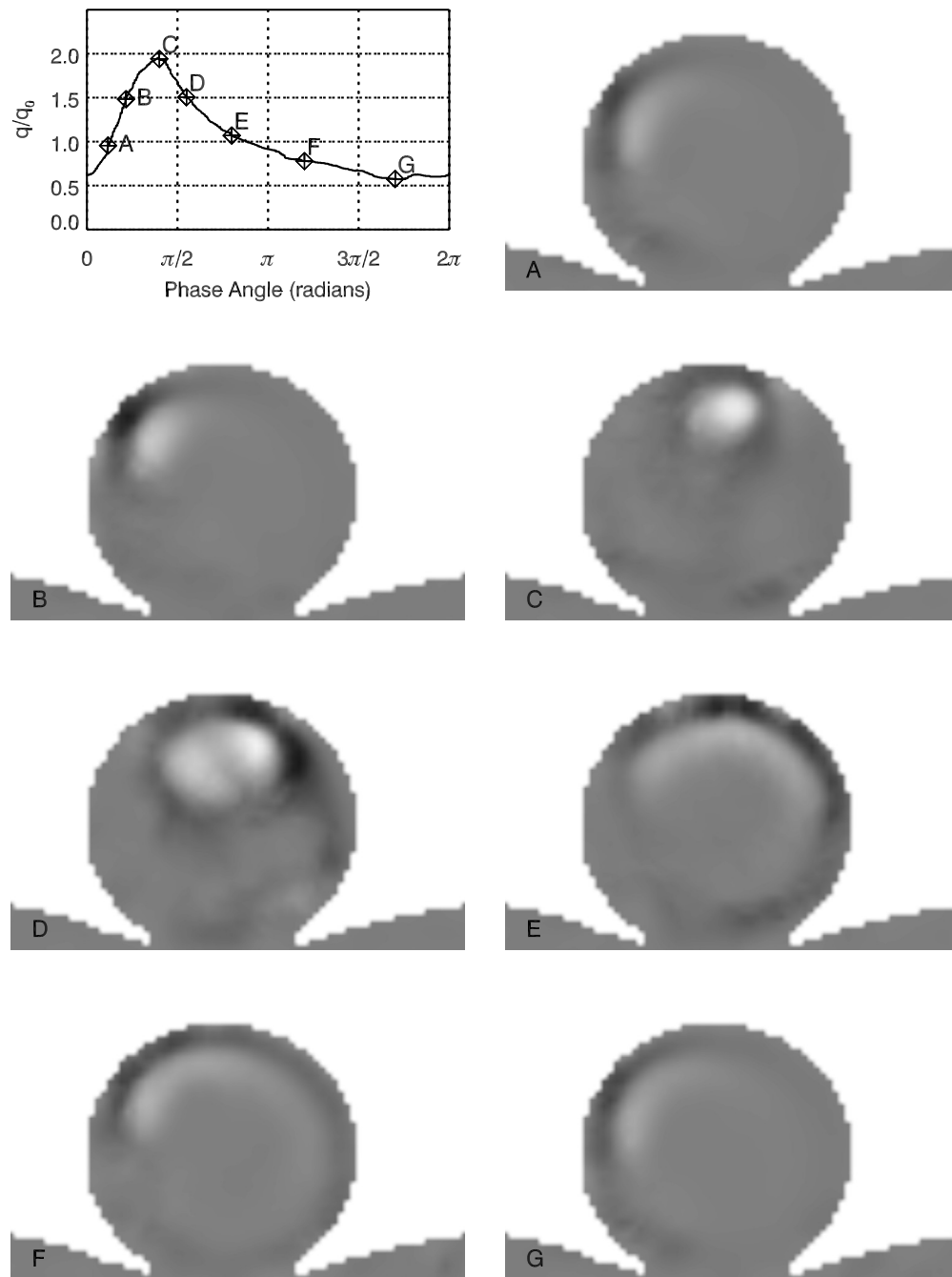


Figure 4.36: Plots of the second invariant of the velocity gradient tensor for the midplane for a branching ratio of 67:33 over one cycle indicated by the points on the waveform cycle.

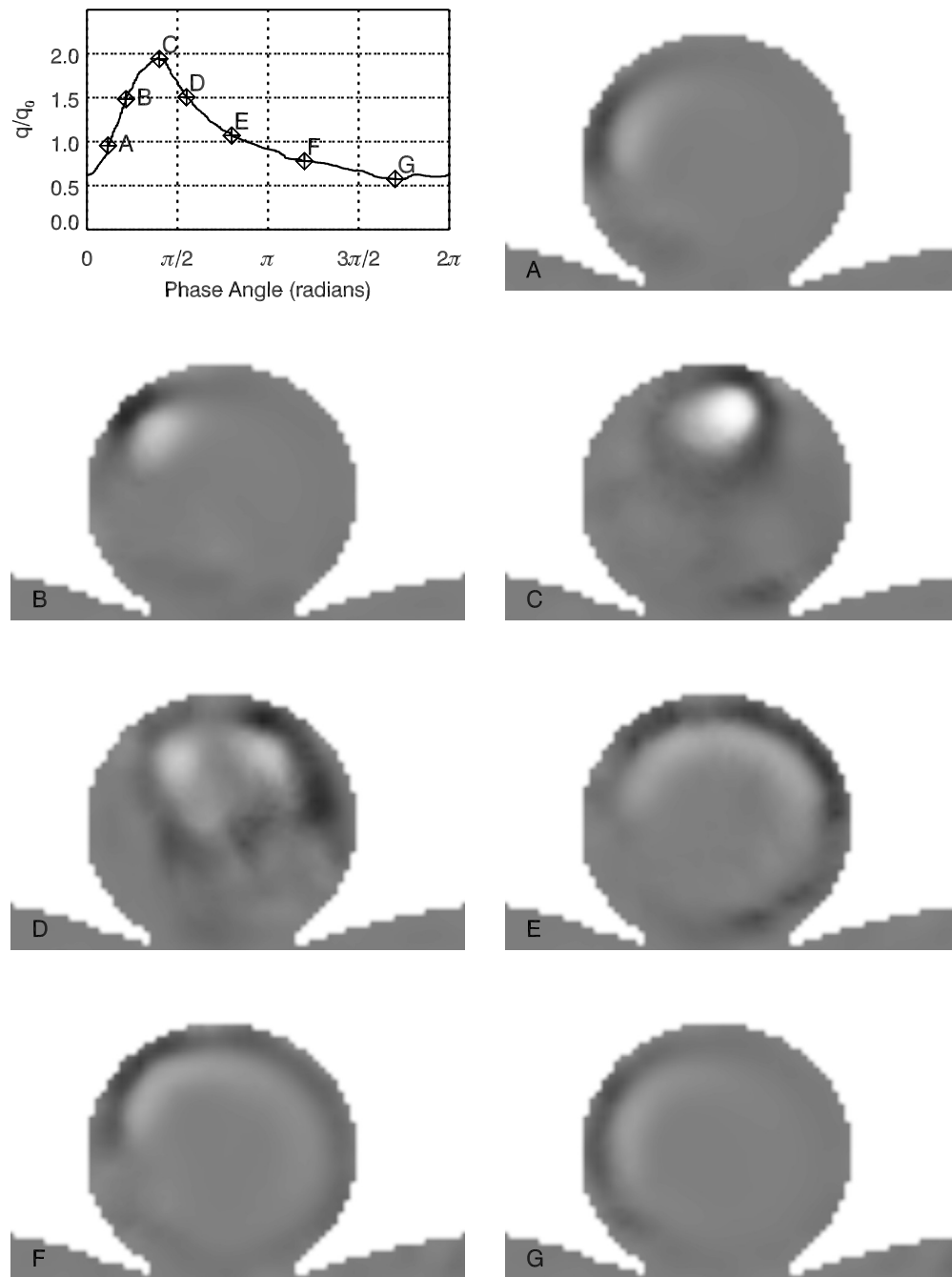


Figure 4.37: Plots of the second invariant of the velocity gradient tensor for the midplane for a branching ratio of 75:25 over one cycle indicated by the points on the waveform cycle.

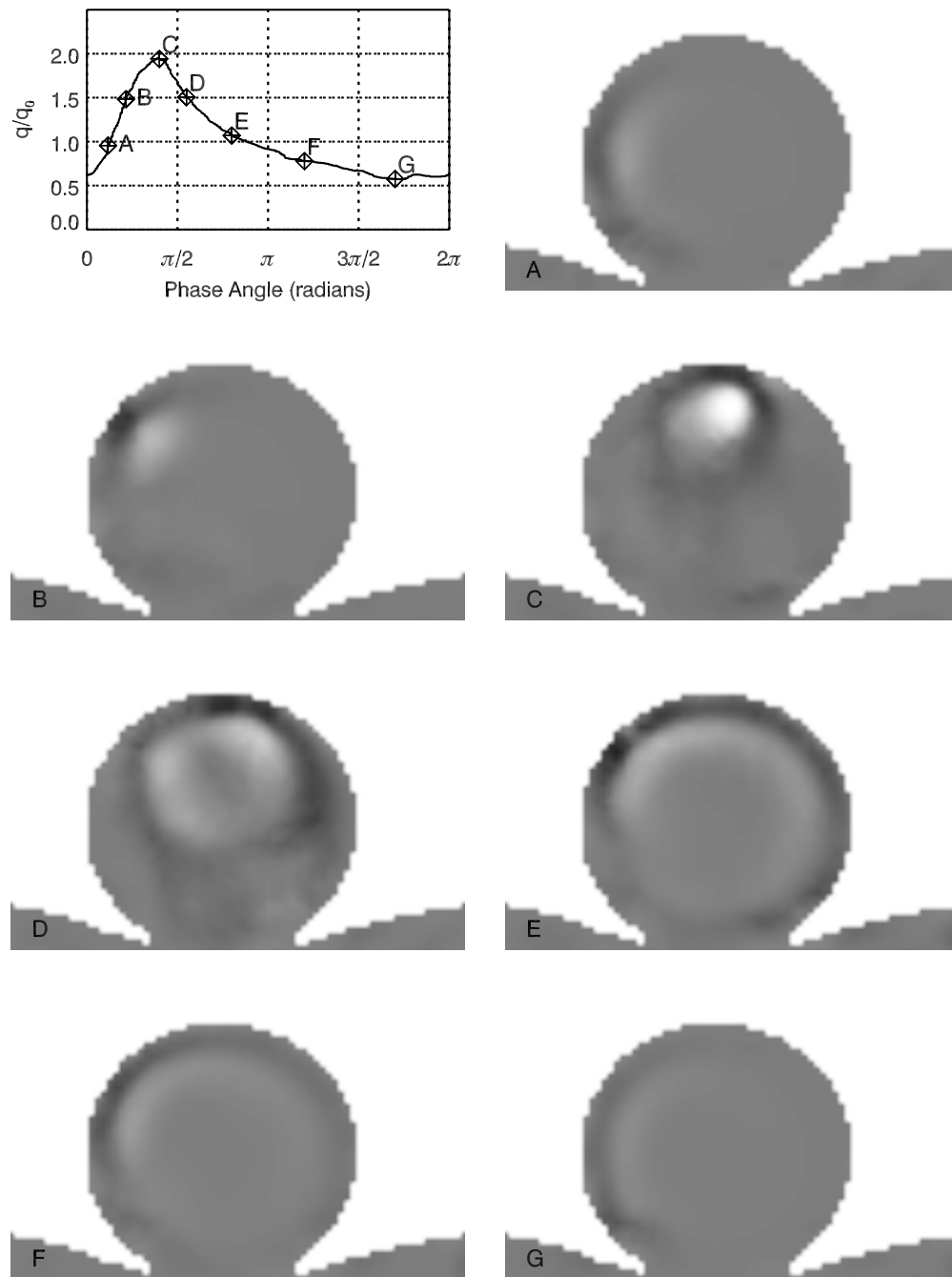


Figure 4.38: Plots of the second invariant of the velocity gradient tensor for the midplane for a branching ratio of 80:20 over one cycle indicated by the points on the waveform cycle.

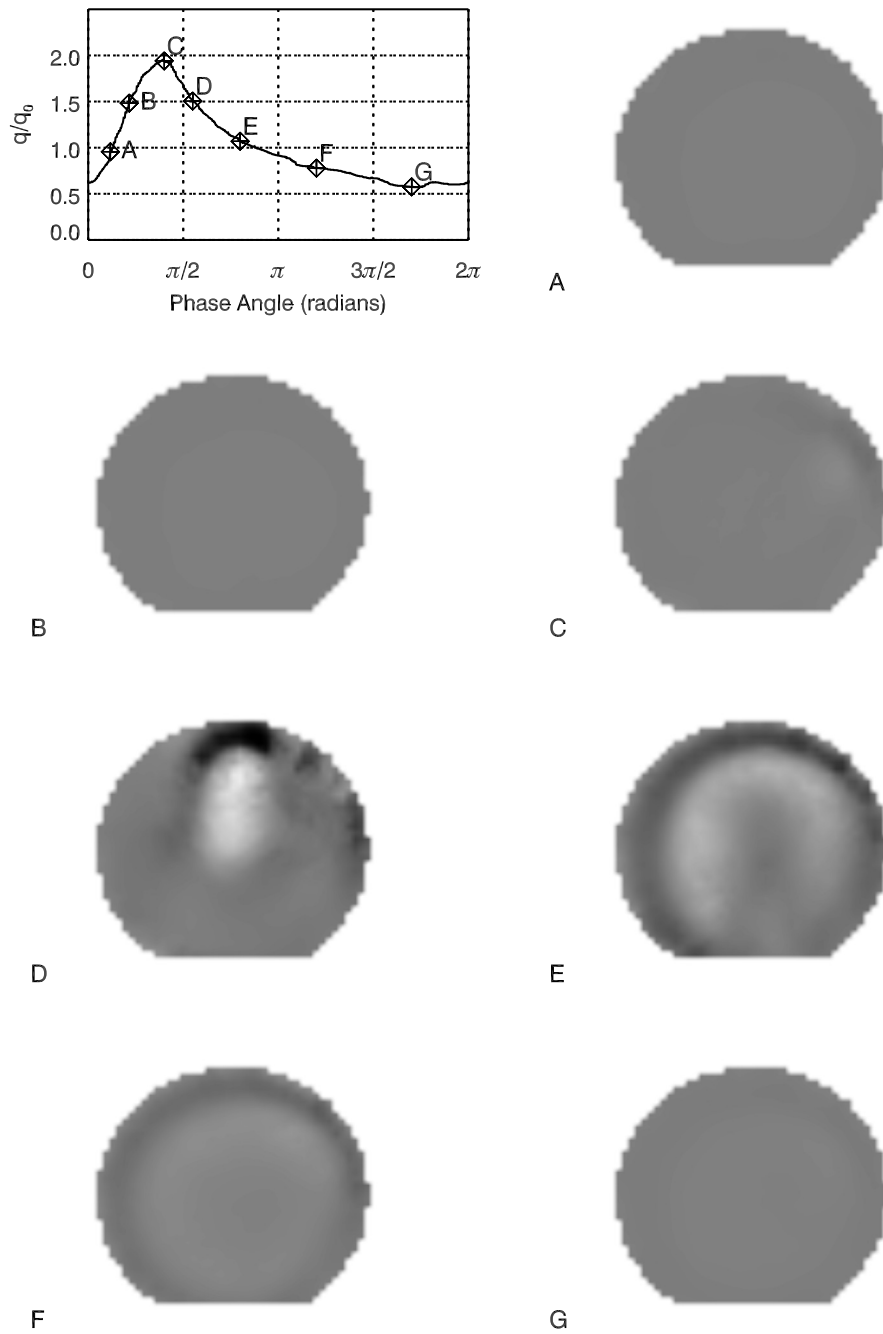


Figure 4.39: Plots of the second invariant of the velocity gradient tensor for the upper quarter-plane for a branching ratio of 20:80 over one cycle indicated by the points on the waveform cycle.

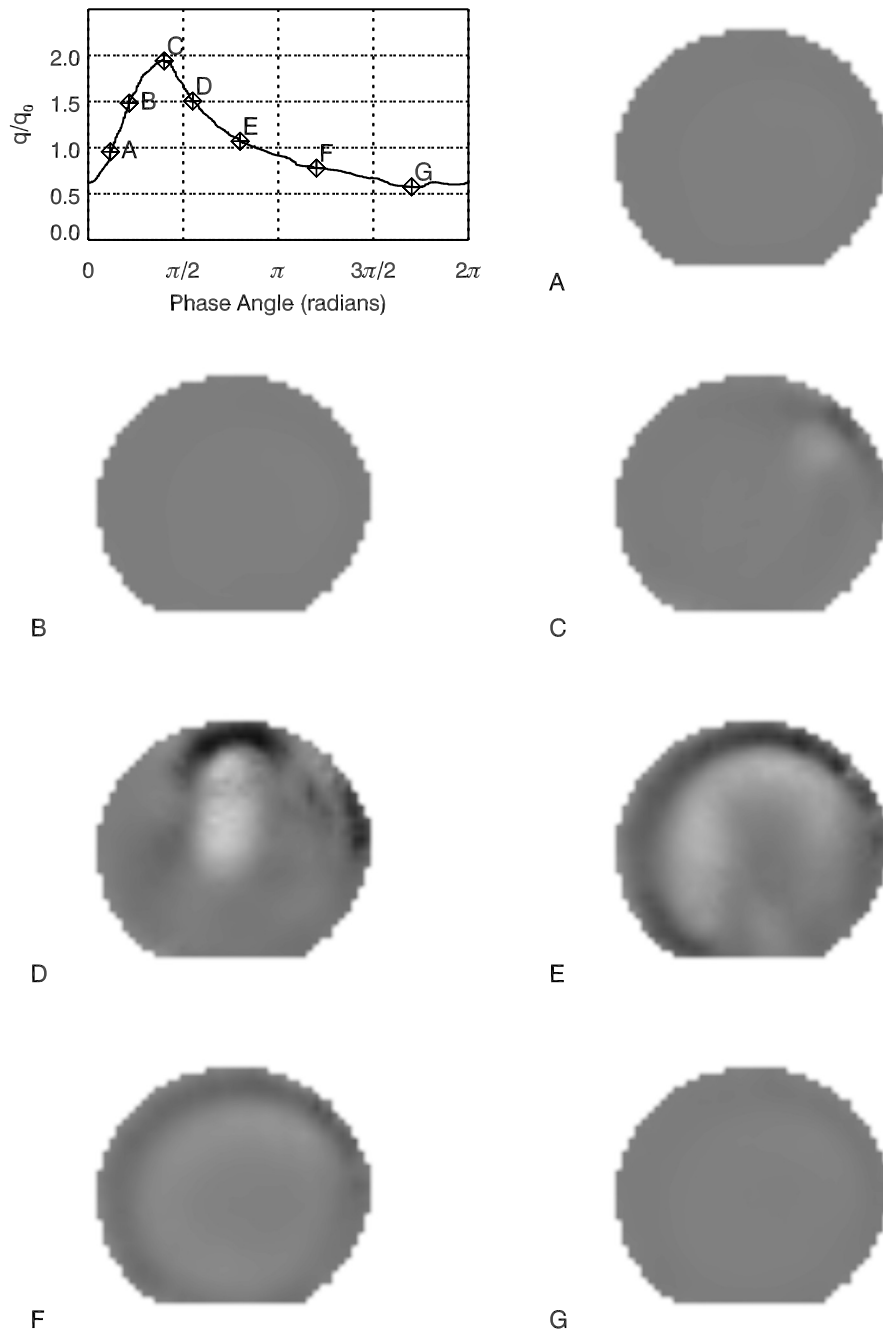


Figure 4.40: Plots of the second invariant of the velocity gradient tensor for the upper quarter-plane for a branching ratio of 25:75 over one cycle indicated by the points on the waveform cycle.

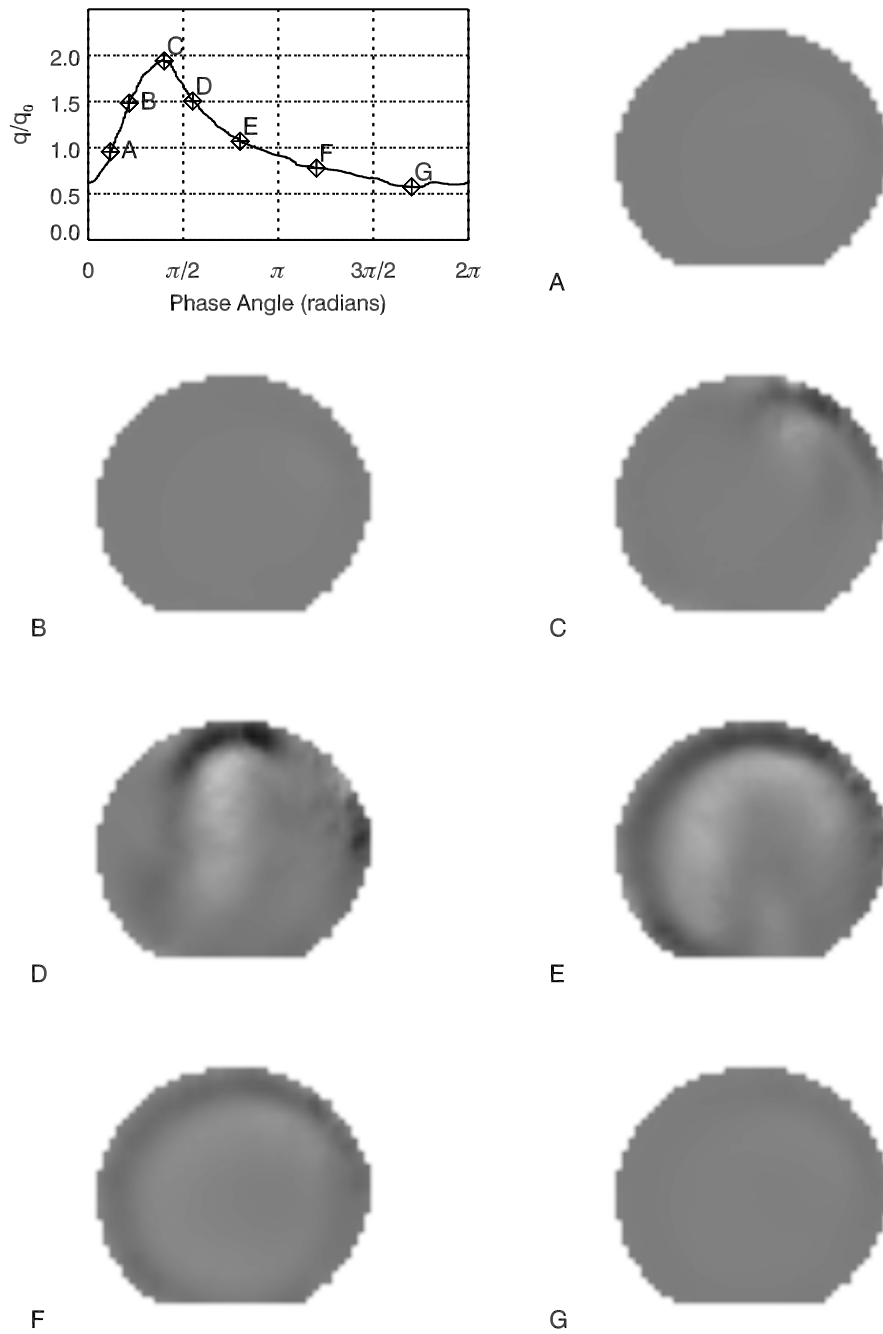


Figure 4.41: Plots of the second invariant of the velocity gradient tensor for the upper quarter-plane for a branching ratio of 33:67 over one cycle indicated by the points on the waveform cycle.

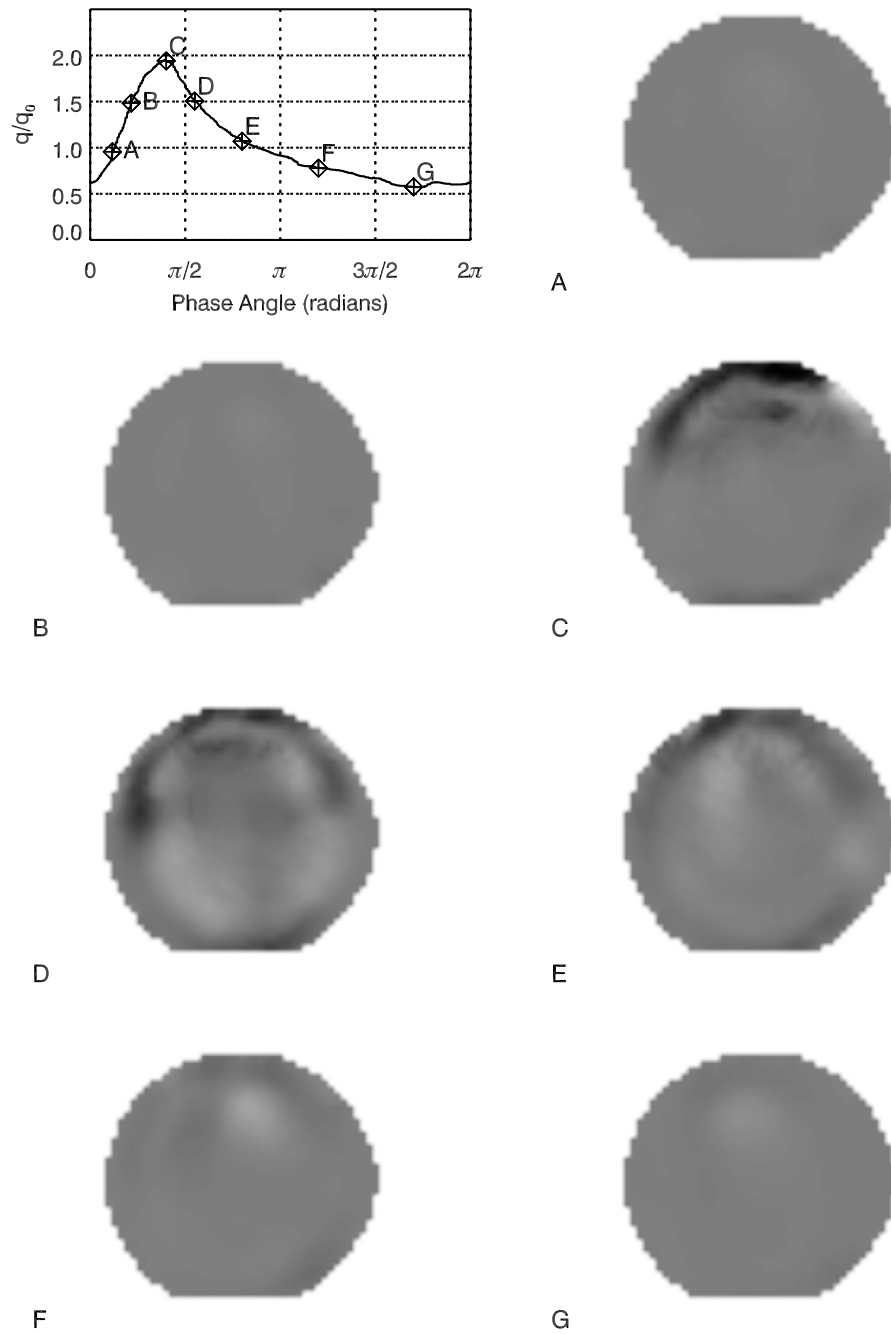


Figure 4.42: Plots of the second invariant of the velocity gradient tensor for the upper quarter-plane for a branching ratio of 46:54 over one cycle indicated by the points on the waveform cycle.

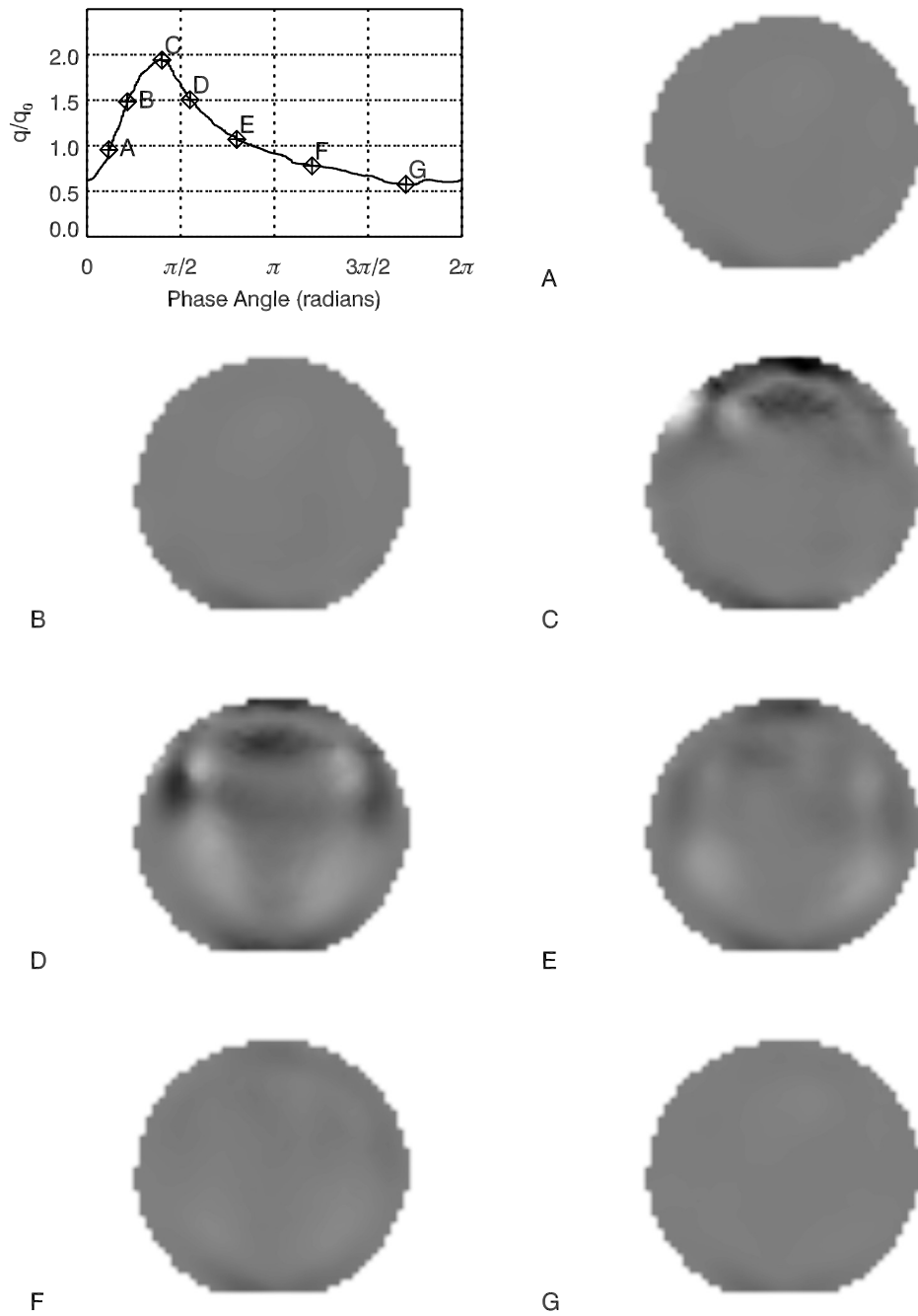


Figure 4.43: Plots of the second invariant of the velocity gradient tensor for the upper quarter-plane for a branching ratio of 48:52 over one cycle indicated by the points on the waveform cycle.

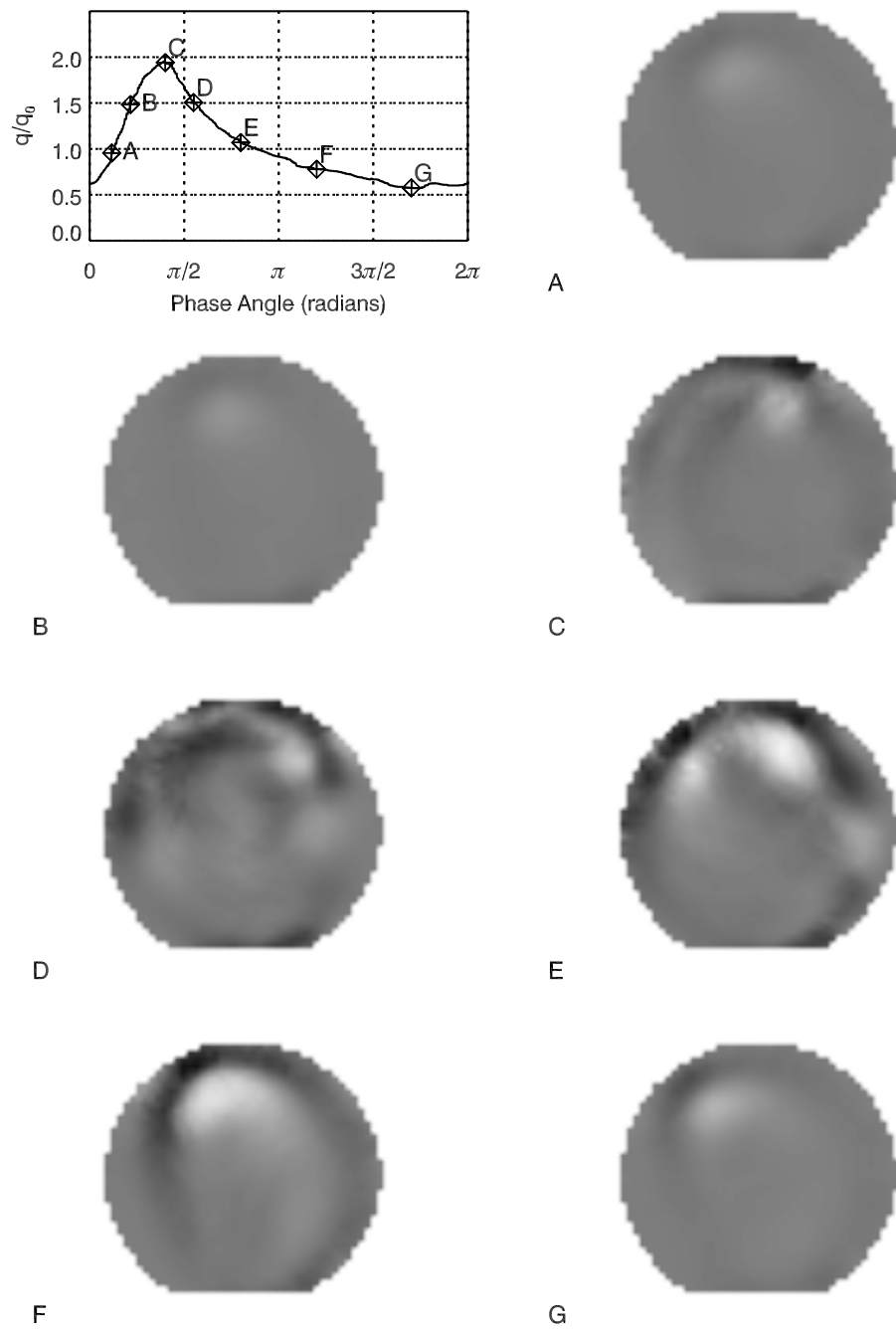


Figure 4.44: Plots of the second invariant of the velocity gradient tensor for the upper quarter-plane for a branching ratio of 50:50 over one cycle indicated by the points on the waveform cycle.

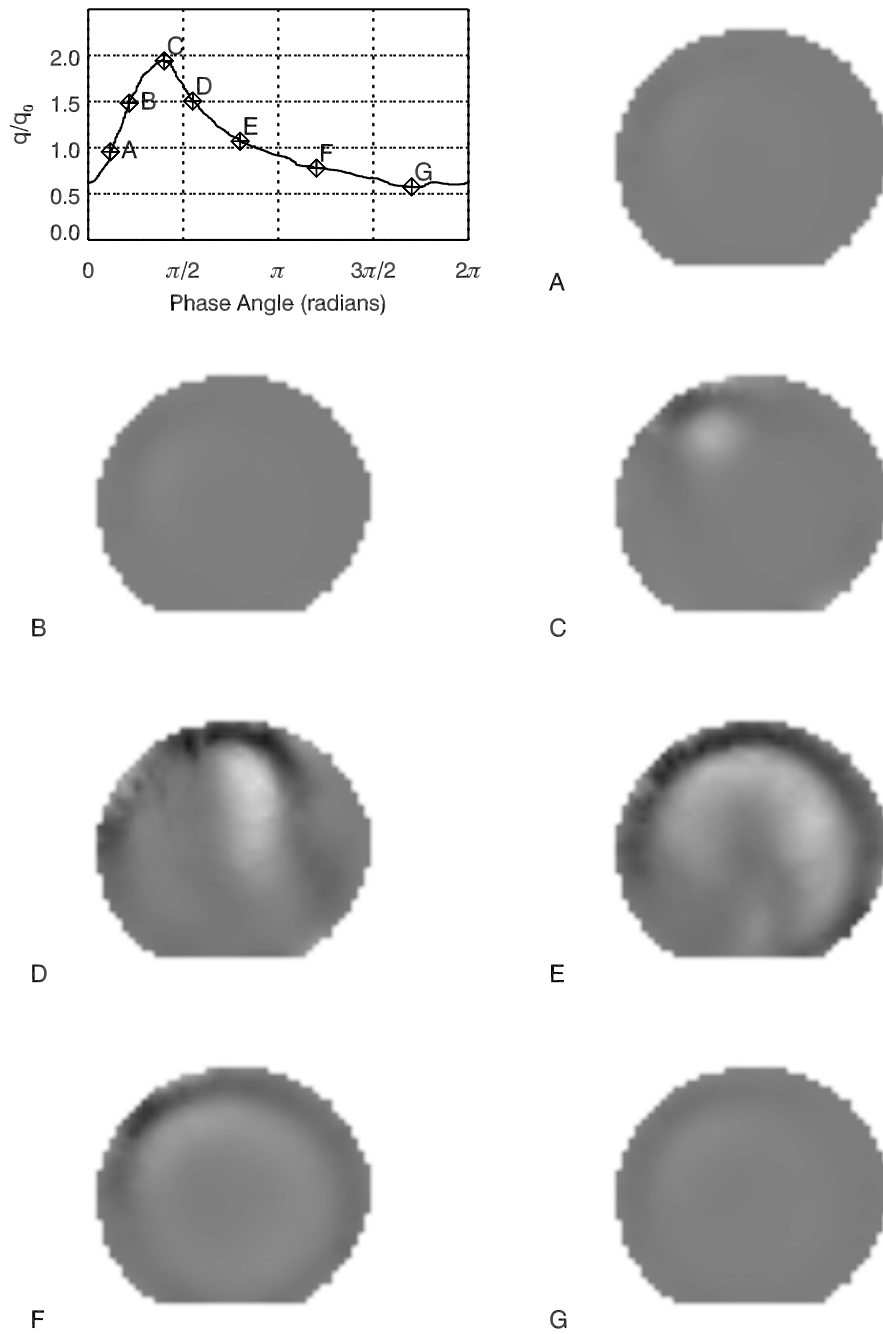


Figure 4.45: Plots of the second invariant of the velocity gradient tensor for the upper quarter-plane for a branching ratio of 67:33 over one cycle indicated by the points on the waveform cycle.

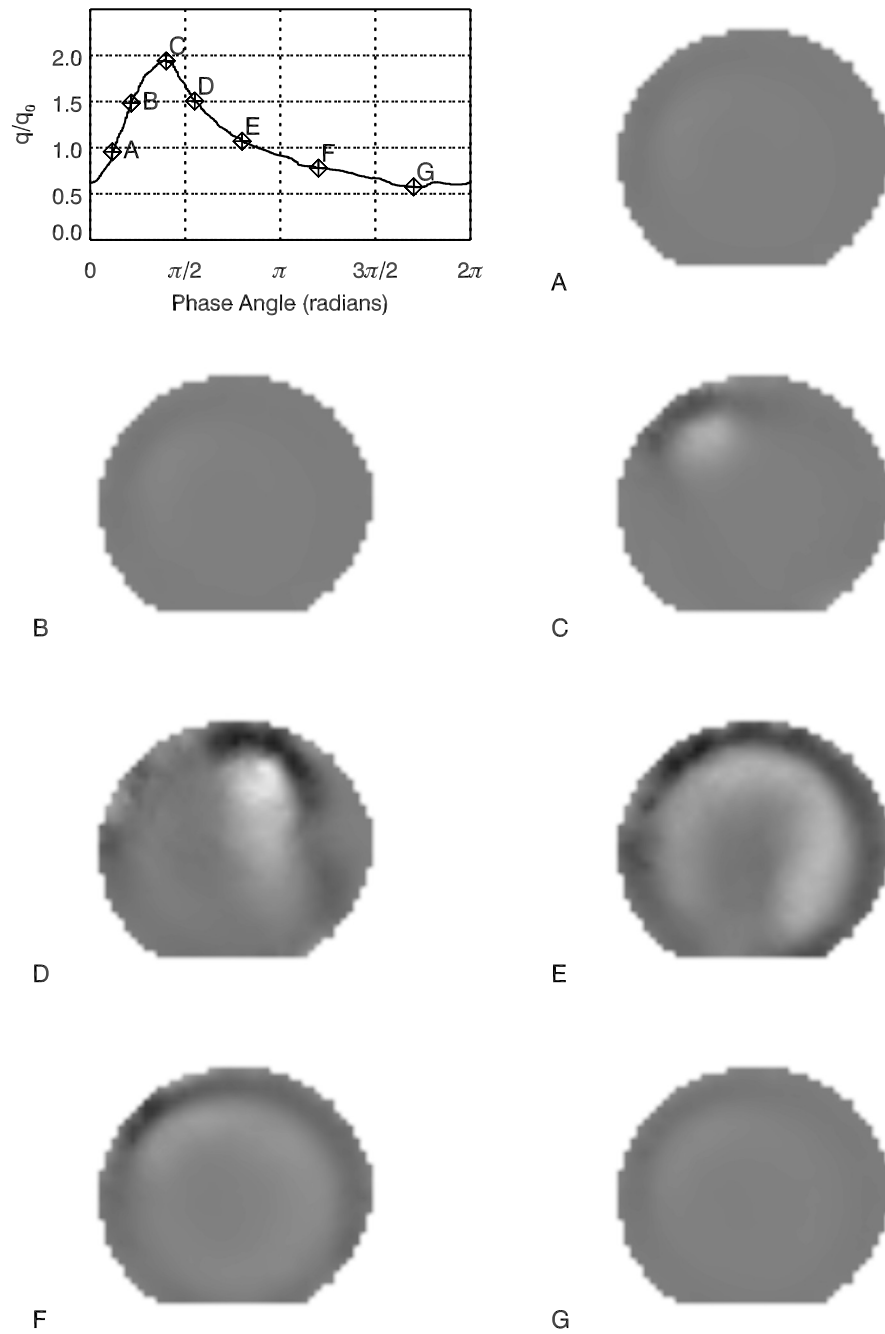


Figure 4.46: Plots of the second invariant of the velocity gradient tensor for the upper quarter-plane for a branching ratio of 75:25 over one cycle indicated by the points on the waveform cycle.

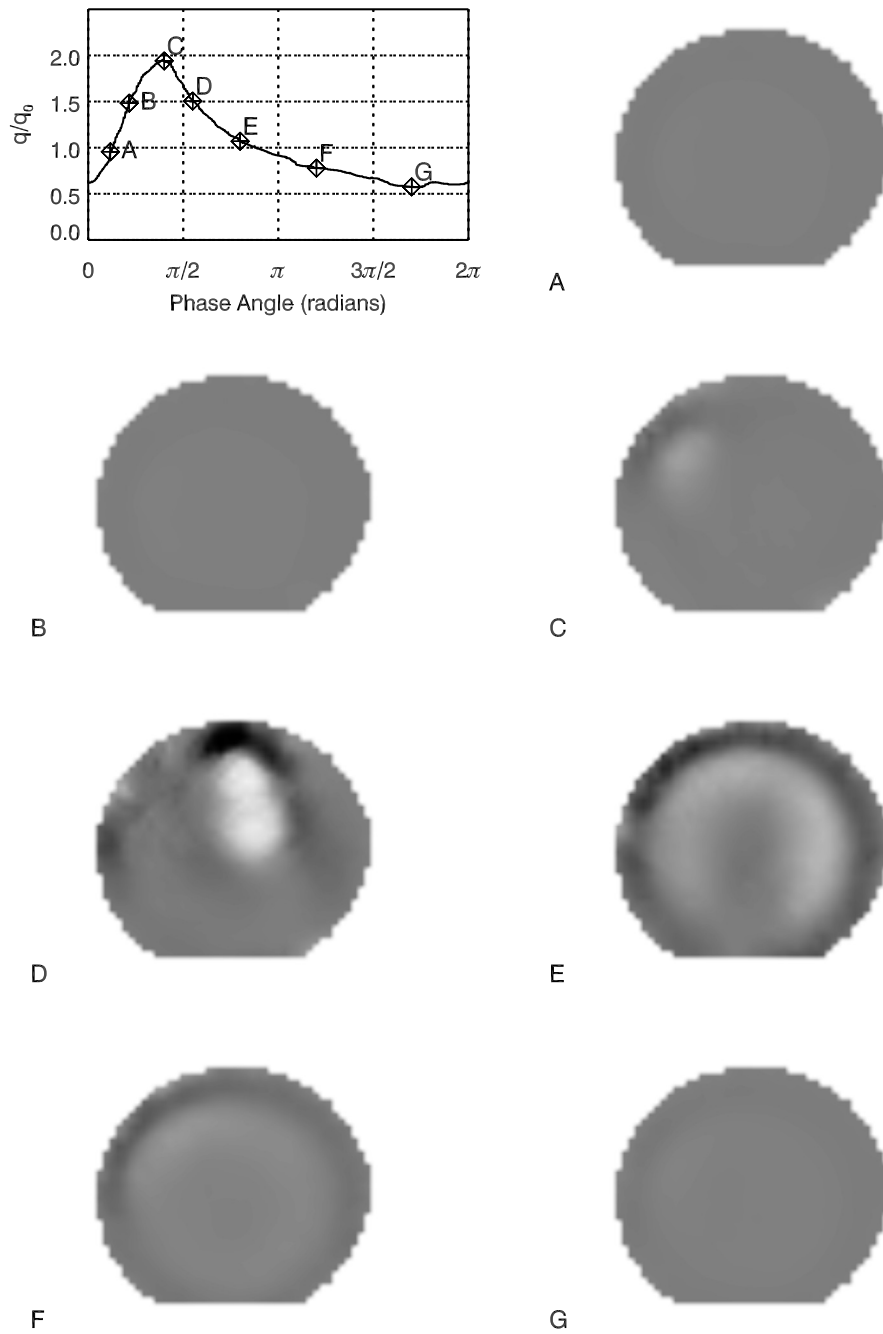


Figure 4.47: Plots of the second invariant of the velocity gradient tensor for the upper quarter-plane for a branching ratio of 80:20 over one cycle indicated by the points on the waveform cycle.

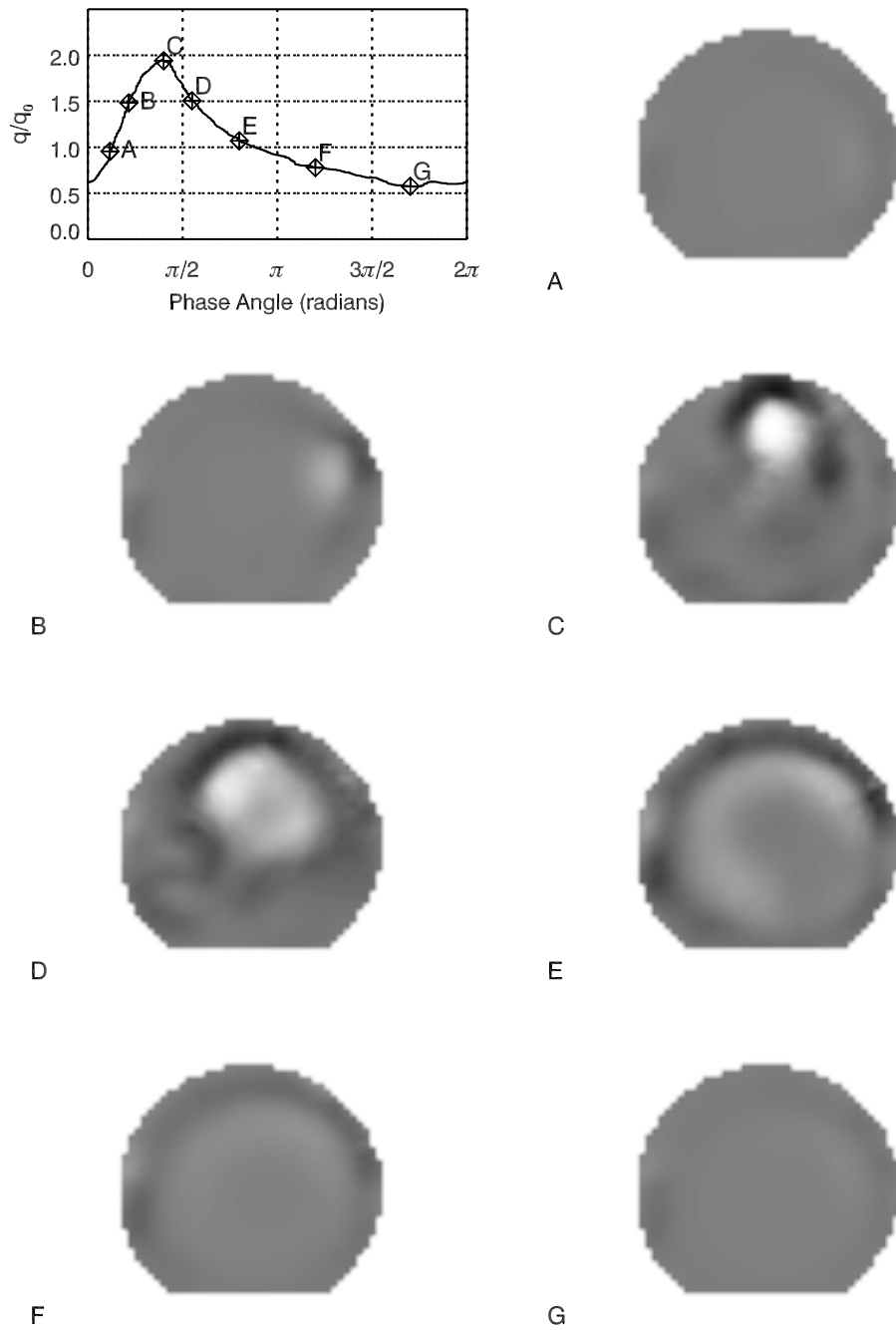


Figure 4.48: Plots of the second invariant of the velocity gradient tensor for the lower quarter-plane for a branching ratio of 20:80 over one cycle indicated by the points on the waveform cycle.

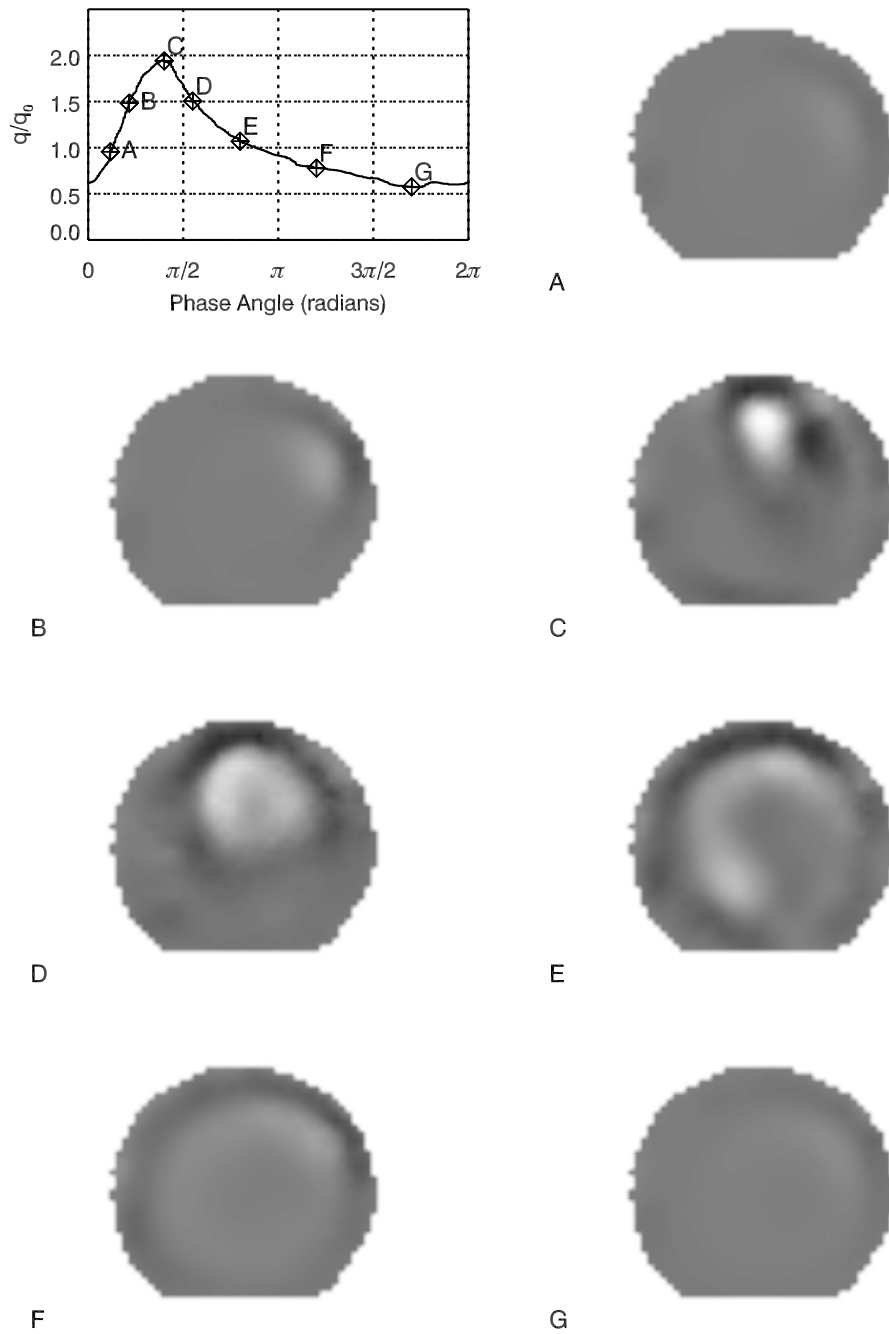


Figure 4.49: Plots of the second invariant of the velocity gradient tensor for the lower quarter-plane for a branching ratio of 25:75 over one cycle indicated by the points on the waveform cycle.

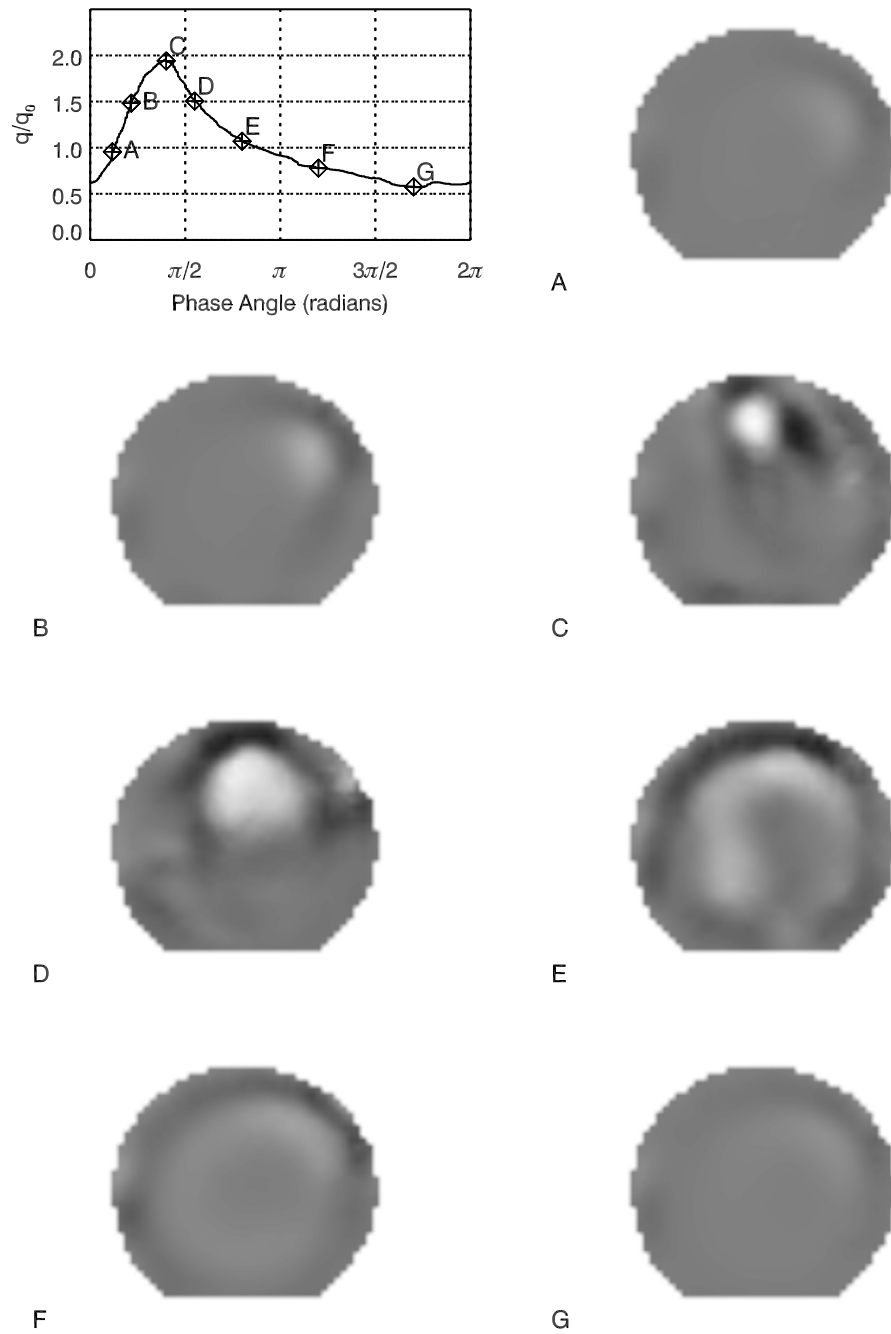


Figure 4.50: Plots of the second invariant of the velocity gradient tensor for the lower quarter-plane for a branching ratio of 33:67 over one cycle indicated by the points on the waveform cycle.

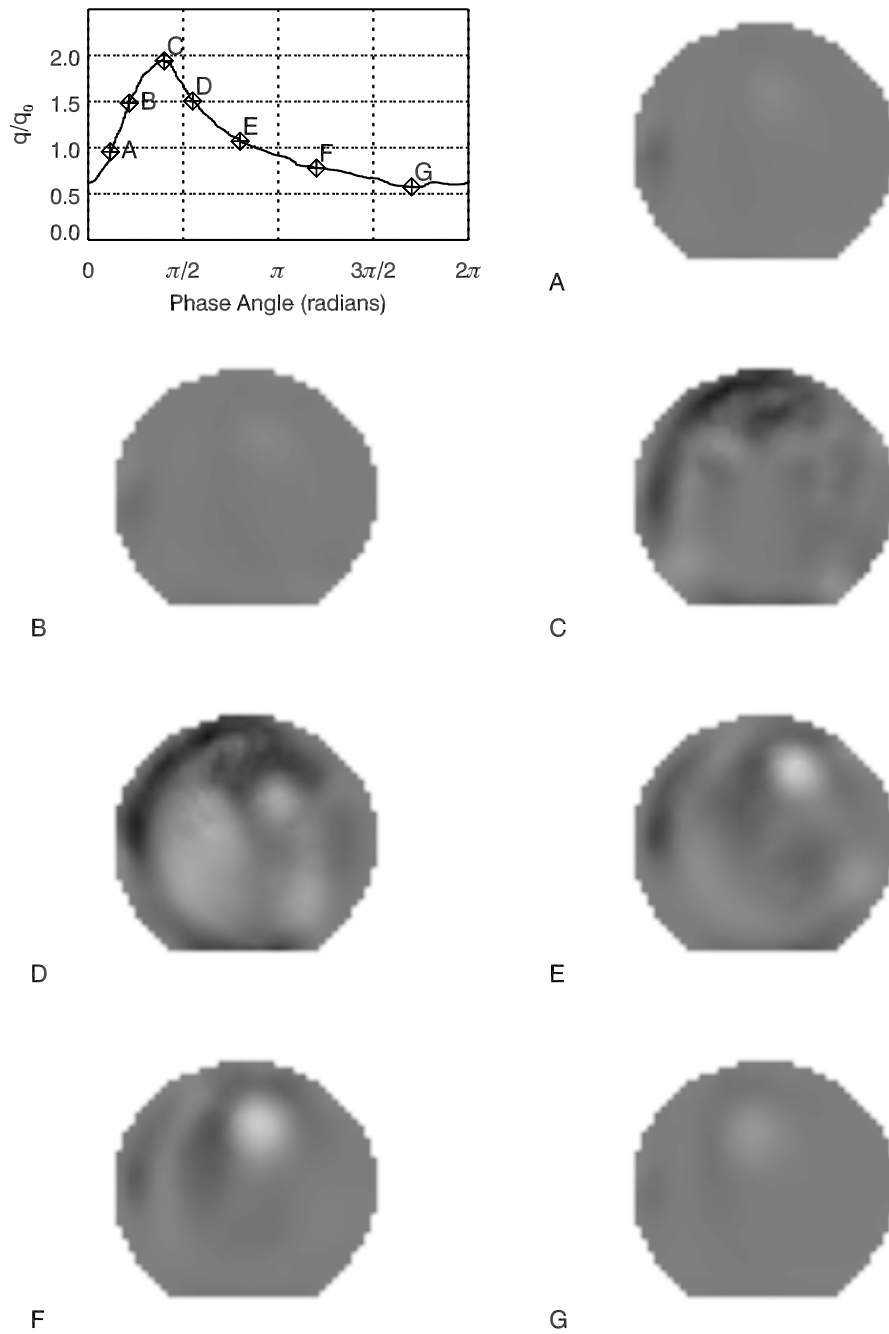


Figure 4.51: Plots of the second invariant of the velocity gradient tensor for the lower quarter-plane for a branching ratio of 46:54 over one cycle indicated by the points on the waveform cycle.

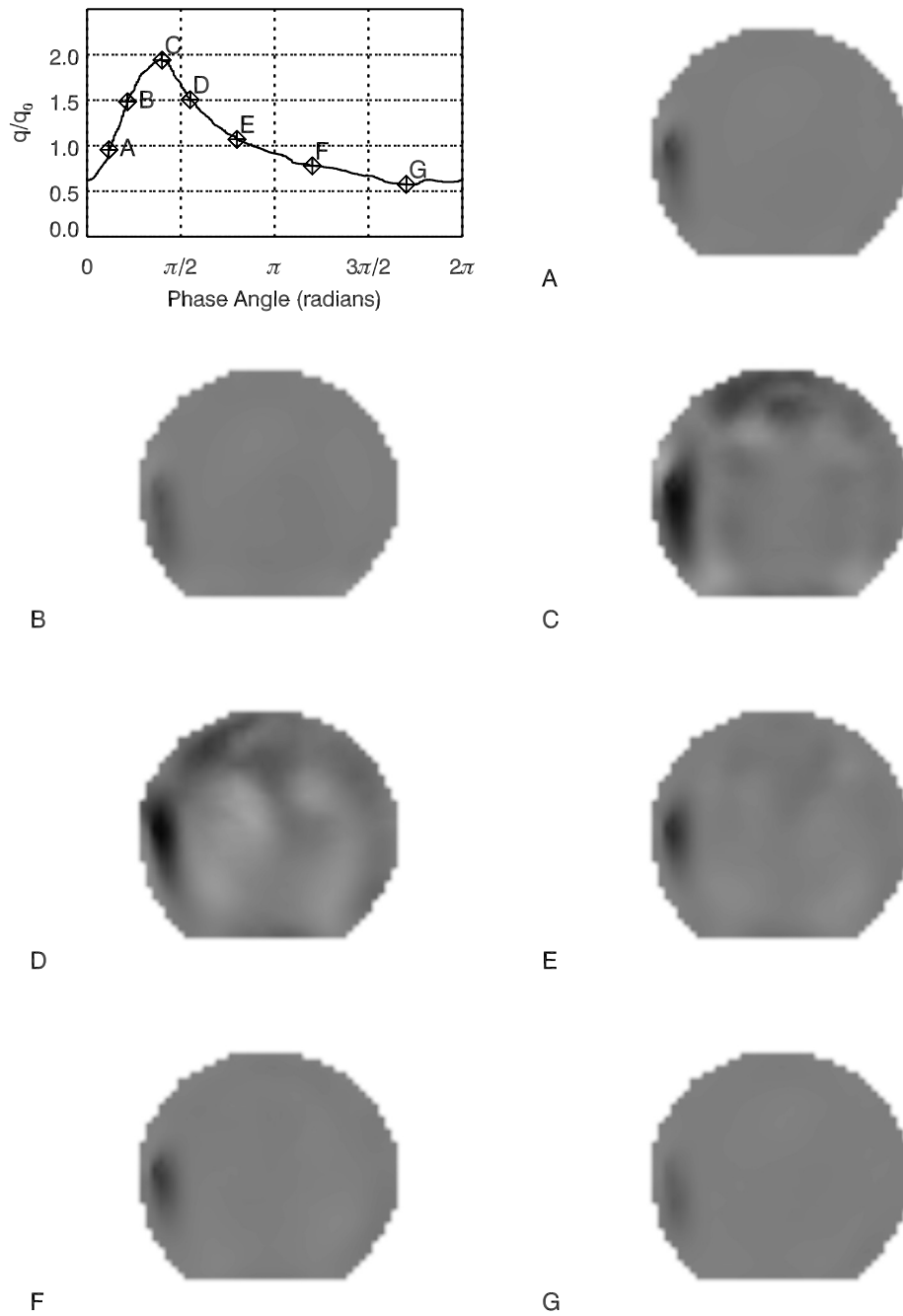


Figure 4.52: Plots of the second invariant of the velocity gradient tensor for the lower quarter-plane for a branching ratio of 48:52 over one cycle indicated by the points on the waveform cycle.

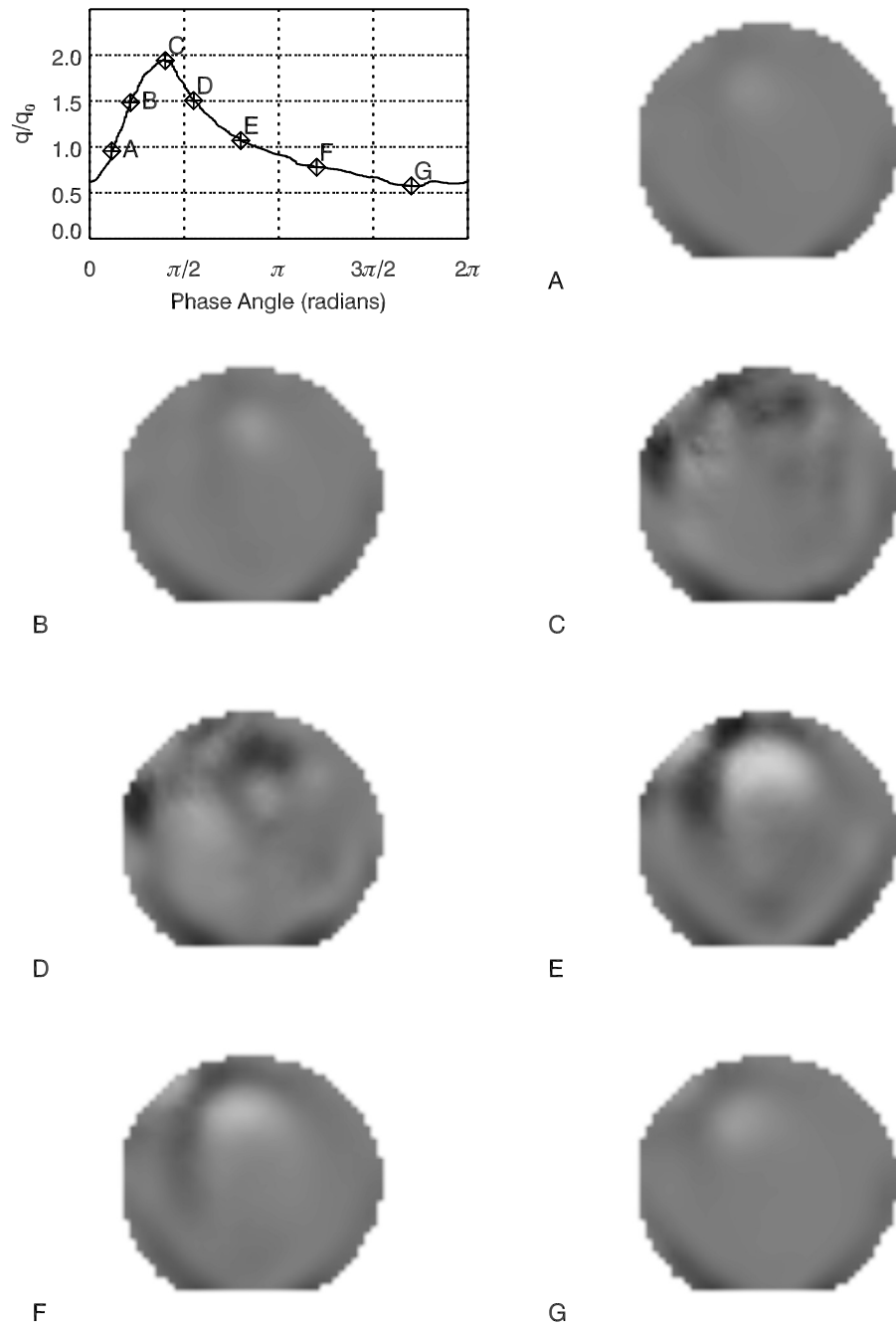


Figure 4.53: Plots of the second invariant of the velocity gradient tensor for the lower quarter-plane for a branching ratio of 50:50 over one cycle indicated by the points on the waveform cycle.

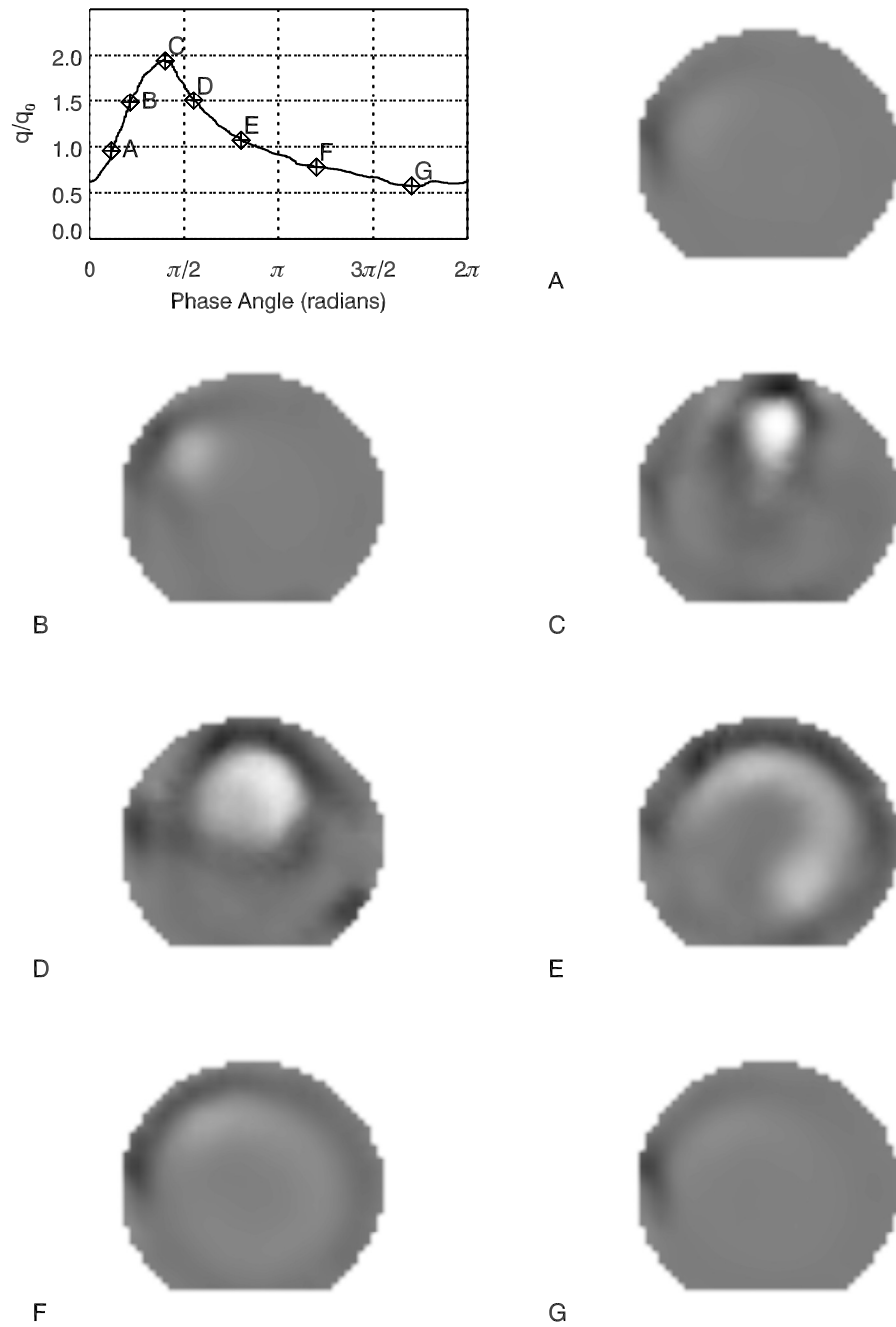


Figure 4.54: Plots of the second invariant of the velocity gradient tensor for the lower quarter-plane for a branching ratio of 67:33 over one cycle indicated by the points on the waveform cycle.

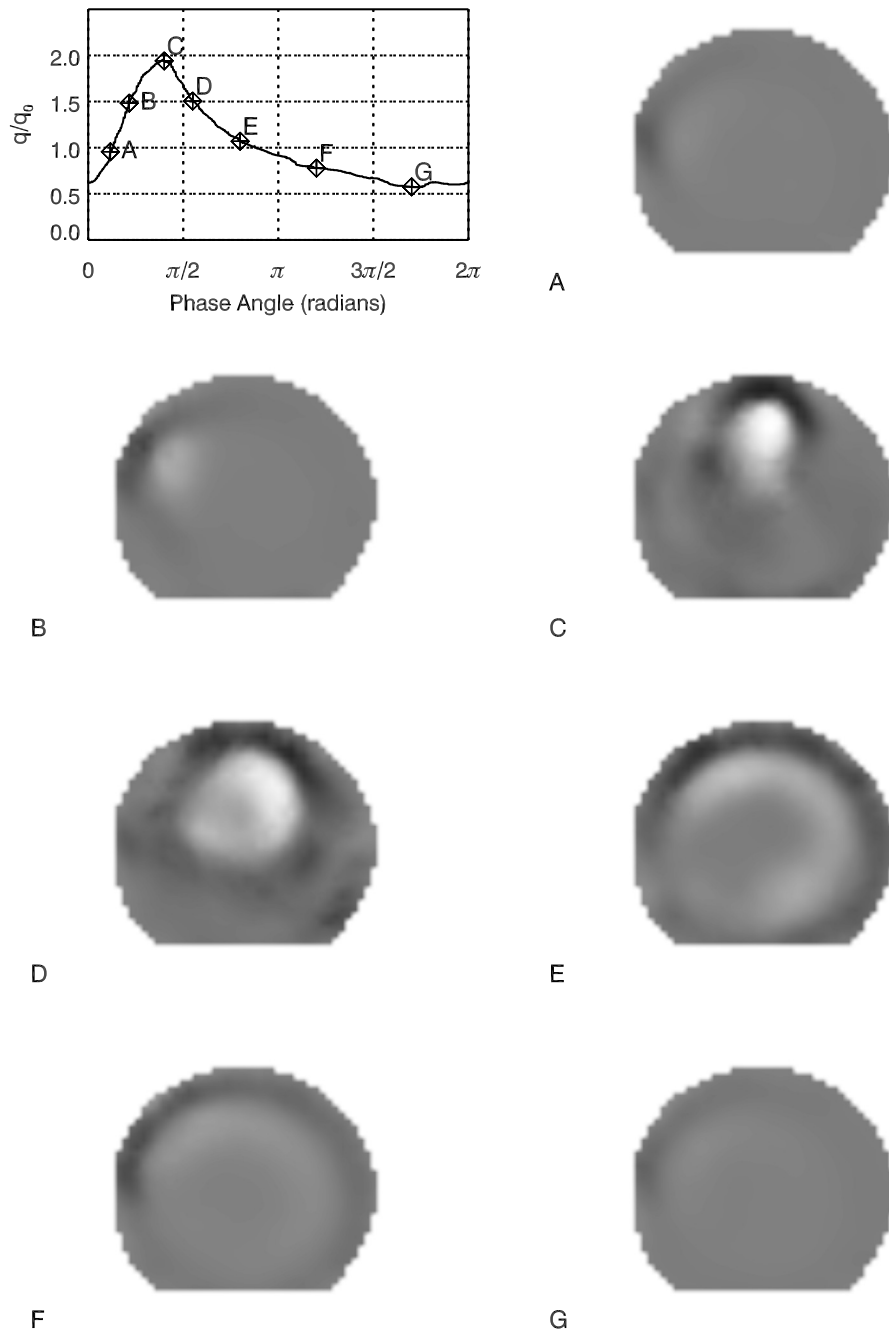


Figure 4.55: Plots of the second invariant of the velocity gradient tensor for the lower quarter-plane for a branching ratio of 75:25 over one cycle indicated by the points on the waveform cycle.

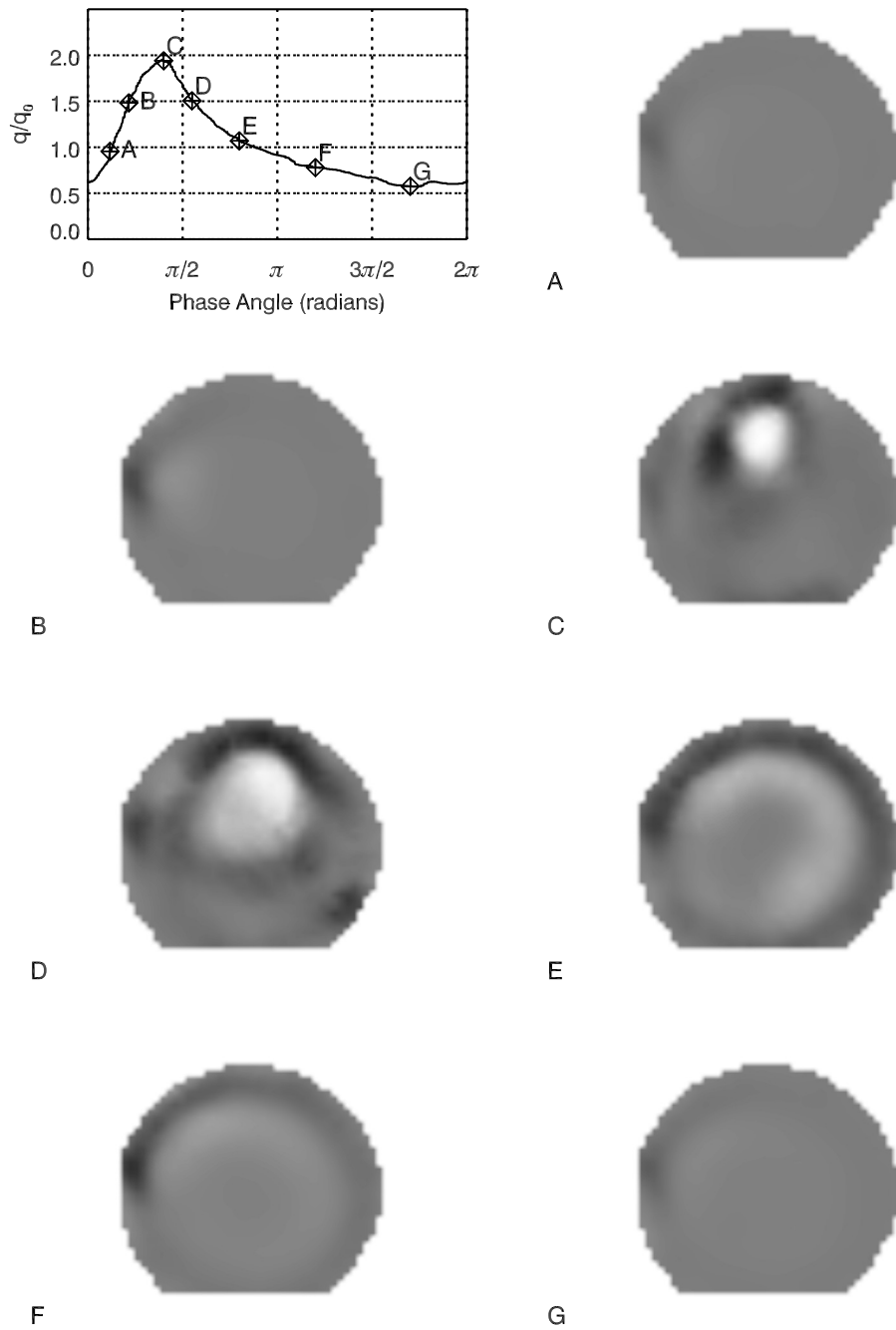


Figure 4.56: Plots of the second invariant of the velocity gradient tensor for the lower quarter-plane for a branching ratio of 80:20 over one cycle indicated by the points on the waveform cycle.

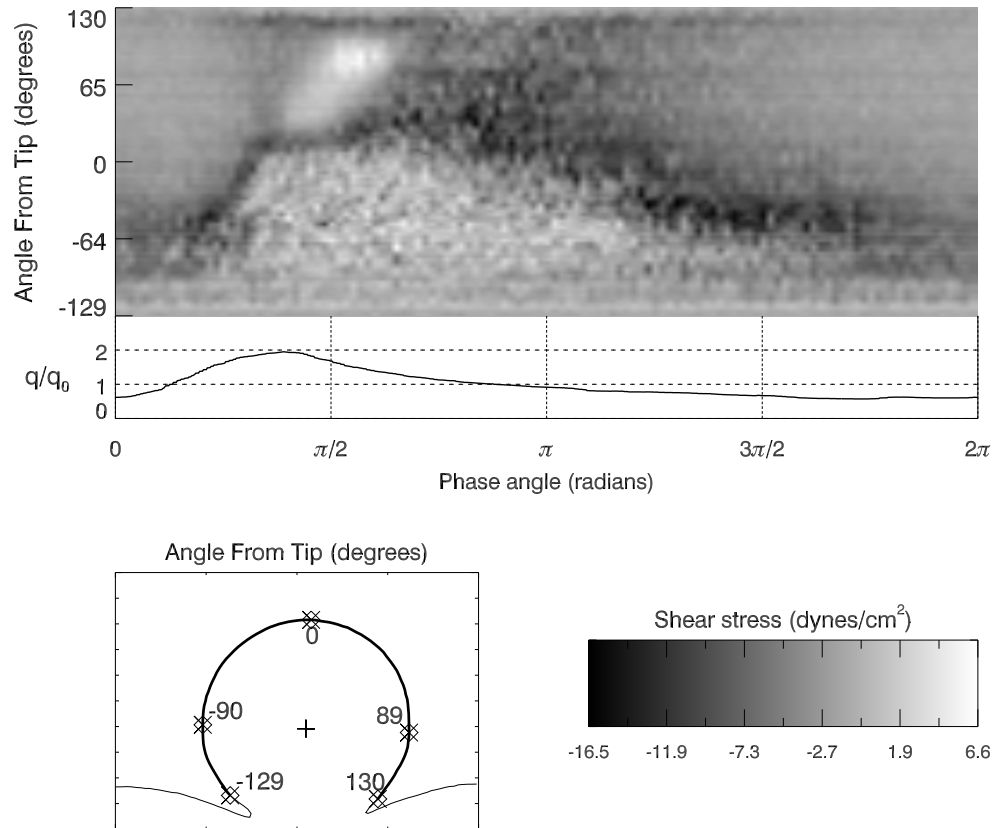


Figure 4.57: In-plane WSS history along the aneurysm dome in the midplane for a branching ratio of 20:80)

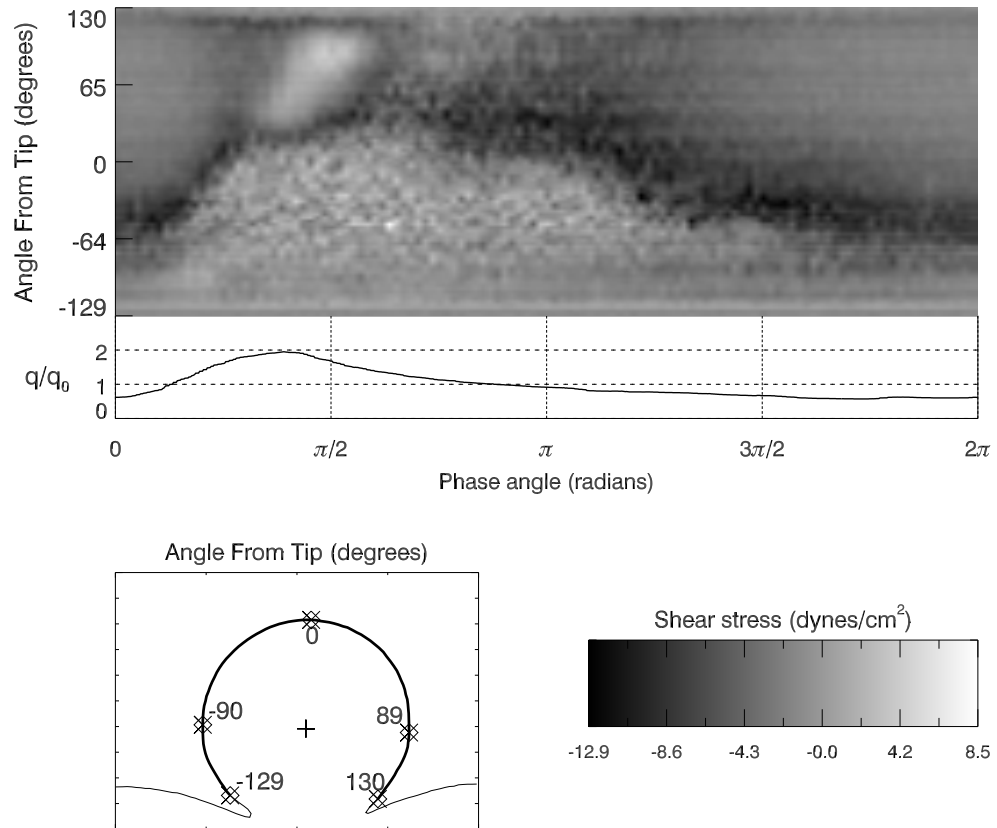


Figure 4.58: In-plane WSS history along the aneurysm dome in the midplane for a branching ratio of 25:75)

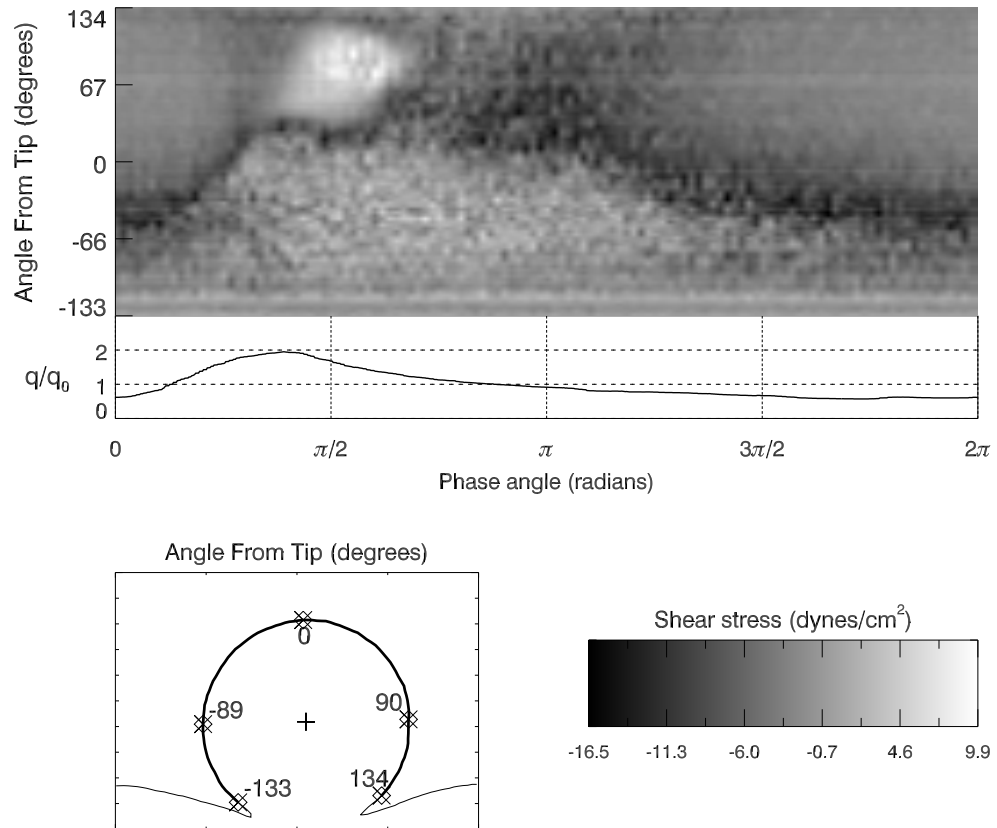


Figure 4.59: In-plane WSS history along the aneurysm dome in the midplane for a branching ratio of 33:67)

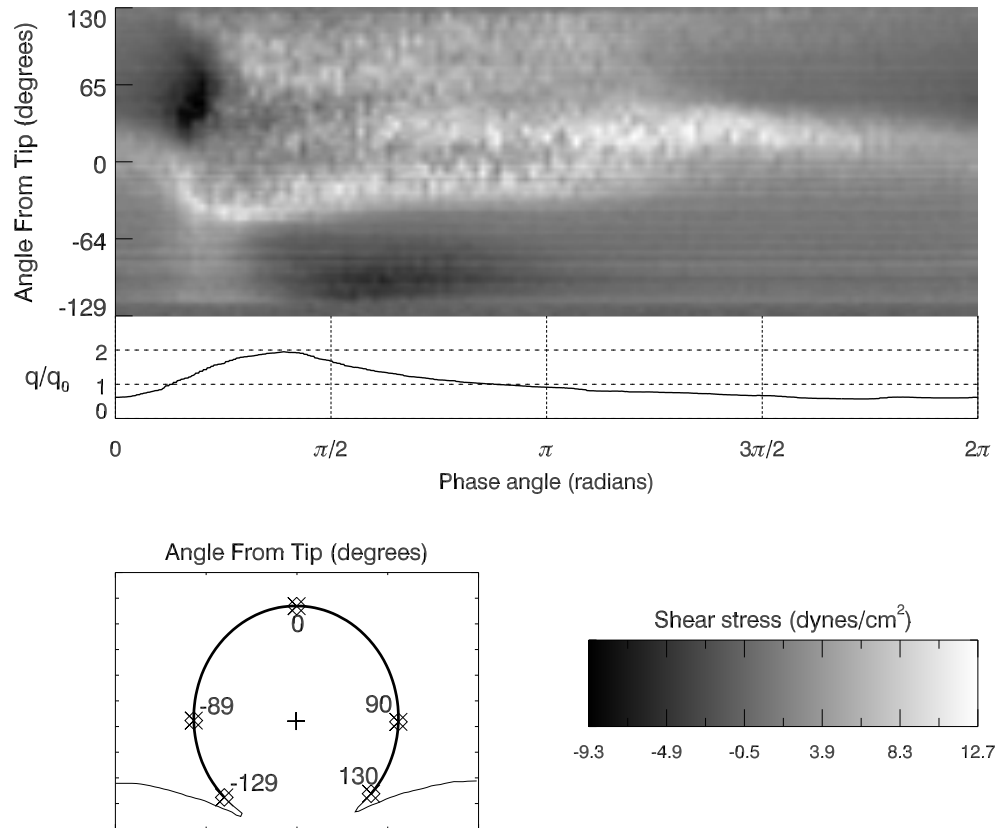


Figure 4.60: In-plane WSS history along the aneurysm dome in the midplane for a branching ratio of 46:54)

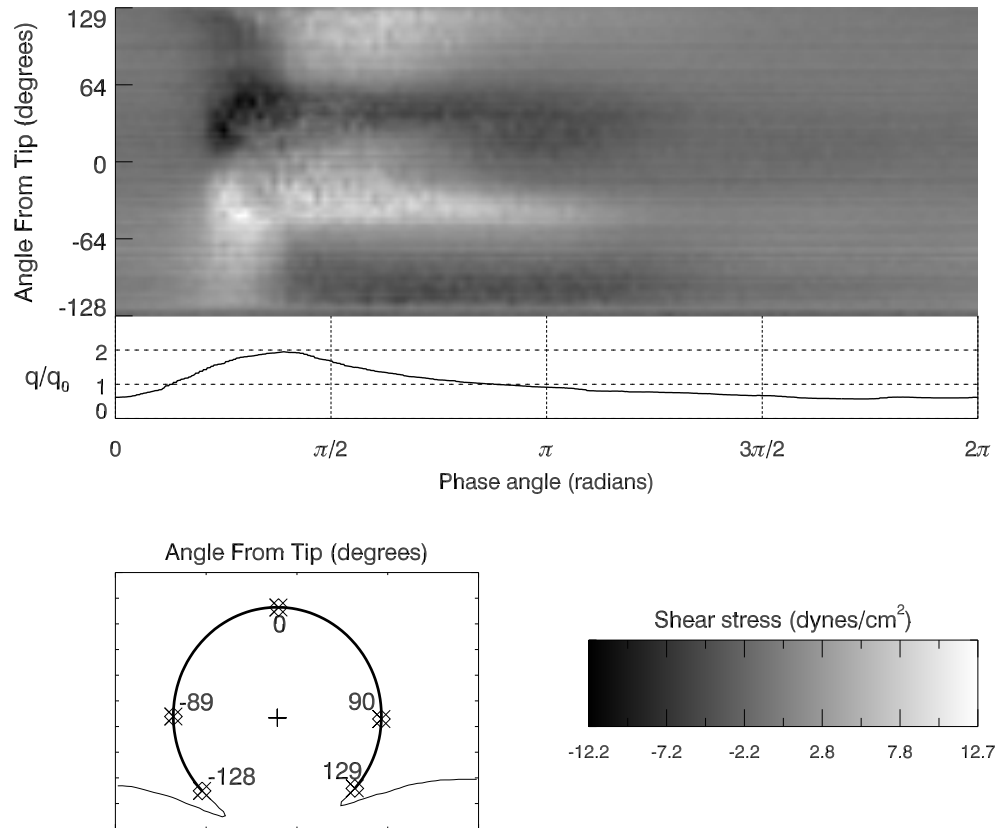


Figure 4.61: In-plane WSS history along the aneurysm dome in the midplane for a branching ratio of 48:52)

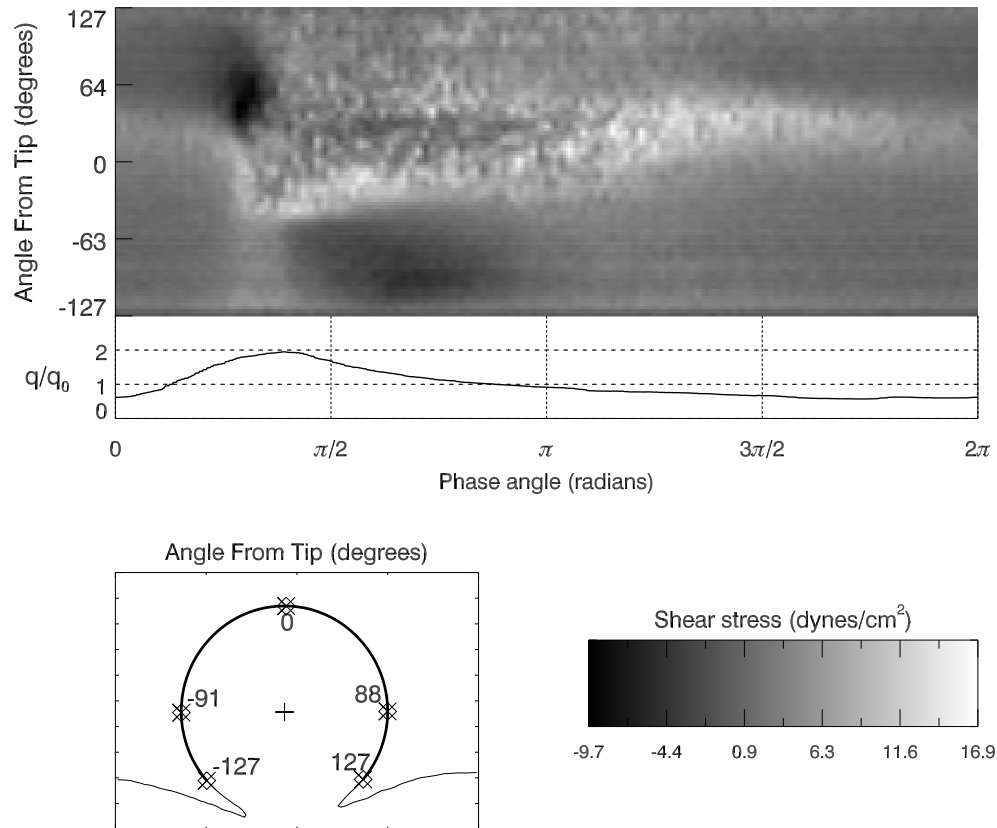


Figure 4.62: In-plane WSS history along the aneurysm dome in the midplane for a branching ratio of 50:50)

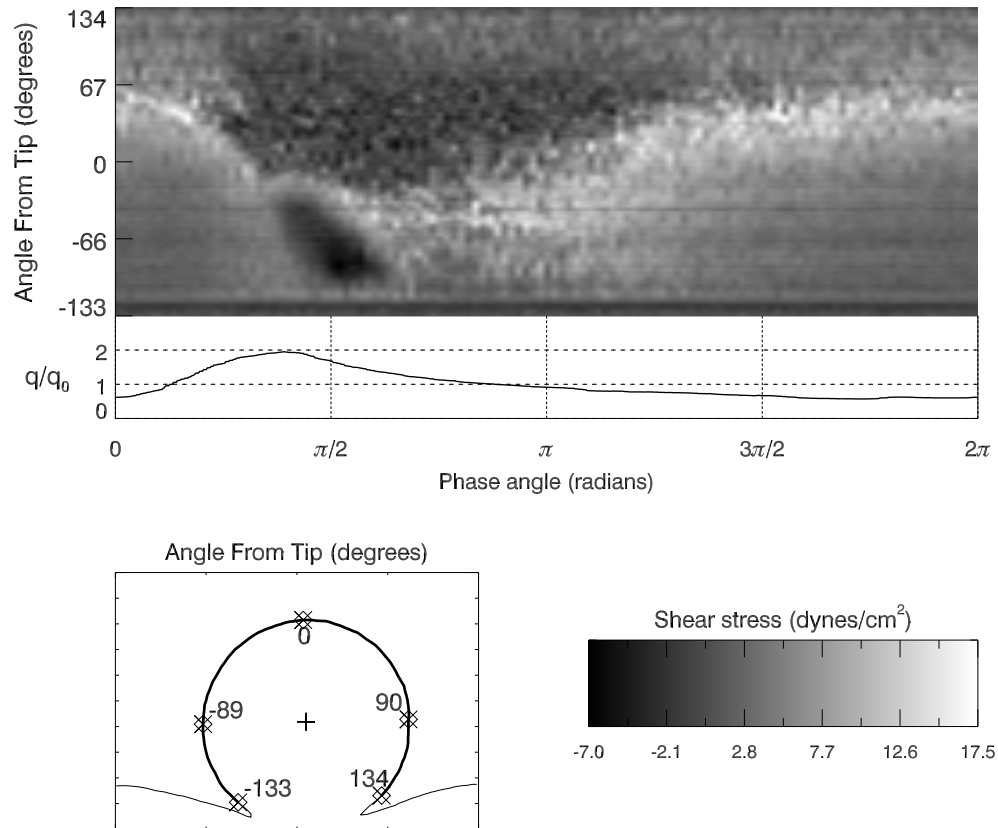


Figure 4.63: In-plane WSS history along the aneurysm dome in the midplane for a branching ratio of 67:33)

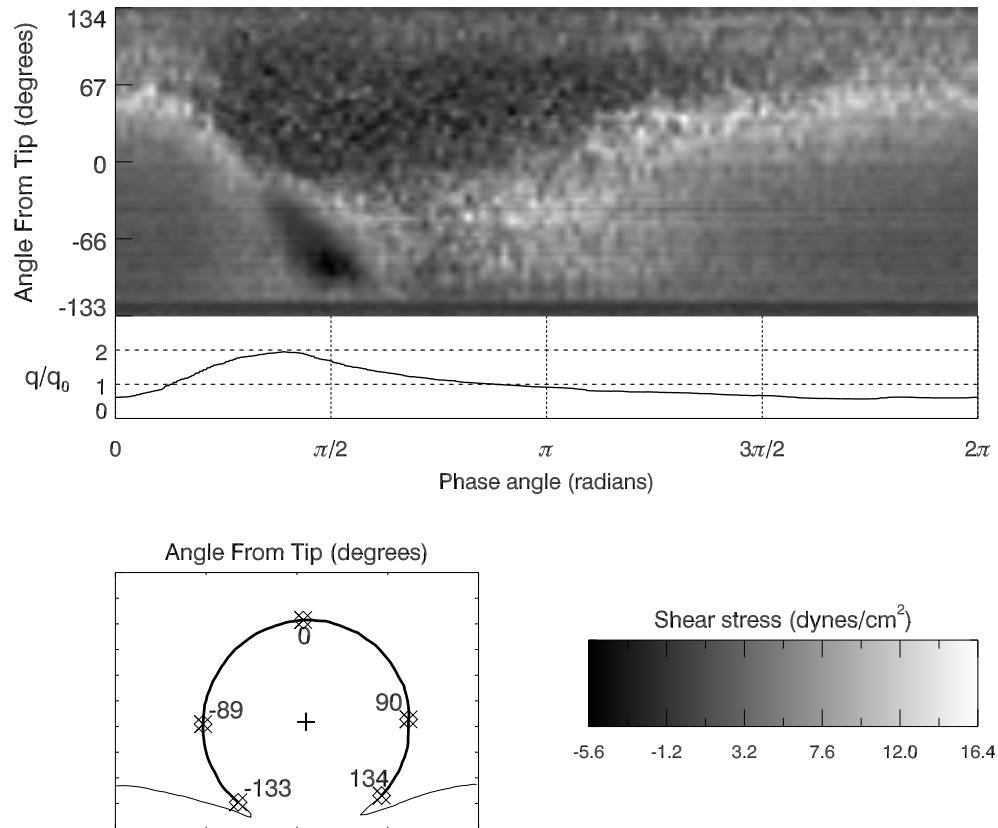


Figure 4.64: In-plane WSS history along the aneurysm dome in the midplane for a branching ratio of 75:25)

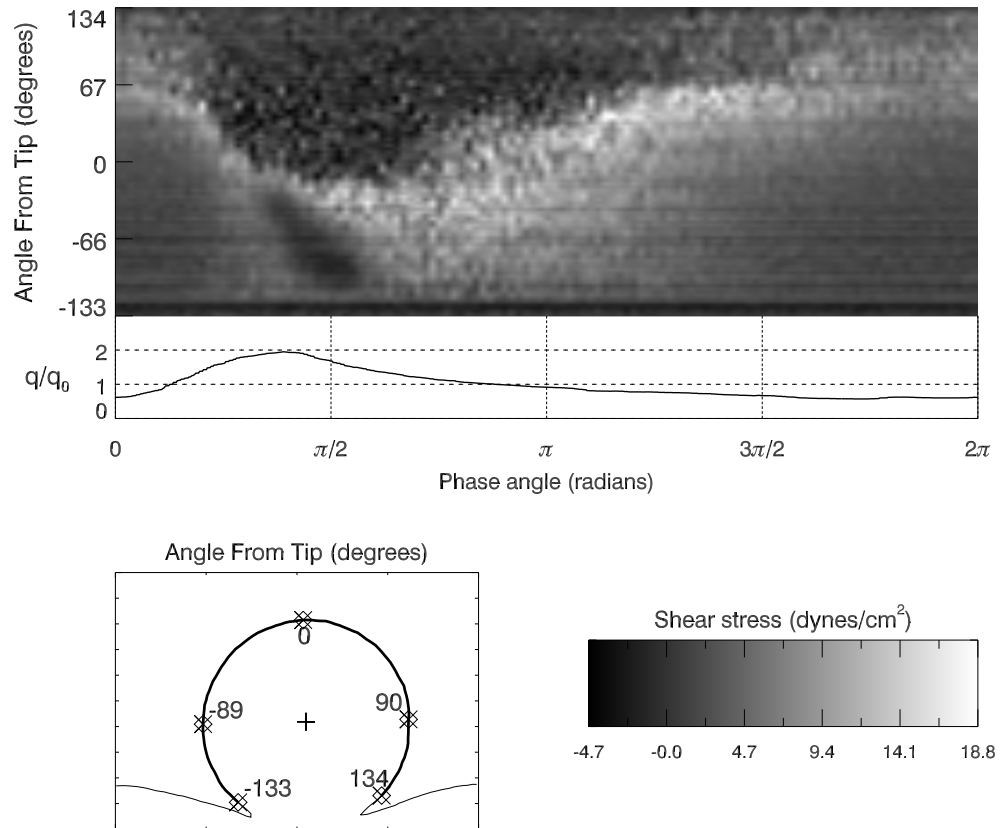


Figure 4.65: In-plane WSS history along the aneurysm dome in the midplane for a branching ratio of 80:20)

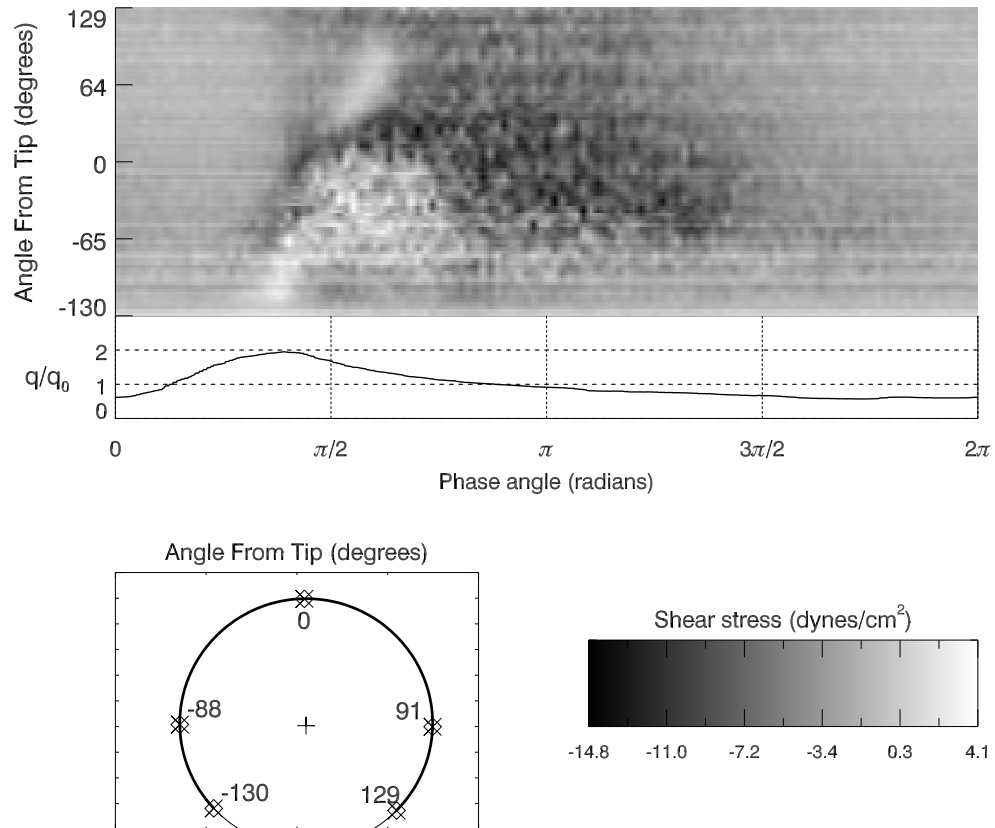


Figure 4.66: In-plane WSS history along the aneurysm dome in the upper quarter-plane for a branching ratio of 20:80)

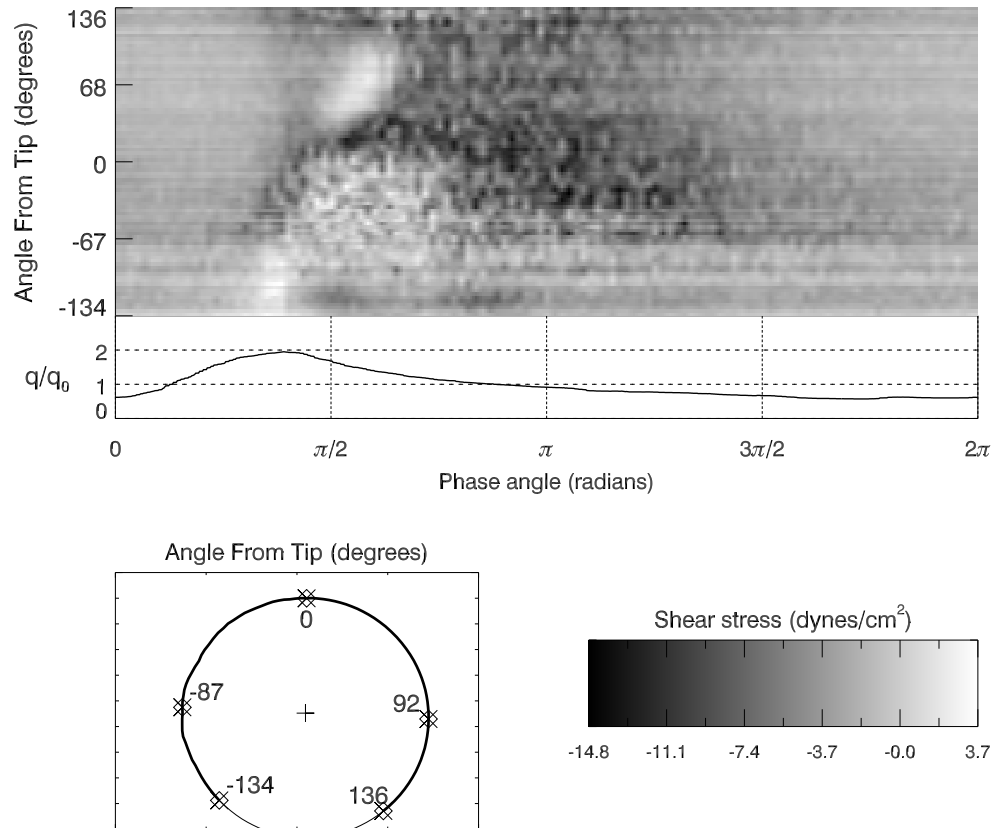


Figure 4.67: In-plane WSS history along the aneurysm dome in the upper quarter-plane for a branching ratio of 25:75)

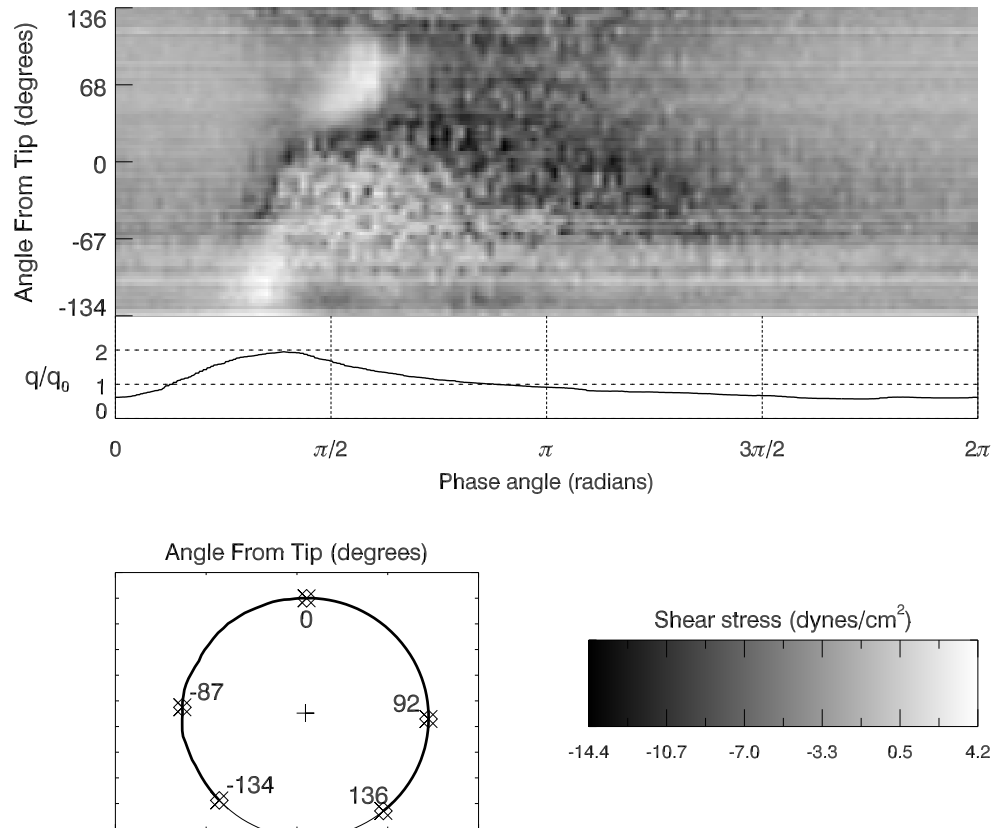


Figure 4.68: In-plane WSS history along the aneurysm dome in the upper quarter-plane for a branching ratio of 33:67)

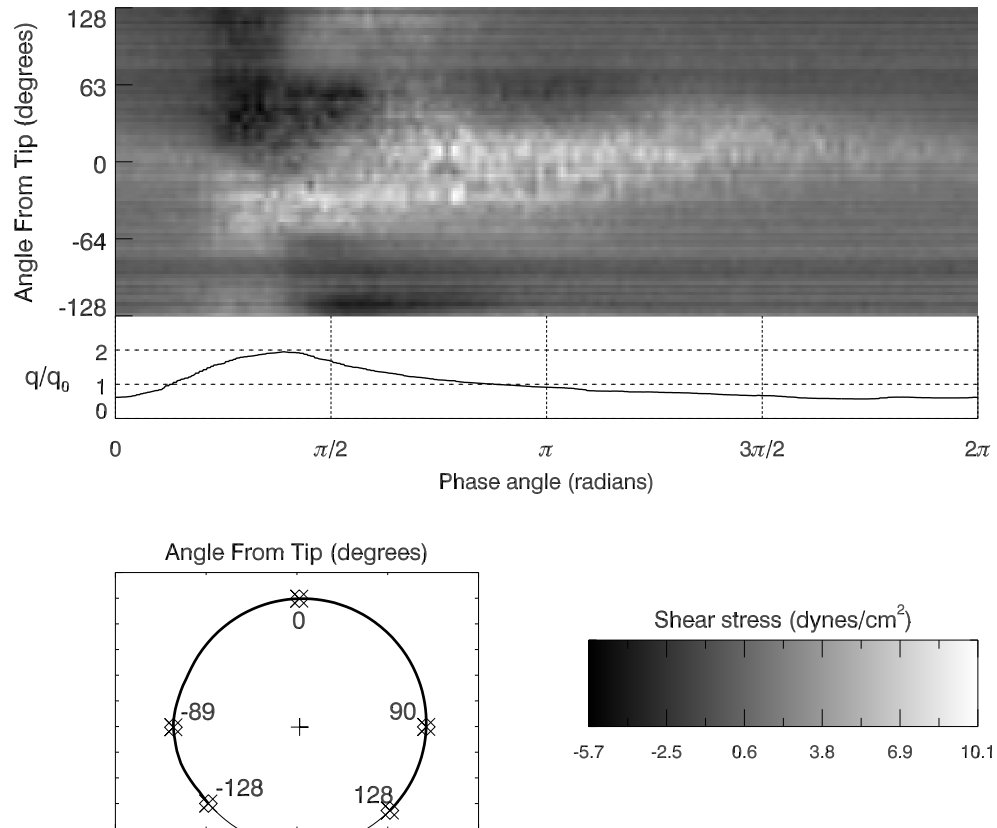


Figure 4.69: In-plane WSS history along the aneurysm dome in the upper quarter-plane for a branching ratio of 46:54)

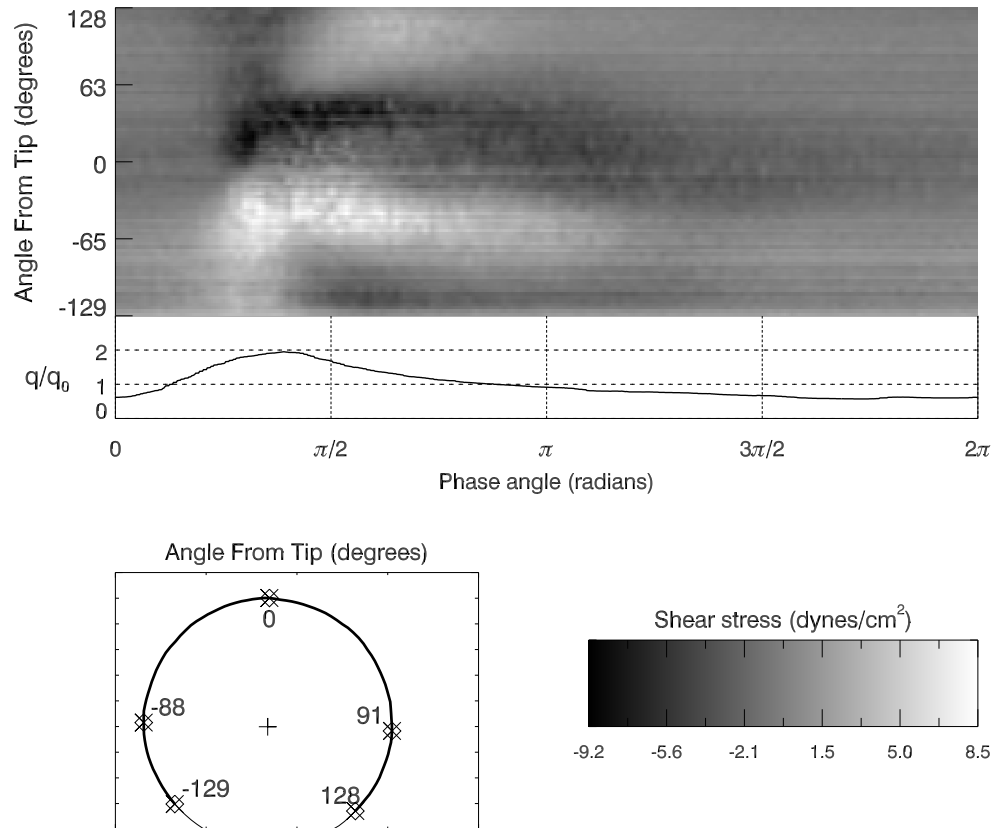


Figure 4.70: In-plane WSS history along the aneurysm dome in the upper quarter-plane for a branching ratio of 48:52)

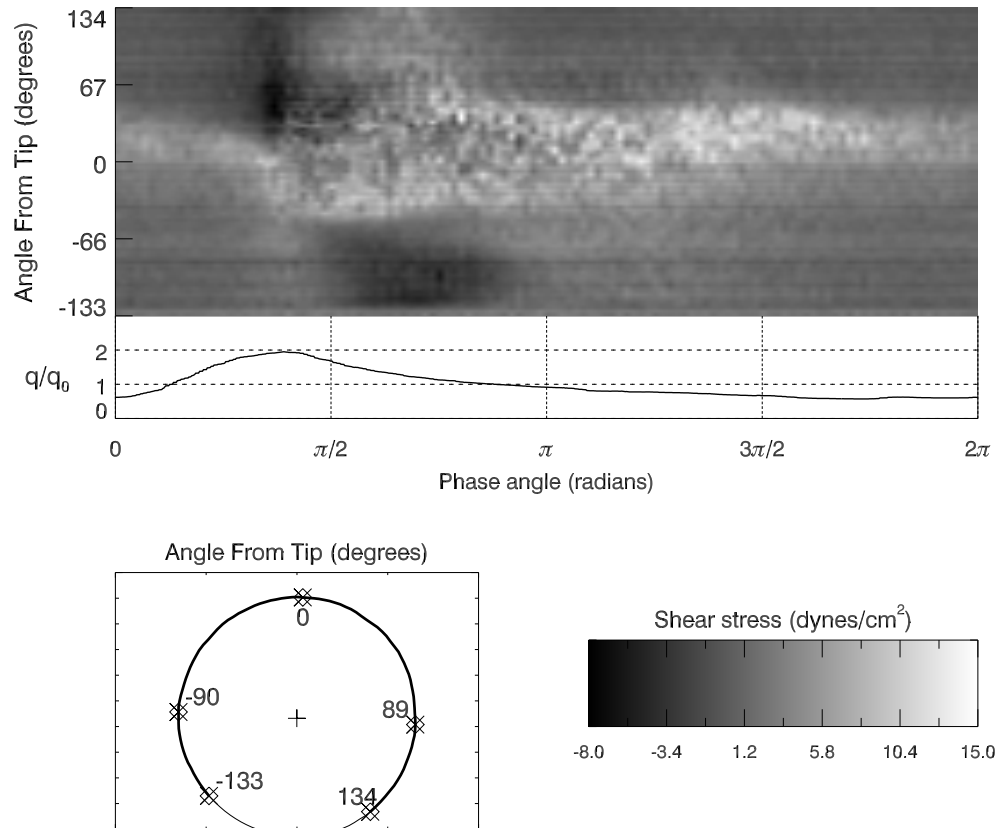


Figure 4.71: In-plane WSS history along the aneurysm dome in the upper quarter-plane for a branching ratio of 50:50)

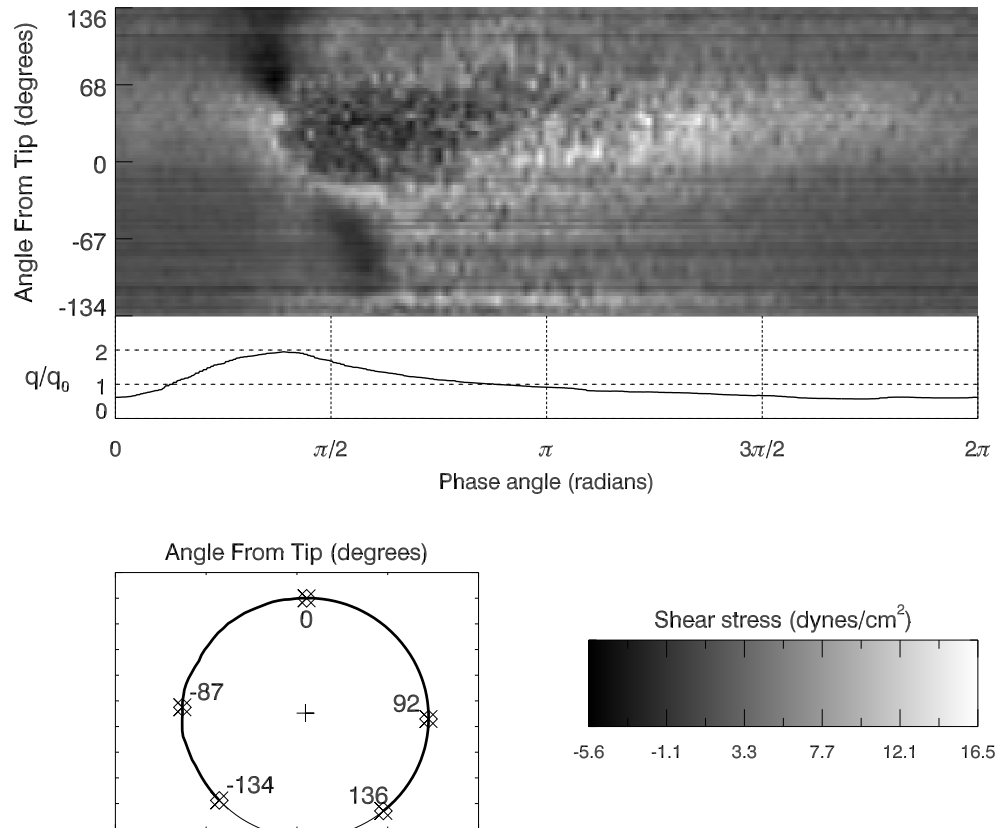


Figure 4.72: In-plane WSS history along the aneurysm dome in the upper quarter-plane for a branching ratio of 67:33)

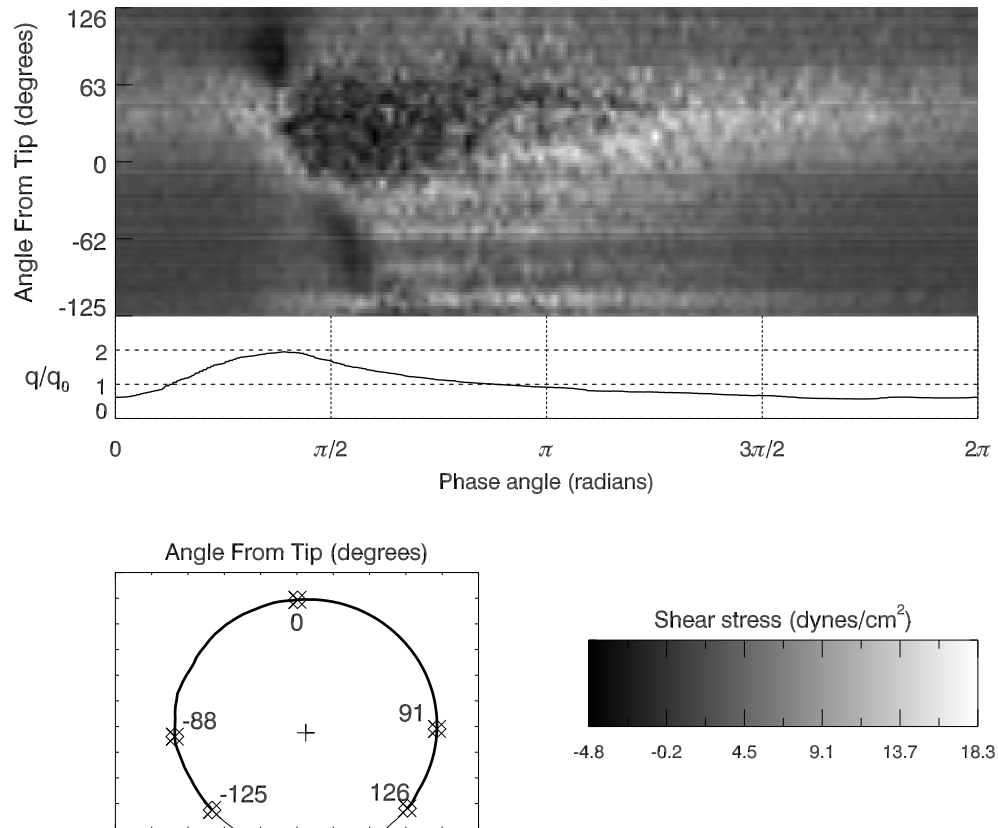


Figure 4.73: In-plane WSS history along the aneurysm dome in the upper quarter-plane for a branching ratio of 75:25)

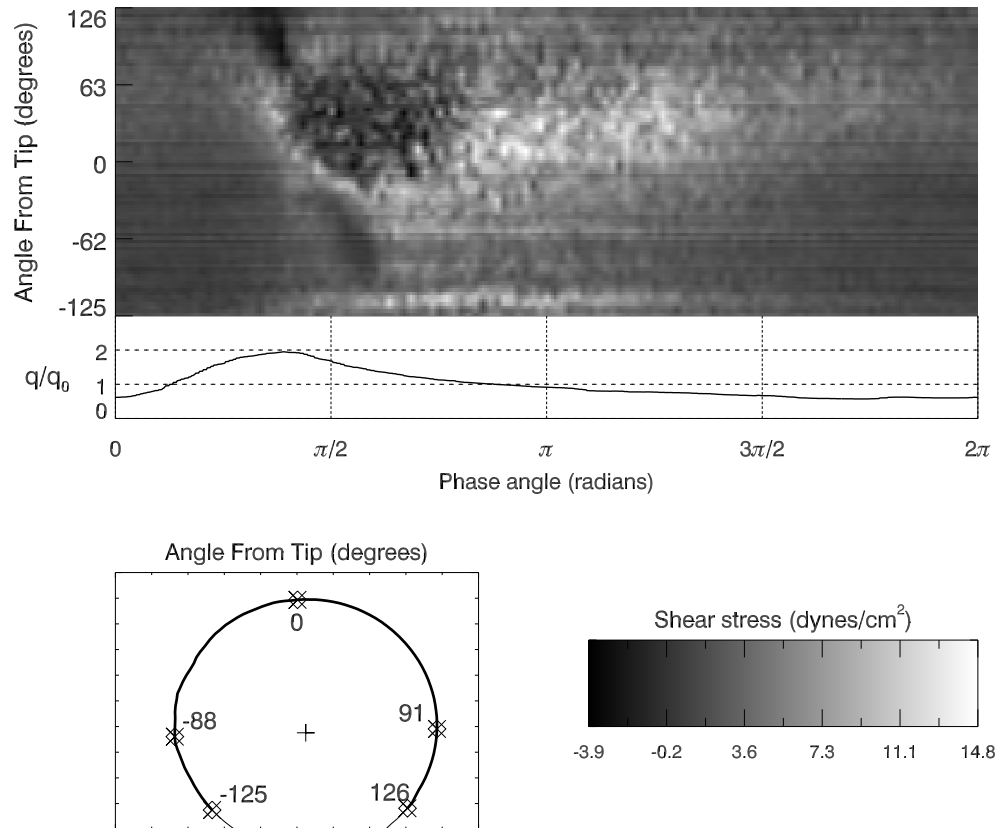


Figure 4.74: In-plane WSS history along the aneurysm dome in the upper quarter-plane for a branching ratio of 80:20)

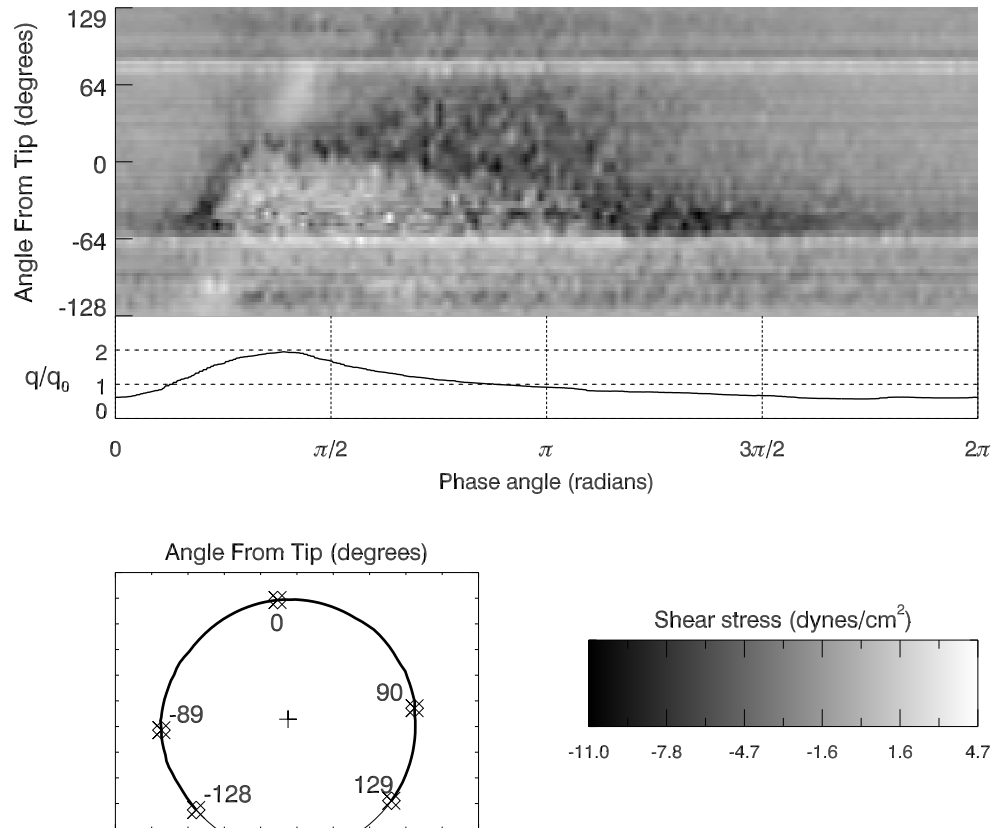


Figure 4.75: In-plane WSS history along the aneurysm dome in the lower quarter-plane for a branching ratio of 20:80)

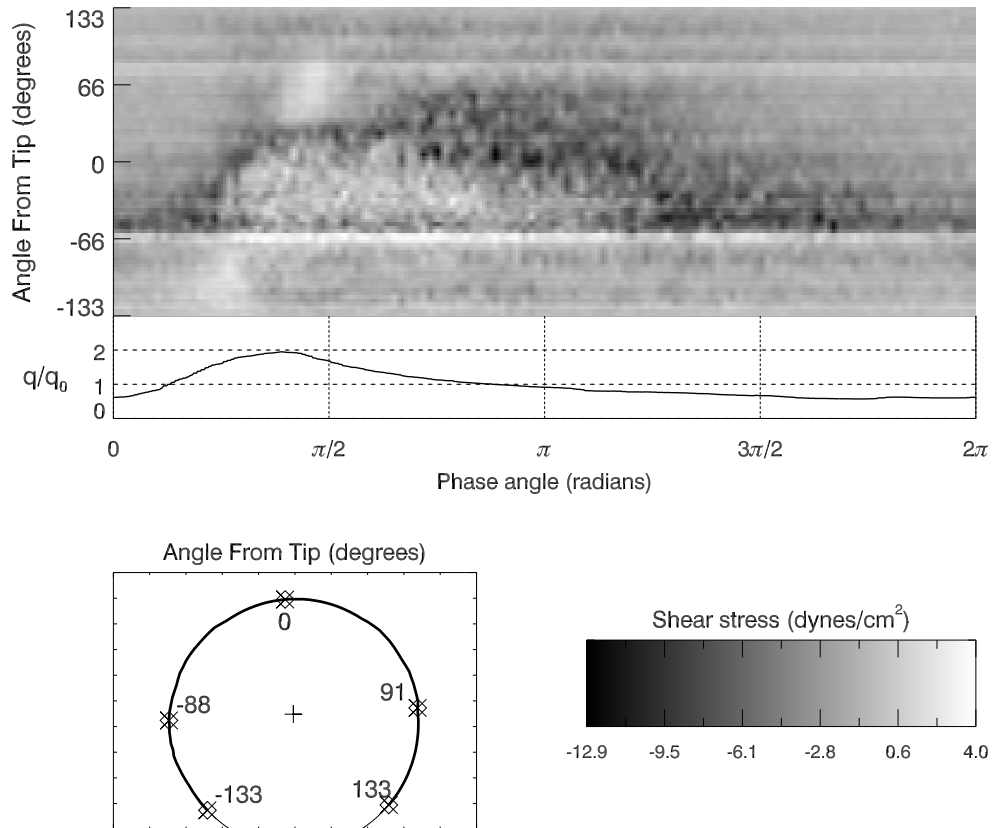


Figure 4.76: In-plane WSS history along the aneurysm dome in the lower quarter-plane for a branching ratio of 25:75)

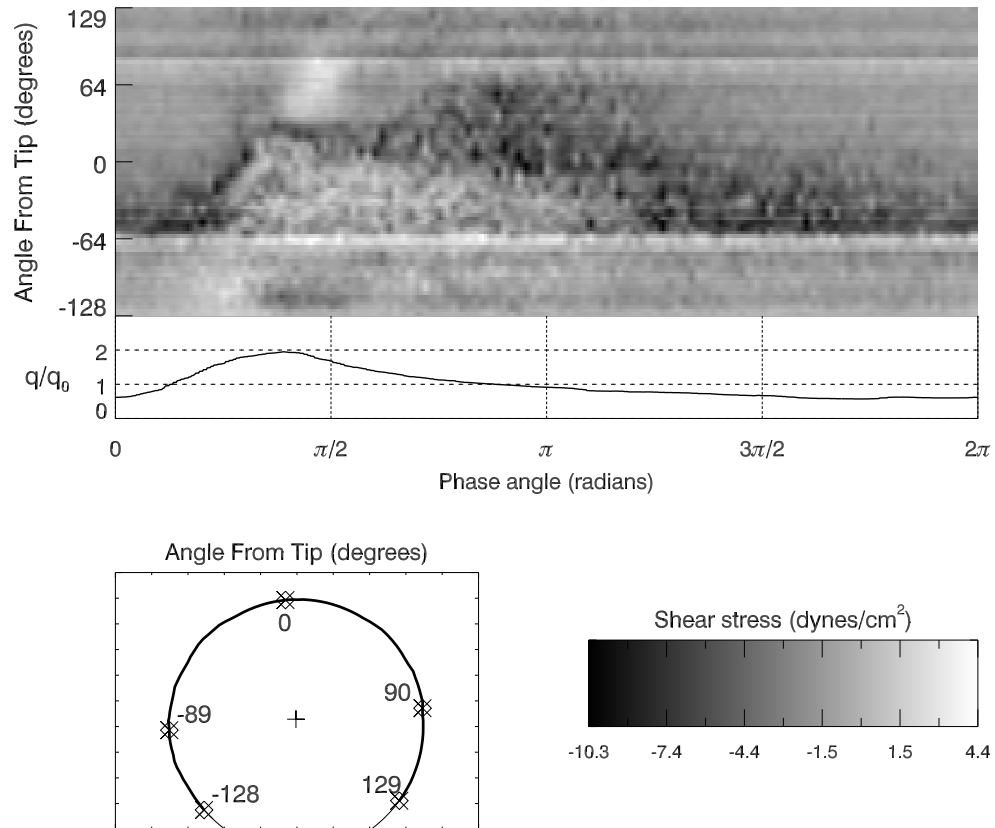


Figure 4.77: In-plane WSS history along the aneurysm dome in the lower quarter-plane for a branching ratio of 33:67)

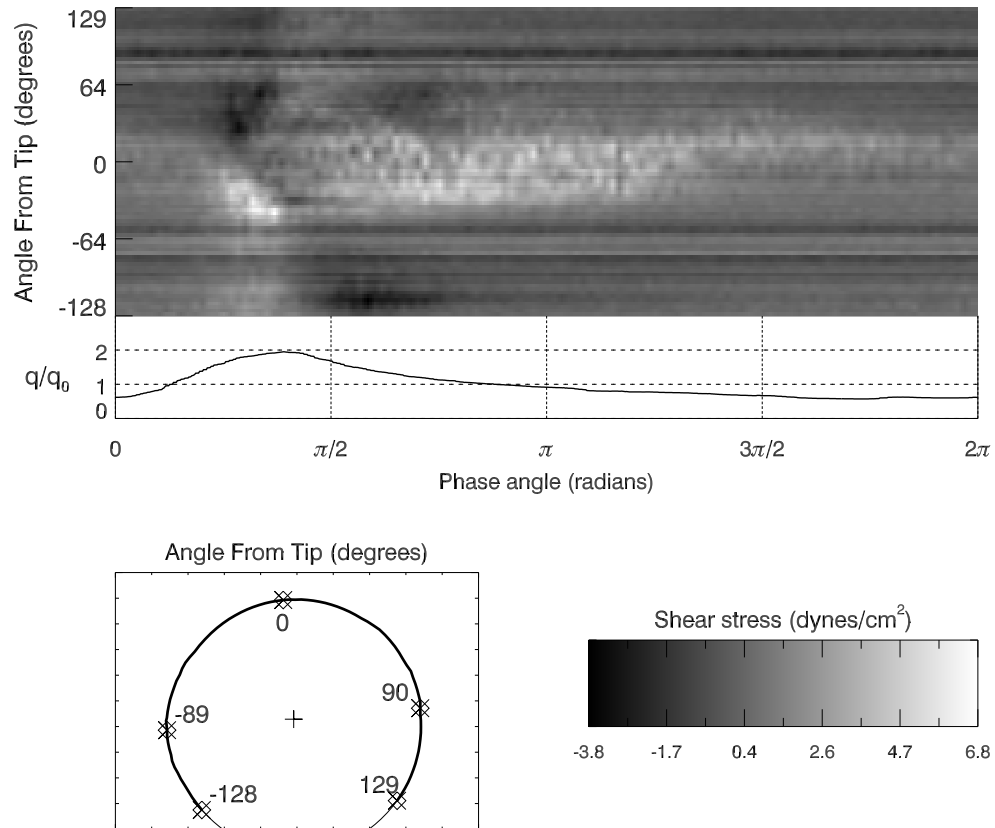


Figure 4.78: In-plane WSS history along the aneurysm dome in the lower quarter-plane for a branching ratio of 46:54)

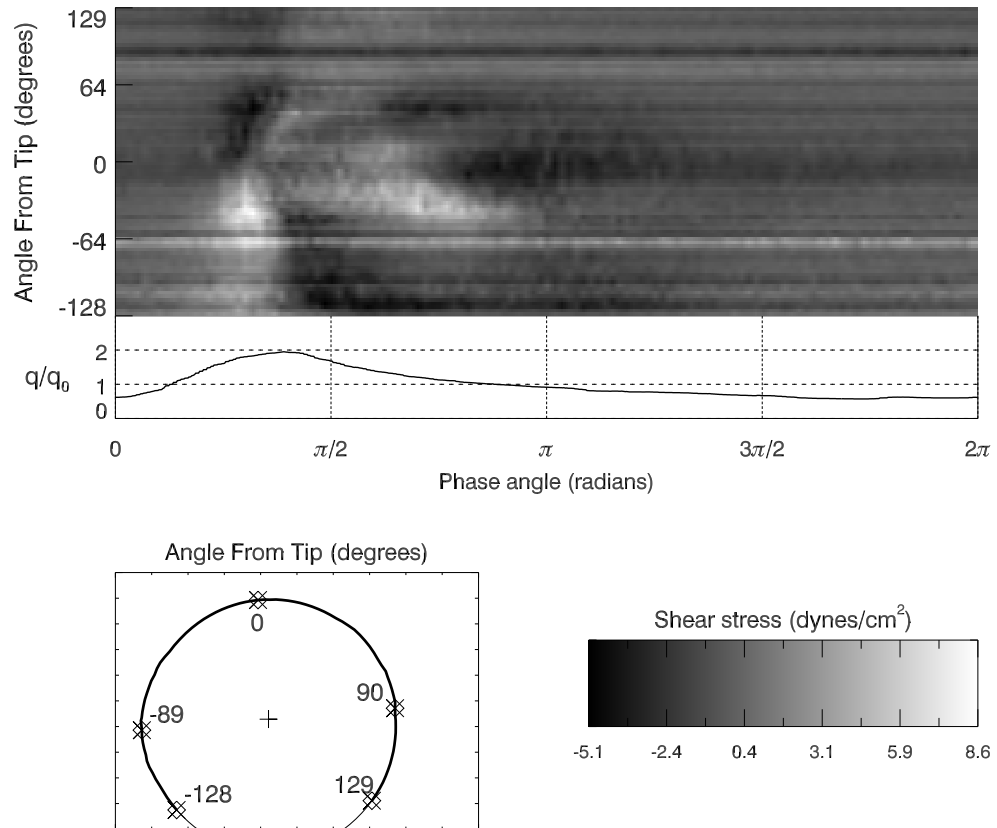


Figure 4.79: In-plane WSS history along the aneurysm dome in the lower quarter-plane for a branching ratio of 48:52)

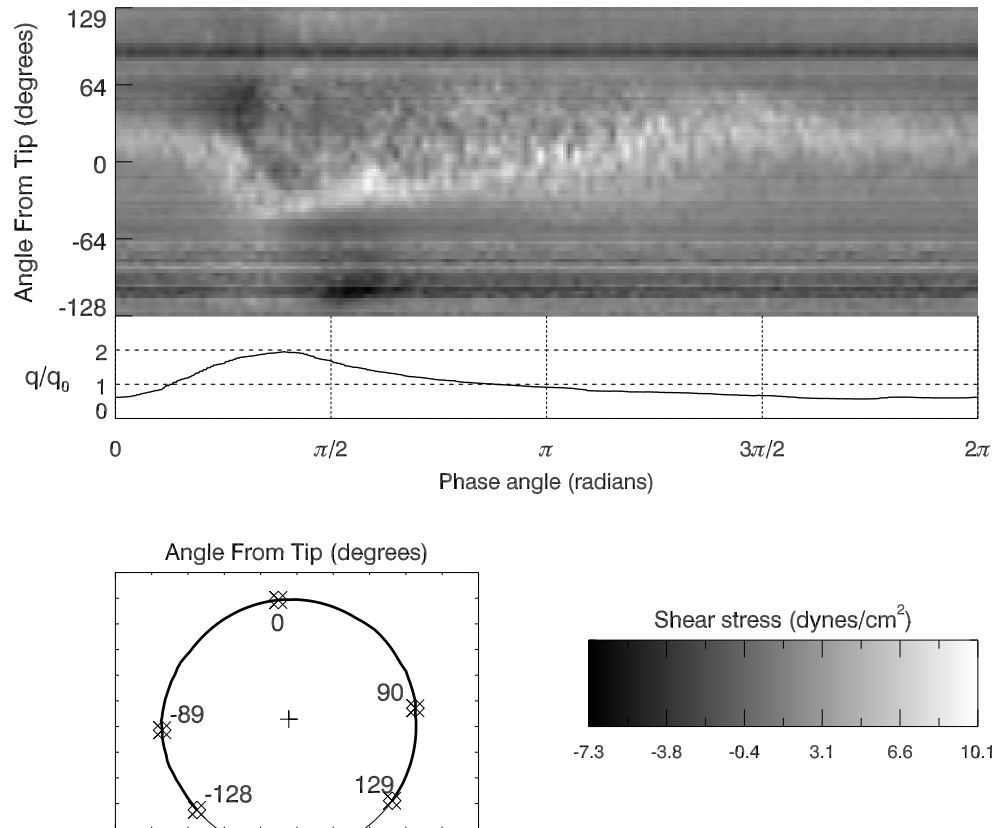


Figure 4.80: In-plane WSS history along the aneurysm dome in the lower quarter-plane for a branching ratio of 50:50)

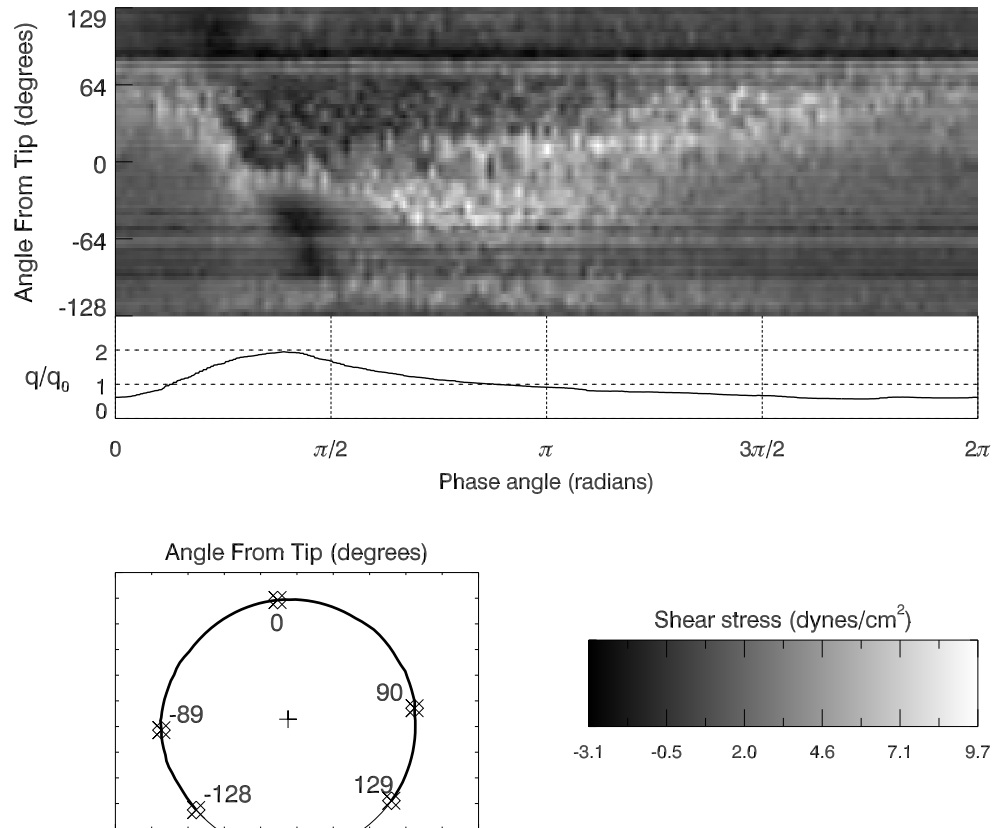


Figure 4.81: In-plane WSS history along the aneurysm dome in the lower quarter-plane for a branching ratio of 67:33)

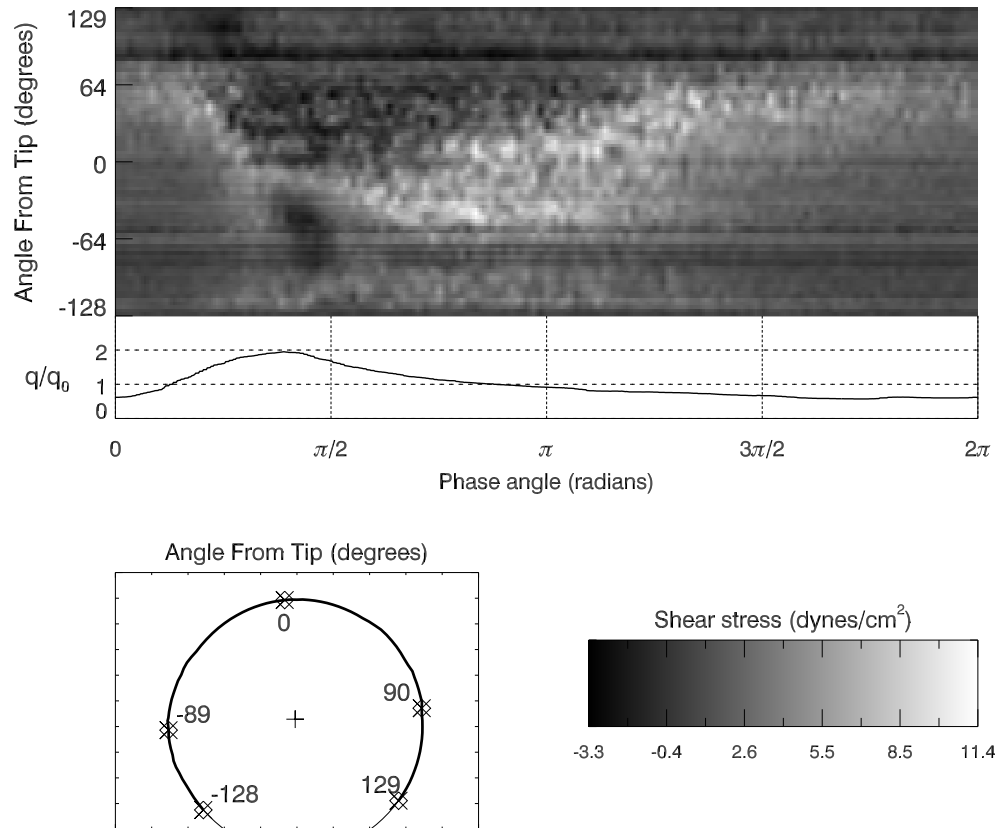


Figure 4.82: In-plane WSS history along the aneurysm dome in the lower quarter-plane for a branching ratio of 75:25)

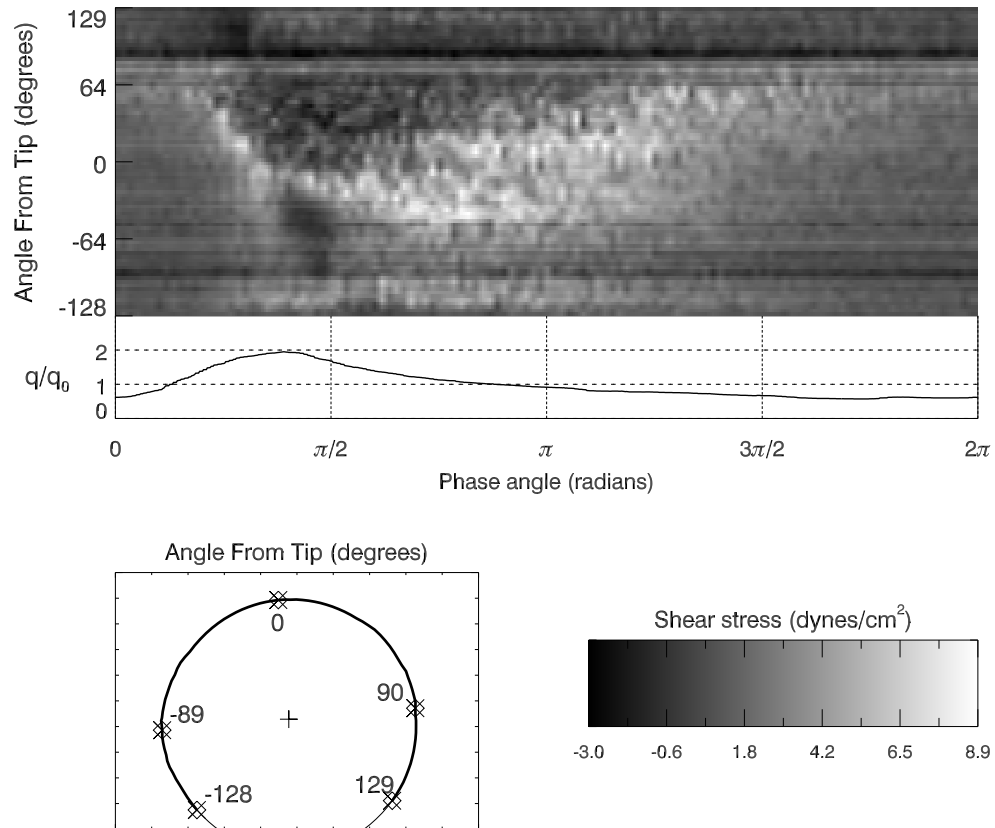


Figure 4.83: In-plane WSS history along the aneurysm dome in the lower quarter-plane for a branching ratio of 80:20)

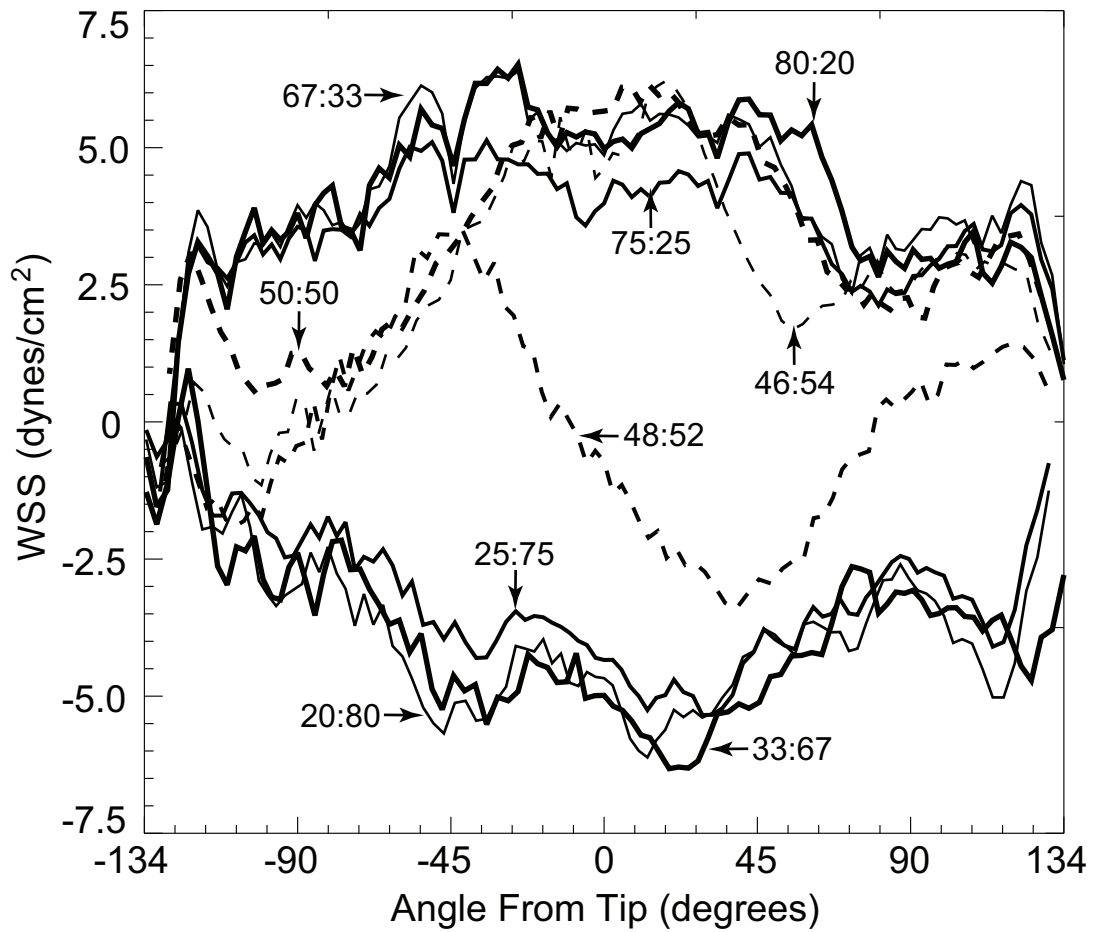


Figure 4.84: Plot of the mean over time of the in-plane WSS for each point along the midplane of the aneurysm dome.

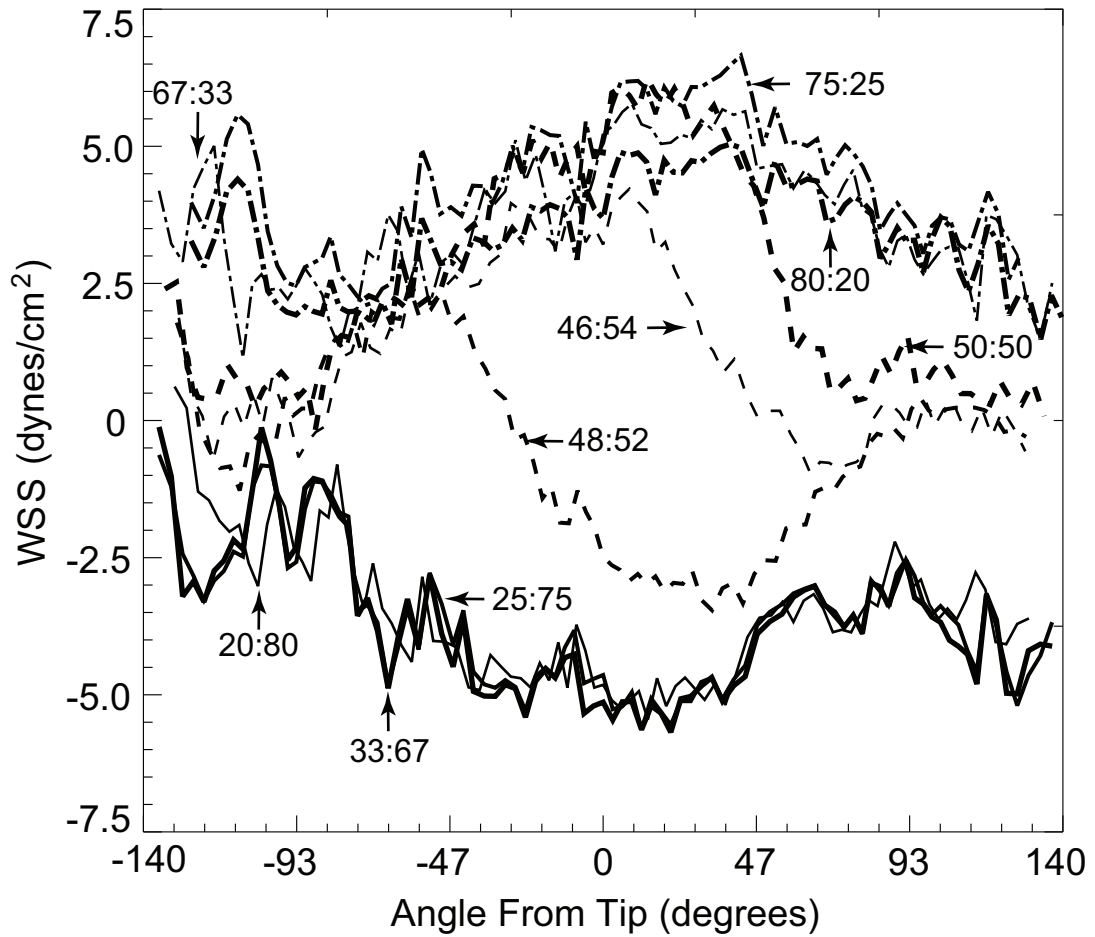


Figure 4.85: Plot of the mean over time of the in-plane WSS for each point along the upper quarter-plane of the aneurysm dome.

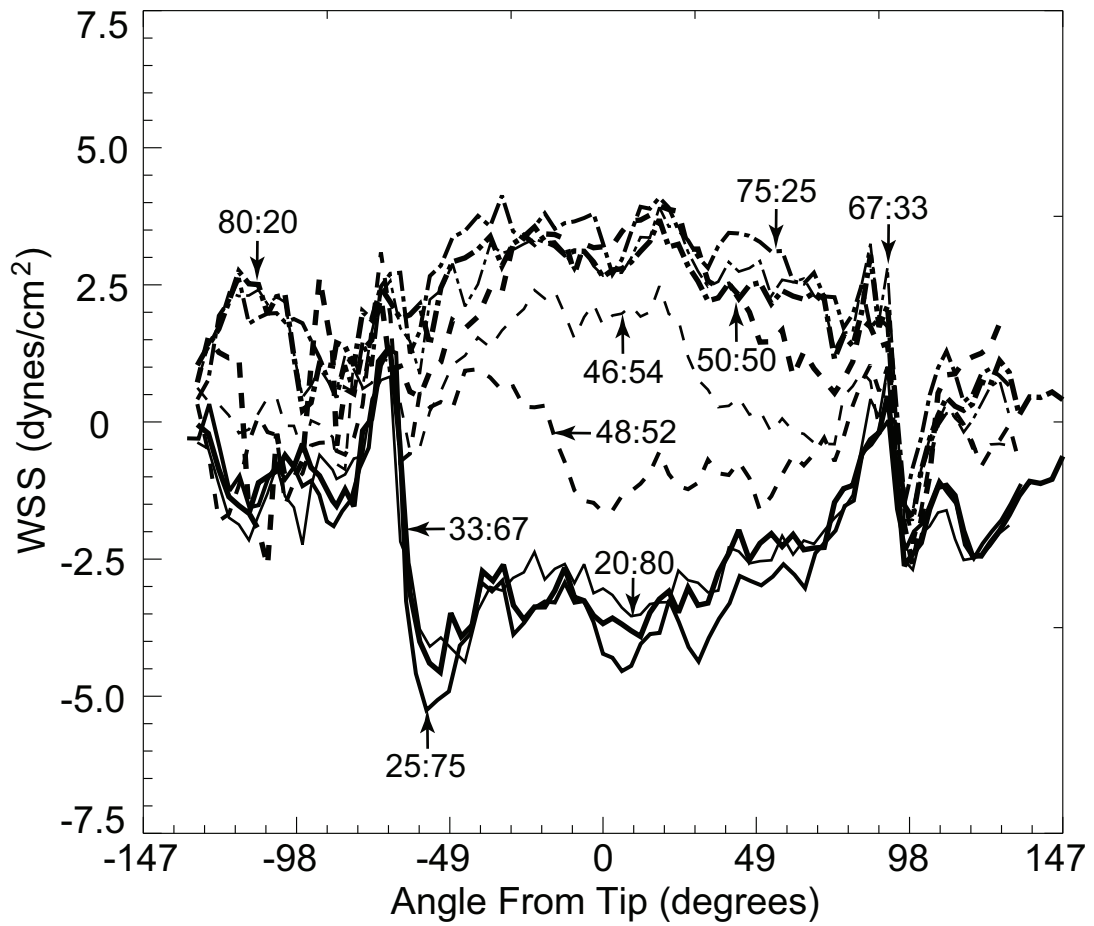


Figure 4.86: Plot of the mean over time of the in-plane WSS for each point along the lower quarter-plane of the aneurysm dome.

4.5 PIV: Discussion

4.5.1 Velocity

The velocity measurements reinforce the observations made in FV. The streamlines illustrate many of the flow structures, while the velocity fields establish flow direction. The ramp up phase (points B and C) is associated with the growth of the wall jet/expanding inlet jet and changes to the circulation region. During the ramp down phase, the divergent flow on the non-dominant side appear as identified by the streamlines originating from a point along the lower portion of the dome wall in point D. The counterflow seen in FV in the lower quarter-planes are identified by the linear streamlines in points C and D. In the upper quarter-plane, the counter-flow is seen at point C. The curvature of the counter-flow increases with outlet differential. The convergence of streamlines in the circulation regions and the formation and termination of streamlines from the walls reinforce the observation that the flow in the dome is highly three dimensional.

The 48:52 case is unique because its behavior is nearly symmetric during the ramp up and ramp down phases. This is evidenced by the flow patterns in the midplane streamline plots. At points C and D, the expanding inlet jet encompasses almost the entire dome with only a small circulation region on the upper portion of the dominant wall of the dome. In the upper and lower quarter-planes, the ramp down phase is characterized by the symmetric counter-flow down the midline of the dome. On either side of the counter-flow are circulation regions. During the ramp down and relaxation phases, there is no sign of the dominant circulation region in the upper quarter-plane that is clearly seen in points F

and A in the lower quarter-plane. The 46:52 case also demonstrates these behaviors but the flow is not as symmetric as the 48:52 case.

Peak speeds in the dome vary by plane: $0.21\text{-}0.25\frac{m}{s}$ in the midplane, $0.15\text{-}0.26\frac{m}{s}$ in the upper quarter-plane, and $0.14\text{-}0.19\frac{m}{s}$ in the lower quarter-plane. Peak speeds are lower for small outlet differentials. In the midplane, the ramp up phase is marked by an accelerating flow that enters from the neck (point A), moves toward the dome wall (point B), and reaches the fundus (point C), the upper portion of the dome including the tip (Figure 1.2). After passing the peak flow rate on the waveform (points E and F), speeds remain high along the walls while decreasing in the circulation region. In the upper and lower quarter-planes, peak speeds are associated with the strong counter-flows that develop within the flow, particularly as they are being narrowed by the expanding circulation region (point D).

4.5.2 Q

The Q plots highlight regions of circulation dominated flow, reinforcing the observations made about the circulation patterns described in the previous section. In the figures, white indicates positive values of Q while black indicates negative values of Q. A common color scale is used within each figure. As a result, the figures primarily track the strongest rotation.

The large outlet differential cases clearly show circulation dominated flows in all three planes associated with points C and D. The motion of the center of the circulation can be followed from points B-D. A similar pattern is seen in the lower quarter-plane, where Q

values peak during frame C and remain positive during point D. In the upper quarter-plane, the strengthening of the circulation region is seen at point D. This matches well with the observation that a counter-flow dominates near point C and that the circulation reforms and gains strength over the ramp down phase.

The small outlet differential cases do not see the same circulation dominated flow seen in large outlet differentials. At points C and D in all three planes, regions of negative Q are the dominant feature. In the midplane, the expanding inlet jet grows to occupy most of the dome during the ramp up and ramp down phases causing the circulation region in the midplane to drastically reduce in area. In the upper and lower quarter-plane, the counter-flow dominates much of the dome leaving only weak circulation regions along the sides that do not stand out. Limited restoration of the circulation can be seen toward the end of the ramp down phase and beginning of the relaxation phase, particularly in the 50:50 case.

4.5.3 WSS

WSS measurements establish the in-plane forces that the wall experiences over the course of one flow waveform. In all of the cases, the feature that stands out is a band over the entire waveform where the *instantaneous peak WSS region* located. The instantaneous peak WSS region refers to the highest WSS magnitude along the dome at that particular point on the waveform on the specified plane; it is not necessarily the absolute peak WSS value over the entire waveform. The description of the WSS data starts at the 0° phase angle seen in the flow rate plot underneath the WSS distribution. The discussion of the

overall WSS behavior (Figures 4.57-4.83) is divided based on the outlet differentials. The final section focuses exclusively on the WSS mean value plots (Figures 4.84-4.86).

Large Outlet Differentials

In the midplane data (Figures 4.57-4.59 and 4.63-4.65), the instantaneous peak WSS is initially located along the non-dominant side of the dome (-65° for right dominant flows and 65° for left dominant flows). During the ramp up phase, the instantaneous peak WSS region moves toward the tip and crosses onto the dominant side. In the wake of this shift, WSS on the non-dominant side change direction. During the ramp down phase, the instantaneous peak WSS region remains at the same angle from the tip. It is not until the relaxation phase that the region gradually returns across the dome to its starting position. This is consistent with the change in the flow pattern from the wall jet to the radiating divergent flow seen in the velocity and FV data. The dominant side of the dome experiences a magnitude increase. This is most likely a result of the increase in speed due to the strengthening of the wall jet or change to an expanding inlet jet. The absolute peak magnitudes are in the range of $12.9-17.5 \frac{\text{dynes}}{\text{cm}^2}$.

In the upper quarter-plane (Figures 4.66-4.68 and 4.72-4.74), the instantaneous peak WSS region is initially located on the non-dominant side of the dome, above the neck (-60° for right dominant flows and 60° for left dominant flows). During the ramp up phase, the region shifts past the tip onto the non-dominant side while two oppositely signed regions of WSS appear. One region occurs on the dominant side just below the start point of the instantaneous peak WSS region ($< -60^\circ$ for right dominant flows and

> 60° for left dominant flows). This region grows in size and strength during the ramp up phase but dissipates quickly at the beginning of the ramp down phase, resulting from the out-of-plane flow. The second region forms along the dominant side, just ahead of the oncoming instantaneous peak WSS region over the course of the ramp down phase. This region corresponds to the small circulation region that forms along the wall. The highest WSS magnitudes in these regions vary from 3-5 $\frac{dynes}{cm^2}$; the larger the outlet differential, the weaker these regions are. Maximum values for the absolute peak WSS magnitudes range from 14.4-18.3 $\frac{dynes}{cm^2}$.

Behavior in the lower-quarter plane (Figures 4.75-4.77 and 4.81-4.83) is quite similar to the upper quarter-plane. The trends for both large and small outlet differentials match the description in the previous paragraph with the modification that the transitions after the ramp up phase are much more gradual over the ramp down and relaxation phases. The absolute peak WSS magnitudes vary from 6.8-12.9 $\frac{dynes}{cm^2}$.

Small Outlet Differentials

Of the small outlet differential cases, the 46:54 (Figures 4.60, 4.69, and 4.78) and 50:50 (Figures 4.61, 4.70, and 4.79) cases are similar. In the midplane (Figures 4.60 and 4.61), the instantaneous peak WSS region moves across the fundus from the non-dominant to dominant side (0° to -40°) during ramp up. Compared to the large outlet differentials, this process occurs over a smaller time span. An oppositely signed WSS develops on the non-dominant side over the course of this shift at 20°-80°. The instantaneous peak WSS region moves back to the non-dominant side during the relaxation phase. WSS magnitude

ranges for the 46:54 and 50:50 cases are $-9.3-12.7 \frac{\text{dynes}}{\text{cm}^2}$ and $-9.7-12.3 \frac{\text{dynes}}{\text{cm}^2}$ respectively. WSS distribution patterns and magnitudes in the upper and lower quarter-planes are quite similar to the large outlet differentials, including the formation of two oppositely signed WSS regions. In the 46:54 case, the WSS magnitudes range from $-5.7-10.1 \frac{\text{dynes}}{\text{cm}^2}$ and $-3.8-6.8 \frac{\text{dynes}}{\text{cm}^2}$ in the upper and lower quarter-planes respectively. In the 50:50 case, the WSS magnitudes range from $-8.0-15.0 \frac{\text{dynes}}{\text{cm}^2}$ and $-7.3-10.1 \frac{\text{dynes}}{\text{cm}^2}$ in the upper and lower quarter-planes respectively.

The plots of WSS distribution for 48:52 critical case (Figures 4.61, 4.70, and 4.79) all share a symmetry near the tip. This is expected given the symmetric nature of the flow during ramp up and ramp down. In the midplane, there is an increase in the WSS on both sides of the dome, spreading along the entire fundus. During the ramp down phase, the WSS magnitudes subside around the peak areas located $\pm 10^\circ$ away from the tip. WSS magnitudes are nearly symmetric as well, ranging from $-12.2-12.7 \frac{\text{dynes}}{\text{cm}^2}$. Symmetry is also seen in the upper quarter-plane (Figure 4.70), with dual instantaneous peak WSS regions on opposite sides of the tip and opposing signs. The points move away from the tip on their respective sides during ramp up and dissipate over the course of the ramp down and relaxation phase. WSS magnitudes are higher on the dominant half, with a range of $-3.8-6.8 \frac{\text{dynes}}{\text{cm}^2}$. The lower quarter-plane behavior (Figure 4.79) mirrors the upper quarter-plane, as has previously been the case with WSS values ranging from $-9.2-8.5 \frac{\text{dynes}}{\text{cm}^2}$.

Mean Values

The plots of mean (averaged over time) WSS magnitudes for each of the points along the dome wall (Figures 4.84-4.86) represent the overall in-plane force that an endothelial cells feel during a waveform. The data can be divided into three groups: 1) right dominant flows with large outlet differentials, 2) left dominant with large outlet differentials, and 3) small outlet differentials.

In the midplane (Figure 4.84), the two large outlet differential groupings are clearly identified. The right dominant flows have an overall negative mean WSS that are highest in the fundus. Left dominant flows show a similar trend but with oppositely signed WSS. For the large outlet differentials, the mean values over much of the dome lie between $2.5\text{-}7\frac{\text{dynes}}{\text{cm}^2}$. The behavior of the flow in the 46:54 and 50:50 cases are quite similar to the left dominant flows. The case that stands out is the 48:52 flow ratio, which experiences vanishing shear near the tip. For the non-dominant (left) half of the dome, the mean WSS is positive while for the dominant (right) half of the dome it is negative. There is a point of vanishing in-plane WSS near the tip (-11°). The remaining small outlet differential cases are similar to the left dominant outlet differentials with the exception that the mean WSS in the dominant region are lower. This region corresponds to the wall jet and suggests that the gradients are on average lower, possibly a result of the slight inflow noted in the FV observations.

The mean plot for the upper quarter-plane (Figure 4.85) exhibits similar behavior but experiences smaller mean WSS magnitudes over all test cases. For large outlet differentials, the pattern continues of an overall negative WSS for right dominant flows and

positive values for left dominant flows. The highest magnitudes are $6 \frac{\text{dynes}}{\text{cm}^2}$ and $6.5 \frac{\text{dynes}}{\text{cm}^2}$ respectively. Small outlet differential cases exhibit a similar pattern of a rapid drop in WSS. In the 48:52 case, the drop occurs to the left of the tip in the vicinity of -47° . The drop goes from $2.5 \frac{\text{dynes}}{\text{cm}^2}$ to $-3 \frac{\text{dynes}}{\text{cm}^2}$ between -60° to 0° . The 46:54 case experiences a similar drop, although the change is not as large, with a shift from $3 \frac{\text{dynes}}{\text{cm}^2}$ to $-1 \frac{\text{dynes}}{\text{cm}^2}$ between 10° and 70° . The 50:50 case experiences a drop from $5 \frac{\text{dynes}}{\text{cm}^2}$ to $0.25 \frac{\text{dynes}}{\text{cm}^2}$ between 20° and 80° . The 46:54 and 48:52 points experience vanishing in-plane WSS over the drop around -50° and 60° respectively.

The mean WSS plot of the lower quarter plane (Figure 4.86) resembles a scaled down version of the mean WSS plot for the upper quarter-plane with a smaller range of WSS values, from $-5.5 \frac{\text{dynes}}{\text{cm}^2}$ to $-4 \frac{\text{dynes}}{\text{cm}^2}$. The behaviors of large and small outlet differentials are similar. Large outlet differentials form identifiable groupings of left dominant and right dominant outlet differentials. The small outlet differentials can be identified by the large drop that occurs in the vicinity of the fundus. For the 46:54 and 48:52 cases, vanishing in-plane WSS can be found at 35° and -20° respectively.

4.6 Conclusion

The PIV velocity measurements quantify the observations made in FV. Many of the observations discussed in Chapter 3 can now be identified through the velocity field and streamline plots. Flow structures, particularly the circulation region and the counter-flow are better visualized through the use of streamlines and plots of Q . Of particular interest is the 46:54 case, where flow patterns for a nearly symmetrical inlet flow are seen. This

velocity picture is used in conjunction with the SPIV data presented in Chapter 5 to build a complete picture of flow within the dome.

WSS measurements provide new information in evaluating flow behavior in the model. The in-plane WSS magnitudes are on the same order as simulations by Steiger et al. [60]. The highest values are found along the midplane, with peak measurements of $18.3 \frac{\text{dynes}}{\text{cm}^2}$. The values from critical case, on the order of $12 \frac{\text{dynes}}{\text{cm}^2}$, match measurements made by Shojima et al. [56]. Overall, increasing the outlet differential corresponds to increases in WSS magnitude and the amplitude of the displacement of the instantaneous highest WSS point. The peak magnitudes are above the lower limit of $3 \frac{\text{dynes}}{\text{cm}^2}$ suggested by Walpola et al. [64]; however, as Shojima et al. suggest, it is possible that the cells within the aneurysm are injured and are more sensitive to lower WSS. The mean WSS magnitudes are considerably lower than the peak values are of the same order as the lower limit. There are multiple points where vanishing in-plane WSS are identified. In particular, the 48:52 case sees this phenomena occur in all three planes. Peak and mean WSS magnitudes are well below the $300 \frac{\text{dynes}}{\text{cm}^2}$ Fry [20] indicated as causing endothelial cell death. However, the argument is incomplete since these WSS measurements only account for one of the two components of WSS. The inclusion of a perpendicular velocity measurement is needed to determine the complete WSS magnitude. The experiments presented in the next chapter provide the orthogonal component of WSS as well as characterizing the 3D nature of the flow field.

Chapter 5

Stereoscopic Particle Image Velocimetry

Stereoscopic particle image velocimetry (SPIV) improves on PIV by allowing three dimensional velocity measurement at plane within a flow. Unlike conventional particle image velocimetry (PIV) or flow visualization (FV), SPIV requires images of a flow from two different angles. Through geometric reconstruction, the images are processed to form a single 3D velocity field. This chapter reviews the principles behind SPIV, describes the setup, presents post-processed results, and discusses its significance.

5.1 SPIV: Theory

As with FV and PIV, SPIV requires a flow seeded with visual markers and illuminated over a plane. However in FV and PIV, the camera is located along the object plane's optical axis. Particle motion parallel to the optical axis (i.e. out-of-plane motion)

cannot be captured by the camera. In SPIV, two image pairs are captured by cameras at different angles to the object plane's optical axis. This creates two unique projections of the displacement within the laser sheet. Using either geometric reconstruction or calibration, the distorted images can be mapped into a three dimensional velocity field.

5.1.1 SPIV Imaging Configurations

Stereoscopic PIV systems most commonly use one of two basic configurations: translational and angular displacement.

Translational SPIV

In the translational configuration, the orientation of the image planes remain parallel with the object plane (Figure 5.1a). The cameras are displaced parallel to the object plane such that the optical axis of the camera and the object are not collinear. This configuration preserves uniform magnification and focus over the entire image. However, having an angled line of sight has disadvantages. Conventional camera lenses are optimized for maximum image quality in the center, along the optical axis whereas the translational system uses the extremities of the lens. The edges of the image plane are prone to distortions which introduce errors in the displacement measurements. This configuration is unfeasible in certain applications where the translation required is beyond the view of the lenses.

Arroyo and Greated [5] developed a derivative of the translational configuration to study an acoustic streaming flow. The modified technique uses two pairs of mirrors parallel to and offset from the object plane's optical axis. The lens and object plane are aligned with the optical axis (Figure 5.1b). The first set of mirrors, located between the

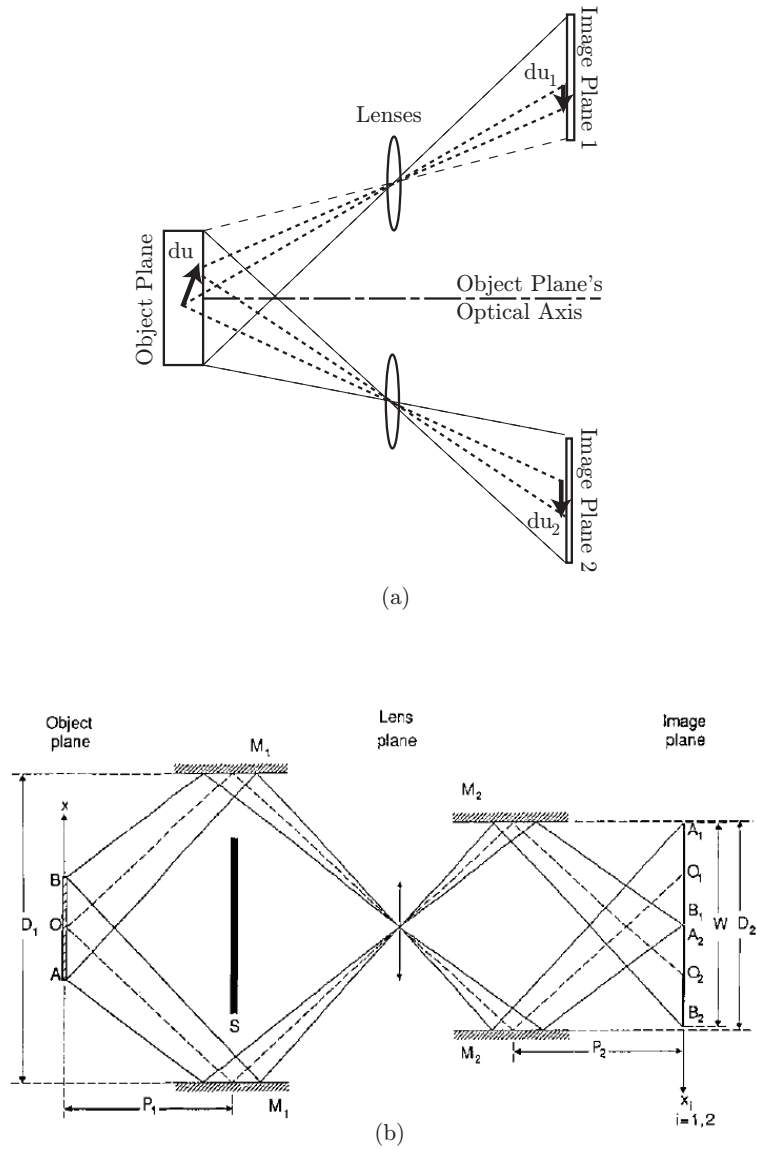


Figure 5.1: Diagrams of the standard translational SPIV configuration (a) and the modified translational SPIV configuration (b) used by Arroyo and Greated [5].

lens and the object plane, reflects an oblique view back toward the lens. The lenses focus the images which then reflect off of another pair of mirrors located between the lens and image plane. This optical path creates two images focused on the image plane. This configuration allows a single image plane to capture both images. An obstruction is required in the line of sight between the lens and the object plane to block out the direct light path. It also makes the conversion from PIV to SPIV simple; the camera remains in place while the mirrors are positioned. Unfortunately, this configuration was impractical for the experiments in this dissertation. Specially modified camera lenses are required to insert the pair of mirrors between the lens and image plane. The long optical light path and the light losses incurred by each optic reduce the light intensity from the fluorescent particles below levels for practical imaging.

Angular Displacement SPIV

In angular displacement, or rotational, configuration, the cameras are rotated such that the lenses' optical axes intersect on the object plane (Figure 5.2). This configuration reduces the limitation on the angle between the image and object plane. It also keeps the object plane in the center of the lens. However, because the object plane is not parallel to the image plane, the image is distorted by non-uniform magnification caused by the variation in the optical path length. The misalignment also means that focusing the entire image requires greater depth of field. Increasing the depth of field comes at the expense of reducing the aperture size and therefore the amount of light that reaches the imaging plane. A balance must be achieved between sufficient depth of field while recovering enough of the

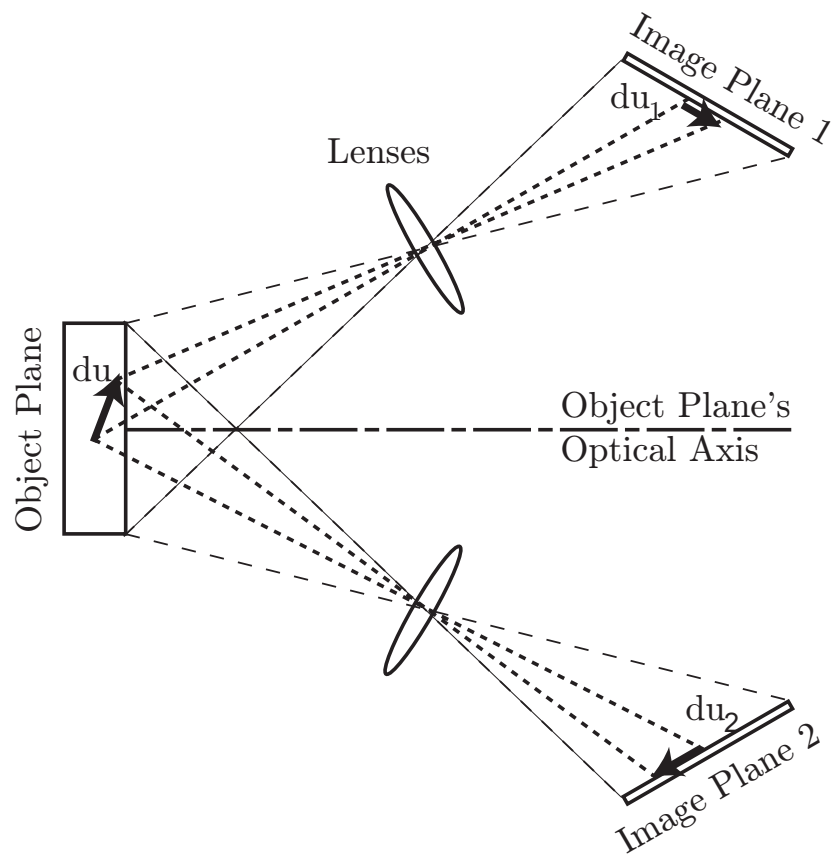


Figure 5.2: Diagram of the standard angular displacement SPIV configuration.

fluoresced light from the particles. Altenhofen [4] applied the Scheimpflug condition, which prescribes how to align the image plane relative to the lens to improve the focus of the object plane. This adjustment reduces the depth of field required but exacerbates the non-uniformities in magnification. Conventional camera lenses are built with the lens and camera planes parallel. Customized commercial lenses that implement the Scheimpflug condition were not available for this experiment. Without the use of the Scheimpflug condition, it is still possible to conduct rotational SPIV as discussed in Section 5.2.3.

The rotational configuration requires the distorted images to be mapped back into normal space. Willert et al. [69] discusses three methods to determine this mapping. The first is ray tracing, which uses complete geometric information of the setup to map the projected displacements calculated by PIV into a single 3D displacement field. This technique can be laborious and difficult to implement when parts of the experiment are inaccessible for measurement. The most common technique is to use a 3D multi-depth calibration grid parallel to the object plane. A calibration image is captured at each depth of the target. The set of calibration images are correlated with the real spatial coordinates. This allows for the development of a mapping from the image space to the object space without any prior knowledge of the experimental geometry. The final technique is the use of a 2D calibration target. The loss of the depth element requires that some knowledge of the geometry of the optics is known. With this calibration, it is possible to adjust the results into the object space, overcoming the problems posed by the varying magnification [38]. The final technique is the method implemented in the SPIV experiments in this chapter.

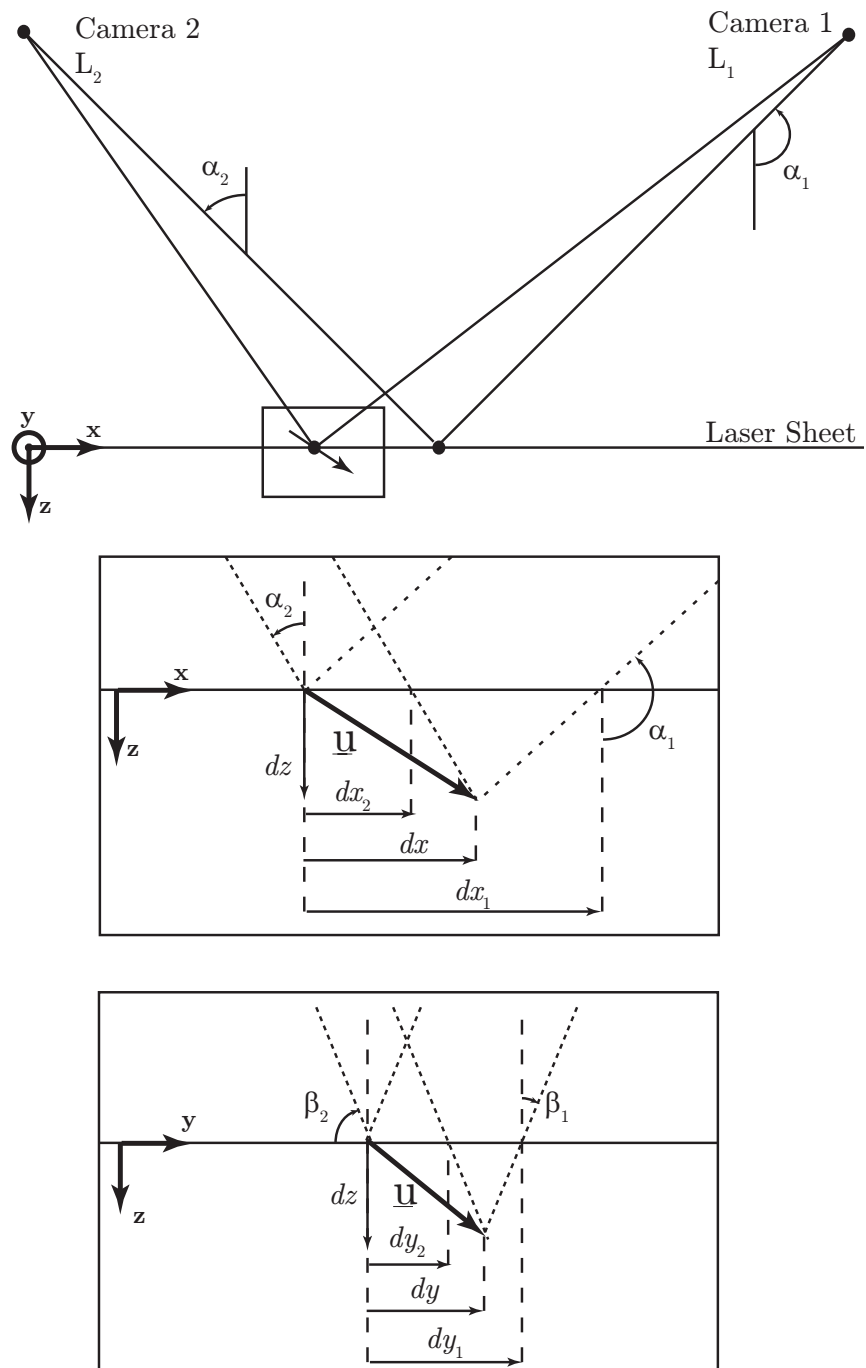


Figure 5.3: An illustration of the camera positions and angles used in velocity reconstruction based on works by Willert [69] and Brücker [7].

5.2 SPIV: Setup

5.2.1 Seed Particles

Fluorescent particles again seed the flow. The changed imaging configuration discussed below reduces the magnification of the model in the images. To maintain the projected particle size on the imaging plane, larger Duke Scientific $107\mu\text{m}$ fluorescent polymer microspheres seed the working fluid. Its fluorescing characteristics are the same as the smaller particles used in PIV, absorbing the 532nm laser light and fluorescing at 607nm . The considerations detailed in Section 3.2.1 are re-evaluated for these particles. The sedimentation speed for these particles is $544\mu\text{m/s}$. The sedimentation distance is up to $0.54\mu\text{m}$ for a single image pair, which is much smaller than the imaging resolution. The relaxation time, t_s for these particles is $51\mu\text{s}$, which is an order of magnitude smaller than the time between image pairs.

5.2.2 Illumination

Illumination is again provided by a NewWave Gemini Nd:Yag laser. The laser sheet optics are adjusted slightly. In PIV, a thin laser sheet is desired to avoid capturing the projection of the out-of-plane velocity component. SPIV requires a laser of finite thickness to capture the projection of the out-of-plane velocity component. For this experiment, the PIV (Figure 3.1) laser optics are used but are placed closer to the model to increase the sheet thickness to 1mm . The time between image pairs range from $400\text{-}1000\mu\text{s}$.

5.2.3 Imaging

For the two camera, angular displacement SPIV configuration a MotionPro X-3 camera and MotionPro Y-3 camera are used. The MotionPro Y-3 has identical resolutions and capture rates as the MotionPro X-3 used in PIV. The camera bodies do vary in the distance from the lens attachment to the CCD, causing a difference in image plane distance and magnification even if the same lens is used. As a result, two different lens sets are used. For the X-3 camera, a C-mount adapter, Vivtar 20mm extension tube, f=50mm Canon lens (f/8 aperture), and +1 diopter Hoya close up lens are used. For the Y-3 camera, a 3mm C-mount extension tube, C-mount adapter, and f=50mm Canon lens (f/8 aperture) Canon lens are used. Both cameras have an Edmund Optics 550nm longpass colored glass filter installed. The cameras are oriented to align the optical axes with the 45° viewing windows. To match magnification, the cameras are positioned at different distances from the model (Figure 5.4)

To calibrate the cameras, a 1 cm square target is embedded into the model, aligned with the laser sheet in the x- and z-direction and offset in the y-direction (Figure 5.5). A 15 x 15 grid of points is printed on to the target. To establish orientation, the grid is marked with an 0 at the center and numbers marking each quadrant of the target, 1-4. The angled windows are wide enough to view the dome and the target. The cameras are attached to a platform mounted on a linear transverse system which allows the cameras to be moved from the target to the dome while constraining motion in all other directions. Both cameras are triggered and synchronized through signals generated by the controlling PC.

Without the use of the Scheimpflug modification to the lens, focus cannot be

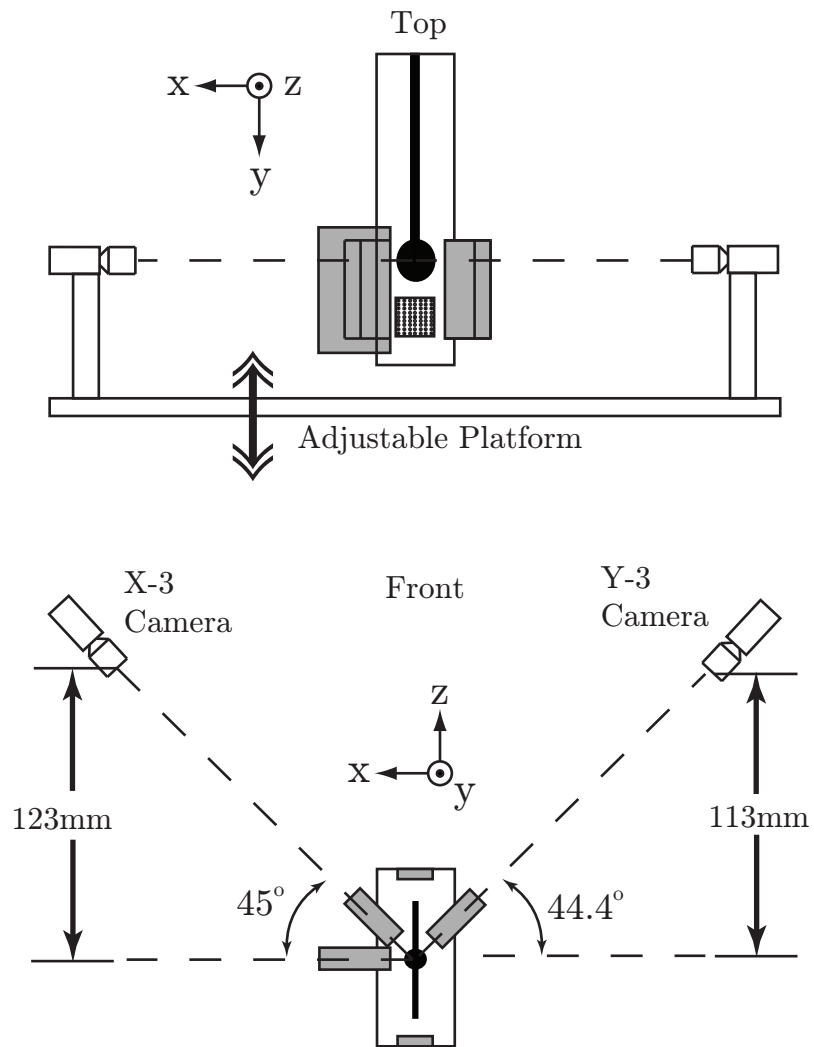


Figure 5.4: Camera configuration for SPIV experiments.

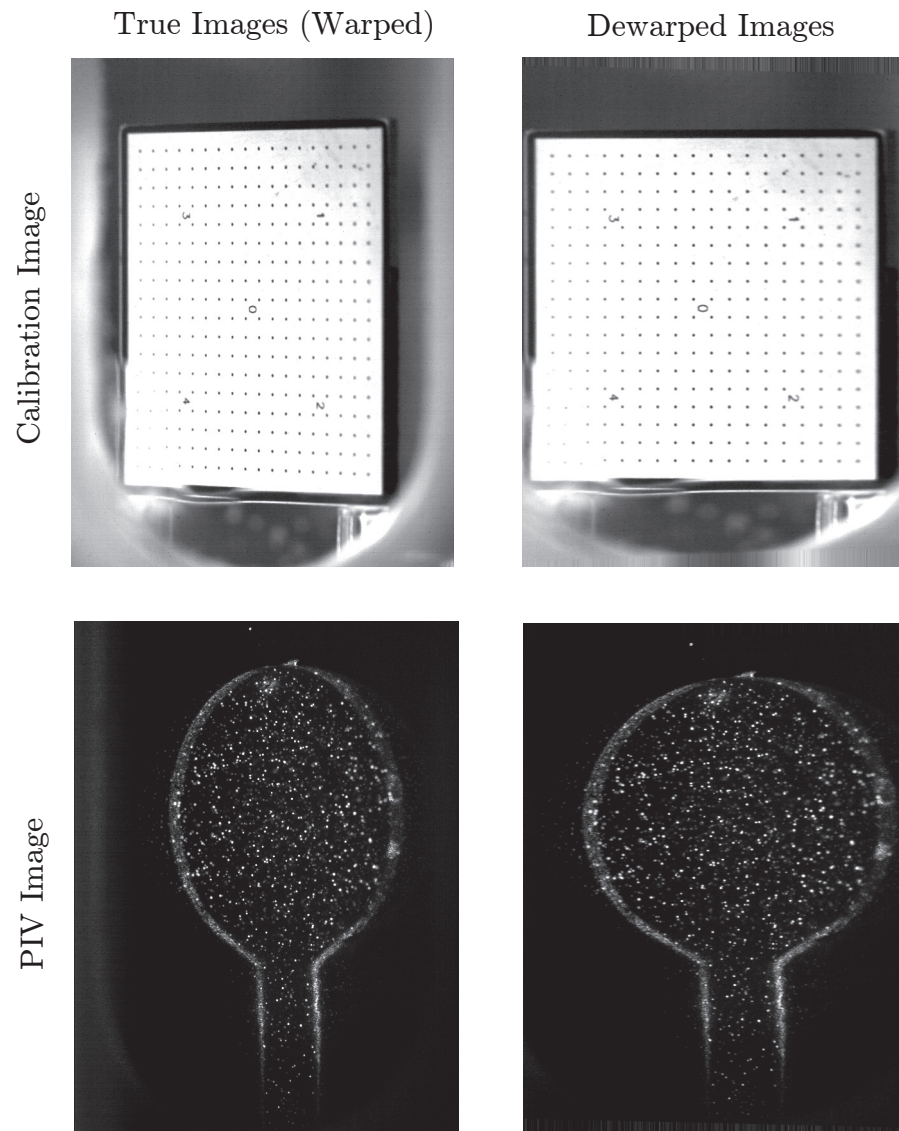


Figure 5.5: Distorted images (*left*) and dewarped images (*right*) of the calibration target (*top*) and the flow plane (*bottom*).

achieved over the entire image plane. This confines accurate imaging to the focused center of the image. The benefit of this configuration is that it minimizes the number of optical component needed for imaging. The amount of light collected by the camera is a major issue when using fluorescent particles; as a result, it is important to maximize the amount of light by reducing components and shortening the optical path. The reduction in complexity means that there are fewer degrees of freedom to constrain when aligning the setup. Any variations in magnification are adjusted during preprocessing through calibration and the use of the target grid.

5.2.4 Algorithms

Dewarping

The images are dewarped prior to PIV processing. The dewarping code consists of a series of functions written in Interface Description Language (IDL). The algorithm accepts a warped image of the calibration plane. The first function locates the grid points on the calibration image using a Sobel edge detection kernel and a search loop that locates each circular edge [1]. A second function uses the grid points to correlate the warped coordinates and dewarped target coordinate. The IDL command POLYWARP is used to find a polynomial curve fit that defines the mapping function that dewarps the image. The mapping function is then applied to the all of the PIV images. The pre-processed images are then sent into the PIV software for analysis.

Processing and Phase Averaging

SPIV processing is done with the adaptive Lagrangian parcel tracking (aLpt) algorithm used in PIV. Image parity exchange (IPX) is used as well to reduce the bias error introduced by the walls. Dewarped pairs of images from each camera are processed and phased average as discussed in section 4.2.4. For the SPIV experiments, the sample point is phased shifted to obtain a resolution of 360 samples per waveform and averaged over 7 image pairs per point.

Displacement Reconstruction

An IDL program processes the two displacement fields by implementing the geometric reconstruction techniques using geometric arguments initially developed by Brücker [7]. The geometric relations are reconstructed for the experimental configuration used in this dissertation in a similar manner to Brücker, including corrections to errors made in the paper. All angles and displacements are defined in Figure 5.3. A pinhole camera approximation is used. Using geometry, the displacement in the x-direction, dx , can be derived relative to each camera:

$$dx = dx_1 + dz \tan \alpha_1, \quad (5.1)$$

$$dx = dx_2 + dz \tan \alpha_2, \quad (5.2)$$

Notice that this expression is true whether the cameras are on the same or opposite sides of the object plane as long as the angles carefully defined. Setting Equations 5.1 and 5.2

equal, the following expression for the displacement in the z -direction, dz , is derived

$$dz = \frac{dx_2 - dx_1}{\tan \alpha_1 - \tan \alpha_2}. \quad (5.3)$$

An expression for dx is developed by adding equations 5.1 and 5.2 and plugging into Equation 5.3 to define dx as

$$dx = \frac{dx_2 \tan \alpha_1 - dx_1 \tan \alpha_2}{\tan \alpha_1 - \tan \alpha_2}. \quad (5.4)$$

By similar methods, it can be shown that the following expression for the displacement in y , dy , is valid as well

$$dy = \frac{dy_2 \tan \beta_1 - dy_1 \tan \beta_2}{\tan \beta_1 - \tan \beta_2}. \quad (5.5)$$

Those equations can be manipulated using geometric relations, to rewrite the expressions for dy and dz

$$dy = \frac{dy_1 + dy_2}{2} + \frac{dx_2 - dx_1}{2} \left(\frac{\tan \beta_2 - \tan \beta_1}{\tan \alpha_1 - \tan \alpha_2} \right), \quad (5.6)$$

$$dz = \frac{dy_2 - dy_1}{\tan \beta_1 - \tan \beta_2}. \quad (5.7)$$

For cases where the difference between $\tan \beta_1$ and $\tan \beta_2$ are small, Equation 5.6 simplifies to the average of dy_1 and dy_2 . The result of the reconstruction is a single 3D displacement field for the flow plane for the time between images within a pair. The final result is a complete velocity field that captures both in and out-of-plane components. Often the cameras are positioned at small, symmetric β , resulting in small values of $\tan \beta_1$ and $\tan \beta_2$. Recall from numerical methods that subtraction and division of small numbers, such as in Equations 5.5 and 5.7, should be avoided. Equations 5.3, 5.4, and 5.6 are used in this dissertation to reconstruct the 3D velocity field.

The out-of-plane velocity in the SPIV experiments is w , the z -component of velocity based on the coordinate system defined in Figure 2.1. This is equivalent to the horizontal component of velocity in the PIV data. Therefore, SPIV out-of-plane velocity measurements along the midline should be equal to PIV horizontal velocity measurements along the same common midline. As a validation, both velocities are plotted at different points along the flow waveform in Figure 5.6. The velocities match over the relaxation phase. During ramp up and ramp down phases, the velocity measurements from SPIV are higher than PIV near the tip where flow reaches a local maximum.

5.3 SPIV:Post-Processing

In PIV, aLPT uses the Fourier transform in cross-correlation to find the velocity gradients during processing. However, these gradients are inaccurate in SPIV because of image distortion. A least-squares differentiation is used on the 3D velocity field to find the local gradients over the entire velocity field [50]. The general form of the local differential of a discrete function, h , at a point i is

$$\frac{dh_i}{dx} = \frac{2h_{i+2} + h_{i+1} - h_{i-1} + 2h_{i+2}}{10\delta x}, \quad (5.8)$$

where δx is the distance between two discrete points along the function [50]. Differentials can be calculated in the in-plane and x and y directions. Through continuity, the differential $\frac{\partial w}{\partial z}$ can be found. However, $\frac{\partial u}{\partial z}$ and $\frac{\partial v}{\partial z}$ are required for calculation of the out-of-plane terms of Q and WSS. Plots of Q presented in the results are in-plane values using Eqn. 4.8. The WSS measurements in this experiment are limited to the in-plane components only except

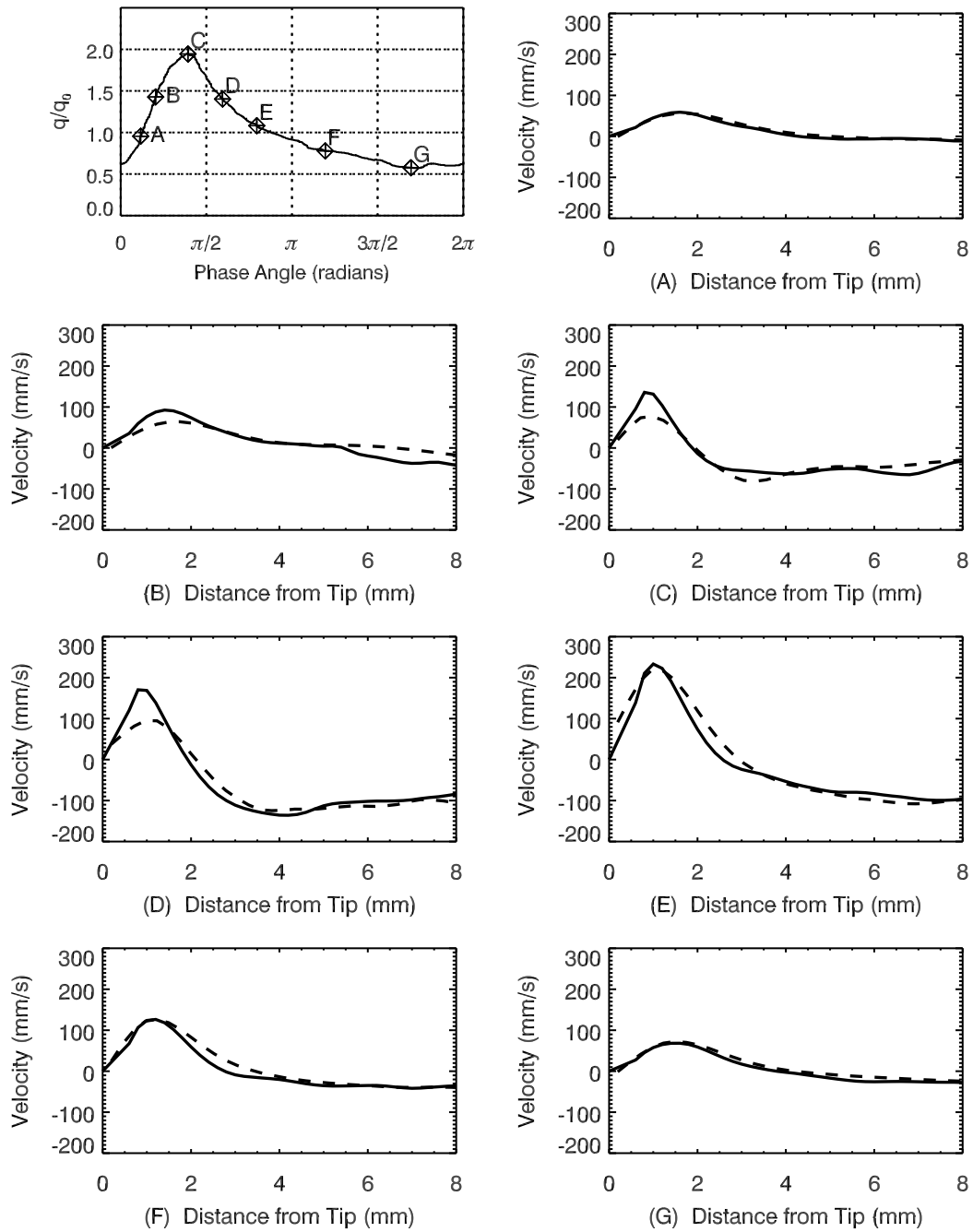


Figure 5.6: Validation of SPIV measurements by comparing out-of-plane SPIV velocity measurements (*solid line*) to the corresponding PIV velocity (*dashed line*).

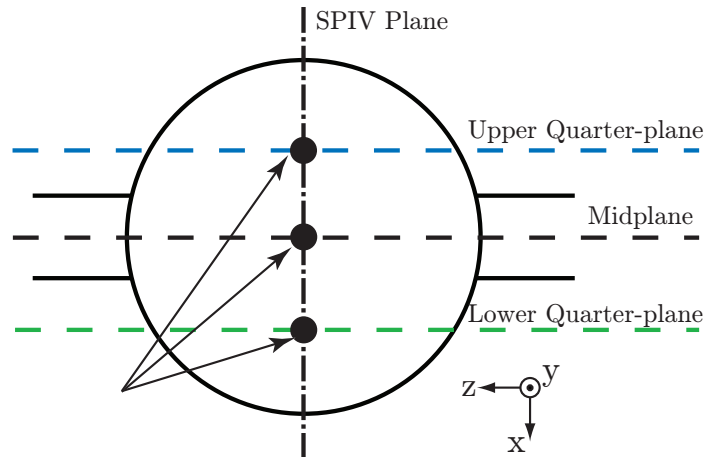


Figure 5.7: Diagram of the PIV and SPIV planes along the dome from an overhead view, as well as the intersection points. The middle intersection point is the tip of the dome.

where a common point is shared with the PIV measurements. This occurs at three points along the fundus where the SPIV plane intersects the upper and lower quarter-planes and at the tip where it intersects the midplane (Figure 5.7).

An angular coordinate system is defined to describe WSS at different points along the dome, similar to the one used in the previous chapter. The definition has changed because the SPIV plane is orthogonal to the PIV planes. For an origin at the center of the dome, all points on the tip can be defined at an angle relative to the tip (Figure 5.8). Again, the coordinate system is clockwise positive.

5.4 SPIV: Results

SPIV results are presented in the following figures. Figures 5.9-5.17 plot vector fields of the in-plane components of velocity and color plots of the out-of-plane velocity

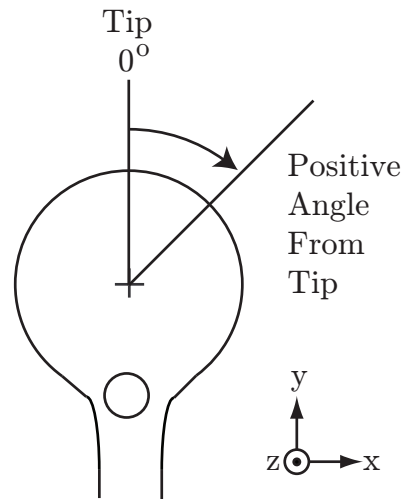


Figure 5.8: Definition of *angle from tip* that is used to describe dome coordinates in the SPIV WSS plots)

component. Figures 5.18-5.26 are plots of Q over the dome during the waveform. Figures 5.27-5.35 plot in-plane WSS vs. wall coordinates for the flow ratios. Figures 5.36-5.44 plot the total WSS magnitude for the 3 intersection points between the PIV and SPIV plane. Table 5.1 lists the peak magnitudes experienced by the three intersection points. Table 5.2 lists the mean magnitudes experienced by the three intersection points.

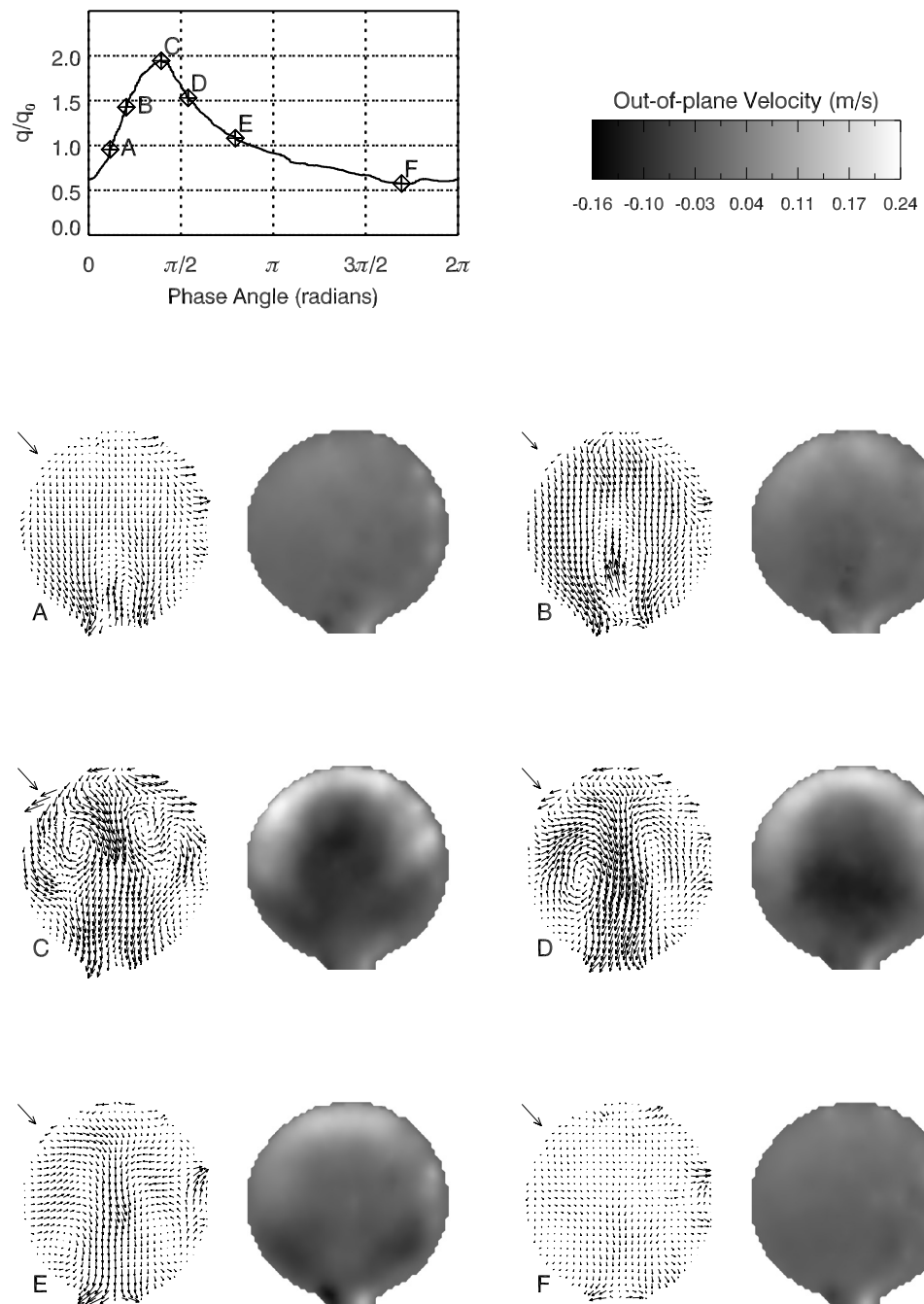


Figure 5.9: Plot of the in-plane velocity vector field (left) and and out-of-plane velocity (right) for a branching ratio of 20:80 over one cycle indicated by the points in the plot of the waveform cycle.

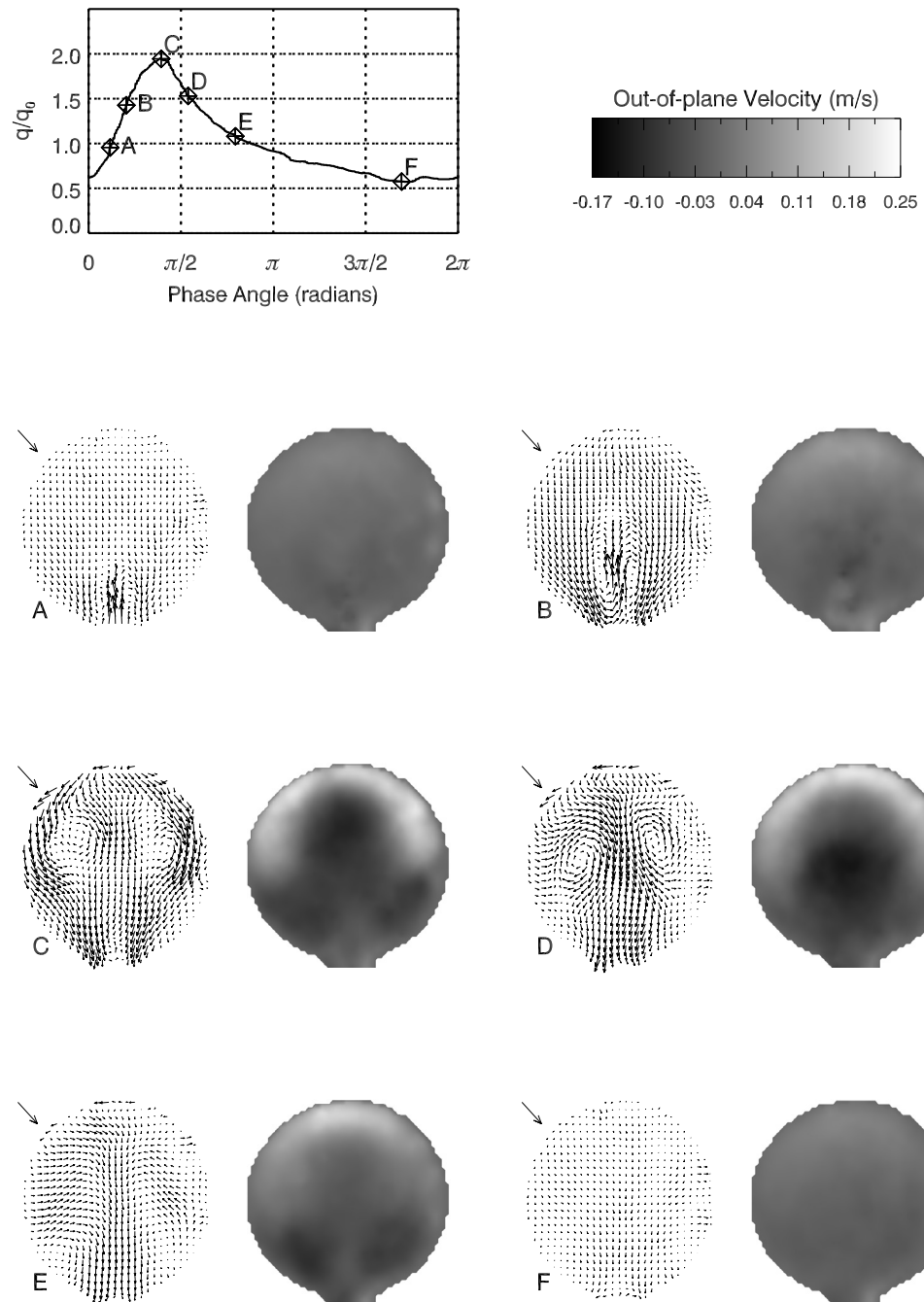


Figure 5.10: Plot of the in-plane velocity vector field (left) and out-of-plane velocity (right) for a branching ratio of 25:75 over one cycle indicated by the points in the plot of the waveform cycle.

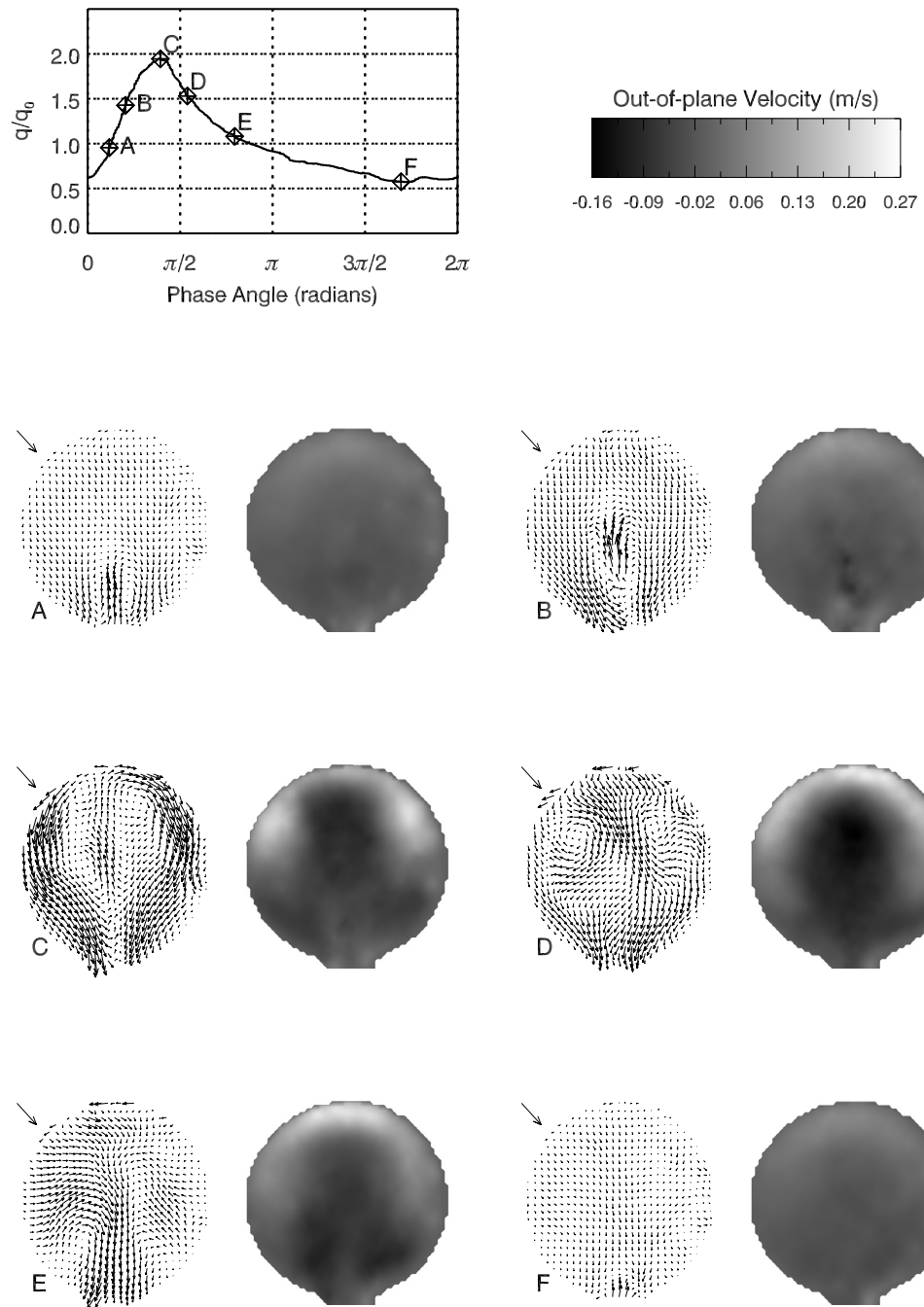


Figure 5.11: Plot of the in-plane velocity vector field (left) and out-of-plane velocity (right) for a branching ratio of 33:67 over one cycle indicated by the points in the plot of the waveform cycle.

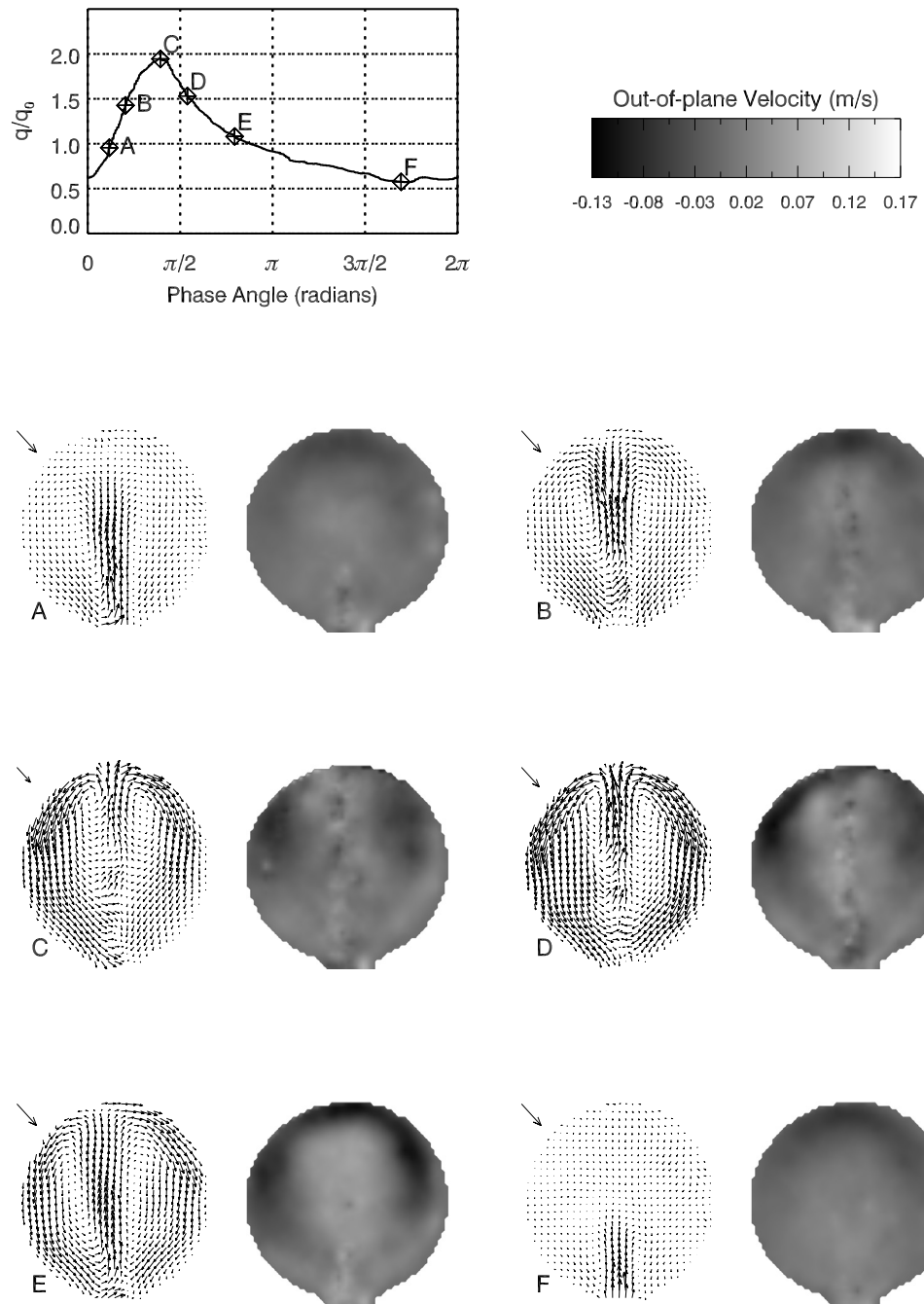


Figure 5.12: Plot of the in-plane velocity vector field (left) and out-of-plane velocity (right) for a branching ratio of 46:54 over one cycle indicated by the points in the plot of the waveform cycle.

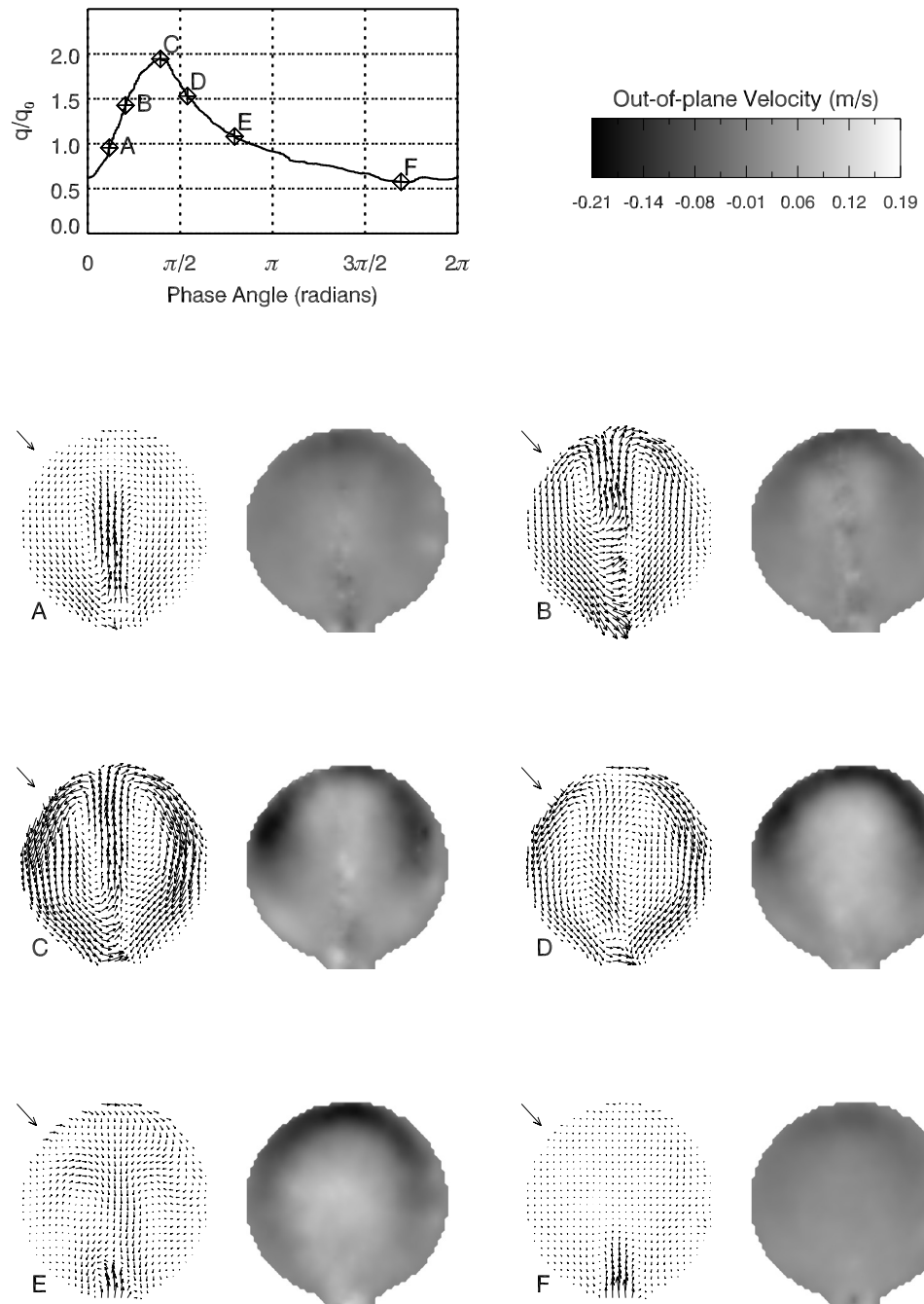


Figure 5.13: Plot of the in-plane velocity vector field (left) and and out-of-plane velocity (right) for a branching ratio of 48:52 over one cycle indicated by the points in the plot of the waveform cycle.

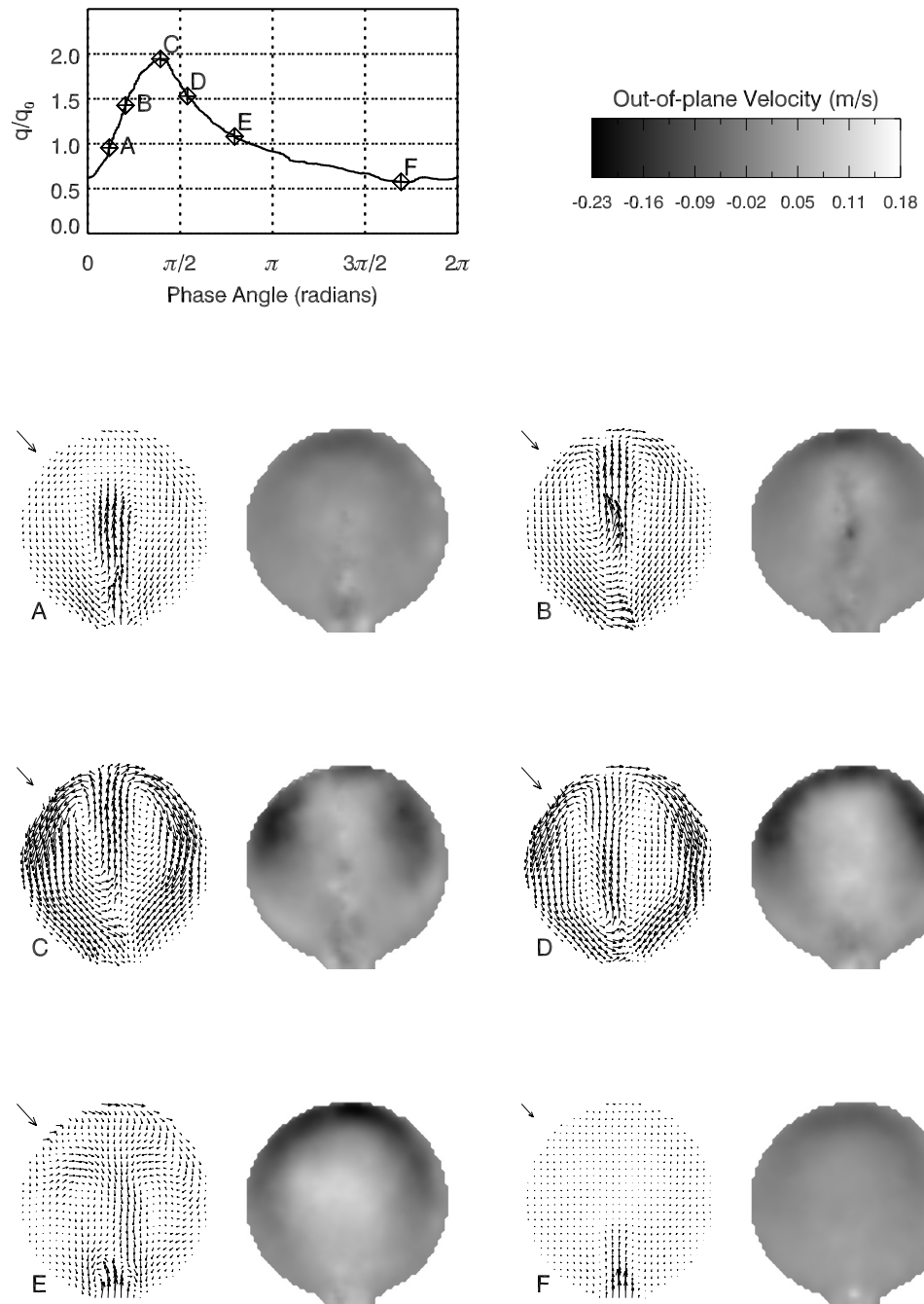


Figure 5.14: Plot of the in-plane velocity vector field (left) and and out-of-plane velocity (right) for a branching ratio of 50:50 over one cycle indicated by the points in the plot of the waveform cycle.

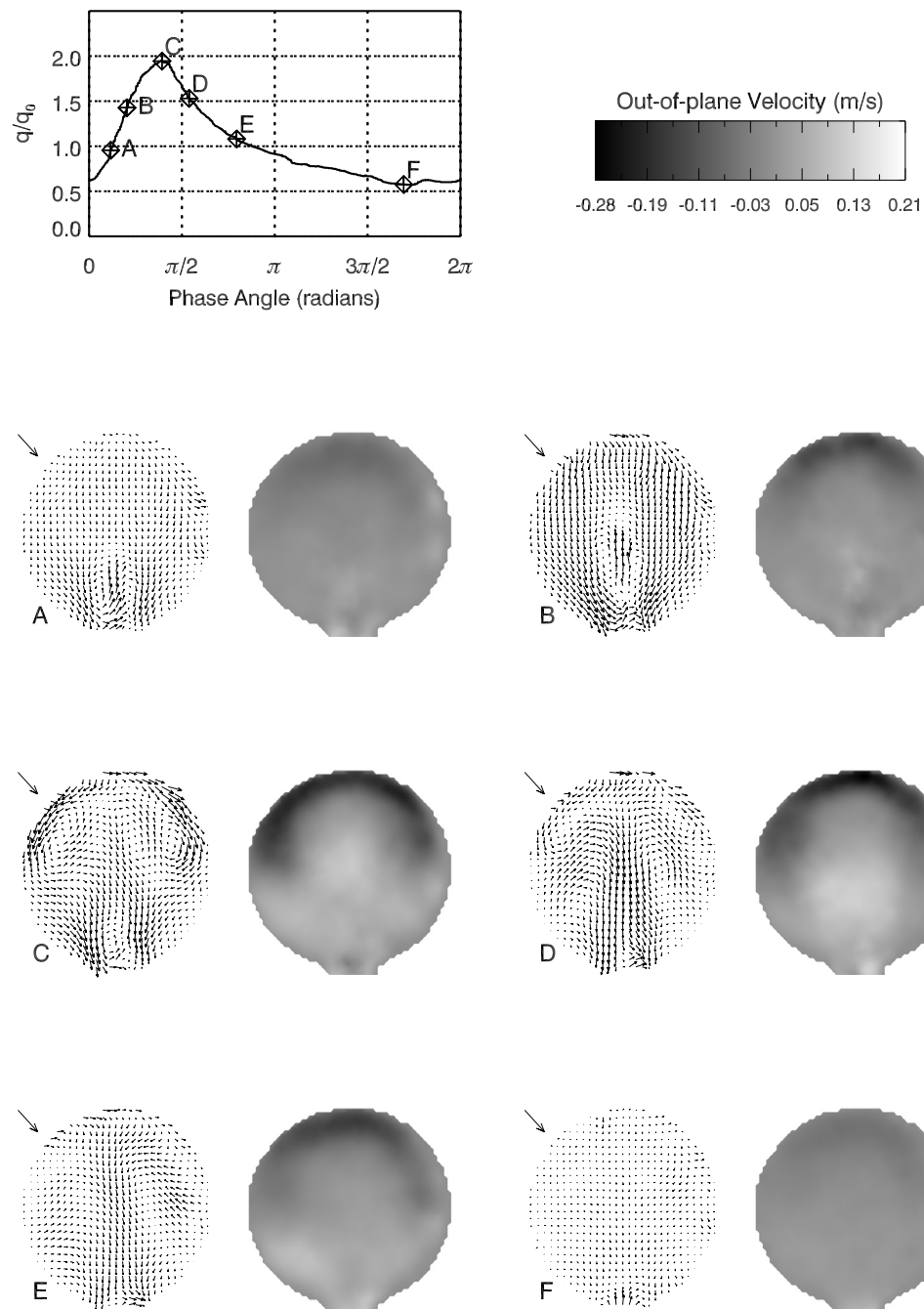


Figure 5.15: Plot of the in-plane velocity vector field (left) and out-of-plane velocity (right) for a branching ratio of 67:33 over one cycle indicated by the points in the plot of the waveform cycle.

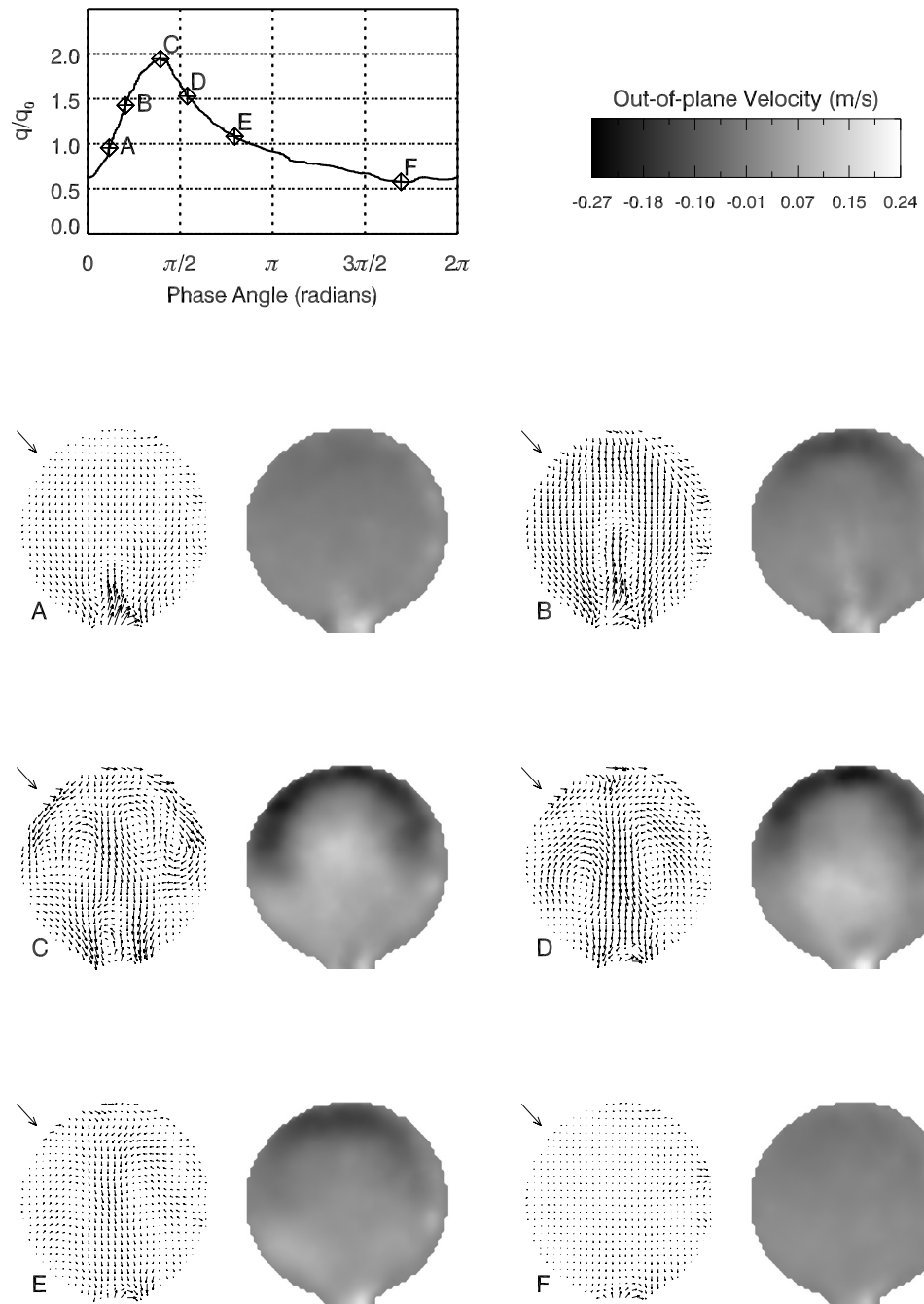


Figure 5.16: Plot of the in-plane velocity vector field (left) and out-of-plane velocity (right) for a branching ratio of 75:25 over one cycle indicated by the points in the plot of the waveform cycle.

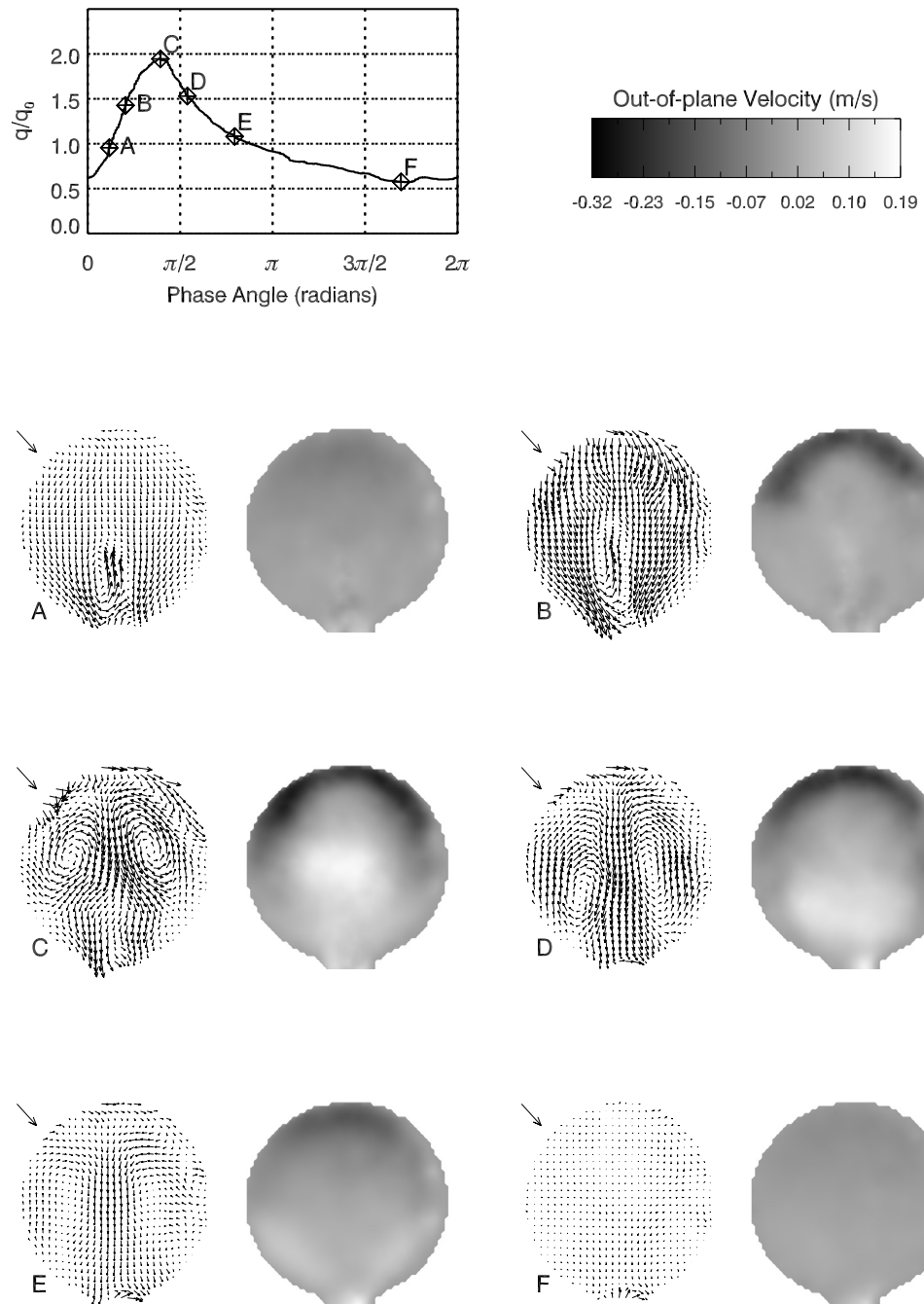


Figure 5.17: Plot of the in-plane velocity vector field (left) and out-of-plane velocity (right) for a branching ratio of 80:20 over one cycle indicated by the points in the plot of the waveform cycle.

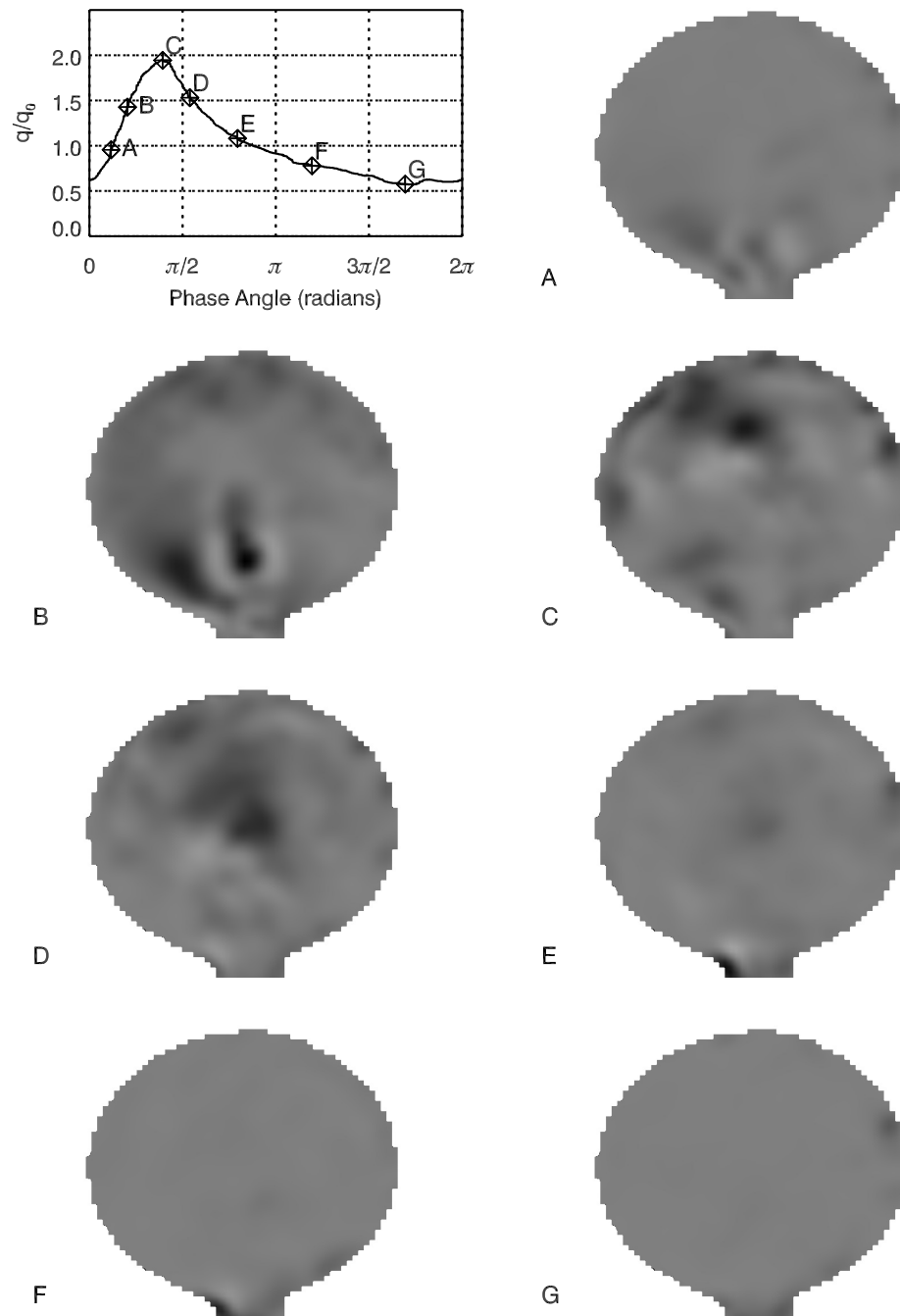


Figure 5.18: Plot of the second invariant of the velocity gradient, Q , for a branching ratio of 20:80 over one cycle indicated by the points in the plot of the waveform cycle.

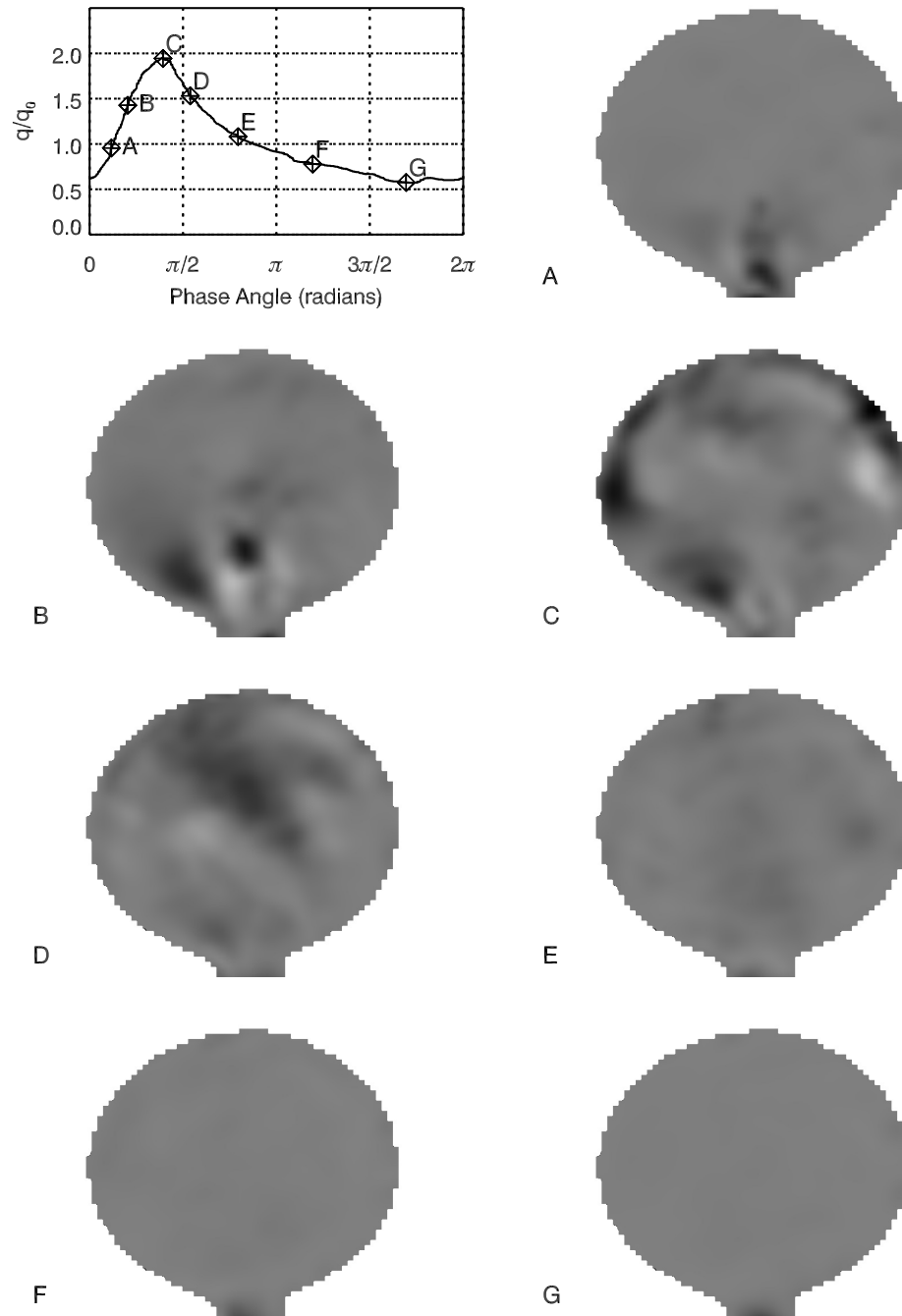


Figure 5.19: Plot of the second invariant of the velocity gradient, Q , for a branching ratio of 25:75 over one cycle indicated by the points in the plot of the waveform cycle.

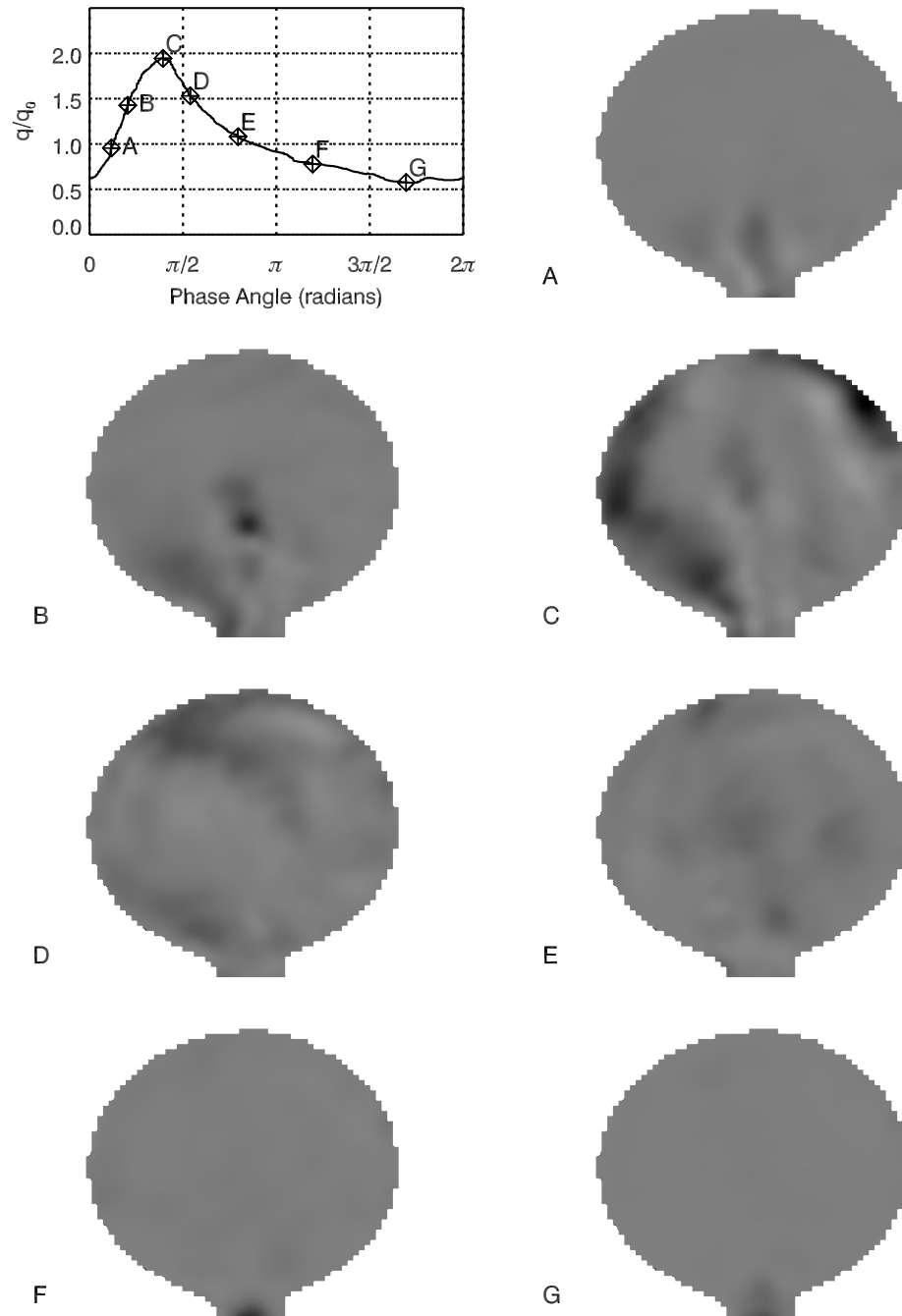


Figure 5.20: Plot of the second invariant of the velocity gradient, Q , for a branching ratio of 33:67 over one cycle indicated by the points in the plot of the waveform cycle.

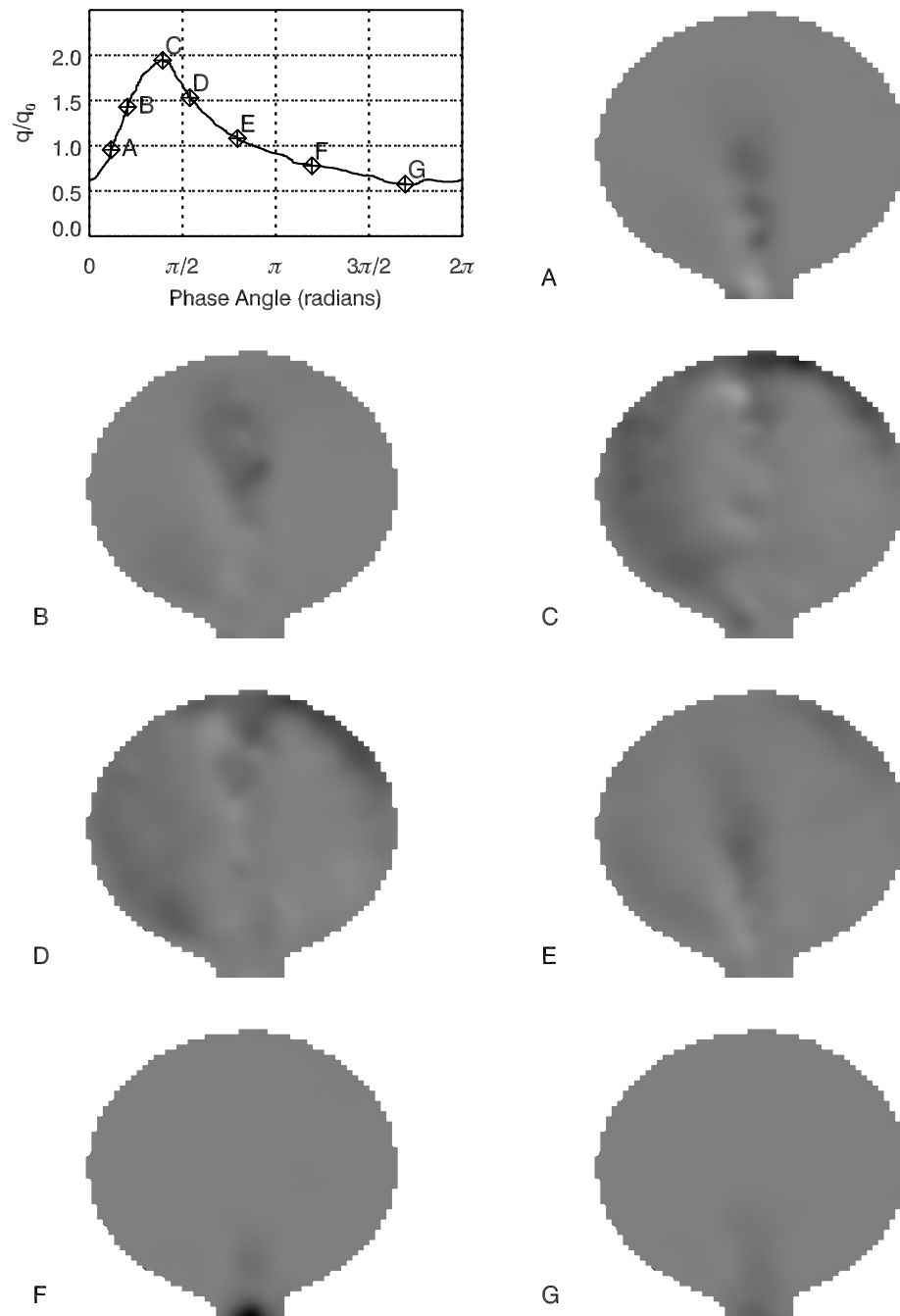


Figure 5.21: Plot of the second invariant of the velocity gradient, Q , for a branching ratio of 46:54 over one cycle indicated by the points in the plot of the waveform cycle.

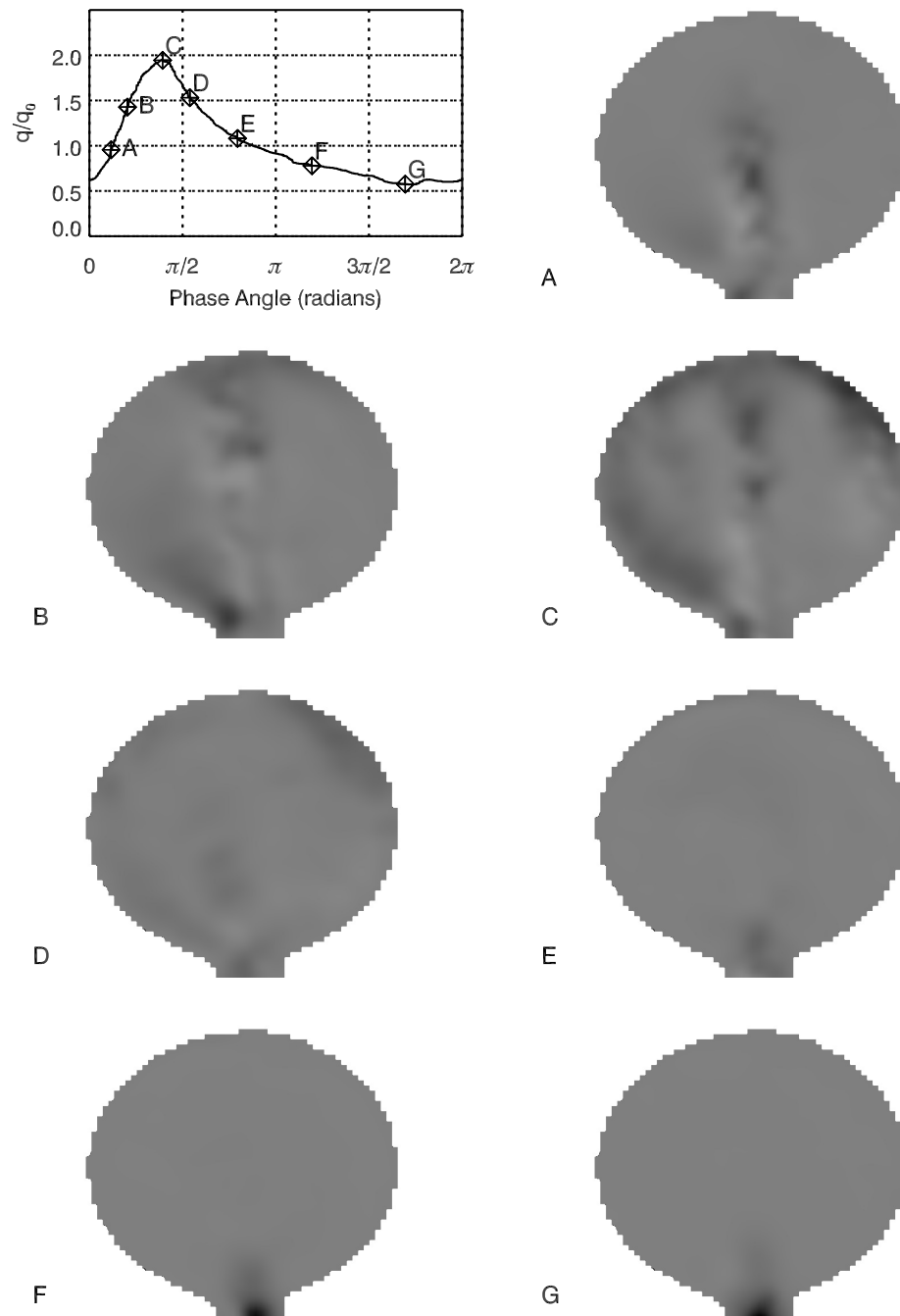


Figure 5.22: Plot of the second invariant of the velocity gradient, Q , for a branching ratio of 48:52 over one cycle indicated by the points in the plot of the waveform cycle.

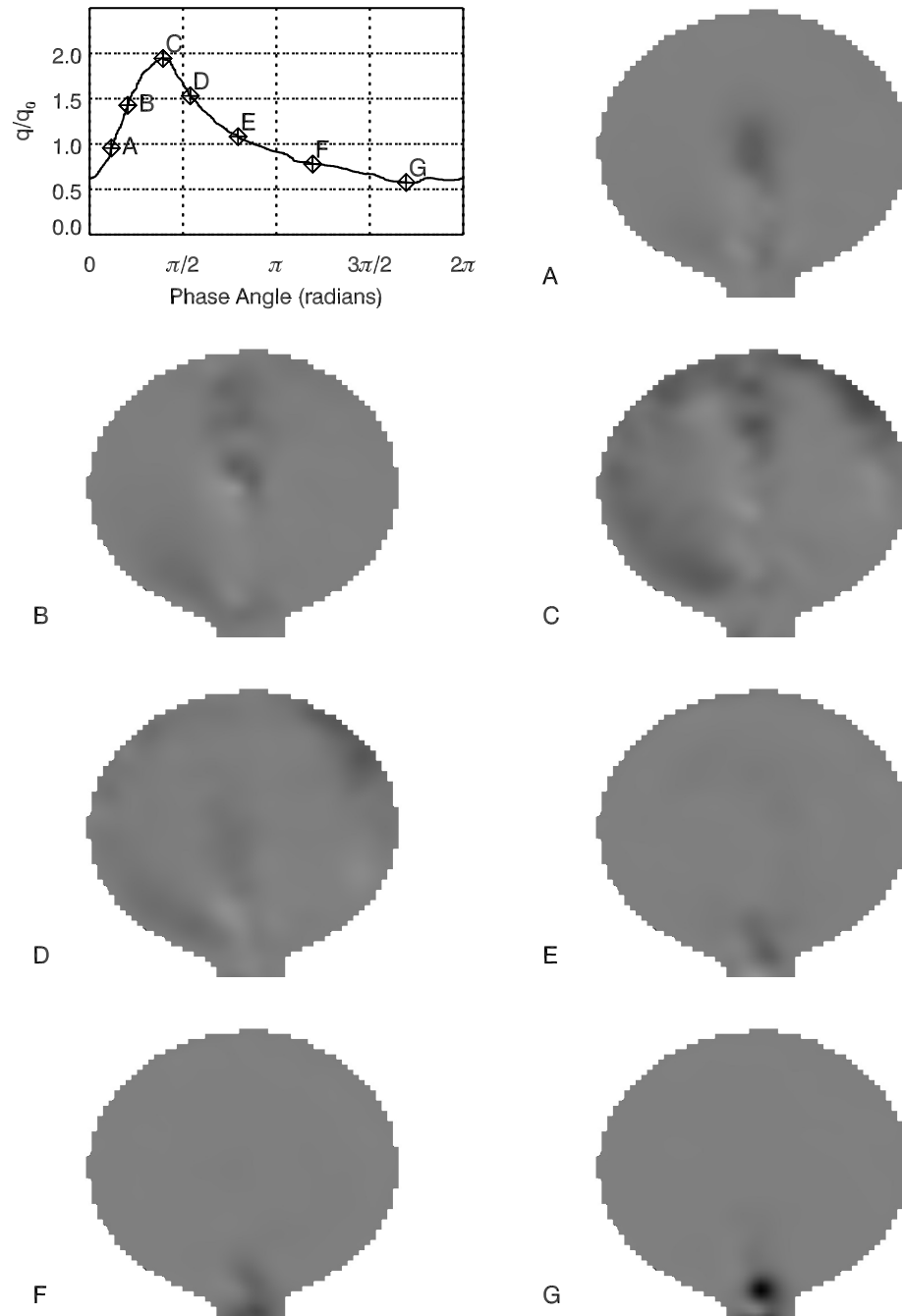


Figure 5.23: Plot of the second invariant of the velocity gradient, Q , for a branching ratio of 50:50 over one cycle indicated by the points in the plot of the waveform cycle.

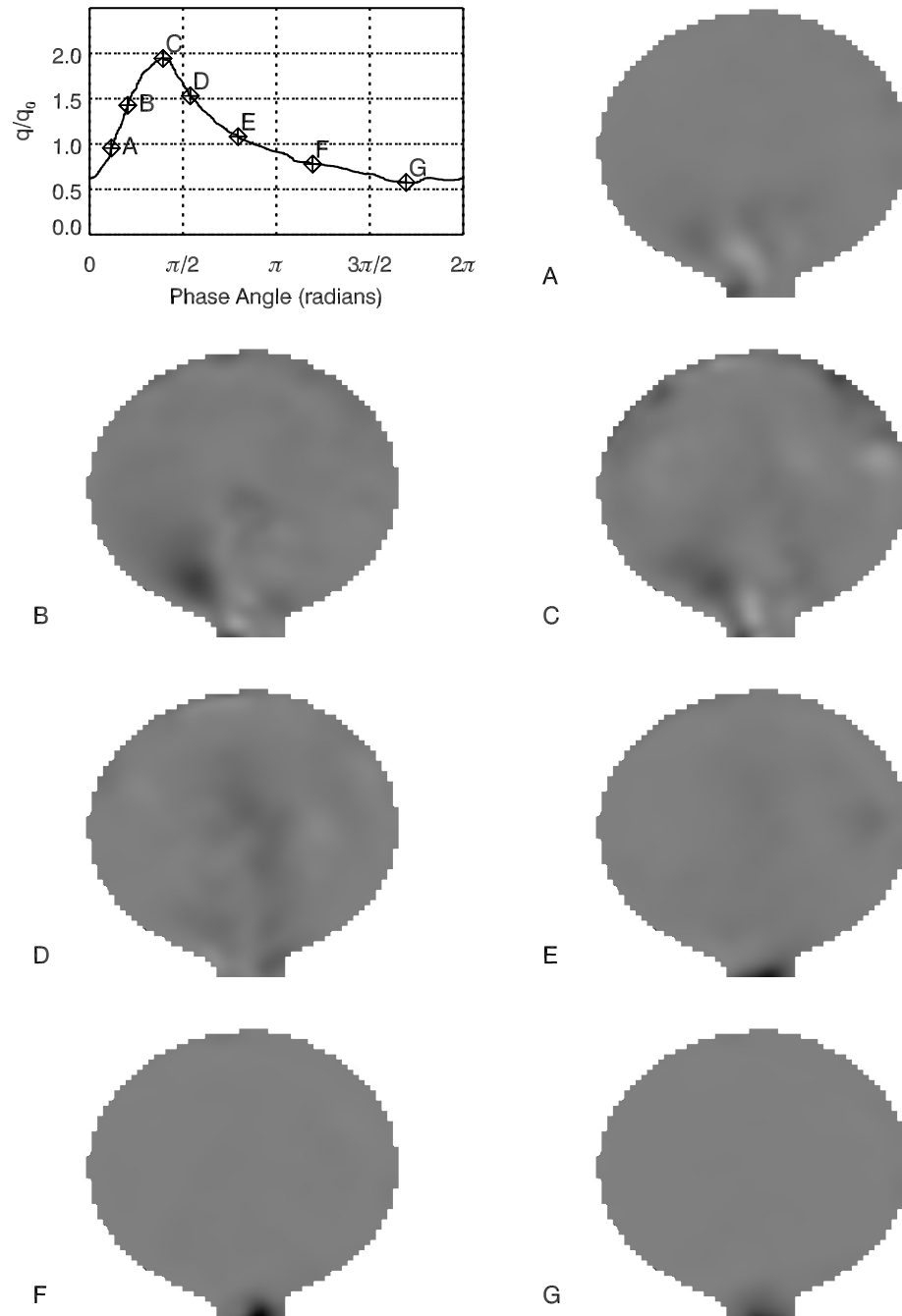


Figure 5.24: Plot of the second invariant of the velocity gradient, Q , for a branching ratio of 67:33 over one cycle indicated by the points in the plot of the waveform cycle.

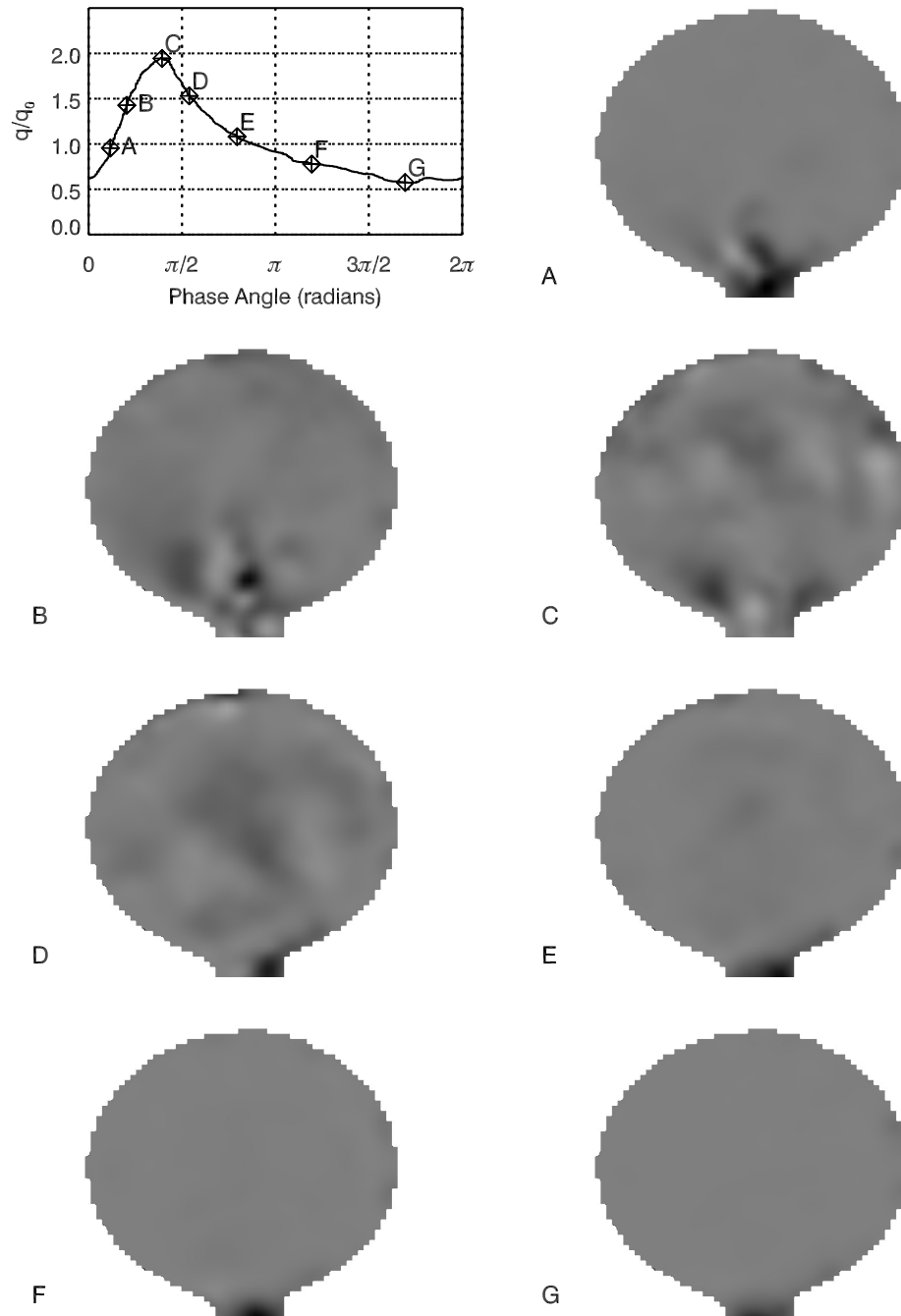


Figure 5.25: Plot of the second invariant of the velocity gradient, Q , for a branching ratio of 75:25 over one cycle indicated by the points in the plot of the waveform cycle.

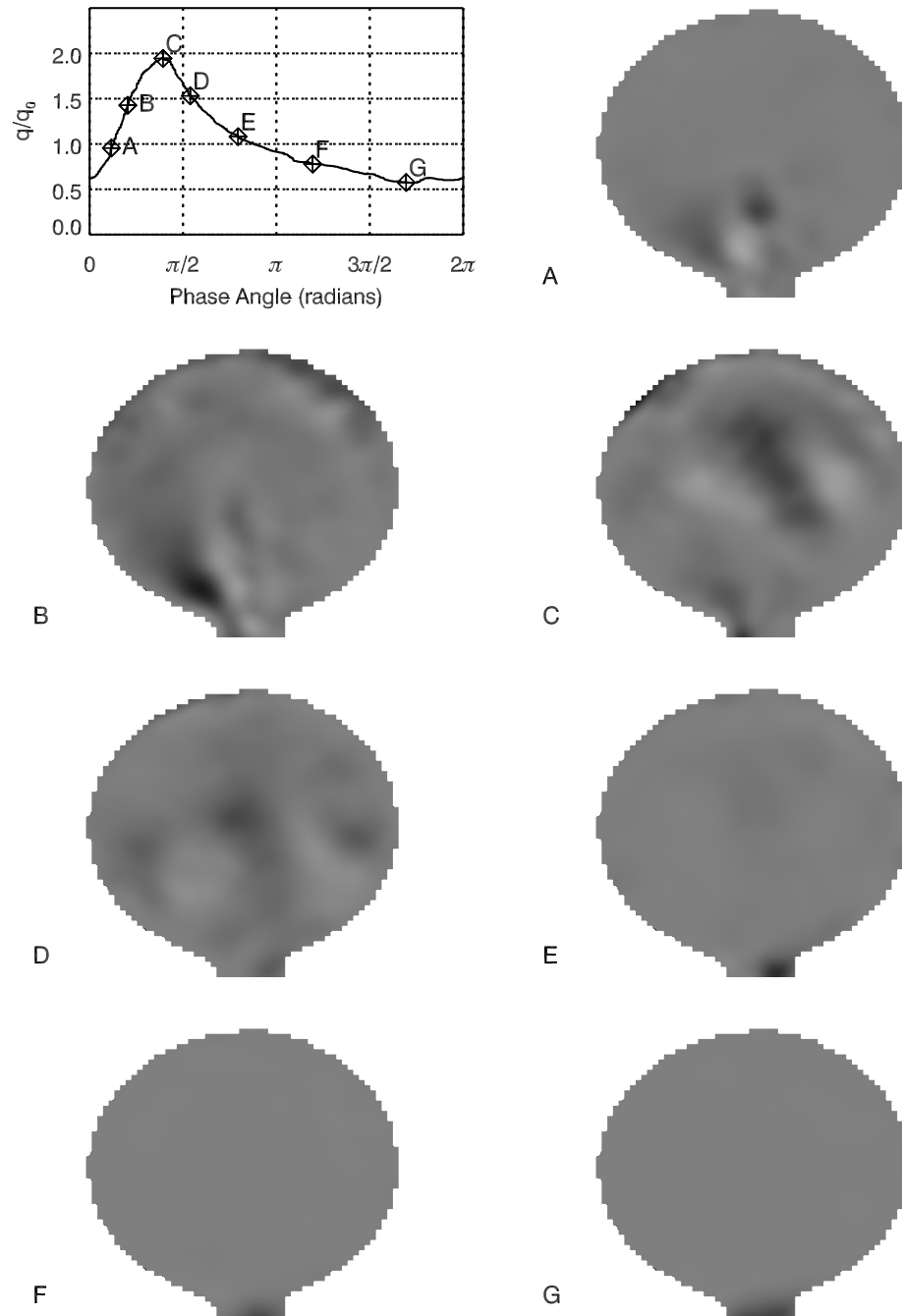


Figure 5.26: Plot of the second invariant of the velocity gradient, Q , for a branching ratio of 80:20 over one cycle indicated by the points in the plot of the waveform cycle.

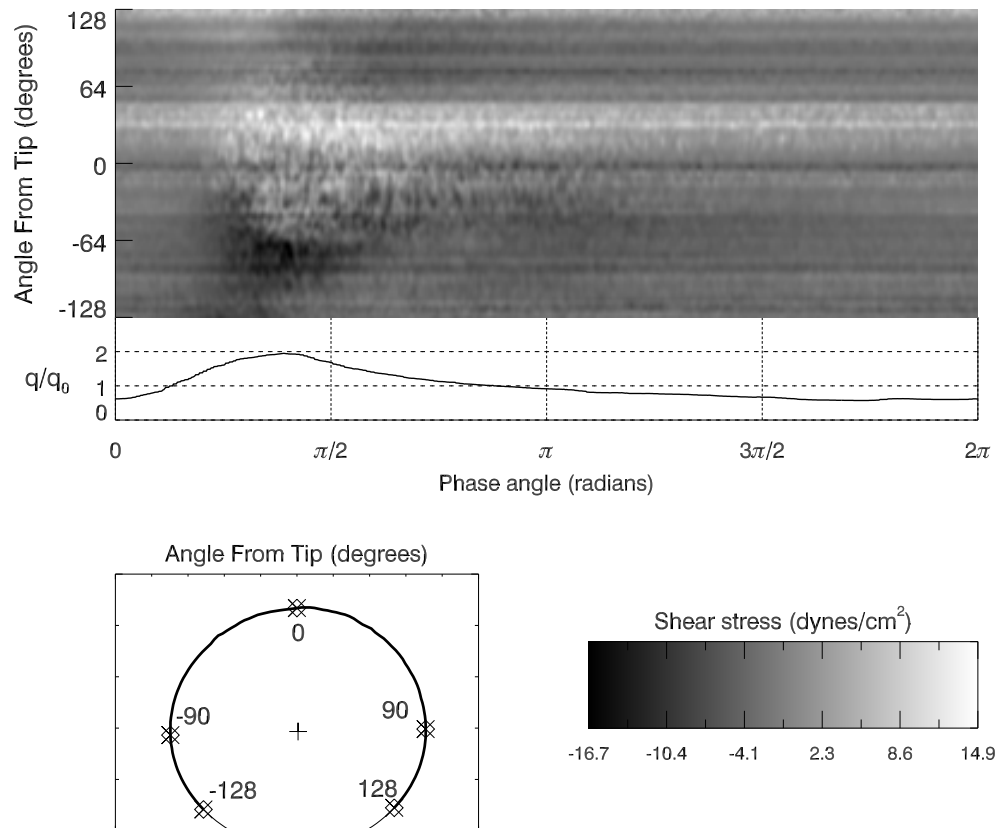


Figure 5.27: In plane WSS history a for a branching ratio of 20:80.

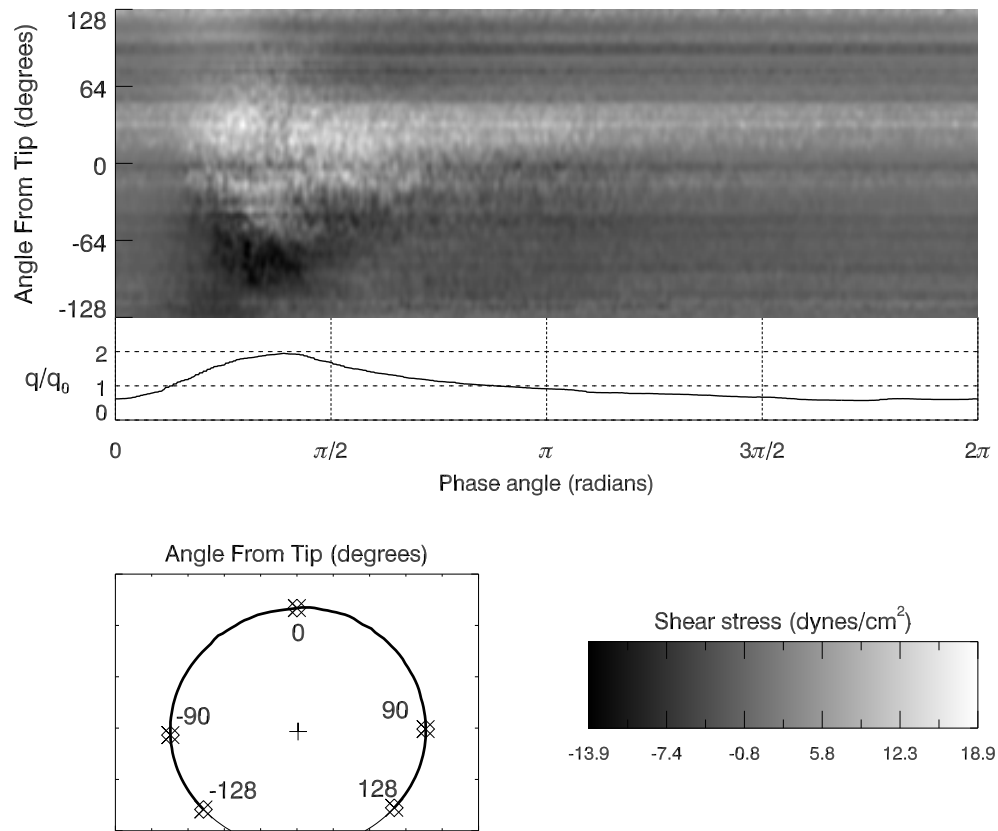


Figure 5.28: In plane WSS history a for a branching ratio of 25:75.

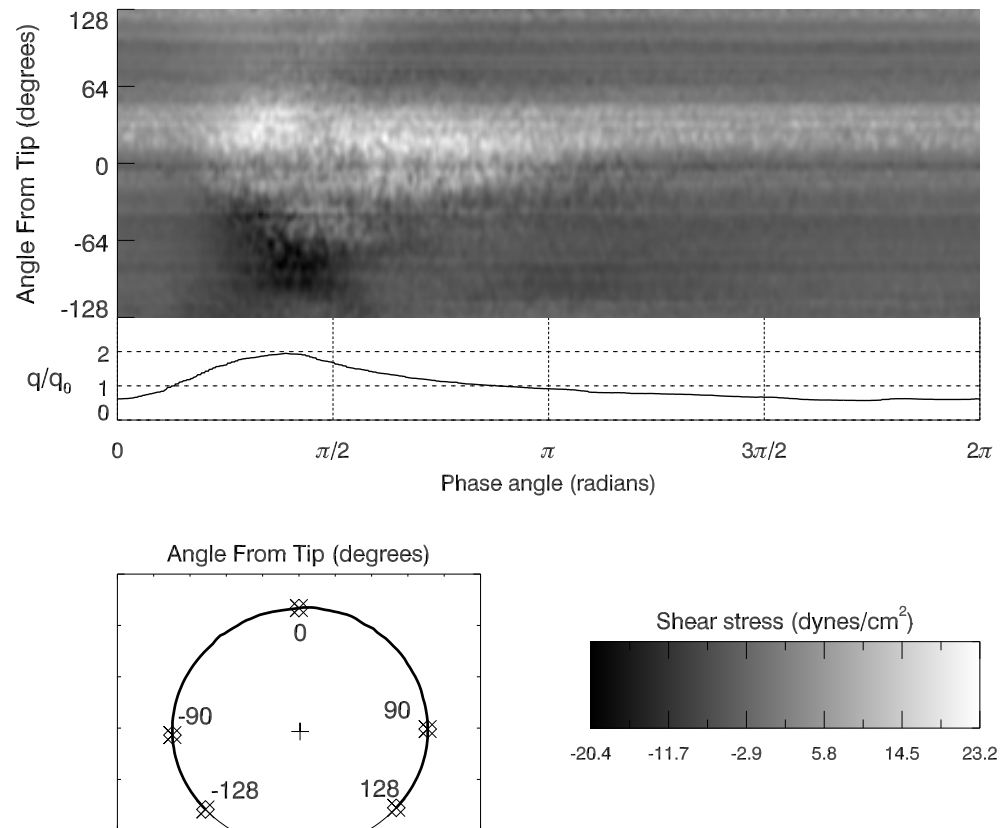


Figure 5.29: In plane WSS history a for a branching ratio of 33:67.

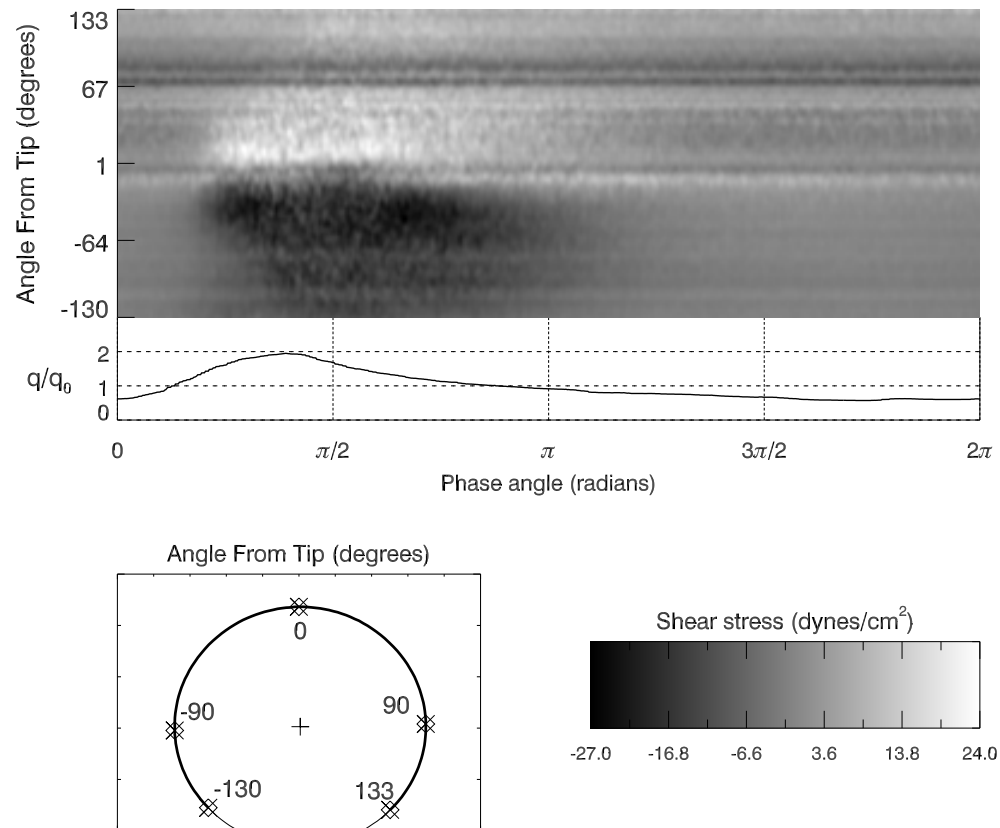


Figure 5.30: In plane WSS history a for a branching ratio of 46:54.

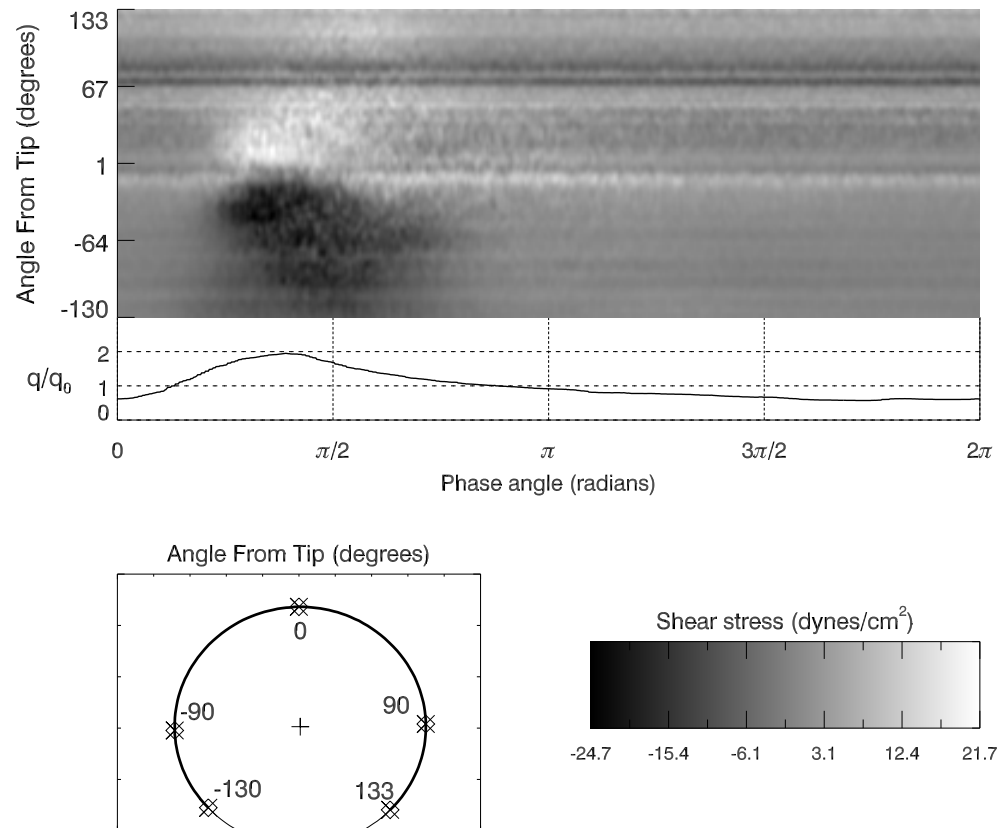


Figure 5.31: In plane WSS history a for a branching ratio of 48:52.

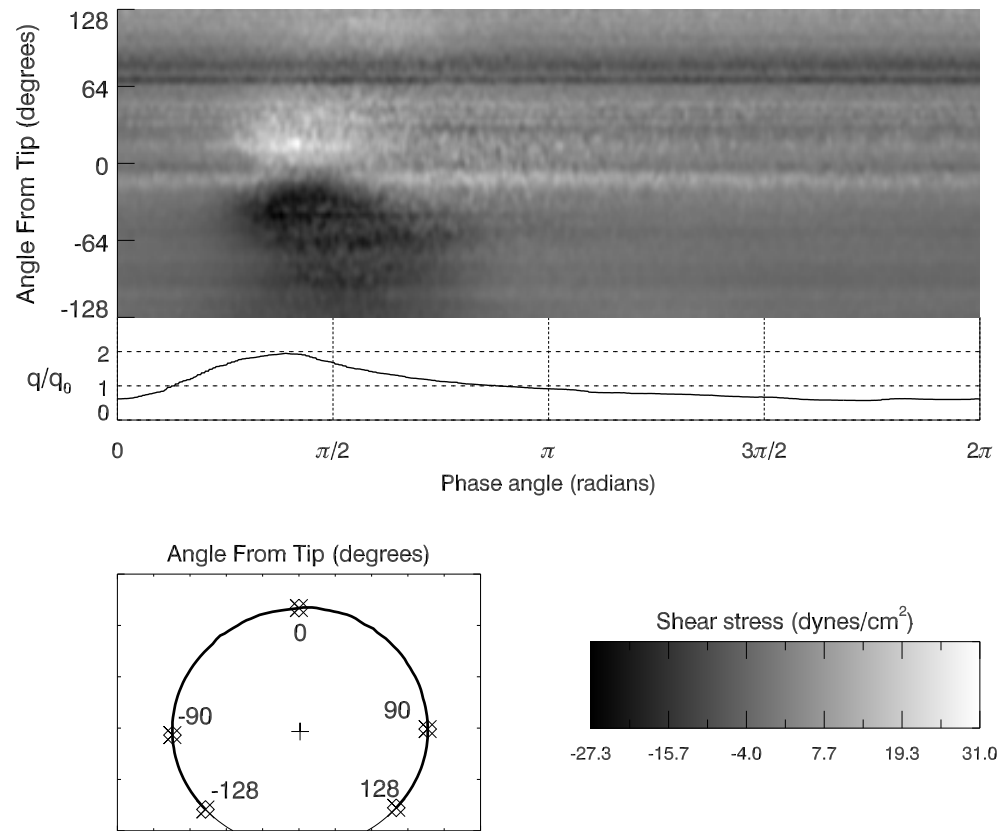


Figure 5.32: In plane WSS history a for a branching ratio of 50:50.

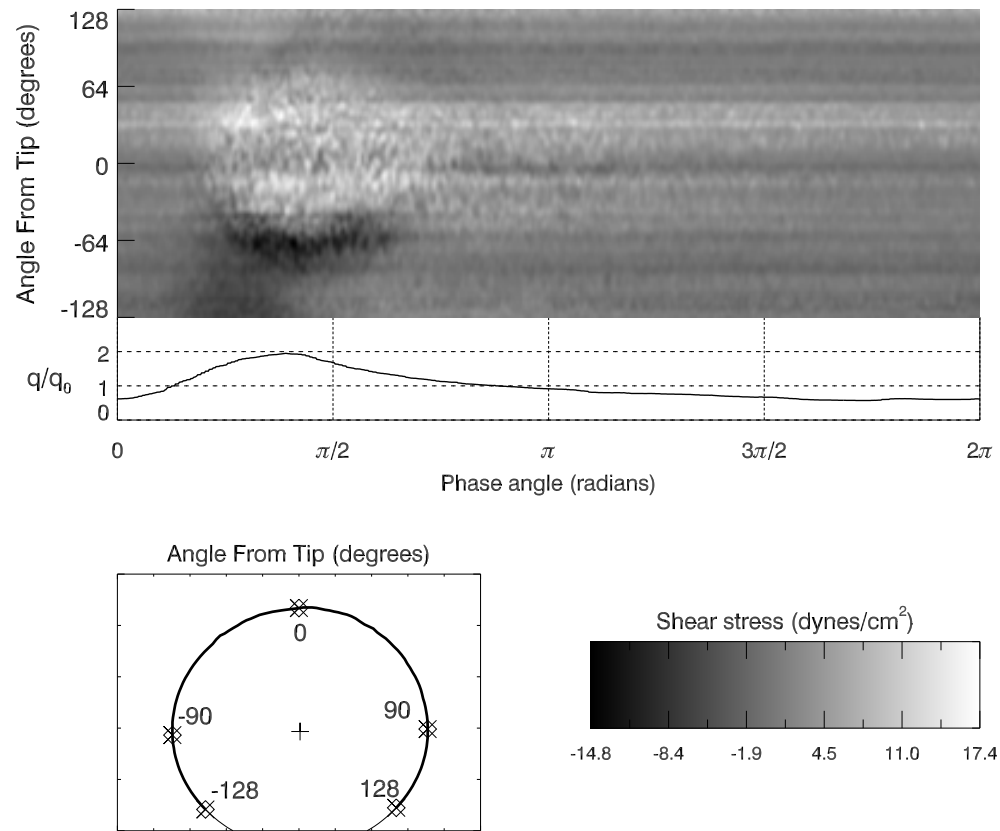


Figure 5.33: In plane WSS history a for a branching ratio of 67:33.

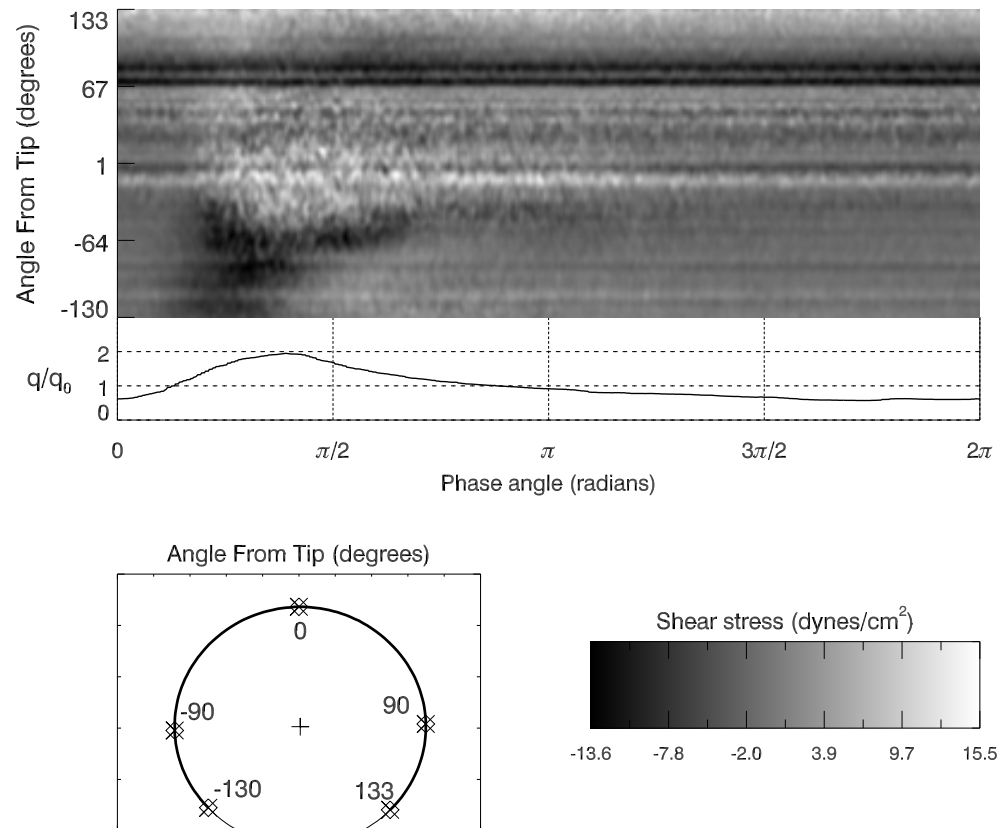


Figure 5.34: In plane WSS history a for a branching ratio of 75:25.

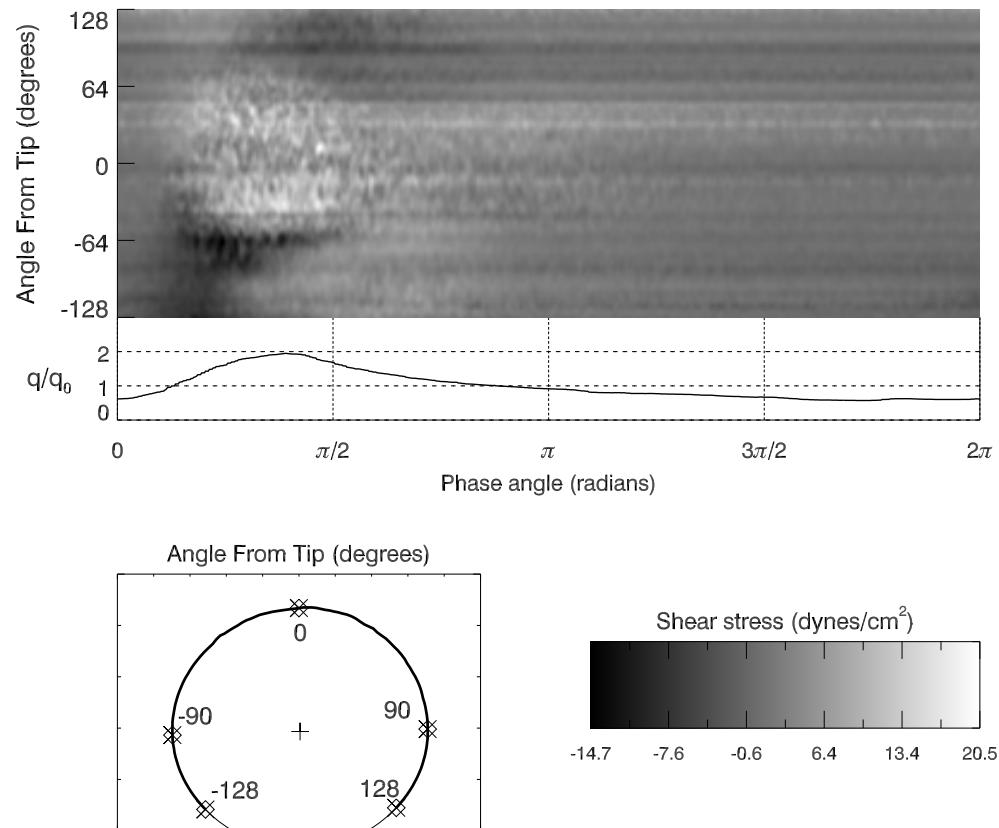


Figure 5.35: In plane WSS history a for a branching ratio of 80:20.

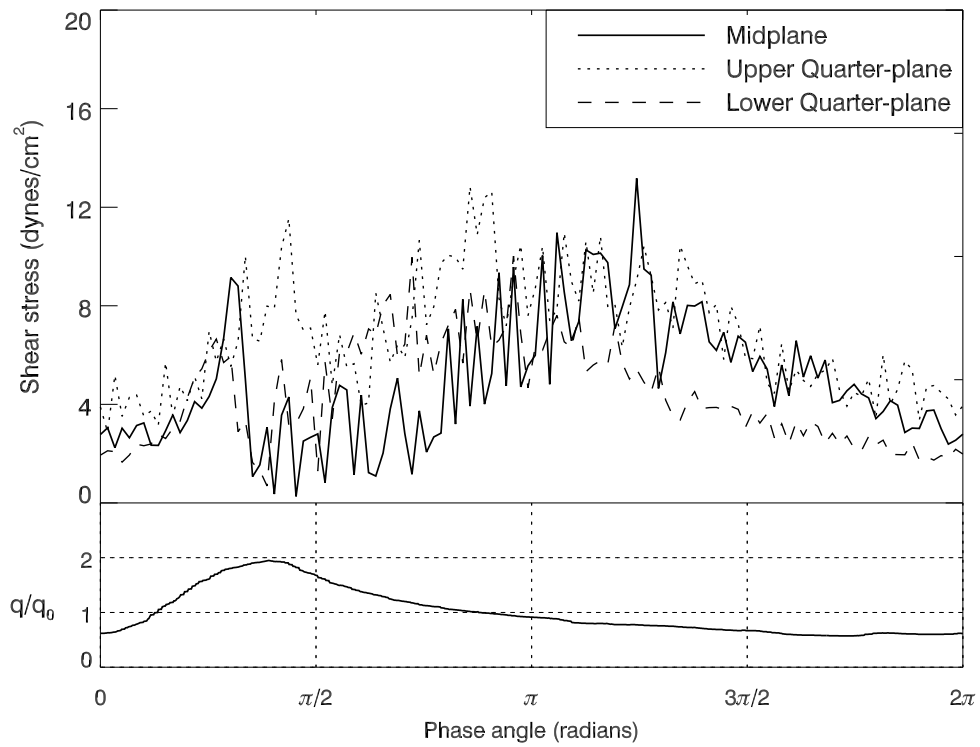


Figure 5.36: WSS magnitudes at the intersection points of the PIV and SPIV imaging planes for a branching ratio of 20:80.

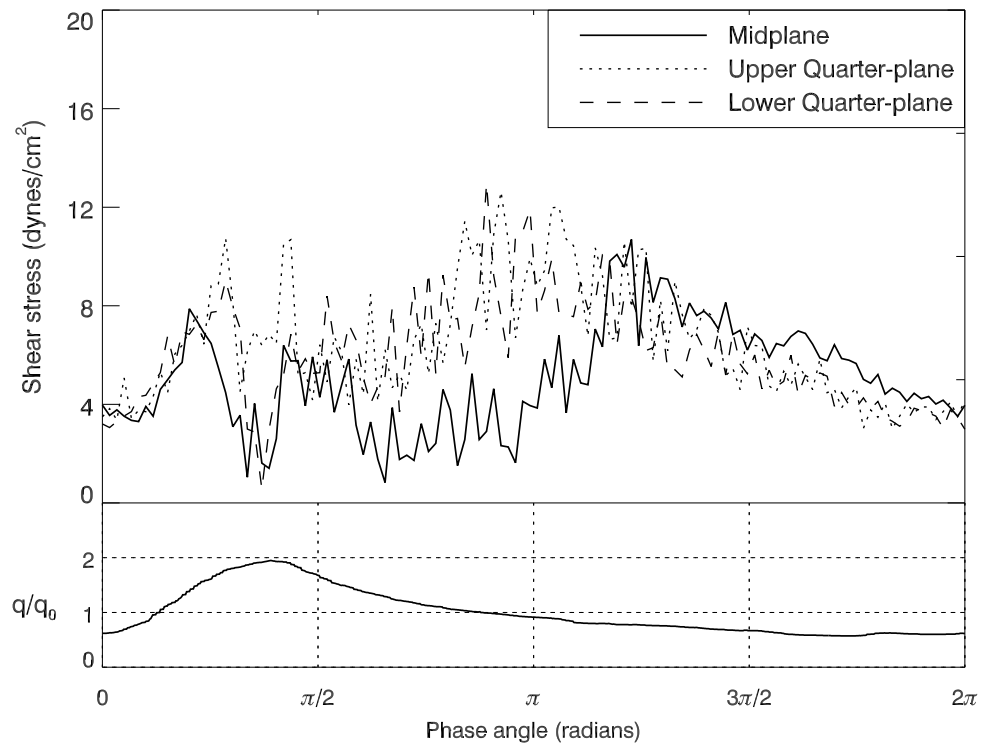


Figure 5.37: WSS magnitudes at the intersection points of the PIV and SPIV imaging planes for a branching ratio of 25:75.

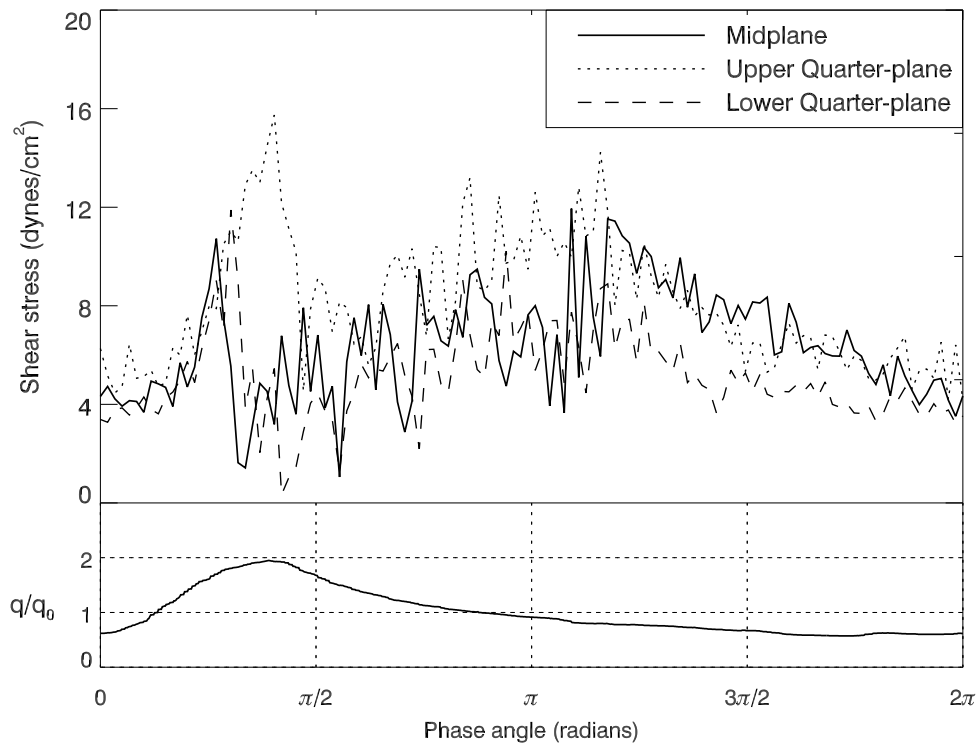


Figure 5.38: WSS magnitudes at the intersection points of the PIV and SPIV imaging planes for a branching ratio of 33:67.

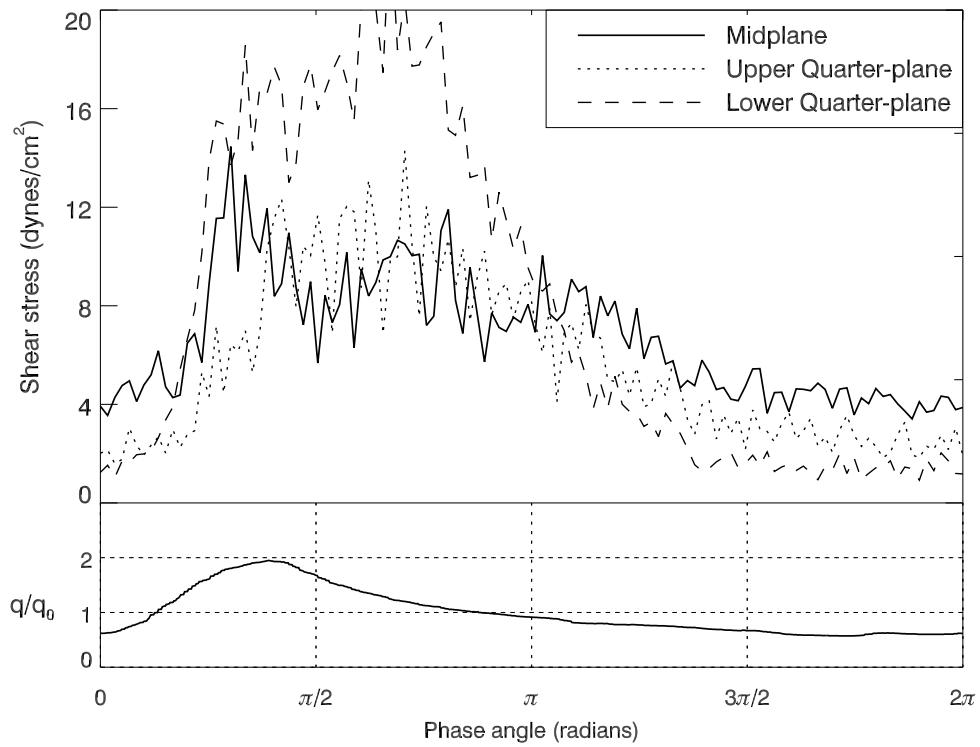


Figure 5.39: WSS magnitudes at the intersection points of the PIV and SPIV imaging planes for a branching ratio of 46:54.

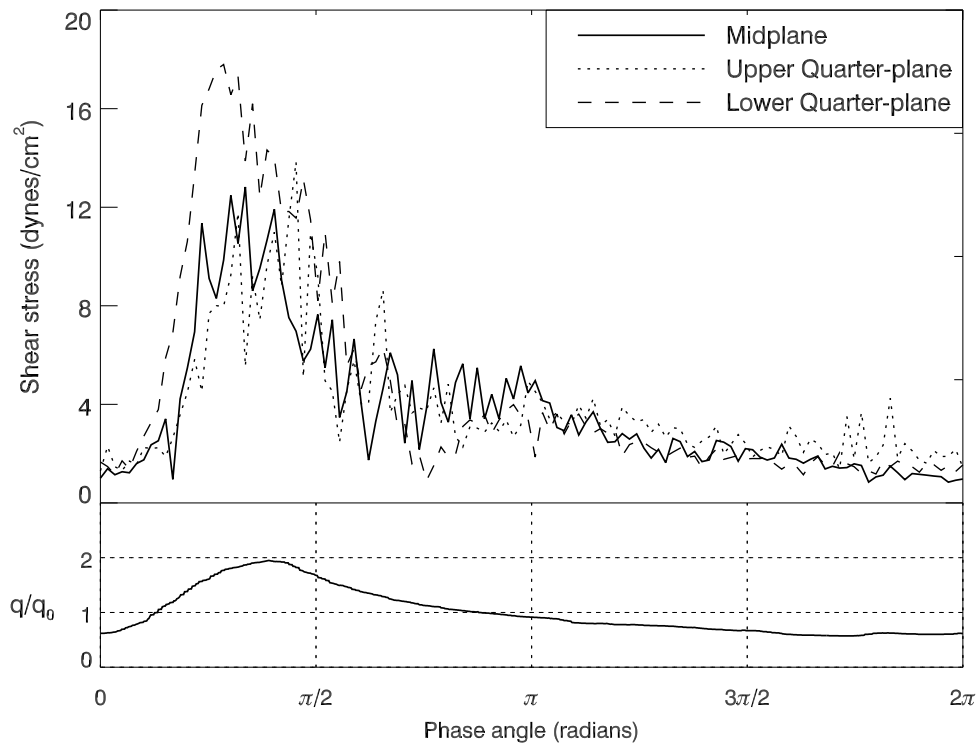


Figure 5.40: WSS magnitudes at the intersection points of the PIV and SPIV imaging planes for a branching ratio of 48:52.

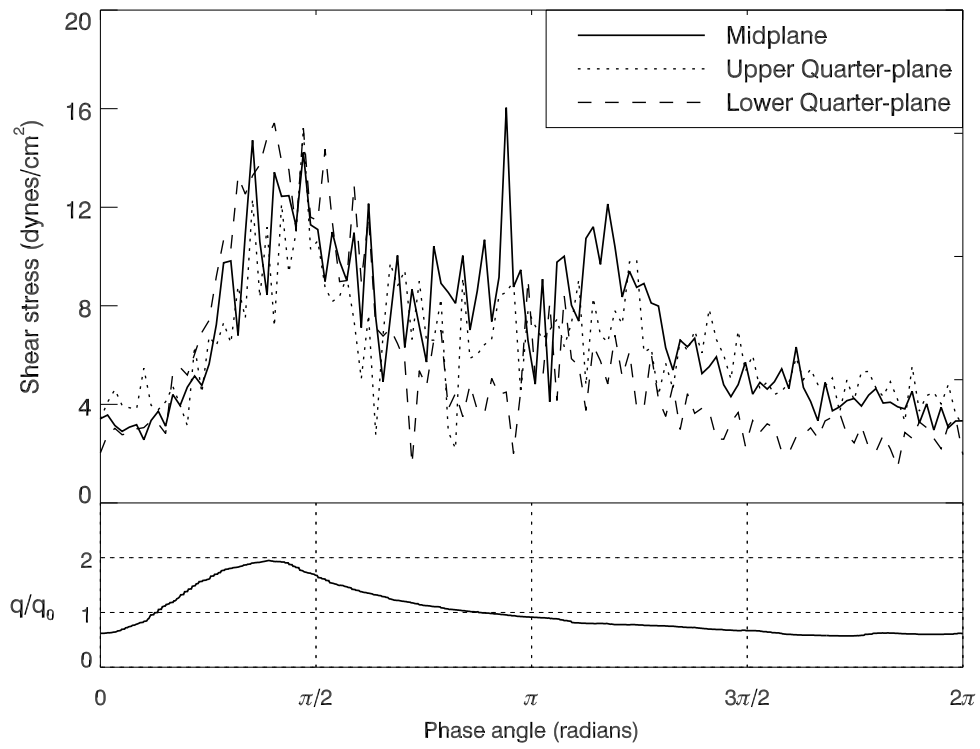


Figure 5.41: WSS magnitudes at the intersection points of the PIV and SPIV imaging planes for a branching ratio of 50:50.

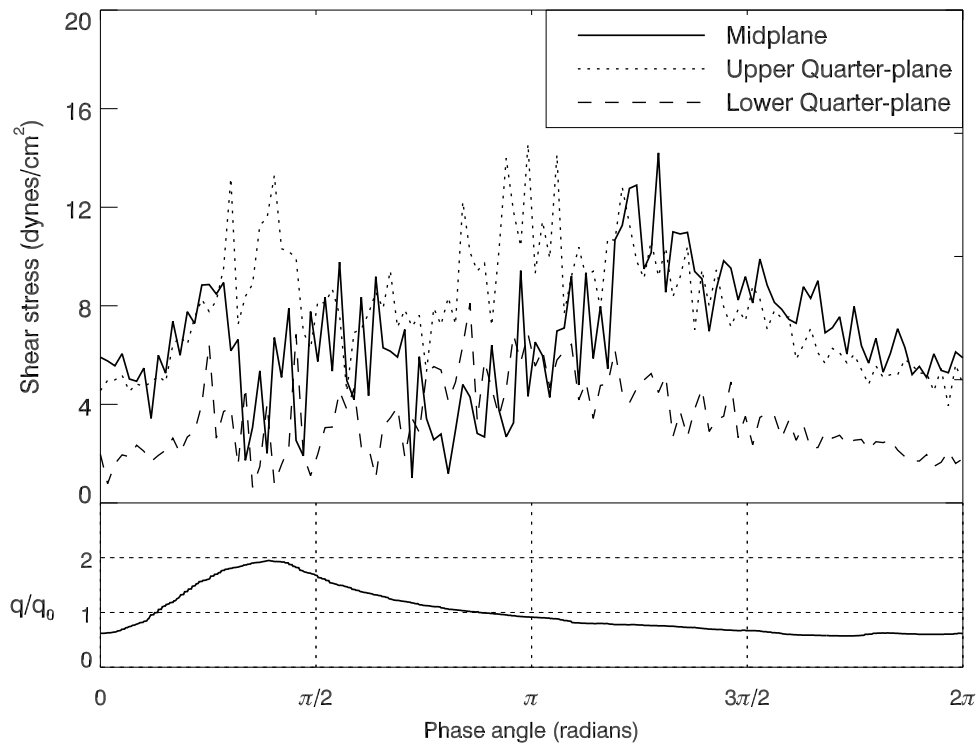


Figure 5.42: WSS magnitudes at the intersection points of the PIV and SPIV imaging planes for a branching ratio of 67:33.

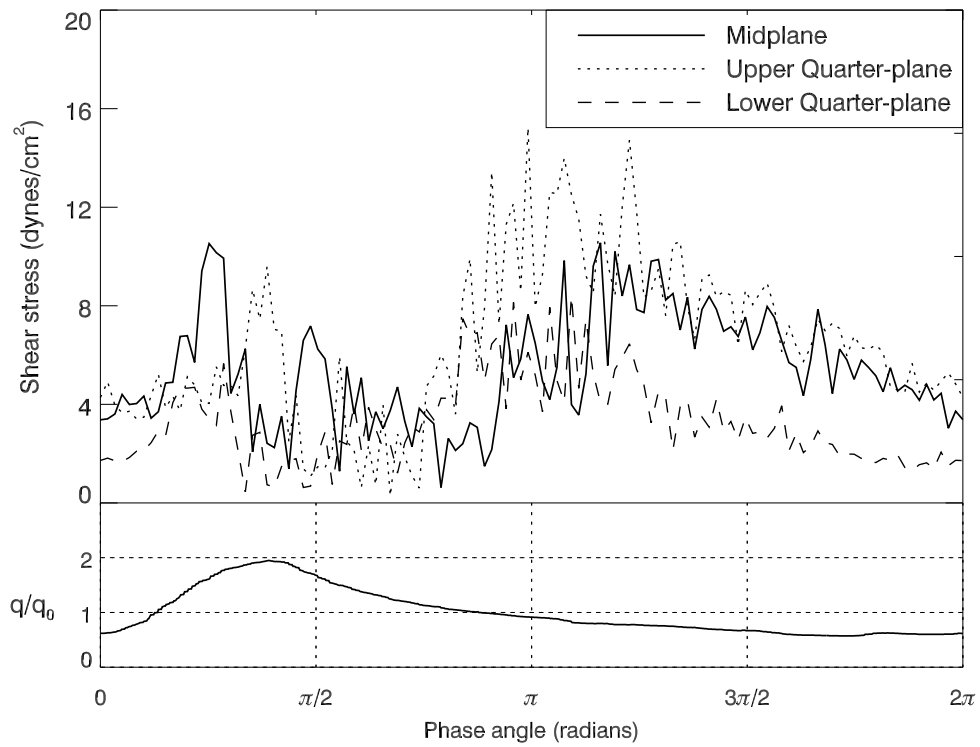


Figure 5.43: WSS magnitudes at the intersection points of the PIV and SPIV imaging planes for a branching ratio of 75:25.

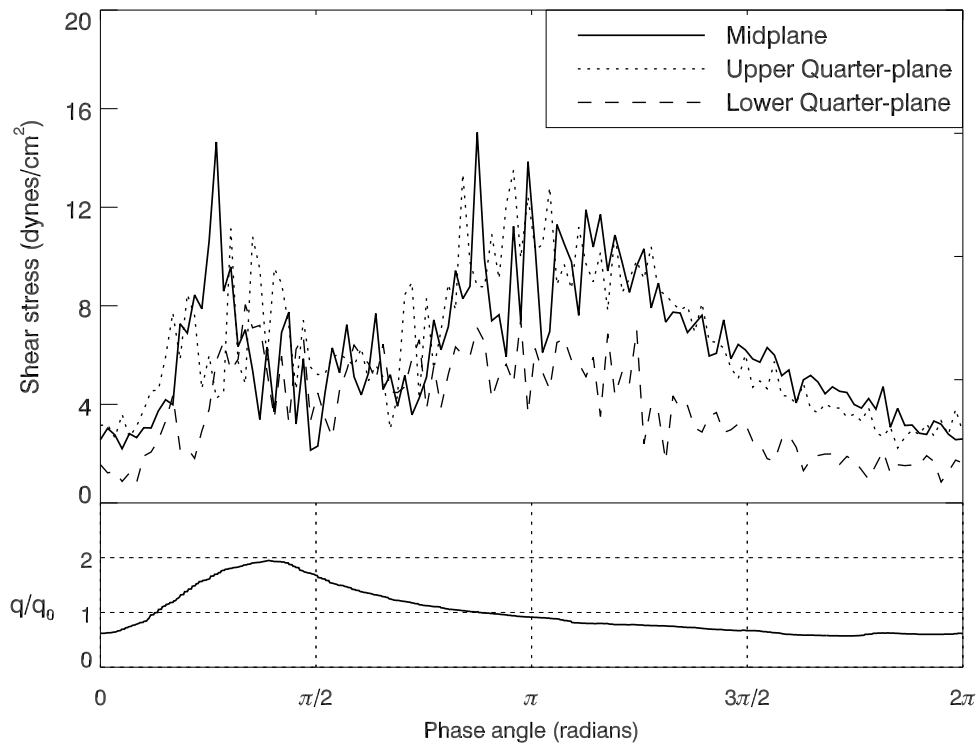


Figure 5.44: WSS magnitudes at the intersection points of the PIV and SPIV imaging planes for a branching ratio of 80:20.

Table 5.1: Maximum WSS values at the intersection points of the PIV and SPIV imaging planes.

Ratio	WSS $\frac{\text{dynes}}{\text{cm}^2}$		
	<i>Midplane</i>	<i>Upper quarter-plane</i>	<i>Lower quarter-plane</i>
20:80	13.2	12.8	10.0
25:75	10.7	12.6	13.0
33:67	12.0	15.7	11.9
46:54	14.5	14.3	23.7
48:52	12.8	13.8	17.8
50:50	16.0	15.1	15.4
67:33	14.2	14.6	8.1
75:25	10.6	15.2	8.4
80:20	15.0	13.5	8.0

Table 5.2: Mean WSS values at the intersection points of the PIV and SPIV imaging planes.

Ratio	WSS $\frac{\text{dynes}}{\text{cm}^2}$		
	<i>Midplane</i>	<i>Upper quarter-plane</i>	<i>Lower quarter-plane</i>
20:80	5.0	6.8	4.4
25:75	5.1	6.5	6.0
33:67	6.4	8.1	5.1
46:54	6.7	5.7	7.8
48:52	3.7	3.9	4.6
50:50	7.0	6.4	5.6
67:33	6.7	7.9	3.4
75:25	5.4	6.5	3.3
80:20	6.3	6.5	3.8

5.5 SPIV: Discussion

The following section discusses the velocity (Figures 5.9-5.17), Q (Figures 5.18-5.26), and WSS (Figures 5.27-5.35) from the SPIV experiments as it relates to understanding the flow within the dome.

5.5.1 Velocity and Q

The velocity field plots are used to determine the flow patterns in this view. It is useful to connect the flow structures found in the FV and PIV to those that appear in the SPIV data. A model of the behavior of the flow within the entire dome can be constructed from this data in conjunction with the PIV data. For instance, the wall jet appears as a jet traveling up the midline, but only near the neck where the SPIV plane intersects the jet. The expanding inlet jet, which travels along the PIV midline, is identified by an upward jet that is visible from neck to the fundus. The circulation region is primarily identified by regions of oppositely signed out of plane velocities. The divergent flow does not intersect the SPIV plane and therefore does not appear in the data.

For the large outlet differentials, the ramp up phase is characterized by the acceleration of the wall jet. The cross section of the wall jet depends on where the SPIV plane divides it. An upward jet can be seen at points A and B where this cross section occurs as well as out-of-plane flow toward the dominant half of the dome. The fluid adjacent to the jet accelerates towards the neck, creating two oppositely signed circulation regions. The circulation regions are driven upward by the jet toward the fundus. As the wall jet decelerates during the ramp down phase, the upward midline jet is replaced with a high velocity

magnitude downward flow. The circulation regions move back down the dome and away from the midline as well. This alters the overall dome pattern as out-of-plane flow is drawn along the dome walls and toward the center before being ejected by the downward jet in the center. By the relaxation phase, the circulation regions have dissipated and the entire dome is dominated by fluid motion downward in a column along the centerline drawing from the entire upper half of the dome like a potential sink.

For small outlet differentials, the expanding inlet jet travels along the length of the centerline. As a result, the cross section of that jet appears longer than for large outlet differentials, connecting from the neck to the dome. Impingement of the jet is clearly visible, driving the flow along the dome wall. A fraction of the flow is driven toward the neck where it exits the dome. The remainder becomes entrained with the upward jet, which clearly outline the circulation regions seen in PIV. Overall behavior in the ramp down and relaxation phases are similar to the large outlet differentials, with the gradual dissipation of the circulation region and the dominance of flow into the neck.

The out-of-plane velocity plots reinforce the observations made in PIV. During the ramp up phase, out-of-plane velocities near the dome wall increase in the direction of the non-dominant side while at the center of the dome, out-of-plane velocities are in the direction of the dominant side. This corresponds to the circulation region in the PIV data along the dome wall of the midplane as well as the curved strong counter-flow and circulation seen in the upper and lower quarter-planes. This pattern persists but reduces in strength during the remainder of the waveform corresponding to the weakening of the flow and restoration of the circulation region that dominates the flow in all of the cases. A

complete picture of the out-of-plane flow allows for some interpolation of the patterns seen in PIV over the entire dome. This suggests the wrapping motion from the impingement of the flow caused by the inlet must wrap over the entire upper hemisphere of the dome during the ramp up and ramp down phase.

The plots of second invariant of the velocity gradient, Q , (Figures 5.18-5.26) provide little detail of the circulation patterns evidenced in the velocity measurements. Q measures the balance between rotation and strain rate. Positive values indicate that the strength of rotation overcomes the strength of the strain locally [16]. Small circulation regions are visible from the velocity plots on either side of the inlet jet. These circulations regions appear at the base of the wall/inlet jet and propagate upward during ramp up before dispersing. The Q plots show no clear sign of these regions. Instead, the only features that stand out are those in black, indicating negative values of Q . The lack of positive regions of Q only indicate that there are no dominant circulation regions with concentrated vorticity, but does not mean that they do not exist.

These observations can be combined to create a model that describes the behavior of flow within the entire dome. A basic schematic of the projected streamlines are presented in Figure 5.45 to aid visualization. The key feature is the wall jet/expanding inlet jet in the PIV data that manifests itself as the upward jet in the SPIV data. During the relaxation phase, the flow is well behaved. For large outlet differentials, this inlet flow originates from the dominant side of the neck, wraps expands around the dome wall on the dominant side, wraps around the dome wall, and merges over the non-dominant half and exits through the non-dominant half of the neck. During the ramp up phase, the inlet flow accelerates

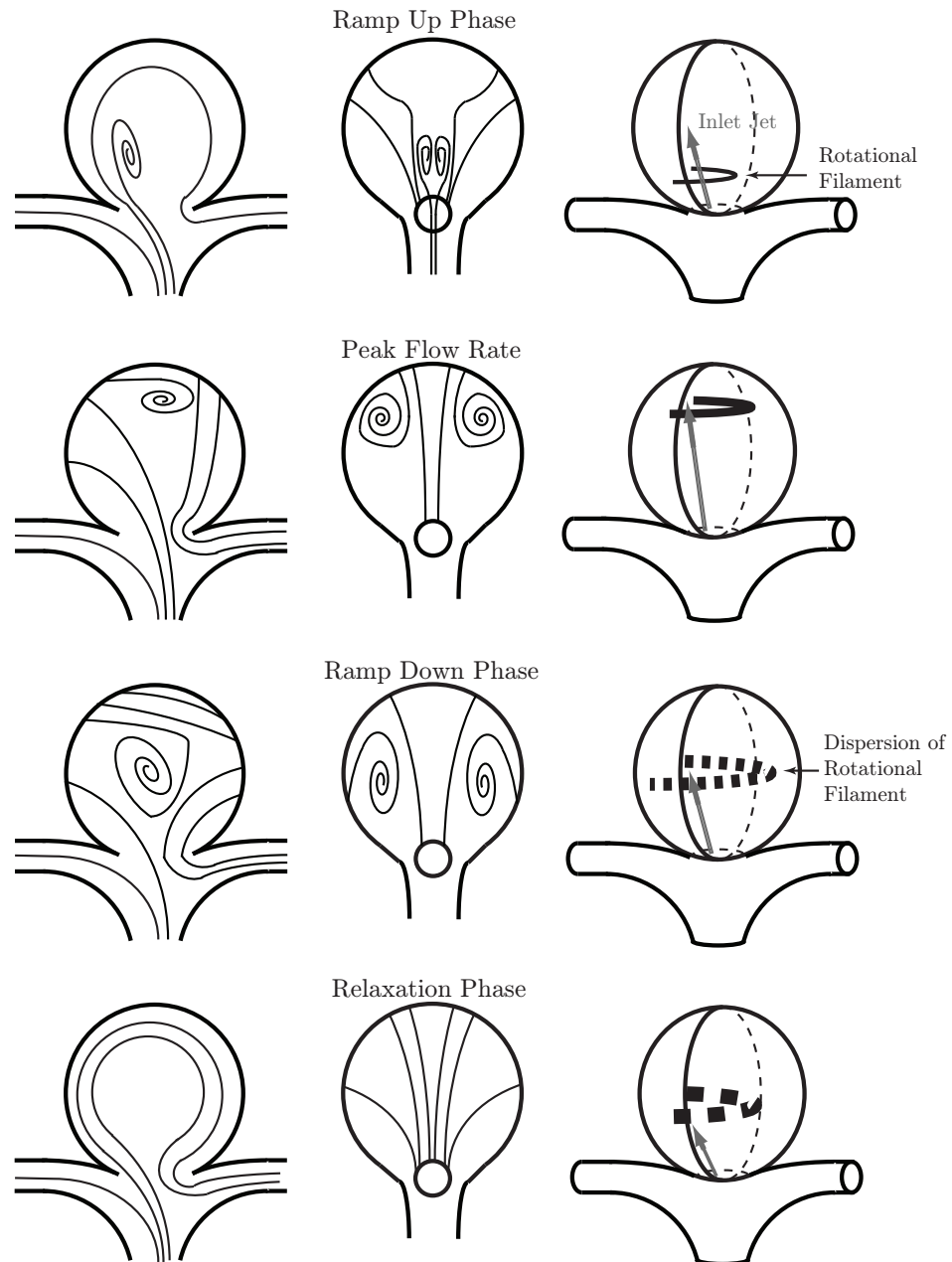


Figure 5.45: Simplified streamlines from the front view (*left*) and right view (*middle*) and a diagram of the rotational filament (*right*) for the general experimental cases.

and forms a jet that impinges on the dome wall in the fundus. The main effect of varying the flow ratio is to change the direction and impingement point of the inlet flow. The smaller the outlet differential, the closer the impingement point is to the tip of the dome. From the impingement point, the flow disperses in all directions as it is drawn toward the non-dominant side of the neck to exit the dome. Looking down upon the dome in the y-direction (i.e. above the tip looking toward the inlet), the projected flow is similar to a doublet. During the ramp down phase, the divergent flow seen in the midplane PIV data is the convergence and divergence of fluid that has wrapped around the dome before exiting the dome at the neck. As the flow enters the relaxation phase, the divergent flow area is relieved with the reduction in the inlet flow.

An alternate method of describing the flow is through tracking the evolution of a *rotational filament* in the dome as shown in the right column of Figure 5.45. A rotational filament is similar in concept to a vortex filament, but for low Reynolds number applications. The filament is the axis of rotation about which fluid parcels around the line rotate around it. As the wall jet accelerates, a filament forms around the neck and increases in size and strength as it travels up the dome. The filament is a U-shaped loop whose ends lie along the wall such that the U-loop encompasses the exposed portion of the wall jet. The filament occurs around the accelerating front of the wall jet, much like the pattern seen in a vortex ring generator. In the latter part of the ramp up phase and the ramp down phase, the cross section of this filament is clearly identified in the PIV Q plots. The magnitude of Q in these plots suggest that that the filament is normal to the PIV planes and that the bulk of rotation occurs in-plane. The SPIV Q plots, which show few positive regions that

stand out, suggest the filament crosses at a skew angle or does not cross the SPIV plane. By the peak flow rate, the rotational filament lies in the upper part of the dome near the fundus. During the ramp down phase, the deceleration of the flow causes the filament to disperse. This dispersion is evidenced by the expansion of the circulation region in the PIV cross sections. Without the expanding inlet jet forcing it upward, the filament travels back toward the neck. By the end of the ramp down phase, the filament reaches an equilibrium point where it will approximately remain throughout the relaxation phase. The filament continues to disperse, encompassing the entire dome before being disrupted by the start of the next cycle.

Interestingly, the observations from the small outlet differentials suggest a simple behavior pattern where the inlet jet is axisymmetric about the midline (Figure 5.46). For this situation, the rotational filament is a ring instead of a U-loop. As the jet accelerates, the rotational ring accelerates and is advected upward. At the peak flow rate, the ring lies just below the fundus. In the velocity plots, this is visualized by the inlet jet rising up along the midline of the dome until it impinges on the fundus and is forced nearly axisymmetrically in all directions. During the ramp down phase, the deceleration of the inlet causes the filament to travel back down the dome and disperse. As with the U-loop, the ring reaches an equilibrium position where it remains during the relaxation phase and continues to disperse until the start of the next cycle. The closest case to this ideal situation is the 48:52 case, where the presence of a pair of circulation regions in the PIV midplane data support the idea of a rotational ring. Even in this case, the flow is by no means symmetric over the entire waveform. During the relaxation phase, the inlet jet favors the

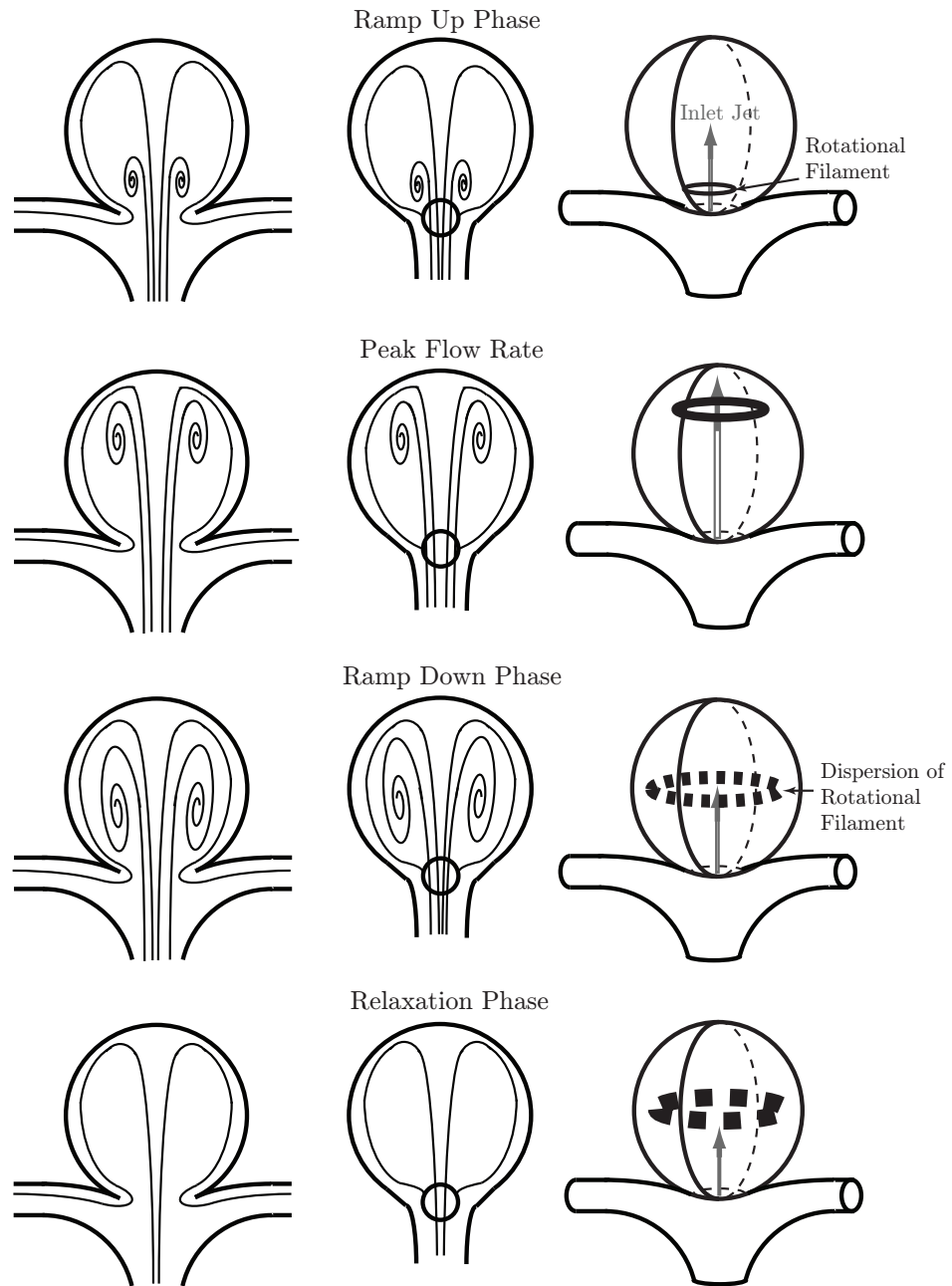


Figure 5.46: Simplified streamlines from the front view (*left*) and right view (*middle*) and a diagram of the rotational filament (*right*) for an idealized symmetric case.

dominant side.

5.5.2 WSS

The WSS behavior in the SPIV plots display simpler characteristics than in PIV. The primary feature is a region of elevated WSS along the fundus (approximately -45° to 45°) during the ramp up and ramp down phase. This is evidenced by the common patterns in Figures 5.27-5.35. The increase in WSS is symmetric about the tip for small outlet differentials; peak magnitudes in the range of $24.7\text{-}27.3 \frac{\text{dynes}}{\text{cm}^2}$ are obtained with opposite directions on either side of the dome. For large outlet differentials, the divide between WSS directions occurs in the -30° to -60° range. Unlike the PIV data, there is no change in WSS over all of the cases. WSS magnitudes for the large outlet differentials range from $15.5\text{-}23.2 \frac{\text{dynes}}{\text{cm}^2}$.

The complete WSS magnitude is calculated for the three intersection points between PIV and SPIV imaging planes on the upper half of the dome. WSS is plotted against the flow waveform for all flow ratios (Figures 5.27-5.35). The points are named by the PIV plane that intersects them. Behaviors for the points corresponding to the intersection of the SPIV plane with the PIV midplane, upper quarter-plane, and lower quarter-plane are similar for a given flow ratio. Peak (Table 5.1) and mean (Table 5.2) WSS magnitudes for these points are tabulated.

For large outlet differentials, the overall trend is a rapid increase during the ramp up phase, followed by a rapid drop at the beginning of the ramp down phase. WSS magnitude remains steady for the following duration in the ramp down phase before gradually

rising during the relaxation phase before slowly decreasing again. This corresponds with the motion of the instantaneous peak WSS seen in the PIV data, which travels along the dome over the course of the waveform. During the ramp up phase, this region approaches the observed points causing the rise in WSS magnitude. After the instantaneous peak WSS region has momentarily crossed the point, the WSS magnitude drops rapidly. The second increase during the ramp down and relaxation phase corresponds to the leveling off of WSS magnitudes seen in the PIV and SPIV data over the entire dome. Peak WSS values for large outlet differentials are in the range of 8.0-15.7 $\frac{\text{dynes}}{\text{cm}^2}$ (Table 5.1).

For small outlet differentials, the WSS magnitudes correlate with the changes in flow rate. Magnitudes at all three points rise during the ramp up phase. The trends in the ramp down phase vary by flow ratio. In the 46:54 case, the midplane and upper quarter-plane WSS magnitudes remain steady before descending in the relaxation phase. In the lower quarter plane, the WSS magnitude continues to rise, peaking in the ramp down phase and falling during the relaxation phase. In the 48:52 case, all three points exhibit a decline in WSS magnitudes after reaching their peak at the maximum of the flow waveform. The 50:50 case exhibits similar behavior to the large outlet differentials. After the ramp up phase, there is a slight drop and rise in WSS magnitudes during the ramp down phase, before gradually declining during the relaxation phase. Peak WSS values for small outlet differentials are in the range of 12.8-23.7 $\frac{\text{dynes}}{\text{cm}^2}$ (Table 5.1).

Mean WSS values range from 3.3-7.9 $\frac{\text{dynes}}{\text{cm}^2}$ (Table 5.2). Lowest mean WSS values are on average at the lower quarter-plane point with the exception of the critical cases. For large outlet differentials, the highest mean WSS is seen at the upper quarter-plane point.

For the 50:50 case, the highest mean WSS is located at the tip and the lowest mean WSS at the lower quarter-plane. In the 46:54 case, mean WSS magnitudes are similar at both the midplane and lower quarter-plane. In the 48:52 case, all mean WSS magnitudes are consistently in the lower range of values. The mean tip WSS value is well lower than all of the other cases at $3.7 \frac{\text{dynes}}{\text{cm}^2}$. This is the case most closely resembles the symmetric flow, with the expanding inlet jet centered along the midline of the dome.

The WSS measurements provide some insight into the factors that may play a role in aneurysm growth. Both the peak ($20 \frac{\text{dynes}}{\text{cm}^2}$) and mean ($5 \frac{\text{dynes}}{\text{cm}^2}$) measured are well below the high WSS damage limit suggested by Fry [20] of $300 \frac{\text{dynes}}{\text{cm}^2}$. Mean WSS magnitudes in all cases are near the low WSS limit of $3 \frac{\text{dynes}}{\text{cm}^2}$ suggested by Walpola et al. [64]; however, peak WSS magnitudes are several times higher than this limit. Recall though that the WSS values from this experiment may underestimate the true *in vivo* WSS by up to 25% because a Newtonian fluid was used. Even accounting for this error, the mean WSS values are on the same order as the values set forth by Walpola et al. In particular, the tip during 48:52 case mean in-plane WSS becomes vanishingly small in the PIV data and measures $3.72 \frac{\text{dynes}}{\text{cm}^2}$ when combined with the SPIV data. This suggests that an aneurysm with a nearly axisymmetric jet along the midline may have a tip that experiences vanishingly small mean WSS. Such a state would leave the tip prone to endothelial cell death. Without more evidence, these data only suggest that high WSS is an improbable factor in WSS growth. Lower than normal WSS magnitudes occur in the dome suggesting a correlation with aneurysm growth. However, without establishing causation, low WSS cannot be confirmed as a cause nor diagnostic criterion at this time.

Chapter 6

Closing Remarks

A series of experiments were conducted to study the overall flow behavior and the wall shear stresses (WSS) acting on a cerebral saccular aneurysm. A flow phantom was constructed that captures the basic geometry of a saccular aneurysm at the basilar artery bifurcation. To replicate physiological conditions, the model used an inlet profile based on patient measurements and matching Reynolds and Sexl-Womersley numbers. Three experiments are detailed in this dissertation. Flow visualization (FV) experiments allow qualitative features of the flow to be identified. Particle image velocimetry (PIV) experiments measured the in-plane velocity and WSS along three planes. Stereoscopic particle image velocimetry (SPIV) was used on a plane orthogonal to the PIV plane. This experiment provided a limited 3D velocity field and in-plane WSS measurements. Combined with the PIV data, the total WSS magnitudes were reconstructed over multiple points over the dome.

The observations made in FV are combined with the velocity measurements from

PIV and SPIV to provide a picture of the flow within the aneurysm model. A strong inflow manifests itself as a wall jet or expanding inlet jet. The jet wraps around the dome, creating a circulation region at the center of the dome. The oscillation of the flow rate alters the behavior of the inlet flow and circulation region. In all of the flows, the flow displayed direction preference that allowed one of the outlets to be termed dominant. An alternate approach to characterizing the flow is through the tracking of a rotational filament. The filament is generated by the acceleration and expansion of the inlet flow. The filament is advected upwards during the ramp up phase before being drawn back toward the center of the dome and dissipating during the ramp down and relaxation phases.

The results from the 48:52 branching ratio suggest the possibility of an axisymmetric flow pattern, where neither outlet is dominant. Steinmann et al. [61] argues that computational fluid dynamics (CFD) simulations that assume a perfectly symmetric boundary condition in aneurysm flows may lose the directional preferences that exist. This experiment serves as an example for this concern. For a perfectly symmetric model, the expected result is an axisymmetric inlet flow jet that forms a rotational ring. This perfectly symmetric flow was impossible to achieve in experiments due to considerations such as small asymmetries in the model or insufficient resolution of the outlet valves. Real aneurysms may have directional preferences that are not captured in simulations. It is important for experiments and patient imaging to determine these directional characteristics and the boundary conditions associated with them.

One of the main aims of the experiments was to determine the WSS in the aneurysm model. In-plane WSS magnitudes from PIV and SPIV experiments were as

high as $18.6 \frac{\text{dynes}}{\text{cm}^2}$ and $31.0 \frac{\text{dynes}}{\text{cm}^2}$ respectively. Changes in the spatial distribution of WSS was primarily seen in the PIV data. Flows with large outlet differentials had the region of instantaneous peak in-plane WSS travel along most of the dome over the course of a cycle. Flows with small outlet differentials had the travel of the region of instantaneous peak in-plane WSS was confined to the fundus. The 48:52 case contained multiple locations where the PIV in-plane WSS became vanishingly small near the tip. Complete WSS magnitude measurements were only available at the three intersections of the PIV and SPIV planes, one of which was the tip. Measured peak WSS magnitudes along the tip ranged from 11.0- $16.0 \frac{\text{dynes}}{\text{cm}^2}$, which match well with the values from simulations by Shojima et al. [56]. Mean WSS magnitudes along the tip ranged from 3.7- $7.0 \frac{\text{dynes}}{\text{cm}^2}$. The lowest value, found in the 48:52 case, is very close to the $3 \frac{\text{dynes}}{\text{cm}^2}$ limit for endothelial cell death suggested by Walpola et al. [64]. If low mean WSS magnitude is directly correlated with aneurysm growth, then the data suggest that the mean values near the fundus may harbor aneurysm growth. However, further study is required of endothelial cells and arterial walls to determine the effects of the mean WSS versus peak WSS before any conclusive cause can be drawn.

While CFD simulations can calculate WSS distributions for an arbitrary geometry, it is important for experiments to be conducted to validate these results and capture any characteristics that maybe lost, such as directional preference. However, future work must be able to determine out-of-plane gradients accurately for a complete WSS measurement. This model could be improved by the addition of an adjustable target, allowing SPIV measurements over multiple closely spaced cross-sections. Newer flow measurement tools such as holographic PIV could capture the flow velocities of a volume of the fluid, although

the experiment complexity increases considerably. Another refinement would be the use of a non-Newtonian working fluid that mimics blood's viscosity profile. Removing this source of error will greatly improve the accuracy of the WSS measurements. Lastly, it would be ideal to use a model based on physiological geometry and with inlet and outlet flow rates based on patient measurements. This experiment has demonstrated that the flow behavior varies considerably with the branching ratio. To determine how this variance manifests itself in reality, it would be useful to apply actual patient flow measurements and see how those results compare with deviations in the boundary conditions. The overall goal of improved research would be the development of more accurate simulations and the application of these simulations to diagnostic tools.

Bibliography

- [1] T. Acharya and A. Ray. *Image Processing: Principles and applications*. Wiley, Hoboken, NJ, 2005.
- [2] S. Ahn, D. Shin, S. Tateshima, K. Tanishita, F. Vinuela, and S. Sinha. Fluid-induced wall shear stress in anthropomorphic brain aneurysm models: MR phase-contrast study at 3t. *Journal of Magnetic Resonance Imaging*, 25:1120–1130, 2007.
- [3] J. Allcock and P. Canham. Angiographic study of the growth of intracranial aneurysms. *Journal of Neurosurgery*, 45:617–621, December 1976.
- [4] R. E. Altenhofen, editor. *Manual of Photogrammetry*, chapter Rectification, page 723. American Society of Photogrammetry, 1980.
- [5] M. P. Arroyo and C. A. Greated. Stereoscopic particle image velocimetry. *Measurement Science Technology*, 2:1181–1186, 1991.
- [6] J. Bale-Glickman. *Experimental Studies of Physiological Flows in Replicated Diseased Carotid Bifurcations*. PhD thesis, University of California, Berkeley, 2005.

- [7] Ch. Brücker. 3-d scanning-particle-image-velocimetry: Technique and application to a spherical cap wake flow. *Applied Scientific Research*, 56:157–179, 1996.
- [8] A. Burleson, C. Strother, and V. Turitto. Computer modeling of intracranial saccular and lateral aneurysms for the study of their hemodynamics. *Neurosurgery*, 37(4):774–784, October 1995.
- [9] P. B. Canham and G. G. Ferguson. A mathematical model for the mechanics of saccular aneurysms. *Neurosurgery*, 15(2):291–295, 1985.
- [10] C. Caro, J. Fitz-Gerald, and R. Schroter. Atheroma and arterial wall shear observation, correlation and proposal of a shear dependent mass transfer mechanism for atherogenesis. *Proceedings of the Royal Society of London*, 177:109–159, 1971.
- [11] J. Cebal, M. Castro, J. Burgess, R. Pergolizzi, M. Sheridan, and C. Putman. Characterization of cerebral aneurysms for assessing risk of rupture by using patient-specific computational hemodynamics models. *American Journal of Neuroradiology*, 26:2550–2559, November 2005.
- [12] The Dow Chemical Company. The dow optim glycerine resources. World Wide Web electronic publication, 2009. <http://www.dow.com/glyverine/resources/index.html>.
- [13] T. Crawford. Some observations on the pathogenesis and natural history of intracranial aneurysms. *Journal of Neurology, Neurosurgery, and Psychiatry*, 22:259–266, January 1959.

- [14] M. R. Crompton. Mechanism of growth and rupture in cerebral berry aneurysms. *British Medical Journal*, 1:1138–1142, January 1966.
- [15] C. Drake. Progress in cerebrovascular disease. management of cerebral aneurysm. *Stroke*, 12:273–283, 1981.
- [16] Y. Dubief and F. Delcayre. On coherent-vortex identification in turbulence. *Journal of Turbulence*, 1(1):11, January 2000.
- [17] J. Edlow and L. Caplan. Avoiding pitfalls in the diagnosis of subarachnoid hemorrhage. *New England Journal of Medicine*, 342(1):29–36, 2000.
- [18] R. Fogelholm, J. Hernesniemi, and M. Vapalahti. Impact of early surgery on outcome after aneurysmal subarachnoid hemorrhage. a population-based study. *Stroke*, 24:1649–1654, November 1993.
- [19] R. Frayne, D. Holdsworth, L. Gowman, D. Rickey, M. Drangova, A. Fenster, and B. Rutt. Computer-controlled flow simulator for MR flow studies. *Journal of Magnetic Resonance Imaging*, 2:605–612, September 1992.
- [20] D. Fry. Acute vascular endothelial changes associated with increased blood velocity gradients. *Circulation Research*, 22:165–197, February 1968.
- [21] Y. C. Fung. *Biomechanics: Mechanical Properties of Living Tissues*. Springer-Verlag, New York, 2nd ed. edition, 1993.
- [22] F. Gijzen, E. Allanic, F. van de Vosse, and J. Janssen. The influence of non-Newtonian

- properties of blood on the flow in large arteries: unsteady flow in a 90° curved tube. *Journal of Biomechanics*, 32:705–713, 1999.
- [23] F. Gijsen, F. van de Vosse, and J. Janssen. The influence of the non-Newtonian properties of blood on the flow in large arteries: steady flow in a carotid bifurcation model. *Journal of Biomechanics*, 32:601–608, 1999.
- [24] H. Gray. *Anatomy of the Human Body*. Bartelby, Philadelphia, 20th ed., www.bartleby.com/107/146.html edition, 2000.
- [25] D. Holdsworth, D. Rickey, M. Drangova, D. Miller, and A. Fenster. Computer-controlled positive displacement pump for physiological flow simulation. *Medical and Biological Engineering and Computing*, 29(6):565–570, November 1991.
- [26] J. Hop, G. Rinkel, A. Algra, and J. van Gijn. Quality of life in patients and partners after aneurysmal subarachnoid hemorrhage. *Stroke*, 29:798–804, 1998.
- [27] P. Hoskins, T. Anderson, and R. Pelissier. A computer controlled flow phantom for generation of physiological doppler waveforms. *Physics in Medicine and Biology*, 34:1709–1717, 1989.
- [28] J. D. Humphrey and C. A. Taylor. Intracranial and abdominal aortic aneurysms: Similar differences, and need for a new class of computational models. *Annual Review of Biomedical Engineering*, 10:221–46, 2008.
- [29] T. Inagawa, Y. Tokuda, N. Ohbayashi, M. Takaya, and K. Moritake. Study of aneurysmal subarachnoid hemorrhage in izumo city, japan. *Stroke*, 26(5):761–766, May 1995.

- [30] S. Inci and R. Spetzler. Intracranial aneurysms and arterial hypertension: A review and hypothesis. *Surgical Neurology*, 53(6):530–542, June 2000.
- [31] J. Jeong and F. Hussein. On the identification of a vortex. *Journal of Fluid Mechanics*, 28:69–94, 1995.
- [32] L. Jou and S. Berger. Numerical simulations of the flow in the carotid bifurcation. *Theoretical and Computational Fluid Dynamics*, 10:239–248, 1998.
- [33] T. Kato, T. Indo, E. Yoshida, Y. Iwasaki, M. Sone, and G. Sobue. Contrast-enhanced 2D cine phase MR angiography for measurement of basilar artery blood flow in posterior circulation ischemia. *American Journal of Neuroradiology*, 23(6):530–542, September 2002.
- [34] K. Khanafer, P. Gadhoke, R. Berguer, and J. Bull. Modeline pulsatile flow in aortic aneurysms: Effect of non-newtonian properties of blood. *Biorheology*, 43:661–679, 2006.
- [35] S. Kondo, N. Hashimoto, H. Kikuchi, F. Hazama, I. Nagata, and H. Kataoka. Cerebral aneurysms arising at nonbranching sites. an experimental study. *American Journal of Neuroradiology*, 28(2):398–403, February 1997.
- [36] D. Krex, H. K. Schackert, and G. Schackert. Genesis of cerebral aneurysms - an update. *Acta Neurochirurgica*, 143(5):429–449, June 2001.
- [37] J. Ku, M. Draney, F. Arko, W. Lee, F. Chan, N. Pelc, C. Zarings, and C. Taylor. *In Vivo* validation of numerical prediction of blood flow in arterial bypass grafts. *Annals of Biomedical Engineering*, 30:743–752, 2002.

- [38] J. A. Lee. Medlineplus medical encyclopedia: Aneurysm. World Wide Web electronic publication, 2006. <http://www.nlm.nih.gov/medlineplus/ency/article/001122.htm>.
- [39] S. Ling, H. Atabek, and D. Patel. Analysis of coronary flow fields in thoracotomized dogs. *Circulation*, 37:752–761, 1975.
- [40] W. T. Longstretch, L. M. Nelson, T. D. Koepsell, and G. vanBelle. Clinical course of spontaneous subarachnoid hemorrhage: a population-based study in king county, washington. *Biorheology*, 43(4):712–718, April 1993.
- [41] P. Mayer, I. Awad, R. Todor, K. Harbaugh, G. Varnavas, T. Lansen, P. Dickey, and R. Harbaugh. Misdiagnosis of symptomatic cerebral aneurysm: Prevalence and correlation with outcome at four institutions. *Stroke*, 27(9):1558–1563, September 1996.
- [42] H. Meng, Z. Wang, Y. Hoi, L. Gao, E. Metaxa, D. D. Swartz, and J. Kolega. Complex hemodynamics at the apex of an arterial bifurcation induces vascular remodeling resembling cerebral aneurysm initiation. *Stroke*, 38:1924–1931, 2007.
- [43] W. Merzkirch. *Flow Visualization*. Academic Press, New York, 2nd ed. edition, 1987.
- [44] P. Mitchell and J. Jakubowski. Estimate of the maximum time interval between formation of cerebral aneurysm and rupture. *Journal of Neurology, Neurosurgery, and Psychiatry*, 69:760–767, 2000.
- [45] T. Nguyen, Y. Biadillah, R. Mongrain, J. Brunette, J.-C. Tardif, and O. F. Bertrand. A method for matching the refractive index and kinematic viscosity of a blood ana-

- log for flow visualization in hydraulic cardiovascular models. *Journal of Biomedical Engineering*, 126(4):529–535, August 2004.
- [46] J. Ortega, D. Maitland, T. Wilson, O. Savas, W. Tsai, and D. Saloner. Vascular dynamics of a shape memory polymer foam aneurysm treatment technique. *Journal of Biomedical Engineering*, 35(11):1870–1884, 2007.
- [47] L. Parlea, R. Fahrig, D. W. Holdsworth, and S. P. Lownie. An analysis of the geometry of saccular intracranial aneurysms. *American Journal of Neuroradiology*, 20:1079–1089, 1999.
- [48] D. Peters, A. Kassam, E. Feingold, E. Heidrich-O’Hare, E. Yonas, R. Ferrell, and A. Brufsky. Molecular anatomy of an intracranial aneurysm: Coordinated expression of genes involved in wound healing and tissue remodeling. *Stroke*, 32:1036–1042, 2001.
- [49] D. Plewes, S. Urchuk, S. Kim, and I. Soutar. An MR compatible flow simulator for intravascular pressure simulation. *Medical Physics*, 22:1111–1115, 1995.
- [50] M. Raffel, C. Willert, S. Wereley, and J. Kompenhans. *Particle Image Velocimetry*. Springer, New York, 2nd ed. edition, 2007.
- [51] E. C. Raps, J. D. Rogers, S. L. Galetta, R. A. Solomon, L. Lennihan, L. M. Klebanoff, and M. E. Fink. The clinical spectrum of unruptured intracranial aneurysms. *Arch Neurol.*, 50(3):265–268, March 1993.
- [52] V. Rayz, L. Bousset, G. Acevedo-Bolton, A. Marin, W. Young, M. Lawton, R. Higashida, and D. Saloner. Numerical modeling of the flow in intracranial aneurysms:

- Prediction of regions prone to thrombus formation. *Annals of Biomedical Engineering*, 36(11):1793–1804, November 2008.
- [53] R. Reneman, T. van Merode, P. Hicks, and A. Hoeks. Flow velocity patterns in and distensibility of the carotid artery bulb in subjects of various ages. *Circulation*, 71(3):500–509, 1985.
- [54] R. L. Sacco, P. A. Wolf, N. E. Bharuch, S. L. Meeks, W. B. Kannel, L. J. Charette, P. M. McNamara, E. P. Palmer, and R. D’Agostino. Subarachnoid and intracerebral hemorrhage: natural history, prognosis, and precursive factors in the framingham study. *Neurology*, 34(7):847–54, July 1984.
- [55] W. Schievink, E. Wijdicks, J. Parisi, D. Piepgras, and J. Whisnant. Sudden death from aneurysmal subarachnoid hemorrhage. *Neurology*, 45(5):871–874, May 1995.
- [56] M. Shojima, M. Oshima, K. Takagi, R. Torii, M. Hayakawa, K. Katada, A. Morita, and T. Kirino. Magnitude and role of wall shear stress on cerebral aneurysm. computational fluid dynamic study of 20 middle cerebral artery aneurysms. *Stroke*, 35:2500–2505, October 2004.
- [57] M. Shojima, M. Oshima, K. Takagi, R. Torii, K. Nagata, A. Morita, and T. Kirino. Role of the bloodstream impacting force and the local pressure elevations in the rupture of cerebral aneurysms. *Stroke*, 36:1933–1938, September 2005.
- [58] M. Sholl and O. Savas. A fast lagrangian piv method for study of general high-gradient flows. *AIAA 35th Aerospace Meetings and Exhibits*, 1:97–0493, 1998.

- [59] H. Steiger, D. Liepsch, A. Poll, and H. Reulen. Hemodynamic stress in terminal saccular aneurysms: A laser-doppler study. *Heart Vessels*, 4:162–169, 1998.
- [60] H. Steiger, A. Poll, D. Liepsch, and H. Ruelen. Basic flow structure in saccular aneurysms: A flow visualization study. *Biorheology*, 24(6):689–710, 1987.
- [61] D. Steinman, S. Kehoe, M. Ford, H. Nikolov, and D. Holdsworth. Dancing on the knife-edge of symmetry: On the misuse of symmetric models for studying blood flow dynamics. In *2003 Summer Bioengineering Conference*, June 2003.
- [62] L. Tsuei and O. Savas. Treatment of interfaces in particle image velocimetry. *Experiments in Fluids*, 29(3):203–214, September 2000.
- [63] H. Ujiie, Y. Tamano, K. Sasaki, and T. Hori. Is the aspect ratio a reliable index for predicting the rupture of a saccular aneurysm. *Neurosurgery*, 48(3):495–503, March 2001.
- [64] P. Walpola, A. Gotlieb, and B. Langille. Monocyte adhesion and changes in endothelial cell number, morphology, and f-actin distribution elicited by low shear stress in vivo. *American Journal of Pathology*, 142(5):1392–1400, May 1993.
- [65] D. Weibers. Unruptured intracranial aneurysms - risk of rupture and risks of surgical intervention. *New England Journal of Medicine*, 339(24):1725–33, December 1998.
- [66] D. Weibers, J. Whisnant, T. Sundt, and M. O’Fallon. The significance of unruptured intracranial saccular aneurysms. *Journal of Neurosurgery*, 66:23–29, 1987.
- [67] B. Weir, C. Amidei, G. Kongable, J. M. Findlay, N. F. Kassell, J. Kelly, L. Dai, and

- T. Karrison. The aspect ratio (dome/neck) of ruptured and unruptured aneurysms. *Journal of Neurosurgery*, 99(3):447–451, September 2003.
- [68] R. L. Whitmore. *Rheology of the Circulation*. Pergamon, London, 1st ed. edition, 1968.
- [69] C. Willert. Stereoscopic digital particle image velocimetry for application in wind tunnel flows. *Measurement Science Technology*, 8:1465–1479, 1997.
- [70] P. Wong, M. Graves, and D. Lomas. Integrated physiological flow simulator and pulse sequence monitoring system for MRI. *Medical and Biological Engineering and Computing*, 46(4):399–406, April 2008.